ABSTRACT

Title of Dissertation:	GENETICS, AGES, AND CHEMICAL COMPOSITIONS OF IRON METEORITES
	Connor Hilton, Doctor of Philosophy, 2020
Dissertation directed by:	Professor Richard Walker, Department of Geology

Comparison of genetic isotopic compositions of iron meteorites with metal-silicate segregation ages suggests that the isotopic composition of the NC reservoir changed with time. By contrast, no such age-linked changes in the genetic isotopic compositions of iron meteorites from the CC reservoir are observed. Results of comparing bulk planetesimal genetic isotopic compositions with bulk planetesimal siderophile element chemical characteristics indicate that the processes responsible for isotopic heterogeneity in the early Solar System are not discerned by the siderophile element chemical characteristics of planetesimals. Iron meteorite parent bodies from the CC reservoir typically have smaller relative cores and a greater proportion of the Fe content in the mantle, consistent with the CC reservoir being a more oxidized environment, such as the outer Solar System, compared to the NC reservoir. The chemical characteristics of iron meteorite parent bodies, including bulk core FeS/Fe ratios and oxidation states, may form relationships with core formation

ages, but whether these characteristics can account for potential differences in the formation ages of NC- and CC-type parent bodies presently cannot be constrained.

GENETICS, AGES, AND CHEMICAL COMPOSITIONS OF IRON METEORITES

by

Connor D. Hilton

Dissertation submitted to the Faculty of the Graduate School of the
University of Maryland, College Park, in partial fulfillment
of the requirements for the degree of
Doctor of Philosophy
2020

Advisory Committee:
Professor Richard J. Walker, Chair
Associate Professor Ricardo D. Arevalo
Research Scientist Richard D. Ash
Dr. Timothy J. McCoy
Professor Alice Mignerey (Dean's Representative)

Preface

Portions of this dissertation have been previously published in peer-reviewed journals or are currently in preparation or revision. Specifically, chapters 2 and 3 have been published. Chapters 4 and 5 are currently in revision and in preparation, respectively. The contributions of each co-author to each chapter of this dissertation are outlined here.

Chapter 2

Hilton C.D., Bermingham K.R., Walker R.J., McCoy T.J. (2019) Genetics, crystallization sequence, and age of the South Byron Trio iron meteorites: New insights to carbonaceous chondrite (CC) type parent bodies. *Geochim. Cosmochim. Acta* **251**, 217-228.

In this study, I collected all Os, Mo, Ru, and W isotope data and performed all trace element and thermal modeling. Katherine Bermingham provided guidance in the laboratory and Rich Walker collected the highly siderophile element and ^{187}Os isotope data. Tim McCoy helped interpret the data. I wrote the first draft of this manuscript and edits were provided by co-authors.

Chapter 3

Hilton C.D. and Walker R.J. (2020) New implications for the origin of the IAB main group iron meteorites and the isotopic evolution of the noncarbonaceous (NC) reservoir. *Earth Planet. Sci. Lett.* **540**, 116248.

I collected all Os, Pt, and W isotope data and wrote the first draft of this manuscript. Rich Walker helped interpret the data and edit the manuscript.

Chapter 4

Hilton C.D., Ash R.D., and Walker R.J. (*In revision*) Origin of the Eagle Station Pallasites from the IIF iron meteorite core. *Meteorit. Planet. Sci*.

In this study, I collected all highly siderophile element and Os isotope data and performed all trace element modeling. Richard Ash collected the siderophile element abundances by LA-ICP-MS. I interpreted all data and wrote the first draft of this manuscript. Richard Ash and Rich Walker provided edits.

Chapter 5

Hilton C.D, Ash R.D., and Walker R.J. (*In prep*) Constraints on the chemical characteristics of the noncarbonaceous (NC) and carbonaceous (CC) nebular reservoirs.

I collected highly siderophile element and Os isotope data for the IIAB, IID, and IIIF iron meteorites and performed all trace element modeling. The highly siderophile element and Os isotope data for the IIIAB iron meteorites were collected by a previous student under the supervision of Rich Walker. I interpreted all data and wrote the first draft of this manuscript. Richard Ash and Rich Walker provided edits.

Acknowledgements

I would like to thank Rich Walker, Ricardo Arevalo, Richard Ash, Tim McCoy, and Alice Mignerey for serving on my PhD committee as well as reading my dissertation and providing feedback. Rich Walker, Ricardo Arevalo, Richard Ash, and Tim McCoy are additionally thanked for their support throughout the proposal process and for their guidance over the course of this PhD. I am grateful for the funding provided by the University of Maryland and NASA for this dissertation and thankful for the meteorites provided to me by Arizona State University, the Cascadia Meteorite Laboratory, the Field Museum, the Maine Mineral and Gem Museum, the Russian Academy of Sciences, the Smithsonian Institution, and the University of California-Los Angeles.

Rich Walker is especially recognized for his role as my PhD advisor and for all the work that entails. I am also grateful for the guidance and friendship that I have received from Richard Ash and Igor Puchtel, and for the support given to me by Michelle Montero, Suzanne Martin, and Todd Karwoski throughout graduate school. The past and present members of the Isotope Geochemistry Laboratory group, including Greg Archer, Katherine Bermingham, Emily Chiappe, Val Finlayson, Mitch Haller, Andi Mundl-Petermeier, Nao Nakanishi, Willie Nicklas, Hope Tornabene, and Emily Worsham, are thanked for their support and advice.

I have fond memories of graduate school and, for that, I thank my fellow graduate students as well as the UMD Geology faculty and staff. I could not have completed my PhD without the support of my family, in particular my mother and sister, as well as my friends, old and new. Finally, I thank my fiancée, Anya, for her love and support, which

helped me through this process immensely. I met Anya within the first two months of graduate school and she has been with me on this journey ever since.

Table of Contents

List of Tables

List of Figures

List of Abbreviations

CAI – Ca-Al-rich inclusion

CC – carbonaceous

CRE – cosmic ray exposure

HSE – highly siderophile elements

ID – isotope dilution

LA – laser ablation

ICP-MS – inductively coupled plasma mass spectrometer

MC – multi collector

MG – main group

Mya – millions of years ago

Myr – millions of years

NC – noncarbonaceous

PES – Eagle Station pallasites

PMG –Main Group pallasites

SBT – South Byron Trio

TIMS – thermal ionization mass spectrometer

Chapter 1: Introduction and Goals

1.1 Driving questions

A fundamental pursuit of planetary science is to understand how the early Solar System formed and evolved. Such a task warrants providing constraints to the origins and evolution of the earliest formed planetary bodies, the histories of which can be probed through the study of meteorites - fragments of asteroids or other planetary bodies that have landed on Earth. By determining when, where, and from what planetary bodies formed, constraints to the distribution and evolution of material in the early Solar System can be placed. This dissertation aims to advance these topics through the coupled study of the genetic isotopic compositions, formation ages, and chemical compositions of the distinct, early-formed planetary bodies sampled by iron meteorites.

1.2 Background

1.2.1 Meteorite classification

Meteorites are commonly classified as either chondrites or achondrites, based on mineralogical, petrological, chemical, and isotopic data (Krot et al., 2004). Chondrites, which can be further divided into carbonaceous, ordinary, enstatite, rumurutite, and kakangari groups, are mixtures of the primary materials of the Solar System, including presolar grains, Ca-Al-rich inclusions (CAIs), chondrules, and matrix. Presolar grains are minerals that were produced in astronomical events, such as supernovae, prior to the formation of the Solar System (e.g., Nittler et al., 2018). Calcium-Al-rich inclusions are interpreted to be the first materials to condense in the Solar System from the gas-rich solar nebula and Pb-Pb ages date CAI formation to 4567.30 ± 0.16 Mya (Connelly et al.,

2012). These inclusions are rich in refractory elements and minerals that are expected to condense from a solar gas composition at high temperatures, suggesting that CAIs formed close to the sun at >1300 K (Grossman, 1972). Chondrules began forming at the same time as CAIs and continued to form for an additional 3 Myr (Connelly and Bizzarro, 2009; Connelly et al., 2012; Brennecka et al., 2015). The origin of chondrules remains highly uncertain and, unlike CAIs, chondrules are interpreted to have formed in diverse locations within the solar nebula. Matrix is interpreted as the final Solar System condensation product from the nebular gas (e.g., McSween and Richardson, 1977).

Achondrites are interpreted to have originated as chondrites that have undergone varying degrees of melting, thus partially or fully homogenizing the presolar grains, CAIs, chondrules, and matrix components. The heat source driving melting can be derived internally from the decay of short-lived radionuclides, like ^{26}Al, or externally from impacts. Achondrites can be primitive, meaning that the meteorite has a bulk chemical composition similar to chondrites, or differentiated, meaning that the meteorites have chemical compositions significantly modified by melting and differentiation processes. Primitive achondrites can be subdivided to include, among others, nonmagmatic iron meteorites. These meteorites are largely interpreted to sample partially differentiated bodies or localized impact melts (Worsham et al., 2016a, Hunt et al., 2018). Differentiated achondrites consist of many subdivisions, such as Lunar meteorites, Martian meteorites, pallasites, and magmatic iron meteorites. Pallasites are metal- and olivine-rich meteorites, which have been interpreted to form either at the core-mantle boundary of differentiated planetary bodies or above the core in the mantle (Anders,

1964; Scott, 1977a; Wood, 1978). Magmatic iron meteorites are interpreted to represent fragments of the cores of differentiated planetary bodies.

Magmatic and nonmagmatic iron meteorites share a common classification scheme and have broadly been divided into four categories (I-IV) based on the concentration ranges observed for certain volatile trace elements, such as Ga and Ge (Goldberg et al., 1951; Lovering et al., 1957). These categories additionally have been divided into lettered groups, which consist of at least five chemically relatable iron meteorites (Wasson, 1974), based primarily on concentrations of Ga, Ge, Ni, and Ir (e.g., Wasson, 1967; Wasson and Kimberlin, 1967). Eleven different magmatic (IC, IIAB, IIC, IID, IIF, IIG, IIIAB, IIIE, IIIF, IVA, and IVB) and two nonmagmatic (IAB-complex and IIE) iron meteorite groups have currently been classified this way. Over 100 iron meteorites also exist with an "ungrouped" designation, due to the current lack of chemically relatable meteorites in the meteorite record to achieve group status.

1.2.2 Genetics

The various isotopes of most elements in the Solar System were produced in various stellar processes, including supernovae. Isotopes of elements heavier than Fe were formed primarily by different combinations of the *p*-, *s*-, and *r*-nucleosynthetic processes, reflecting photodisintegration reactions, slow neutron capture reactions, and rapid neutron capture reactions, respectively (Burbidge et al., 1957; Wallerstein et al., 1997). Studies of the nucleosynthetic isotopic compositions of Solar System primary materials have reported distinct variations in the isotopic compositions of various elements in presolar grains, CAIs, chondrules and matrix (e.g., Budde et al., 2016a,b). For example,

presolar grains, such as graphite and silicon carbides, have isotopic compositions of Mo with variable *s*-process enrichments and/or coupled *r*- and *p*-process depletions, relative to terrestrial materials, with μ^{95}Mo variations between -600,000 and +200,000 (μ is the part per 1,000,000 variation in the isotopic ratio of a sample relative to a terrestrial standard) (Nicolussi et al. (1998a,b). Calcium-Al-rich inclusions have μ^{95}Mo compositions between +185 to +1,106 (Burkhardt et al., 2011), whereas chondrules and matrix have μ^{95}Mo compositions between -125 to -49 and +142 to +398, respectively (Budde et al., 2016a). The reason behind the distinct isotopic compositions of these primary planetary building blocks is not well understood. Some studies have proposed that it is due to the formation of these materials in isotopically distinct regions, inherited from an isotopically heterogeneous parental molecular cloud, of the Solar nebula (e.g., Dauphas et al., 2002). Other studies have argued that the parental molecular cloud was isotopically homogenous and isotopic variations in the Solar nebula developed through the thermal processing, physical sorting, or late addition of isotopically distinct materials (e.g., Regelous et al., 2008; Trinquier et al., 2009; Brennecka et al., 2013).

Nucleosynthetic isotopic heterogeneities exist in bulk meteorites for some elements, indicating that isotopically distinct primary materials were heterogeneously accreted by planetary bodies (e.g., Dauphas et al., 2002; Qin et al., 2008; Chen et al., 2010; Burkhardt et al., 2011, Fischer-Gödde et al., 2015; Kruijer et al., 2017; Bermingham et al., 2018). Studies coupling the nucleosynthetic isotopic compositions of multiple elements in meteorites have uncovered that at least two isotopically distinct reservoirs existed during the early Solar System (e.g., Warren 2011; Budde et al., 2016a; Kruijer et al., 2017). Warren (2011) termed these reservoirs the noncarbonaceous (NC) and carbonaceous

(CC) reservoirs after noting coupled isotopic variations for Cr, Ti, O, and Ni in silicate-rich meteorites. Additional variations in siderophile (iron-loving) elements, such as Mo, Ru, W, and Pd, have since been noted (Budde et al., 2016a; Kruijer et al., 2017; Poole et al., 2017; Worsham et al., 2017, 2019; Bermingham et al., 2018; Ek et al., 2019), allowing for the study of the genetic isotopic variability within and between the NC and CC reservoirs through iron meteorites.

1.2.3 Metal-silicate segregation ages

The ^{182}Hf-^{182}W system is a short-lived chronometer, in which ^{182}Hf ($t_{1/2}$ = 8.9 Myr) beta decays to stable ^{182}W, through short-lived ^{182}Ta ($t_{1/2}$ = 114 days) (Vockenhuber et al., 2004). This system is widely applied to constrain the timing of asteroidal melting and silicate-metal fractionation in the early Solar System because Hf is lithophile and remains in the silicate melt of a planetary object, while W is moderately siderophile and preferentially partitions into metallic liquids (Kleine et al., 2009). By measuring the W isotopic composition of iron meteorites and comparing this composition to the W isotopic composition of chondrites (reflecting the Hf/W ratio of a bulk parent body) and CAIs (reflecting the Solar System initial W isotopic composition), the relative timing of metal-silicate melting and segregation leading to the formation of an iron meteorite can be constrained. For magmatic iron meteorites, this age is interpreted to reflect the timing of planetary differentiation and core formation (e.g., Kruijer et al., 2014a) while for nonmagmatic irons, the interpretation of this age is uncertain (e.g., Worsham et al., 2017). For magmatic iron meteorites, an age of core formation can be then combined with thermal models, which can be used to calculate the heat production and heat loss in

a planetary body over time, to determine when an iron meteorite parent body accreted (Kruijer et al., 2014a, 2017; Hunt et al., 2018).

1.2.4 Chemical compositions

The abundances of siderophile elements in iron meteorites are set by numerous processes occurring during planetary accretion, differentiation, and crystallization. These include nebular fractionations, which reflect the temperatures at which materials condensed prior to parent body accretion, as well as subsequent parent body processing, including oxidation, metal-silicate partitioning, parent body outgassing, volatile loss due to impacts, and fractional crystallization (Scott, 1972). Siderophile elements can be grouped in multiple ways based on their geochemical behavior during these different processes, such as metal-silicate partitioning behavior and volatility. For example, highly siderophile elements (HSE) are defined as elements that have metal-silicate partition coefficients of ≥10,000 at 1 bar pressure, moderately siderophile elements have partition coefficients from ~3 to 1,000 and slightly siderophile elements have partition coefficients slightly above 1 (Walker, 2016). Siderophile elements can also be grouped based on volatility, including refractory elements (50% condensation temperatures >1335 K at 1E-4 atm), moderately volatile elements (50% condensation temperature <1335 K and >665 K), and volatile elements (50% condensation temperature <665 K) (Davis, 2006). By studying the abundances of multiple siderophile elements with different geochemical behaviors in iron meteorites, it is, in some cases, possible to provide constraints to the various processes occurring before and after planetary accretion.

1.2.5 Origins of the NC and CC reservoirs

Despite numerous studies exploring the link between different nucleosynthetic isotope systematics and the extent of isotopic heterogeneity observed among meteorites, the origin of the NC and CC reservoirs continues to be debated. Past studies have proposed that the isotopic heterogeneity observed within and between the NC and CC reservoirs was due to the selective removal of isotopically distinct materials, such as through thermal processing (e.g., Poole et al., 2017; Worsham et al., 2019) or physical sorting of materials (e.g., Burkhardt et al., 2019). Other studies have proposed that the isotopic heterogeneity observed within and between the NC and CC reservoirs was due to the addition of isotopically distinct materials, such as through late injection of material to the outer Solar System (e.g., Kruijer et al., 2017). It has also been proposed that it was inherited from an isotopically heterogeneous parental molecular cloud (Dauphas et al., 2002). Regardless of the mechanism, a widely accepted hypothesis is that the NC and CC reservoirs reflect the inner and outer Solar System, respectively, which became separated by the formation of proto-Jupiter (e.g., Warren, 2011; Budde et al., 2016a; Kruijer et al., 2017; Burkhardt et al., 2019; Nanne et al., 2019). Yet, many questions remain about how, when, and where the NC and CC reservoirs formed and evolved.

1.3 Research goals

The primary goals of this research are to gain new insights to the origin and evolution of the isotopically distinct NC and CC reservoirs in the early Solar System. This dissertation seeks to advance these fields through the analysis and interpretation of the isotopic compositions and chemical abundances of siderophile elements in NC- and CC-

type meteorites. Specifically, the nucleosynthetic Mo, Ru and W isotopic compositions of iron meteorites are reported in order to constrain the extent of isotopic heterogeneity among different planetary bodies, the short-lived ^{182}Hf-^{182}W chronometer is employed to provide temporal constraints to the timing of planetary body formation, and the concentrations of HSE, including Re, Os, Ir, Pu, Pt, and Pd, are used to constrain the chemical compositions of bulk planetary bodies. These separate data sets are used together to advance the understanding of these early reservoirs by providing insights to the genetics, ages, and chemical compositions of bulk planetary bodies sampled by iron meteorites.

Chapter 2: Genetics, crystallization sequence, and age of the South Byron Trio iron meteorites: New insights to carbonaceous chondrite (CC) type parent bodies

Note: This chapter has been previously published in the following publication:

Hilton C.D., Bermingham K.R., Walker R.J., McCoy T.J. (2019) Genetics, crystallization sequence, and age of the South Byron Trio iron meteorites: New insights to carbonaceous chondrite (CC) type parent bodies. *Geochim. Cosmochim. Acta* **251**, 217-228.

2.1 Abstract

The nucleosynthetic Mo, Ru, and W isotopic compositions of the South Byron Trio iron meteorite grouplet (SBT) are consistent with all three meteorites originating on a single parent body that formed in the carbonaceous chondrite (CC) isotopic domain within the Solar nebula. Consistent with a common origin, the highly siderophile element (HSE) concentrations of the SBT can be related to one another by moderate degrees of fractional crystallization of a parental melt with initially chondritic relative abundances of HSE, and with initial S and P contents of ~7 and ~1 wt. %, respectively. Tungsten-182 isotopic data for the SBT indicate the parent body underwent metal-silicate differentiation 2.1 ± 0.8 Myr after calcium aluminum rich inclusion formation, and thermal modeling suggests the parent body formed 1.1 ± 0.5 Myr after CAI formation. This accretion age is not resolved from the accretion ages of other CC and most noncarbonaceous (NC) type iron meteorite parent bodies. Comparison of the projected parental melt composition of the SBT to those projected for the IVA and IVB iron meteorite groups suggests that at least some portions of the CC nebular domain were more oxidized compared to the NC domain. In addition, comparison of the SBT parental

melt S content to estimates for parent bodies of the IIAB, IIIAB, IVA, IID, and IVB "magmatic" iron meteorite groups suggests that CC type iron meteorite parental melts were characterized by a general depletion in S, in addition to depletions in some other moderately volatile elements.

Based on chemical and O isotope similarities, prior studies have suggested the possibility of a common parent body for the SBT and the Milton pallasite. Molybdenum and Ru isotopic compositions of Milton also provide permissive evidence for this. The HSE concentrations in the Milton metal, however, cannot be related to the SBT by any known crystal-liquid fractionation or mixing path. Thus, Milton more likely formed on a different, chemically distinct, but genetically identical parent body present in the CC nebular domain.

2.2 Introduction

Two isotopically and likely chemically distinct nebular domains, referred to as "noncarbonaceous" (NC) and "carbonaceous" (CC), were originally identified to have existed in the early Solar System through studies of Ni, Cr, Ti, and O isotopic compositions in meteorites (Warren, 2011). The list of isotopically diverse elements to discriminate between these domains has been expanded to include the siderophile elements Mo, Ru, and W, which allow for the NC and CC classification to be extended to iron meteorites and pallasite metal (e.g., Fisher-Gödde et al., 2015; Budde et al., 2016a; Kruijer et al., 2017; Poole et al., 2017; Worsham et al., 2017; Bermingham et al., 2018). Mass independent isotopic heterogeneity observed for Mo, Ru, and W among early Solar System materials is due to the incorporation of variable proportions of presolar

components with isotopically diverse compositions reflecting different nucleosynthetic origins (e.g., Dauphas et al., 2002; Qin et al., 2008; Chen et al., 2010). The distinct Mo, Ru, and W isotopic compositions of the NC and CC isotopic domains have been interpreted to represent the division and isolation of the inner and outer Solar System, possibly due to the formation of proto-Jupiter (Warren, 2011; Budde et al., 2016a; Kruijer et al., 2017). As the outer Solar System is expected to be a more oxidizing and volatile-rich environment compared to the inner Solar System, coupled studies of isotopic and chemical compositions of CC type iron meteorites may provide new insights into the NC and CC division, and nebular heterogeneity.

So called "magmatic" iron meteorite groups consist of multiple meteorites whose chemical differences can be accounted for by crystal-liquid fractionation and mixing processes originating from a single melt. Most of the major magmatic iron meteorite groups have been characterized as NC or CC based on Mo, Ru, and W isotopic compositions. The NC type irons include the IC, IIAB, IIIAB, IIIE, and IVA groups, and the CC type irons include the IIC, IID, IIF, IIIF, and IVB groups (Fisher-Gödde et al., 2015; Budde et al., 2016a; Kruijer et al., 2017; Poole et al., 2017; Worsham et al., 2017; Bermingham et al., 2018). Of these ten iron groups, the CC type irons tend toward greater Ni contents and more limited ranges in Ir concentrations compared to NC irons, although there is considerable overlap (**Fig. 2.1**). Additional chemical comparisons between NC and CC type iron meteorites are limited. For example, the highly siderophile element (HSE; Re, Os, Ir, Ru, Pt, Pd) concentrations of parental melts have only been estimated for the IVA and IVB iron meteorites (Campbell and Humayun, 2005; Walker et al., 2008; McCoy et al., 2011). In addition, S contents of iron meteorite parental melts have been

determined using multiple approaches that are not always consistent, limiting direct comparisons (e.g., Chabot, 2004; Wasson et al., 2007).

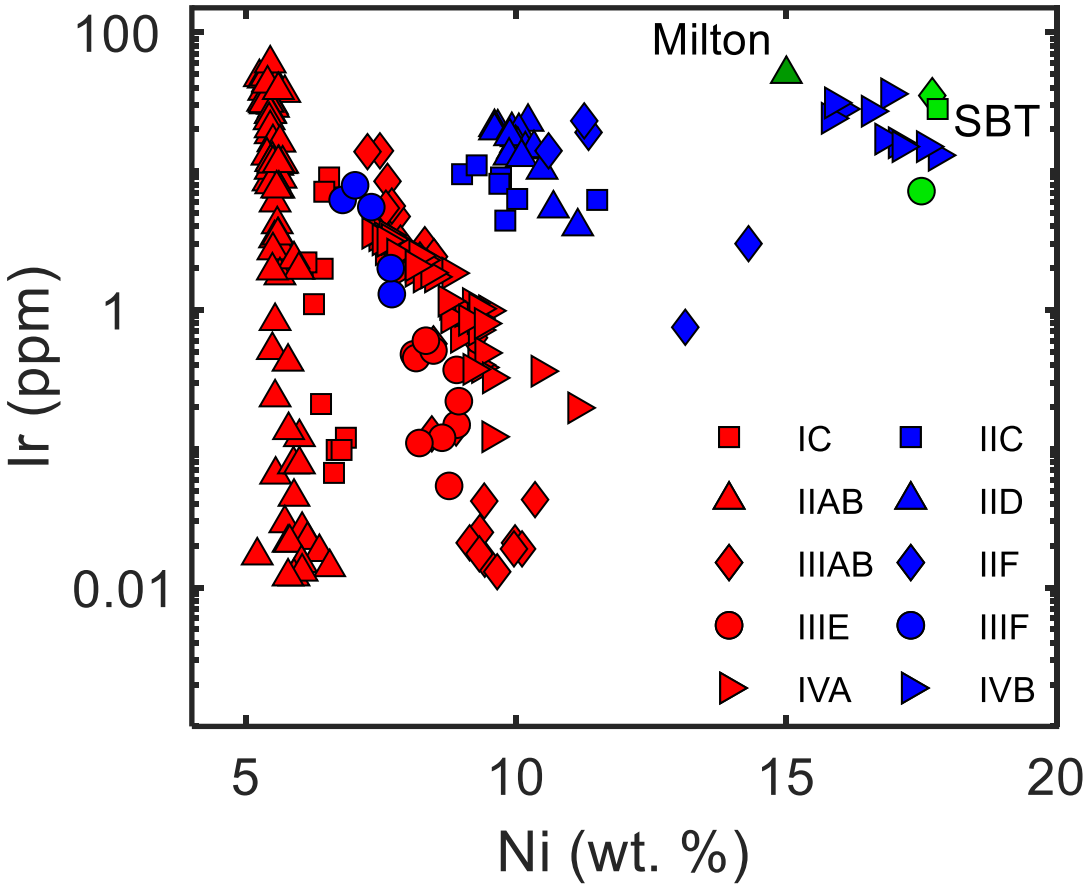

Fig. 2.1. Compilation of Ni *vs*. Ir concentration data for the magmatic iron meteorite groups. Blue symbols represent CC type meteorites and red symbols represent NC type meteorites. Milton and the SBT are shown as dark and light green symbols, respectively. Data are compiled from Wasson (1969), Schaudy and Wasson (1972), Scott et al. (1973), Scott and Wasson (1976), Scott (1977b), Wasson et al. (1989), Wasson (1999), Wasson and Richardson (2001), Jones et al. (2003), Wasson and Huber (2006), and Wasson et al. (2007).

The South Byron Trio (SBT) iron meteorite grouplet provides an opportunity to expand knowledge regarding the chemical and isotopic variability of the Solar nebula. The SBT consists of three ungrouped iron meteorites, Babb's Mill (Troost's Iron, herein

referred to as Babb's Mill), South Byron, and Inland Forts 83500 (ILD 83500), which were recognized as having similar Ni, Ga, and Ge concentrations (17.5-17.8 wt. %, 18.6-20.0 ppm, 41.0-47.9 ppm, respectively) and ataxitic structures by Wasson et al. (1989). In addition to potentially originating from the same parent body, the SBT have been suggested to also be related to the ungrouped Milton pallasite. Several prior studies have noted chemical and isotopic similarities between the SBT and the Milton pallasite, warranting study of this potential iron meteorite-pallasite relationship (Jones et al., 2003; McCoy et al., 2017).

In this study, the mass independent isotope systematics of some siderophile elements and the modeling of HSE, and Hf-W chronometry are employed to assess the nature of the possible relationship among the SBT meteorites, as well as to assess the HSE, S, P, and C contents of the parental melt. The short-lived Hf-W system ($^{182}Hf \rightarrow {}^{182}W + 2\beta^-$, $T_{1/2}$ = 8.9 Ma; Vockenhuber et al., 2004) is used to constrain the thermal history of the parent body including the timing of primary differentiation. Further, the potential relationship of the Milton pallasite to the SBT is evaluated using Mo and Ru isotopic compositions and chemical modeling.

2.3 Materials and methods

2.3.1 Sample preparation

Samples of Milton and South Byron were obtained from the Smithsonian Institution, Department of Mineral Sciences, National Museum of Natural History. Babb's Mill was obtained from Arizona State University and ILD 83500 was obtained from the US Antarctic Meteorite Program. Pieces were cut from each meteorite sample using a water-

cooled *Leco Vari-cut* saw and a 12.7 cm diamond-wafering blade. The blade was cleaned with carborundum prior to cutting each meteorite. Prior to dissolution, the surface of each cut meteorite piece was polished using a range of coarse- to fine-grit sandpaper to remove sawblade marks, and then sonicated multiple times in ethanol.

2.3.2 Isotopic measurements

Approximately 1-2 g pieces of each of the SBT irons and a 6 g piece of the Milton pallasite were dissolved in 40-120 mL 8M HCl at 130 °C for 72 hours in Teflon® beakers. The resulting solution was then centrifuged and the supernatant was divided into four aliquots to be separately processed for Os, Mo, Ru, and W isotopic measurements. Due to limited material, Milton was not processed for W. Details regarding the chemical and mass spectrometric procedures have been previously published (Worsham et al., 2016b; Bermingham et al., 2016; Archer et al., 2017), reviewed in Appendix 2, and briefly described here. Aliquots for Os isotopic analysis were oxidized in sealed Pyrex® Carius tubes with 2:1 HNO_3:HCl at 220 °C and then Os was extracted from the solution using CCl_4 solvent-extraction methods, and further purified using microdistillation techniques (Shirey and Walker, 1995; Cohen and Waters, 1996; Birck et al., 1997). Molybdenum aliquots were processed through three anion columns (Worsham et al., 2016b) and Ru aliquots were processed through a cation column and then further purified using microdistillation techniques (Bermingham et al., 2016). Iron was removed from the W aliquots using a diisopropyl ether extraction procedure and then the aliquots were processed through a cation column and three anion columns (Dodson et al., 1936; Touboul and Walker, 2012). Isotopic compositions for Os, Mo, Ru, and W were

measured by thermal ionization mass spectrometry (TIMS) at the University of Maryland (UMd).

The typical blanks for these procedures were <10 pg Os, <1 ng Mo, <10 pg Ru, and <1 ng W, which were inconsequential for the measurements reported here. Analytical uncertainty was assessed by measuring standard solutions multiple times (n>6) during an analytical campaign and assigning the two-standard deviation (2SD) value for the standards, which were always greater than the two-standard error (2SE) of the sample analyses, to the sample value. Reproducibility per analytical campaign of the Johnson Matthey Os standard (2SD) ranged from $^{189}Os/^{188}Os$ = 5-8 ppm and $^{190}Os/^{188}Os$ = 4-18 ppm, and the *Alfa Aesar Specpure*® Ru standard (2SD) was $^{100}Ru/^{101}Ru$ = 9-12 ppm. The reproducibility of the *Alfa Aesar Specpure*® W standard (2SD) was $^{182}W/^{184}W$ (186/184 normalized) = 6 ppm, $^{183}W/^{184}W$ = 6-7 ppm, and the *Alfa Aesar Specpure*® Mo standard (2SD) was $^{94}Mo/^{96}Mo$ = 10-26 ppm, $^{95}Mo/^{96}Mo$ = 8-15 ppm, and $^{97}Mo/^{96}Mo$ = 5-6 ppm. Results of isotopic measurements are reported in μ units (Eq. 1; e.g., Os).

Eq. 1: $$\mu^{189}Os = \left(\frac{\frac{189}{188}Os_{sample}}{\frac{189}{188}Os_{standard}} - 1 \right) * 1{,}000{,}000$$

2.3.3 Isotope dilution

Concentration data for Re, Os, Ir, Ru, Pt, and Pd were obtained by isotope dilution using a chemistry procedure outlined in Walker et al. (2008). About 10-150 mg metal pieces of each meteorite were digested with 5 ml of concentrated HNO_3 and 2.5 ml of concentrated HCl, and equilibrated with a combined platinum-group element spike (^{191}Ir, ^{99}Ru, ^{194}Pt, and ^{105}Pd) and a Re-Os spike (^{185}Re and ^{190}Os) for at least 24 h at 220 °C in

Pyrex® Carius tubes (Shirey and Walker, 1995). Once the tubes were opened, Os was separated and purified using the same techniques as discussed in Appendix 2 for unspiked Os samples. Spiked Os samples were separately analyzed by TIMS to determine Os concentrations and $^{187}Os/^{188}Os$ ratios (Cook et al., 2004). The remaining HSE were purified using an anion column procedure, an additional anion column was used for Re and Ru purification (Walker et al., 2008), and solutions were measured using a *Nu Plasma* multi-collector inductively-coupled plasma mass spectrometer at UMd. The blanks for these methods were typically <1 pg for Re and Os, and <30 pg for Ir, Ru, Pt, and Pd. Blank corrections were made but were not significant. The uncertainties for $^{187}Re/^{188}Os$ ratios were estimated to be ±0.15 %, the uncertainties for $^{187}Os/^{188}Os$, and Os and Re concentrations were estimated to be ±0.1 %, and the uncertainties for Ir, Ru, Pt, and Pd concentrations were estimated to be <2 % based on the reproducibility of similar samples using identical methods (Walker et al., 2008; McCoy et al., 2011).

2.4 Results

2.4.1 Osmium, Mo, Ru, and W isotopic results

Cosmic ray exposure (CRE) can result in neutron capture reactions within meteorites (Leya and Masarik, 2013). Such reactions can alter the Mo, Ru, and W isotopic compositions of a meteorite (e.g., Wittig et al., 2013; Worsham et al., 2017; Bermingham et al., 2018). The effects of CRE are dependent on the neutron fluence, which reflects both exposure duration and depth from surface (e.g., Wittig et al., 2013). Consequently, CRE must be monitored and corrected for in the same meteorite piece as measured for mass independent and radiogenic isotopic compositions. Both Os and Pt isotopes have

been applied to monitor and correct for CRE effects on siderophile elements (e.g., Walker, 2012; Kruijer et al., 2013; Wittig et al., 2013). Osmium is used as the dosimeter here, of which the $^{189}Os/^{188}Os$ ratio is most sensitive for assessing CRE effects. Increasingly greater CRE effects result in increasingly negative $\mu^{189}Os$ values. Based on the 2SD reproducibility (± 6-8 ppm) of the $^{189}Os/^{188}Os$ ratio of the terrestrial laboratory standard analyzed for this study, it is assumed that meteorite pieces with $\mu^{189}Os$ values within ± 8 ppm of zero were minimally affected by CRE. Milton, Babb's Mill, South Byron, and ILD 83500 have $\mu^{189}Os$ values ranging from -4 ± 8 to +8 ± 7, which are not resolved from the terrestrial standard (0 ± 8) (**Table A2.1**) and indicate that these meteorites were minimally affected by CRE. Of these four meteorites, Milton has the most negative $\mu^{189}Os$ value of -4 ± 8. Assuming a maximum expansion of error to a $\mu^{189}Os$ value of -12 ppm would require a CRE correction for $\mu^{97}Mo$ and $\mu^{100}Ru$ values of only -2 and +5 ppm, respectively, which are smaller than the measurement uncertainties of $\mu^{97}Mo$ and $\mu^{100}Ru$ values (Worsham et al., 2017; Bermingham et al., 2018). Of the meteorites measured for $\mu^{182}W$, Babb's Mill has the most negative $\mu^{189}Os$ value of +1 ± 6. In this case, the maximum expansion of error to a $\mu^{189}Os$ value of -5 ppm would require a CRE correction for $\mu^{182}W$ of -7 ppm, which is only slightly greater than the measurement uncertainty of $\mu^{182}W$ values to ±6 ppm (Worsham et al., 2017). Therefore, no CRE corrections have been made to the Mo, Ru, and W isotopic results for these meteorites.

The Mo and Ru isotopic compositions of Milton, Babb's Mill, South Byron, and ILD 83500 are provided in **Table 2.1**. These meteorites are characterized by a limited range of $\mu^{94}Mo$ values from +121 ± 13 to +132 ± 9, $\mu^{95}Mo$ values from +99 ± 9 to +104 ± 9, and

μ^{97}Mo values from +46 ± 3 to +54 ± 5. Ruthenium isotopic compositions range from μ^{100}Ru = -104 ± 10 to -114 ± 15. Tungsten isotopic compositions are reported in **Table 2.2**. The measured μ^{182}W values for the SBT range from -307 ± 6 to -319 ± 6, and the measured μ^{183}W values range from +4 ± 7 to +15 ± 6. Collectively, the Mo and Ru isotopic compositions of the SBT and Milton, and the W isotopic compositions of the SBT are all identical, within analytical uncertainties.

Table 2.1. Molybdenum and Ru isotopic compositions of Milton, the SBT, and the average value of the SBT parent body.

Sample	n[a]	μ^{94}Mo	±	μ^{95}Mo	±	μ^{97}Mo	±	n[a]	μ^{100}Ru	±
Milton	2	+130	26	+104	9	+54	5	3	-114	15
Babb's Mill	5	+132	9	+104	5	+46	3	2	-104	9
South Byron	4	+127	12	+104	6	+50	3	3	-111	9
ILD 83500	4	+121	13	+99	9	+50	2	3	-104	10
SBT average	13	+127	7	+103	4	+49	2	8	-107	5

[a] n is the number of analyses for Mo and Ru isotopic composition. The reported isotopic values reflect the average values obtained for each meteorite piece. Uncertainties reflect the largest (of n analyses) 2SD of the standards run during an analytical campaign ($n \leq 3$) or 2SE ($n > 3$) of the sample values.

Table 2.2. Tungsten isotopic compositions of the SBT.

Sample	n[a]	$\mu^{182}W_{Measured}$	±	$\mu^{183}W_{Measured}$	±	$\mu^{182}W_{Corrected}$	±	ΔT_{CAI}	±
Babb's Mill	1	-307	6	+11	6	-323	10	2.3	1.0
Babb's Mill (*rep*)	1	-312	6	+4	7	-318	12	2.8	1.2
South Byron	1	-311	6	+15	6	-332	10	1.4	0.9
ILD 83500	1	-319	6	+7	6	-329	10	1.7	1.0
SBT average	4	-312	5	+9	5	-325	8	2.1	0.8

[a] n is the number of analyses. The measured μ^{182}W and μ^{183}W values are reported for each meteorite piece and the uncertainties reflect the 2SD of the standards run during an analytical campaign. The corrected μ^{182}W represents the value corrected for the μ^{183}W positive anomaly per sample, where $\mu^{182}W_{corrected} = \mu^{182}W_{Measured} - (1.41 \pm 0.06 * \mu^{183}W)$ (Kruijer et al., 2014b), and the uncertainties reflect the uncertainties from $\mu^{182}W_{Measured}$, $\mu^{183}W_{Measured}$, and the μ^{183}W correction. The SBT average $\mu^{182}W_{Corrected}$ values were calculated using the SBT average $\mu^{182}W_{Measured}$ and $\mu^{183}W_{Measured}$ values, and errors represent 2SE. The ΔT_{CAI} ages were calculated from the $\mu^{182}W_{Corrected}$ values.

2.4.2 ^{187}Re-^{187}Os and highly siderophile element concentrations

The ^{187}Re-^{187}Os chronometer is a useful tool for broadly constraining the age of metal crystallization, as well as evaluating open-system behavior of HSE. Osmium-187 is the β- decay product of ^{187}Re, which has a half-life of 41.6 Gyr (Smoliar et al., 1996). The ^{187}Re-^{187}Os results are reported in **Table 2.3**. The ^{187}Re-^{187}Os data were regressed using ISOPLOT (Ludwig, 2003) and the isochron yields an age of 4587 ± 230 Ma and an initial ^{187}Os/^{188}Os of 0.0953 ± 0.0019 (MSWD = 6.4). The limited range in Re/Os coupled with the limited number of meteorites result in the large uncertainty for these values, compared to some other groups (e.g., McCoy et al., 2011). Milton and the SBT all plot on or near a chondritic 4.568 Ga reference isochron (**Fig. 2.2**). These meteorites have Δ_{Os} values, calculated as the part per 10,000 deviation from the ^{187}Os/^{188}Os ratio of a sample to the reference isochron, ranging from -0.1 ± 2 to +3.9 ± 2. These results are consistent with these meteorites experiencing limited open-system behavior for the HSE since crystallization in the early Solar System.

Table 2.3. Rhenium-Os isotopic and HSE composition data for Milton and the SBT.

Sample	Wt.	Ni	Re	Os	Ir	Ru	Pt	Pd	$^{187}Re/^{188}Os$	$^{187}Os/^{188}Os$	$^{\Delta}Os$
Milton Metal	0.011	15.0	5052	46554	42260	31840	36620	5338	0.5237	0.13711	+3.9
Babb's Mill	0.051	17.7	2858	41286	29990	27250	32990	5205	0.3332	0.12177	+0.8
South Byron	0.053	17.8	2750	39741	28690	26550	32200	5422	0.3332	0.12174	+1.1
ILD 83500	0.147	17.5	511.5	4470.0	7159	18910	25610	6934	0.5522	0.13897	-0.1

Samples are listed in order of descending Re concentration. Units of sample weight are in g. Nickel concentrations are given in wt. % as compiled from Scott et al. (1973), Wasson et al. (1989), and Jones et al. (2003). All other concentrations were determined by isotope dilution and are reported in ng/g. The uncertainties for $^{187}Re/^{188}Os$ ratios are ±0.15 %, the uncertainties for $^{187}Os/^{188}Os$, and Os and Re concentrations are ±0.1 %, and the uncertainties for Ir, Ru, Pt, and Pd concentrations are <2 %. Δ is the deviation of $^{187}Os/^{188}Os$ of a sample from a primordial isochron in units of per mil, with an uncertainty of ±2 per mil (Cook et al., 2004). A primordial isochron was calculated using a Solar System $^{187}Os/^{188}Os = 0.09531$, present day chondritic $^{187}Os/^{188}Os = 0.1270$ and $^{187}Re/^{188}Os = 0.40186$, and $\lambda = 1.666 \times 10^{-11}$ yr^{-1} (Smoliar et al., 1996; Shirey and Walker, 1998).

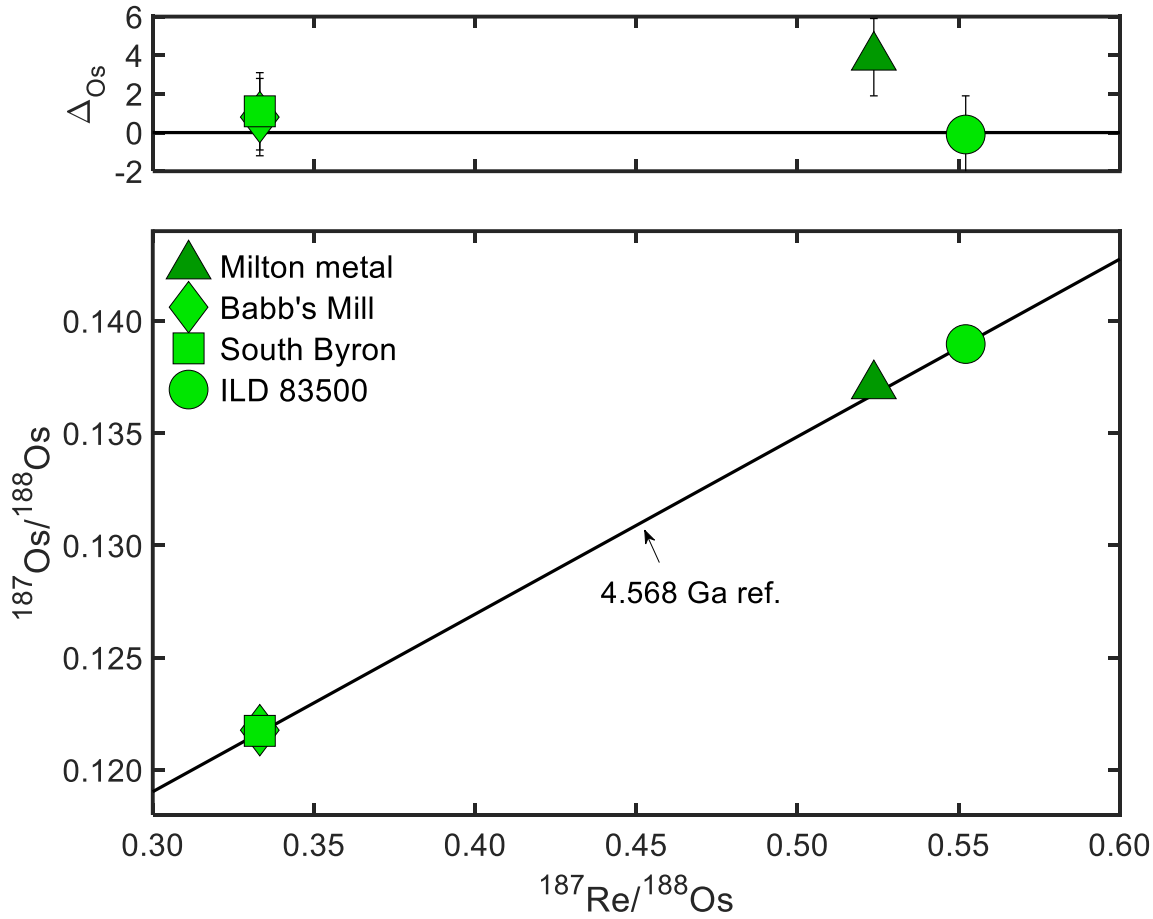

Fig. 2.2. (Top) $^{187}Re/^{188}Os$ *vs.* Δ_{Os} plot for the Milton metal and SBT, where Δ_{Os} is the parts per 10,000 deviation of the $^{187}Os/^{188}Os$ ratio of a sample from a 4.568 Ga reference line. (Bottom) $^{187}Re/^{188}Os$ *vs.* $^{187}Os/^{188}Os$ plot for the Milton metal and SBT. Reference line represents the 4.568 Ga hypothetical evolution of the $^{187}Os/^{188}Os$ ratio in chondrites, assuming an initial $^{187}Os/^{188}Os$ = 0.09531, present day chondritic $^{187}Os/^{188}Os$ = 0.1270 and $^{187}Re/^{188}Os$ = 0.40186, and $\lambda = 1.666 \times 10^{-11}$ yr^{-1} (Smoliar et al., 1996; Shirey and Walker, 1998).

The HSE abundances of Milton metal and the SBT are reported in **Table 2.3**. Of the suite, Milton has the highest concentrations of Re, Os, Ir, Ru, and Pt, and the lowest concentration of Pd. The concentrations of HSE in Babb's Mill and South Byron are similar, with Babb's Mill slightly enriched in all of the HSE, except for Pd, compared to South Byron. ILD 83500 has the lowest concentrations of Re (approximately 10x less than Milton metal), Os, Ir, Ru, and Pt, and the highest concentration of Pd. The

concentrations of Re and Ir in ILD 83500 are within 2 % of the concentrations reported by Wasson et al. (1989) and the Ir concentrations for Babb's Mill and South Byron are within 15 % of the concentrations reported by Scott et al. (1973). The concentrations of Re, Ir, and Pt reported by Jones et al. (2003) for Milton metal are within 20 % of the concentrations reported here.

2.5 Discussion

2.5.1 Genetics

Differences in the proportions of the nucleosynthetic components incorporated into NC and CC bodies allow for "genetic" comparisons of meteorites. For example, NC type meteorites have Mo and Ru isotopic compositions that reflect a constant *r*-process input with variable *s*-process depletion (**Fig. 2.3, A2.1**). Variations in $^{97}Mo/^{96}Mo$ and $^{100}Ru/^{101}Ru$ define a linear trend (Dauphas et al., 2004; Fischer-Gödde et al., 2015; Bermingham et al., 2018). By contrast, CC type meteorites have Mo and Ru isotopic compositions that reflect an additional *s*-process depletion (**Fig. A2.1**), and Mo and W isotopic compositions that reflect an additional *r*-process component (**Fig. A2.2**) (Kruijer et al., 2017).

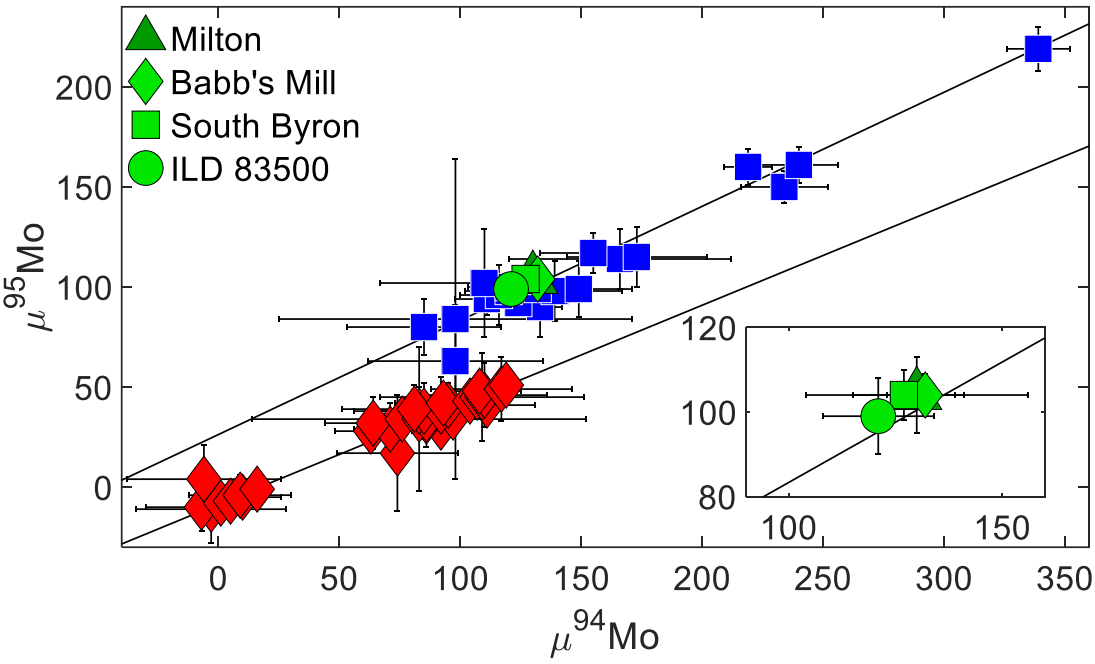

Fig. 2.3. Compilation of μ^{94}Mo *vs*. μ^{95}Mo data for iron meteorites and pallasites from Burkhardt et al. (2011), Kruijer et al. (2017), Poole et al. (2017), and Worsham et al. (2017). Some data have not been corrected for CRE. Blue squares represent meteorites classified as CC type and red diamonds represent meteorites classified as NC type. Data from this study for the SBT and Milton are also plotted. Black lines were obtained by regressing the NC and CC data using ISOPLOT (Ludwig, 2003); the CC line has a slope of 0.57 ± 0.05 and a y-intercept of 26.3 ± 7.5 (MSWD = 1.15) and the NC line has a slope of 0.50 ± 0.04 and a y-intercept of -8.5 ± 3.2 (MSWD = 0.49). The inset shows an enlarged view of the Mo isotopic compositions of the SBT and Milton without other meteorites.

The observation that the SBT have Mo, Ru, and ^{183}W isotopic compositions that are analytically indistinguishable provides permissive evidence that these meteorites sample the same parent body. If so, the isotopic data for the three meteorites can be averaged to obtain a more robust constraint on the isotopic characteristics of the parent body. The average μ^{94}Mo, μ^{95}Mo, and μ^{97}Mo values of the SBT meteorites are +127 ± 7, +103 ± 4, and +49 ± 2, respectively, where the uncertainties cited are 2SE. Further, the average μ^{100}Ru value is -107 ± 5 and the average μ^{183}W value is +9 ± 5. The average Mo and

^{183}W isotopic compositions of the SBT are identical, within analytical uncertainty, to those determined for the CC type IID, IIF, IIIF, and IVB iron meteorite groups (**Fig. 2.3, A2.1, A2.2**) (Budde et al., 2016a; Kruijer et al., 2017; Poole et al., 2017; Worsham et al., 2017; Bermingham et al., 2018), and the average Ru isotopic composition of the SBT is identical to the CC type IID and IVB iron meteorite groups (Fischer-Gödde et al., 2015; Bermingham et al., 2018). Ruthenium isotopic data have not yet been determined for IIF and IIIF irons. Collectively, the genetic isotopic data indicate that the SBT should be defined as CC type meteorites. Because of the limited isotopic variation among CC irons, however, these isotopic systems are not useful for discriminating the SBT from most other known CC parent bodies.

The Mo and Ru isotopic compositions of Milton are indistinguishable from the SBT, providing permissive evidence for an origin on the SBT parent body, consistent with the identical O isotopic composition reported by McCoy et al. (2017). Thus, the Milton pallasite should also be defined as a CC type meteorite, and it can be presumed that, at the very least, Milton and the SBT were derived from similar presolar materials, likely forming in the same region of the Solar nebula.

2.5.2 Crystallization sequence modeling of the SBT

Given the identical Mo, Ru, and ^{183}W isotopic compositions of the SBT to other CC type iron meteorite groups, it is imperative to test the possible SBT relationship through chemical modeling. The change in HSE concentrations among the SBT iron meteorites are broadly consistent with fractional crystallization in that the concentrations of Re, Os, Ir, Ru, and Pt typically decrease in crystallizing metal as the concentration of Pd

increases. This trend is in agreement with the observation by Wasson et al. (1989) that, given the changes in As, Au, W, and Ir concentrations among these irons, the SBT could have originated by fractional crystallization. The similar HSE concentrations determined here for Babb's Mill and South Byron suggest that these irons crystallized at a similar point in a crystallization sequence. By contrast, ILD 83500 has about 17 % of the Re content and 130 % of the Pd content of Babb's Mill, indicating that, if they are related, ILD 83500 crystallized from a more evolved melt.

To examine further possible relationships resulting from fractional crystallization, we model HSE data for the SBT. To do this, appropriate solid metal-liquid metal D values (concentration ratios) must be applied. Some prior studies have derived relative D values for HSE for specific iron groups from the slopes of inter-element log-log plots (e.g., Campbell and Humayun, 2005; Walker et al., 2008; McCoy et al., 2011), coupled with experimental partitioning data for P or Ir, in order to model a crystallization sequence. However, due to the similar HSE concentrations of Babb's Mill and South Byron, the data for the SBT essentially define two-point lines. For this reason, we use the approach developed by Jones and Malvin (1990) and advanced by Chabot and Jones (2003) and Chabot et al. (2017), which uses experimentally derived partitioning data for siderophile elements in the Fe-Ni-S, Fe-Ni-P, and Fe-Ni-C systems to determine the D values for HSE for given S, P, and C contents. A more detailed description of this approach is provided in Appendix 2.

Here we constrain the initial P content of the SBT parental melt by coupling the measured P content of Babb's Mill and South Byron (0.12-0.22 wt. % P) reported in Buchwald (1975) with a solid metal-liquid metal partition coefficient of 0.1 (Chabot et

al., 2017). This suggests a P content in the melt of about 1 wt. % at the point where these two irons crystallized. The initial S content was then varied along with different HSE initial melt compositions until a model crystallization sequence was generated that matched the SBT HSE concentrations.

The optimal initial light-element concentrations determined are 7 wt. % S, 1 wt. % P, and <0.05 wt. % C. This model reproduces the HSE abundances of the SBT through fractional crystallization of an initial parental melt with chondritic relative abundances of the HSE. The model matches the HSE concentration of Babb's Mill as the first 1 % of metal to crystallize. South Byron is reproduced as 2 % of metal to crystallize, and ILD 83500 matches the solid HSE composition at 42 % crystallization (**Fig. 2.4**).

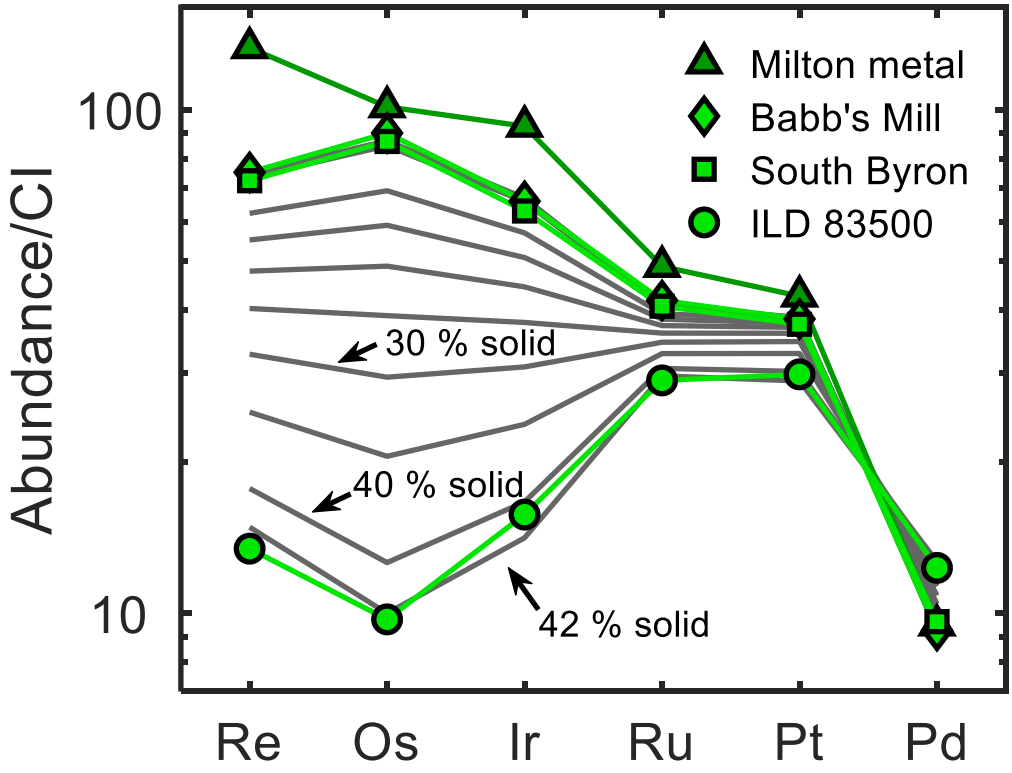

Fig. 2.4. CI-chondrite normalized HSE contents of Milton and the SBT, and HSE abundance results of a fractional crystallization model (grey lines). Babb's Mill, South Byron and ILD 83500 match 1 %, 2 %, and 42 % metal crystallization in this model, respectively. Model results are shown for 10 % to 40 % solid in 5 % increments, as well as the 1 %, 2 %, and 42 % model matches to the SBT. Model results for 1 % and 2 % are covered by patterns for Babb's Mill and South Byron.

The calculated initial parental melt HSE composition for the SBT (**Table 2.4**) is shown in **Fig. 2.5**, normalized to the CI-chondrite Orgueil (Horan et al., 2003; Fischer-Gödde et al., 2010). This initial melt composition has Re/Os, Ir/Os, Ru/Os, Pt/Os, and Pd/Os ratios of 0.082, 0.90, 1.1, 1.7, and 0.89, respectively, which are all within the ranges of ratios observed in bulk chondrites of 0.059-0.101, 0.77-1.02, 1.1-2.0, 1.4-2.5, and 0.54-2.01, respectively (Horan et al., 2003; Fischer-Gödde et al., 2010).

Table 2.4. Parental melt compositions calculated for HSE, S, P, and C for the best-fit model to reproduce the SBT chemical patterns, and comparison to IVA and IVB systems.

	Re	Os	Ir	Ru	Pt	Pd	S	P	C
SBT parental melt	770	9400	8500	13000	16000	8400	7	1	<0.05
IVA parental melt[a]	295	3250	2700	3900	5900	4500	3	0.1	0
IVB parental melt[b]	1410	21600	17500	19600	29800	10900	2	0.65	0

Concentrations are in ng/g for HSE and wt. % for S, P, and C.
[a] From McCoy et al. (2011).
[b] From Walker et al. (2008).

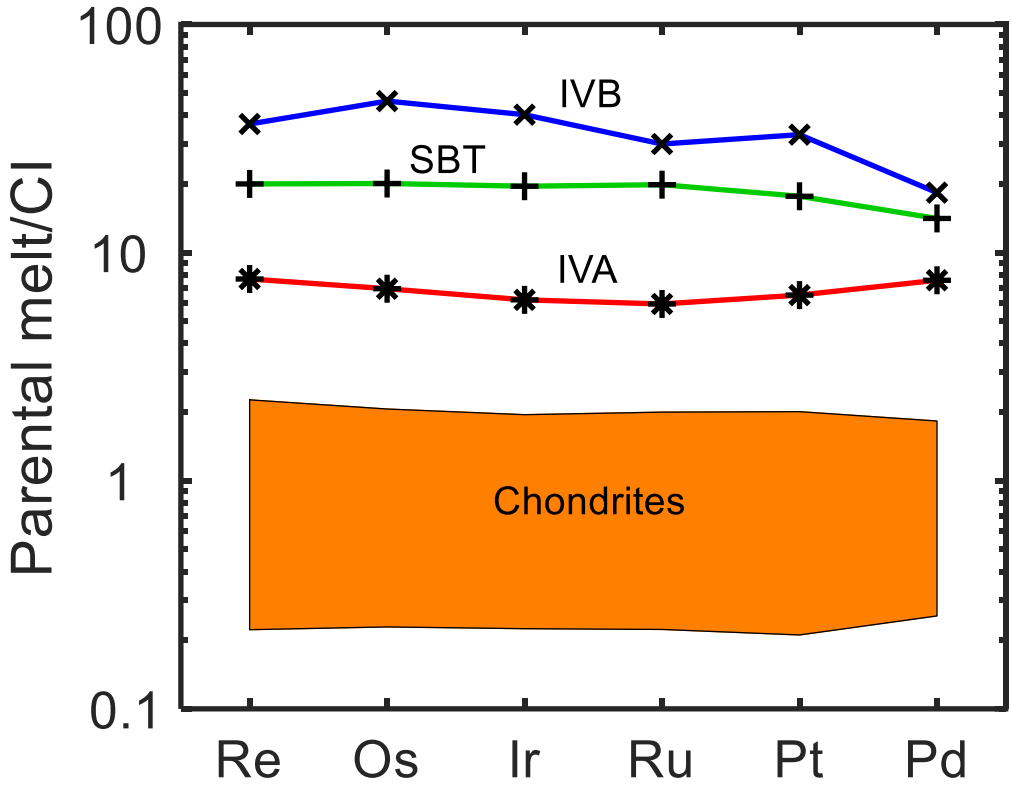

Fig. 2.5. CI-normalized calculated HSE parental melt composition of the SBT, assuming 7 wt. % S, 1 wt. % P, and <0.05 wt. % C. Also shown are CI-normalized calculated parental melt compositions for the IVA irons (McCoy et al., 2011), IVB irons (Walker et al., 2008), and the range of HSE concentrations in chondrites (Horan et al., 2003; Fischer-Gödde et al., 2010).

The calculated initial parental melt HSE composition of the SBT is about 10 times more concentrated than the upper range of HSE concentrations in chondrites. If this upper

range is assumed to represent the starting concentration of the SBT parent body, and if it is assumed that ~99 % of the HSE were extracted into the core, then the SBT parental melt would have accounted for ~10 % the mass of the body. This result suggests that the SBT represent samples of a planetesimal core and should be considered magmatic iron meteorites. Past studies have estimated the parental melt compositions for the magmatic IVA and IVB iron meteorites (Walker et al., 2008; McCoy et al., 2011). The modeled HSE parental melt composition of the SBT parent body falls between the compositions previously estimated for the parent bodies of the group IVA and IVB iron meteorites (**Fig. 2.5**). As suggested for the IVB parent body, the high HSE concentration of the SBT parental melt may suggest a comparatively oxidized body. In this scenario, a greater proportion of oxidized iron would remain in the mantle compared to a more reduced body, resulting in relatively higher concentrations of HSE in the core. An oxidized SBT body is also supported by the high Ni content (17-18 wt. %) of these meteorites.

2.5.3 Crystallization sequence modeling of Milton

Since Mo, Ru, and O isotopic compositions of Milton and the SBT only provide permissive evidence of a common parent body, a potential relationship for these meteorites is further evaluated through chemical modeling. Milton metal has a Pt/Os ratio that is similar to that for Babb's Mill, which is estimated to represent the first 1 % of metal to crystallize, yet a Re/Os ratio that is similar to ILD 83500, which is estimated to represent crystallization at 42 %. Attempts were made to model Milton as part of the same solid metal-liquid metal fractional crystallization sequence as the SBT by varying the initial HSE, S, P, and C contents of the system. Changes to the initial S, P, or C

contents can have large effects on the concentration of HSE in crystallizing metal, however, such changes cannot account for the Re/Os and Pt/Os ratios observed for Milton. An example of the modeling is shown in **Fig. A2.3**.

Modeling involving solid metal-liquid metal mixing was also undertaken in an attempt to relate Milton metal to the SBT. Metal mixing of primitive and evolved metals from the core along with residual metal in the mantle has been suggested for the formation of the main group pallasites on the IIIAB iron meteorite parent body (Scott, 1977c; Wasson and Choi, 2003). Such models failed to reproduce Re/Os and Pt/Os ratios for Milton and were, therefore, unsuccessful at relating Milton metal and the SBT to the same metal system (**Fig. A2.4**). Consideration was also given to the crystallization of Milton metal and the SBT from two immiscible metal melts (one P rich and one S rich) within the same core. Models of metal liquid immiscibility have been invoked for the IID iron meteorites (Wasson and Huber, 2006) and to relate the IIAB irons to the IIG irons (Wasson and Choe, 2009). Milton metal has a similar P content to Babb's Mill and South Byron, however, which suggests that they did not form from immiscible metal melts (McCoy et al., 2017). Due to the lack of models that can reproduce the SBT and Milton metal HSE concentrations from the same metal liquid, we conclude that Milton metal was most likely not generated from the parental melt to the SBT.

The HSE concentrations in Milton metal suggest a parental melt that was characterized by several HSE ratios outside of the range observed in known bulk chondrites. Examples of three possible parental melt compositions, which can reproduce Milton metal as an early fractional crystallizing metal, are shown in **Fig. A2.5**. For these three models, we assume parental melt abundances of 1 wt. % S, 1 wt. % P, <0.05 wt. %

C; 5 wt. % S, 2 wt. % P, <0.05 wt. % C; and 10 wt. % S, 3 wt. % P, <0.05 wt. % C. All three models are characterized by calculated parental melt Re/Os ratios (0.12, 0.13 0.15) and Ir/Os ratios (1.05, 1.04, 1.10) that are 2 to 50% above the range observed in bulk chondrites (Horan et al., 2003; Fischer-Gödde et al., 2010). By contrast, all Pt/Os ratios (1.4, 1.5, 1.8), and most Ru/Os ratios (1.1, 1.5, 2.5) and Pd/Os ratios (0.43, 0.73, 1.88) are within the range of bulk chondrites.

It is possible that such parental melts described above existed on the SBT parent body without interacting with the SBT parental melt, or may have been generated through the mixing of variable amounts of liquid metal or solid metal from the SBT crystallization sequence with a metal source with fractionated relative abundances of some HSE compared to bulk chondrites. Generating and maintaining these separate metal domains within the same planetesimal, however, is difficult to envision. Hence, it is more likely that Milton formed on a chemically distinct, but genetically identical parent body to the SBT. This interpretation would expand the number of chemically distinct parent bodies with identical Mo, Ru, and O genetic isotopic compositions to at least three (e.g., SBT, Milton, and IVB irons; Corrigan et al., 2017; McCoy et al., 2017; Bermingham et al., 2018).

As may be the case for Milton, the parental melt to the IVB iron meteorites was likely non-chondritic with respect to the relative abundances of some HSE (Campbell and Humayun, 2005; Walker et al., 2008). Campbell and Humayun (2005) and Walker et al. (2008) suggested that the volatile siderophile element depletions projected for the IVB parent body may have resulted from high temperature condensation processes. Such a model is less plausible for the Milton parent body, as the meteorite is significantly

enriched in volatile siderophile elements, such as Ga and Ge, compared to the IVB irons (Walker et al., 2008; McCoy et al., 2017). The three parental melt compositions for Milton modeled in this study are characterized by Re/Os and Ir/Os ratios that are suprachondritic. Both Re/Os and Ir/Os tend to increase as a consequence of crystal liquid fractionation (see above modeling of SBT) so it is possible that the parental melt to Milton represents a modestly evolved liquid that was somehow segregated from earlier formed solids. This could potentially have occurred on the parent body as a result of hit and run impacts followed by core dismemberment, melting, and recrystallization, as suggested for the group IVA iron meteorites in order to explain rapid rates of cooling in the least evolved members (McCoy et al., 2011).

2.5.4 Age of the SBT

The identical Mo, Ru, and ^{183}W isotopic compositions of the SBT and the ability to relate the HSE concentrations of these meteorites through crystal-liquid fractionation provide permissive evidence that the SBT meteorites originated on the same parent body and are related by fractional crystallization from a common melt. The average μ^{182}W value for this body is -312 ± 5 and the average μ^{183}W value is +9 ± 5. As has been done for other CC type iron meteorites (e.g., Kruijer et al., 2017), the μ^{182}W value is corrected for additional *r*-process input revealed by the ^{183}W excess, yielding an average $\mu^{182}W_{Corr}$ value of -325 ± 8 (see Appendix 2 for details). The $\mu^{182}W_{Corr}$ value of the SBT is not resolved from the $\mu^{182}W_{Corr}$ values of other CC type iron meteorites or NC type iron meteorites, except the IC and IIAB groups (Kruijer et al., 2017). The $\mu^{182}W_{Corr}$ value of the SBT parent body results in a ^{182}W model age of 2.1 ± 0.8 Myr after calcium

aluminum rich inclusion (CAI) (**Fig. 2.6**), which is not resolved from other CC type or NC type iron meteorite parent bodies, except for the IC and IIAB groups (Kruijer et al., 2017). This differentiation age is within the lifetime of ^{26}Al, allowing for the differentiation event to have been driven by internal heating, consistent with the interpretation that the SBT are magmatic iron meteorites formed in the core of the SBT parent body.

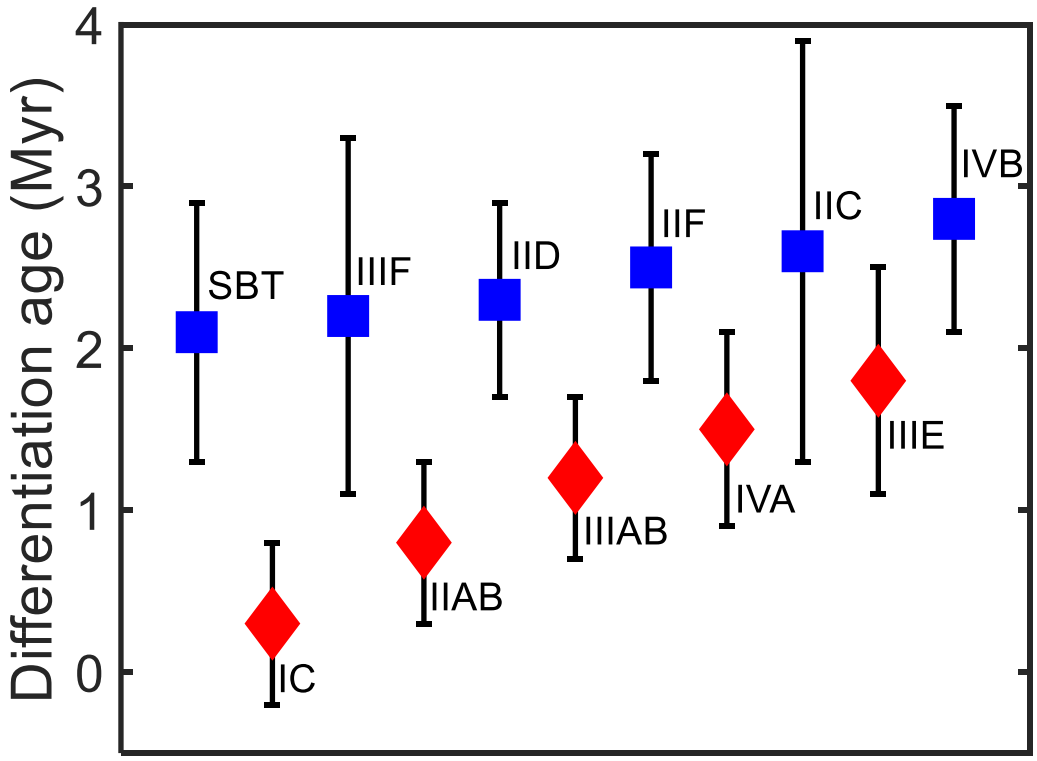

Fig. 2.6. Tungsten model metal-silicate differentiation ages (post CAI formation in Myr) in ascending order of ages for the SBT parent body compared to data for other CC type (blue) and NC type (red) bodies from Kruijer et al. (2017). The SBT has a W model age that overlaps with the other CC type bodies and most NC type bodies, within uncertainty.

Differentiation ages can be used to estimate parent body accretion ages by making certain assumptions regarding the time required for a parent body to heat sufficiently to

allow metal-silicate segregation. Based on this reasoning, Kruijer et al. (2017) proposed that all NC type iron meteorite parent bodies accreted simultaneously about 0.5 Myr prior to the accretion of all CC type iron meteorite parent bodies. This conclusion relied on the averaging of data for only Groups I and II (volatile rich) irons. To estimate a separate parent body accretion age for the SBT, we use a similar thermal model to that described by Kruijer et al. (2017), which calculates the heat produced from ^{26}Al, the primary heat producing radionuclide during the early Solar System. Details about this model are provided in Appendix 2. Uncertainties for the model accretion ages represent the range of accretion ages calculated using the range of Al concentrations and differentiation age uncertainties. For the SBT parent body, the differentiation age, coupled with an assumed Al concentration range of 0.86-1.68 wt. % for the parent body, based on the range of Al concentrations found in carbonaceous chondrites (Lodders and Fegley, 1998), corresponds to a parent body accretion age of 1.1 ± 0.5 Myr after CAI formation (**Fig. A2.6**). Because of differences in the calculation of heat production, our thermal model differs somewhat from that of Kruijer et al. (2017). To facilitate comparisons, accretion ages for other iron meteorite parent bodies were recalculated using our model coupled with the differentiation ages reported by Kruijer et al. (2017) (**Table 2.5**). When considering the uncertainties associated with ^{182}W differentiation ages, NC type iron meteorite parent bodies have accretion ages ranging from 0.3 ± 0.3 to 1.0 ± 0.5 Myr after CAI formation, whereas CC type iron meteorite parent bodies have accretion ages from 1.1 ± 0.5 to 1.4 ± 0.5 Myr after CAI formation. Uncertainties of ~0.5 Myr for each body mean that permissible model ages of accretion for both CC and NC types overlap.

Table 2.5. Model accretion ages for NC and CC type iron meteorites determined using the thermal model described in Appendix 2.

Iron meteorite group	Differentiation age ± 2σ (Myr)	Accretion age (Myr)
NC type		
IC	0.3 ± 0.5	0.3 ± 0.3
IIAB	0.8 ± 0.5	0.5 ± 0.5
IIIAB	1.2 ± 0.5	0.7 ± 0.4
IIIE	1.8 ± 0.7	1.0 ± 0.5
IVA	1.5 ± 0.6	0.9 ± 0.5
CC type		
SBT	2.1 ± 0.8	1.1 ± 0.5
IIC	2.6 ± 1.3	1.2 ± 0.6
IID	2.3 ± 0.6	1.2 ± 0.4
IIF	2.5 ± 0.7	1.3 ± 0.5
IIIF	2.2 ± 1.1	1.1 ± 0.6
IVB	2.8 ± 0.7	1.4 ± 0.5

All model differentiation age data are from Kruijer et al. (2017) except for the SBT.

Kruijer et al. (2017) argued that the assumptions behind a single-stage core formation accretion model at a certain temperature are affected by the volatile-enrichment or depletion of the parent body, so it is important to compare iron meteorite parent bodies from the same volatile type. Kruijer et al. (2017) found that the CC type IIC, IID, and IIF irons have $\mu^{182}W_{Corr}$ values that are resolved from the NC type IIAB irons, which was argued to suggest that CC type iron meteorite parent bodies accreted later than NC type iron meteorite parent bodies. The accretion age results of our preferred thermal model, however, overlap for the NC type IIAB and the CC type IIC, IID, and IIF irons. In addition, the NC type IIIAB and IIIE irons have accretion ages that overlap with the CC type IIIF and SBT accretion ages. There is also overlap among the NC type IVA and the CC type IVB accretion ages. Thus, we conclude that NC and CC type iron meteorite parent body accretion ages cannot be resolved at present, given the current level of uncertainties associated with parent body differentiation ages and Al content.

Since differences in accretion ages cannot explain the differences in $\mu^{182}W_{Corr}$ values for Group II irons with current uncertainties, we examine the effects of S content on differentiation. Kruijer et al. (2014a) showed that there was a correlation between S content of a parental melt with $\mu^{182}W_{Corr}$ values for the IIAB, IIIAB, IVA, IID, and IVB irons. The determination of the S content for the SBT parent body allows for a reexamination of this correlation with three NC and three CC bodies. The S *vs.* $\mu^{182}W_{Corr}$ value of the SBT falls directly on the correlation and reduces the scatter observed for the IID and IVA iron meteorites (**Fig. 2.7**). The six meteorites define a single trend with a MSWD = 2.7, which may suggest that the S content of a parental melt is the controlling factor for $\mu^{182}W_{Corr}$ values, possibly by affecting the temperature at which metal melting and differentiation begins. Further studies to define the S content of other NC and CC type iron parental melts are needed to evaluate this potential correlation.

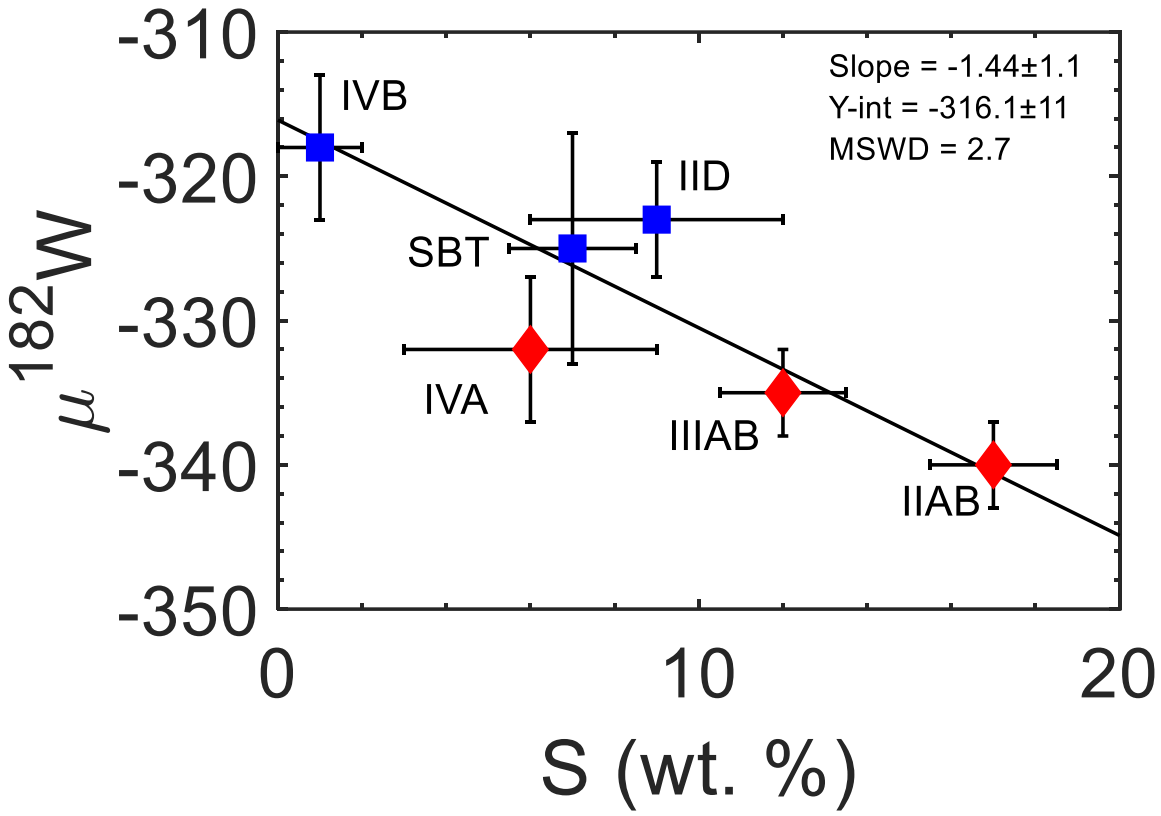

Fig. 2.7. Parental melt S content *vs.* $\mu^{182}W_{Corr}$ values. The IIAB, IIIAB, IVA, IID, SBT, and IVB irons define a single trend. Sulfur contents are from Chabot (2004) and Goldstein et al., (2009), and $\mu^{182}W$ values are from Kruijer et al. (2017).

2.5.5 Comparison of the SBT chemical composition to NC and CC bodies

The HSE parental melt models of the CC type SBT and IVB iron meteorites, and the NC type IVA iron meteorites provide new insights into the chemical conditions of the NC and CC nebular domains. The SBT and IVB iron meteorites have parental melt HSE compositions that are 2-7 times more concentrated than the IVA parent body. Presuming that the concentrations are directly related to the ratio of core metal to silicate shell, this result suggests that the SBT and IVB iron meteorite parent bodies had proportionally smaller cores than NC type parent bodies, and therefore most likely accreted in more oxidizing environments, compared to, e.g., the IVA parent body. Previous studies have

proposed that the NC and CC domains represent the inner and outer Solar System, respectively, that were separated by the formation of Jupiter (Warren, 2011; Budde et al., 2016a; Kruijer et al., 2017). Such a model could account for the more oxidizing environment of the SBT and IVB parent bodies.

Additional chemical differences are observed for NC and CC parental melts when comparing S content. Past studies, also using experimentally derived partitioning data for siderophile elements in the Fe-Ni-S, Fe-Ni-P, and Fe-Ni-C systems to determine D values, have concluded that the IIAB, IIIAB, IVA, IID, and IVB iron meteorite parental melts had S contents of 17 ± 1.5, 12 ± 1.5, 6 ± 3, 9 ± 3, and 1 ± 1 wt. %, respectively (Chabot, 2004; Goldstein et al., 2009). When iron meteorites are compared based on volatile content, there is an additional S depletion for CC parental melts compared to NC parental melts (**Fig. 2.8**). This additional depletion in S may reflect parent body processes more common on CC type parent bodies, such as core separation into S-rich and P-rich liquids, or may be a consequence of nebular processes.

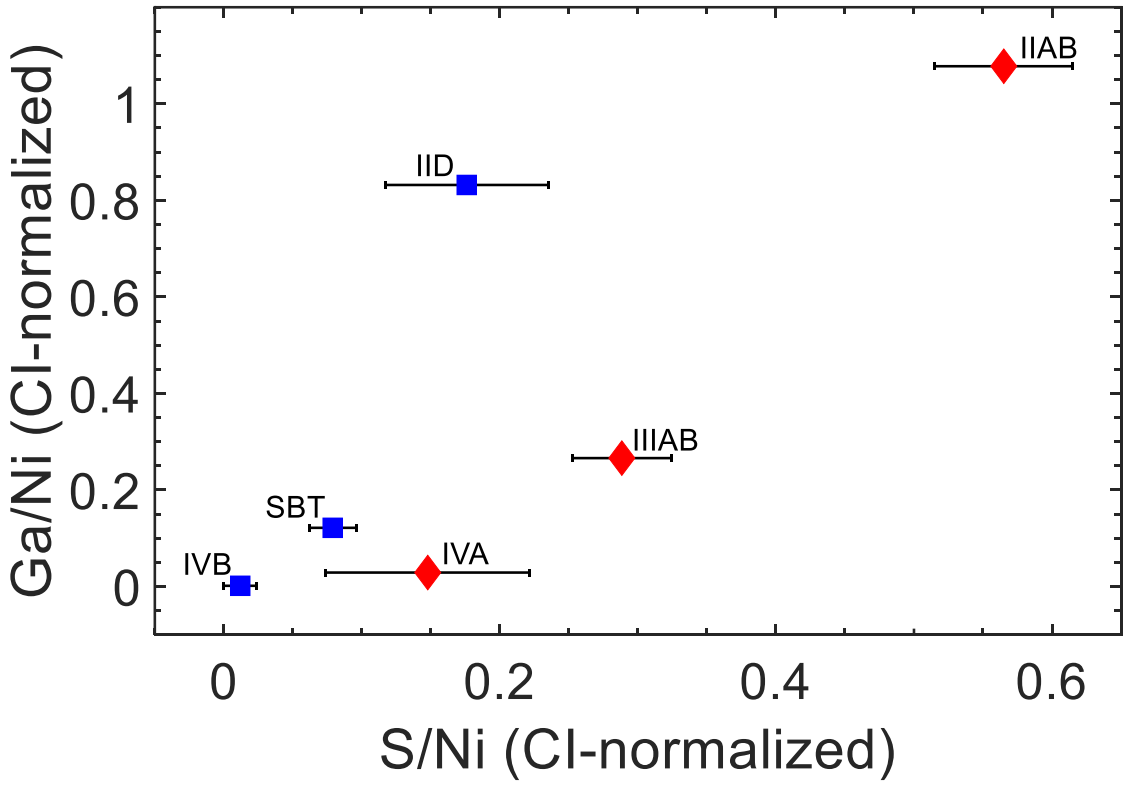

Fig. 2.8. S/Ni (CI-normalized) *vs*. Ga/Ni (CI-normalized) plot for the IIAB, IIIAB, IVA, IID, SBT, and IVB irons. Blue symbols are CC bodies and red symbols are NC bodies. There are two distinct trends observed for the NC and CC bodies, suggesting that the CC parental melts have an additional S depletion not observed for NC parental melts. Since the offset is not observed for Ga concentrations, the depletion in S for CC parental melts relative to NC parental melts is likely not due to volatile depletion.

2.6 Conclusions

The isotopic and chemical data presented here for Babb's Mill, South Byron, and ILD 83500 support the interpretation that these meteorites sample a core from the same parent body and that they should be considered together as a trio.

1) The SBT parent body originated in the CC nebular domain, based on Mo, Ru, and ^{183}W isotopic data. Thermal modeling indicates the parent body likely accreted 1.1 ± 0.5 Myr after CAI formation and the Hf-W isotopic system indicates that the parent body differentiated 2.1 ± 0.8 Myr after CAI formation. Both accretion and

differentiation ages are similar to the ages for other NC and CC type iron meteorite parent bodies.

2) The siderophile element concentrations of the SBT suggest that Babb's Mill crystallized from a primitive melt, followed soon afterward by South Byron. ILD 83500 crystallized later in the sequence from a more evolved melt. The HSE patterns of these meteorites can be reproduced by a fractional crystallization model, in which Babb's Mill represents the first 1 % of solid to crystallize. South Byron can be modeled as the solid composition after 2 % crystallization, and ILD 83500 represents the solid composition at 42 % crystallization. This model suggests an initial melt composition of 7 wt. % S, 1 wt. % P, <0.05 wt. % C, and a HSE initial melt composition with chondritic HSE ratios.
3) The bulk concentrations of the HSE in the SBT parental core suggest that it comprised about 10 % the mass of the body, assuming the upper range of HSE concentrations observed in chondrites as a starting parent body composition. This in turn suggests that the SBT parent body was oxidized, which is also consistent with the comparatively high average Ni content for the SBT (17-18 wt. % Ni).
4) Milton has identical Mo and Ru isotopic compositions to the SBT, providing permissive evidence of being from the same parent body. The HSE content of Milton, however, cannot be directly related to the SBT by fractional crystallization or any other process we attempted to model. Milton metal was likely derived from a parental melt with relative abundances of some HSE that were modestly fractionated from known chondritic ratios, most likely on a different parent body from the SBT.

5) Comparison of modeled HSE parental melt compositions of the SBT to the IVA (NC) and IVB (CC) iron meteorite parent bodies provides further evidence that portions of the CC nebular domain were more oxidizing than the NC domain. In addition, comparison of the S parental melt compositions of the IIAB, IIIAB, IVA, IID, SBT, and IVB iron meteorites suggest that there was a general S depletion among CC type iron meteorite parental melts, compared to NC type bodies.

2.7 Acknowledgements

We gratefully acknowledge the Smithsonian Institution, Arizona State University, and the US Antarctic Meteorite Program, which is a cooperative venture of the Smithsonian, NASA and the National Science Foundation, for providing access to the samples for this study. We also thank Frederic Moynier, Thomas Kruijer, and two anonymous reviewers for helpful comments that improved the manuscript. This study was supported by NASA Emerging Worlds grant NNX16AN07G (to RJW).

2.8 Appendix 2

2.8.1 Isotopic measurements

The aliquots for Os isotopic analysis were added into chilled Pyrex® Carius tubes, along with 5 ml of concentrated HNO_3 and 2.3 ml of concentrated HCl. The Carius tubes were sealed and then heated for at least 24 h at 220 °C (Shirey and Walker, 1995). Osmium was extracted from the solution using CCl_4 solvent-extraction methods (Cohen and Waters, 1996), and then further purified using microdistillation from a dichromate solution (Birck et al., 1997). This procedure resulted in ~70 % yield for Os. Between 70-

300 ng of purified Os were loaded onto outgassed Pt filaments in HBr, activated with $Ba(OH)_2$, and analyzed as OsO_3^- by a *Thermo-Fisher Triton* thermal ionization mass spectrometer (TIMS) at the University of Maryland (UMd) (Walker, 2012). Osmium isotopic data were corrected for instrumental and natural mass fractionation by normalizing $^{192}Os/^{188}Os$ to 3.08271 (Allègre and Luck, 1980). Isobaric interferences from OsO_3^- species with ^{17}O or ^{18}O were corrected using the O isotopic composition reported by Nier (1950).

Molybdenum aliquots were prepared following the methods described in Worsham et al. (2016b). In brief, aliquots were dried, dissolved in 1 M HF, and loaded onto an anion column of AG 1-X8 (200-400 mesh) resin. Molybdenum was eluted using 6 M HNO_3-3 M HF, dried, and dissolved in 6 M HCl. The Mo solution was then added to a smaller anion column with ~0.3 mL AG 1-X8 (200-400 mesh) resin and eluted with 1 M HCl. This elution was repeated a second time. This procedure resulted in ~50 % yield for Mo. Purified Mo aliquots were treated with concentrated HCl and HNO_3 multiple times in order to destroy organics. The samples were then dissolved in 6 M HCl, about 500-1000 ng Mo were loaded onto outgassed Re filaments, and activated with ~ 2 µL of a 5 µg/µL $La(NO_3)_3$ solution. A double filament assembly was used and the same amount of $La(NO_3)_3$ was added to the ionization Re filament. Molybdenum was measured as MoO_3^- by the *Thermo-Fisher Triton Plus* TIMS at UMd. The $^{100}Mo^{18}O^{16}O_2^-$ species was measured using a 10^{13} Ω resistor amplifier for O isotope interference corrections. Molybdenum isotopic data were corrected for instrumental and natural mass fractionation by normalizing $^{98}Mo/^{96}Mo$ to 1.453171 (Lu and Masuda, 1994).

Aliquots for Ru isotopic analysis were prepared following the procedure discussed by Bermingham et al. (2016). In brief, aliquots of the primary dissolution were dried and dissolved in 0.15 M HCl and then processed through a cation column of AG50WX8 (200-400 mesh) resin. Ruthenium was immediately eluted using 0.15 M HCl and dried to about 5 µL for microdistillation, in which $H_2Cr_2O_7$ was used as the oxidant and 6 M HCl was used as the trap solution and reductant. This procedure resulted in ~50 % yield for Ru. About 1000 ng of purified Ru were loaded onto outgassed single Pt filaments in HBr, activated with $Ba(OH)_2$, and analyzed as RuO_3^- by a *Thermo-Fisher Triton Plus* TIMS. Ruthenium isotopic data were corrected for instrumental and natural mass fractionation by normalizing $^{99}Ru/^{101}Ru$ to 0.745075 (Chen et al., 2010). The O isotopic composition reported by Nier (1950) was used to determine and correct for in-run ^{17}O and ^{18}O molecular interferences.

Tungsten aliquots from the primary dissolution were exposed to air for 1-2 weeks in order to oxidize Fe in the solution from +2 to +3. Ferrous Fe was then removed using a diisopropyl ether extraction procedure (Dodson et al., 1936). The resulting solution was dried, dissolved in 1 M HCl-0.1 M HF, and eluted through a cation column of AG50-X8 (200-400 mesh) resin with 1 M HCl-0.1 M HF. The solution was then dried, dissolved in 0.5 M HCl-0.5 M HF, loaded onto a column of AG1-X8 (100-200 mesh) resin, and eluted with 6 M HCl-1 M HF. This elution was repeated twice using progressively less resin and acid (Touboul and Walker, 2012). This procedure resulted in ~60 % yield for W. Organics accrued during the column chemistry were removed by drying the sample multiple times in concentrated HCl and HNO_3. About 300-1000 ng of purified W were then dissolved in 1 M HCl- 0.01 M HF, loaded onto outgassed single Re filaments,

activated with 1 µL of a 5 µg/µL La-5 µg/µL Gd solution, and measured as WO_3^- using a *Thermo-Fisher Triton* TIMS following the method of Archer et al. (2017). This method allowed independent measurement of both $^{182}W/^{184}W$ and $^{183}W/^{184}W$. Potential mass interference from ReO_3^- species were also monitored and corrected for. Tungsten isotopic data were corrected for instrumental and natural mass fractionation by normalizing $^{186}W/^{184}W$ to 0.92767 (Volkening et al., 1991).

Some prior studies of terrestrial and cosmochemical materials have observed deviations in $^{183}W/^{184}W$ ratios for reference standards and samples that were processed through certain column chemistry procedures and analyzed by multi-collector inductively-coupled plasma mass spectrometry (e.g., Kruijer et al., 2013; Cook and Schönbächler, 2016; Kruijer and Kleine, 2018). Such deviations have been interpreted to be the result of nuclear field shift effects, requiring corrections to be made to account for the observed deviations (Cook and Schönbächler, 2016). However, no such effects have been observed for reference standards, terrestrial samples, or meteorite samples using the column chemistry procedures described here, coupled with thermal ionization mass spectrometry (Archer et al., 2017; Mundl et al., 2017; Mundl et al., 2018; Archer et al., 2019). Consequently, no corrections to the measured $^{183}W/^{184}W$ ratios from this study have been made.

Values of $\mu^{182}W$ for the SBT were corrected for nucleosynthetic variations using the method reported by Kruijer et al. (2014b). In this correction, variation in the *r*-process component for irons is subtracted from the $\mu^{182}W$ value using $\mu^{183}W$ as an *r*-process component proxy. This correction is based on the $^{182/184}W$ *vs.* $^{183/184}W$ isotopic composition of fine- and coarse-grained CAI, which give a $^{182/184}W$ *vs.* $^{183/184}W$ (186/184

normalized) correlation of +1.41 ± 0.06. The ΔT_{CAI} ages were then calculated using the CAI initial value $\mu^{182}W$ of -349 ± 7 (Kruijer et al., 2014b), the present-day chondritic $\mu^{182}W$ value of -190 ± 10 (Kleine et al., 2004), and the decay constant for ^{182}Hf of 0.078 ± 0.002 Myr^{-1} (Vockenhuber et al., 2004). The ΔT_{CAI} ages for Babb's Mill, South Byron, and ILD 83500 were calculated from the $\mu^{182}W$ and $\mu^{183}W$ values determined by normalizing to $^{186}W/^{184}W$. The uncertainties for the ΔT_{CAI} ages include the 2SD determined from the analysis of standards run during an analytical campaign for $\mu^{182}W$ and $\mu^{183}W$ compositions, and the uncertainty associated with the $\mu^{183}W$ *r*-process correction only (Kruijer et al., 2014b). Tungsten isotopic data were not obtained for Milton because there was insufficient material to make this measurement.

2.8.2 Fractional crystallization modeling

In this study, Eq. S1 is used to calculate the concentration of an element throughout the evolution of a liquid melt, where F_n is the fraction of liquid (n = 100 is pure liquid), C_{Ln} is the concentration of an element in the liquid phase at F_n, and D_n is the partition coefficient of an element. The concentration of an element is calculated at each 0.1 % fraction of liquid with respect to the concentration of the previous liquid fraction. For S, a constant partition coefficient of 0.001 is used (Walker et al., 2008). The partition coefficients for P and C are determined at each F_n by considering the concentration of S and P or S and C, respectively, in the liquid at F_{n+1}. Equation S2 is used to account for the effects of S on P and C partitioning behavior (Chabot and Jones, 2003).

Values of D_o for P and C are taken from Chabot et al. (2017) and Worsham et al. (2016a), respectively. The β_{SPC} variable is determined using Eq. S3 (Jones and Malvin,

1990), in which β_S and β_P are taken from Chabot et al. (2017) and β_C is taken from Worsham et al. (2016a). For P, the effects of C are not considered and for C, the effects of P are not considered. The β_{SPC} and "Fe domains" (Eq. S4; Chabot et al., 2017) variables are calculated at each F_n, where X_i is the mole fraction of an element.

$$\text{Eq. S1: } C_{Ln-1} = \frac{C_{Ln}}{(F_{n-1} + 1 - F_{n-1}D_{n-1})}$$

$$\text{Eq. S2: } \frac{1}{D} = \frac{[\text{Fe domains}]^{\beta_{SPC}}}{D_o}$$

$$\text{Eq. S3: } \beta_{SPC} = \left[\frac{2X_S}{2X_S + 4X_P + 4X_C}\right]\beta_S + \left[\frac{4X_P}{2X_S + 4X_P + 4X_C}\right]\beta_P + \left[\frac{4X_C}{2X_S + 4X_P + 4X_C}\right]\beta_C$$

$$\text{Eq. S4: Fe domains} = \frac{1 - 2X_s - 4X_P - 4X_C}{1 - X_s - 3X_P - 3X_C}$$

$$\text{Eq. S5: } C_{Sn} = C_{Ln}D_n$$

After determining the concentration of S, P, and C at each F_n, the D values for the HSE are calculated at each F_n using Eq. S2-S4 by collectively considering the changes in S, P, and C content in the liquid (Jones and Malvin, 1990; Chabot and Jones, 2003; Worsham et al., 2016a; Chabot et al., 2017). The concentration of HSE in the liquid at each F_n is then determined using Eq. S1 and the solid composition (C_{Sn}) at each F_n is determined using Eq. S5.

2.8.3 Thermal accretion model

This study uses a thermal accretion model (Eq. S6) that describes a solid sphere, which gains heat through ^{26}Al decay and loses heat by conduction (Carslaw and Jaeger, 1959). The model solves for the temperature at a certain depth within the sphere at any

time (t) after accretion and we assume that differentiation occurred instantaneously when the temperature halfway to the center of the body from the surface reached 1600 K (Kruijer et al., 2017). This assumption is made since ~50 % of silicate melt fractions may be necessary for core formation (Taylor, 1992). In order to be consistent with past studies, we assume a radius of R = 40 km for the parent body and the temperature is evaluated at a depth of r = 20 km (Kruijer et al., 2017). The background nebular temperature is represented as T_0, thermal conductivity is represented as K, thermal diffusivity is represented as k, and a ^{26}Al decay constant of $\lambda = 9.83 \times 10^{-7}$ yr^{-1} is used with a Solar System initial $^{26}Al/^{27}Al$ ratio of 5.23×10^{-5} (Norris et al., 1983; Jacobsen et al., 2008). All values used in this model are listed in **Table A2.2**.

Eq. S6: $$T = T_o + \frac{kA}{K\lambda} e^{-\lambda t} \left(\frac{R \sin\left(r * \left(\frac{\lambda}{k}\right)^{\frac{1}{2}} \right)}{r \sin\left(R * \left(\frac{\lambda}{k}\right)^{\frac{1}{2}} \right)} - 1 \right) + \frac{2R^3 A}{r\pi^3 K} \sum_{n=1}^{\infty} \frac{(-1)^n}{n\left(n^2 - \frac{\lambda R^2}{k\pi^2}\right)} \sin\left(\frac{n\pi r}{R}\right) e^{-kn^2\pi^2 t/R^2}$$

The background temperature is assumed to be 250 K, consistent with models by Hevey and Sanders (2006), Kruijer et al. (2014a), and Kruijer et al. (2017), which is the average temperature estimated for a circumsolar disk at 2.5 AU and 1 Myr after T-Tauri star formation (Woolum and Cassen, 1999). The power per unit volume A ($W\ m^{-3}$) = H*ρ, where H is the power per unit mass ($W\ kg^{-1}$) and ρ is the density of the planetesimal ($kg\ m^{-3}$). The power per unit mass, H, is equal to (total Al atoms/kg)*($^{26}Al/^{27}Al$)*(2.0×10^{-26} W/atom), where ($^{26}Al/^{27}Al$) is a function of time, the parent body concentration of Al is based off of the range observed in carbonaceous chondrites (0.86-1.68 wt. %; Lodders and Fegley, 1998), and the decay power of ^{26}Al is calculated from a decay energy of ^{26}Al of 6.4×10^{-13} J/atom with its half-life of 9.83×10^{-7} yr^{-1} (Hevey and

Sanders, 2006). We note that this calculation of heat production differs from that reported by Kruijer et al. (2017). Kruijer et al. (2017) report using a range of Al concentration from 8.65-16.8 wt. %, which is an order of magnitude greater than used here. In addition, Kruijer et al. (2017) report calculating heat production as A = Al concentration*($^{26}Al/^{27}Al$) and it is calculated in this study as A = (total Al atoms/kg)*($^{26}Al/^{27}Al$)*(2.0 x 10^{-26} W/atom)*(ρ), where ($^{26}Al/^{27}Al$) is a function of time in both models. Despite these differences between the model inputs, the results of both models differ by less than 0.2 Myr. For this study, 0.86 wt. % Al relates to A = 12.3*($^{26}Al/^{27}Al$), 1.20 wt. % Al relates to A = 17.1*($^{26}Al/^{27}Al$) and 1.68 wt. % Al relates to A = 23.9*($^{26}Al/^{27}Al$). Therefore, the results in this study for 0.86 wt. % Al and 1.20 wt. % Al are similar to the results by Kruijer et al. (2017) for 12 wt. % Al and 16.8 wt. % Al, respectively.

Supplementary Tables

Table A2.1. Osmium isotopic composition data for Milton and the SBT.

Sample	n[a]	$\mu^{189}Os$	2SD	$\mu^{190}Os$	2SD
Milton	1	-4	8	25	18
Babb's Mill	2	1	6	-4	7
Babb's Mill (*rep*)	1	8	7	-1	4
South Byron	3	8	7	-4	7
ILD 83500	1	3	6	-3	7

[a] n is the number of analyses. The reported $\mu^{189}Os$ and $\mu^{190}Os$ values reflect the average values obtained for each meteorite piece. Uncertainties reflect the largest (of n analyses) 2SD of the standards run during an analytical campaign.

Table A2.2. Terms and values used in the thermal accretion model.

Term	Symbol	Units	Value	Source
Al concentration	Al	Wt. %	0.86-1.68	Lodders and Fegley (1998)
Ambient temperature	T_o	K	250	Woolum and Cassen (1999)
Decay constant	λ	yr^{-1}	9.83×10^{-7}	Norris et al. (1983)
Decay energy	E	J $atom^{-1}$	6.4×10^{-13}	Hevey and Sanders (2006)
Density	ρ	kg m^{-3}	3200	Kruijer et al. (2017)
Diffusivity	k	m^2 s^{-1}	5×10^{-7}	Kruijer et al. (2017)
Initial $^{26}Al/^{27}Al$	$^{26}Al/^{27}Al_i$	atom/atom	5.23×10^{-5}	Jacobsen et al. (2008)
Power per unit mass	H	W kg^{-1}	[a]	
Power per unit volume	A	W m^{-3}	H x ρ	
Depth assessed for temperature	r	km	20	Kruijer et al. (2017)
Radius of body	R	km	40	Kruijer et al. (2017)
Thermal conductivity	K	W m^{-1} K^{-1}	2.1	LaTourrette and Wasserburg (1998)

[a] H = (Al atoms/kg)*($^{26}Al/^{27}Al$)*($E*\lambda_{sec}$), where ($^{26}Al/^{27}Al$) is a function of time and λ is in units of s^{-1}.

Supplementary Figures

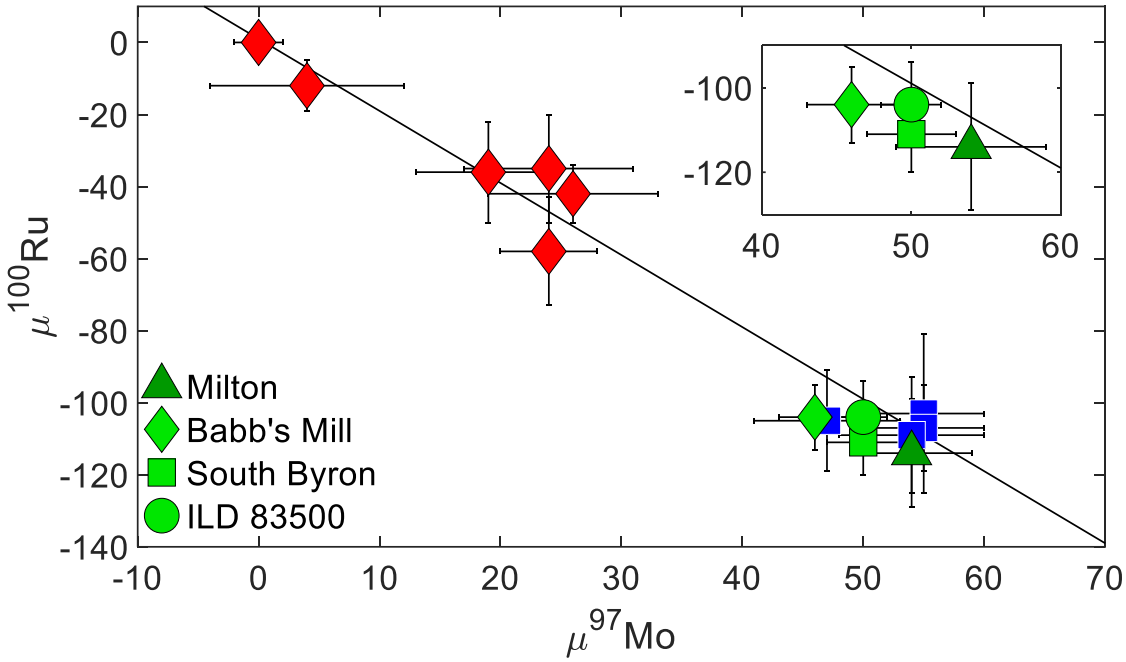

Fig. A2.1. Compilation of CRE-corrected μ^{97}Mo *vs*. μ^{100}Ru data for iron meteorites from Bermingham et al. (2018). Blue squares represent meteorites classified as CC type and red diamonds represent meteorites classified as NC type. Data from this study for the SBT and Milton are also plotted. The black line represents the regression of the Mo-Ru cosmic correlation from Bermingham et al. (2018). The inset shows the Mo and Ru isotopic composition of the SBT and Milton without other meteorites.

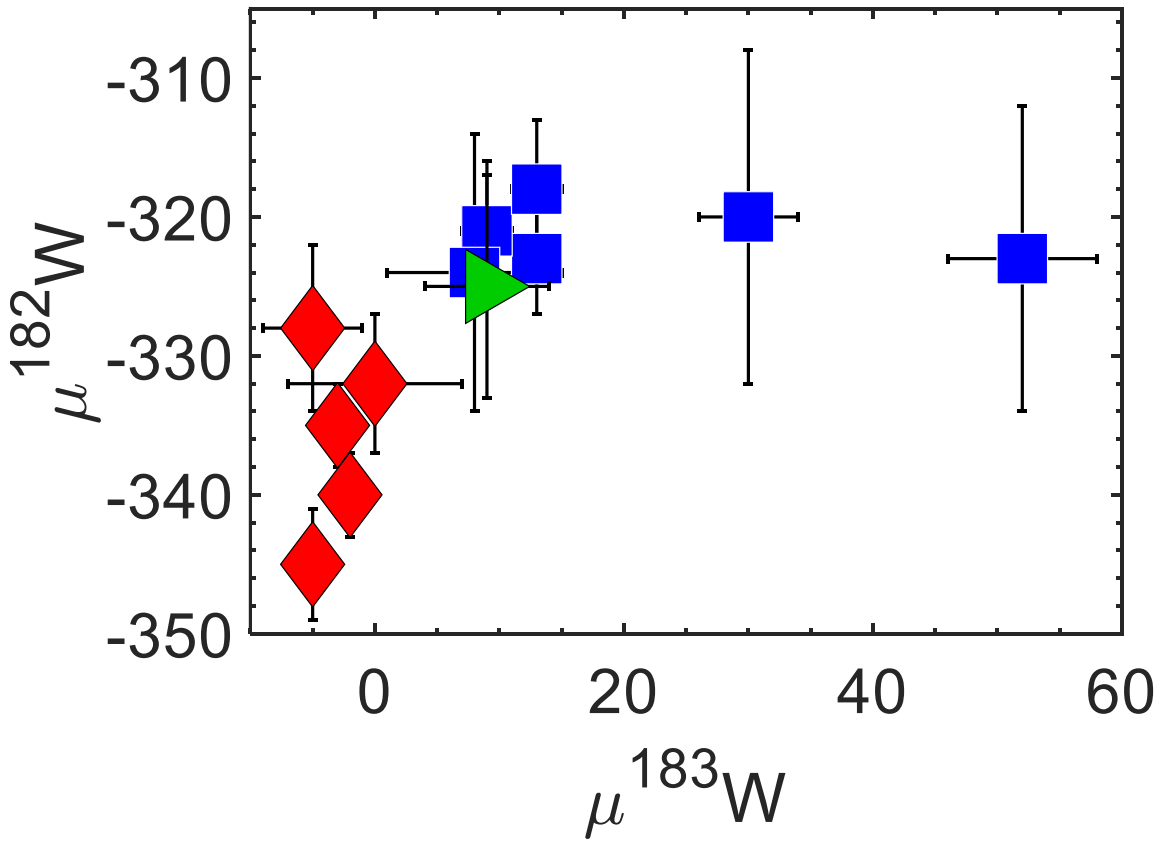

Fig. A2.2. Compilation of $\mu^{183}W$ *vs*. $\mu^{182}W$ data for iron meteorites from Kruijer et al. (2017). Blue squares represent meteorites classified as CC type and red diamonds represent meteorites classified as NC type. The average SBT W isotopic composition is also plotted (green triangle). The average $\mu^{183}W$ value for the SBT (+9 ± 5, 2SE, n = 4) is resolved from the W standard value obtained during the analytical campaigns for this work (0 ± 2, 2SE, n = 16).

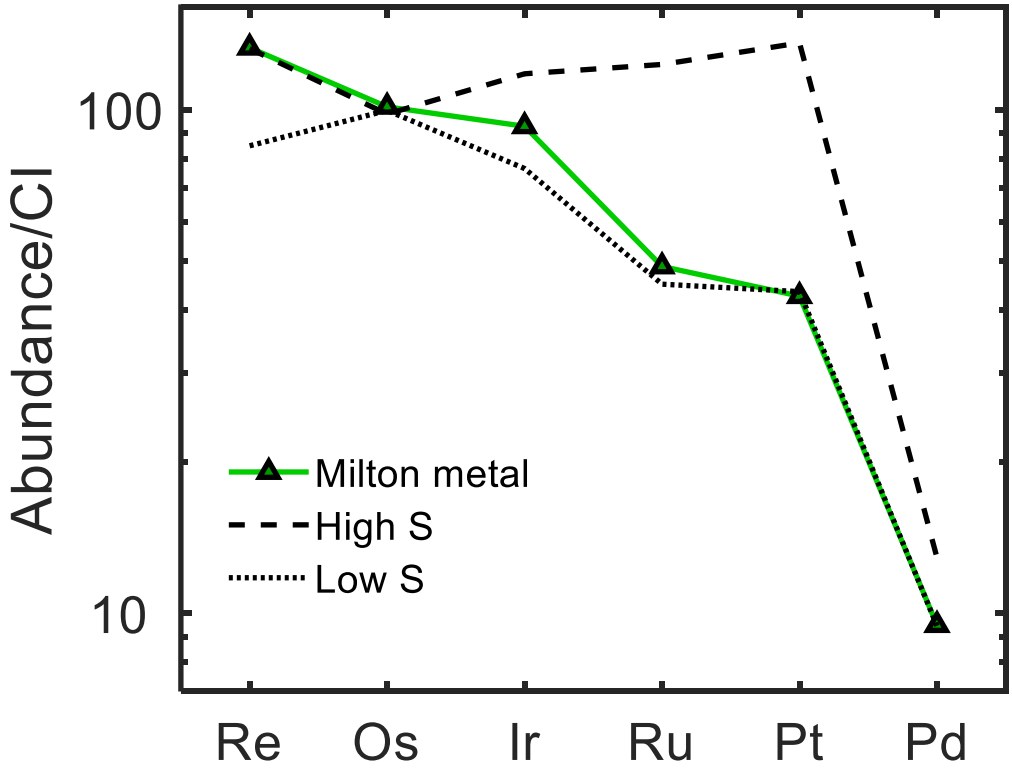

Fig. A2.3. CI-normalized HSE patterns calculated from a constant HSE initial concentration from Table 2.4 and varying S and P parental melt compositions. Assuming Milton metal crystallized in the first ~10% of solid, the Re/Os of Milton metal resembles a high S system with 17 wt. % S, 1.5 wt. % P, and <0.05 wt. % C. However, the Pt/Os of Milton metal resembles a lower S system with 8 wt. % S, 1 wt. % P, and <0.05 wt. % C.

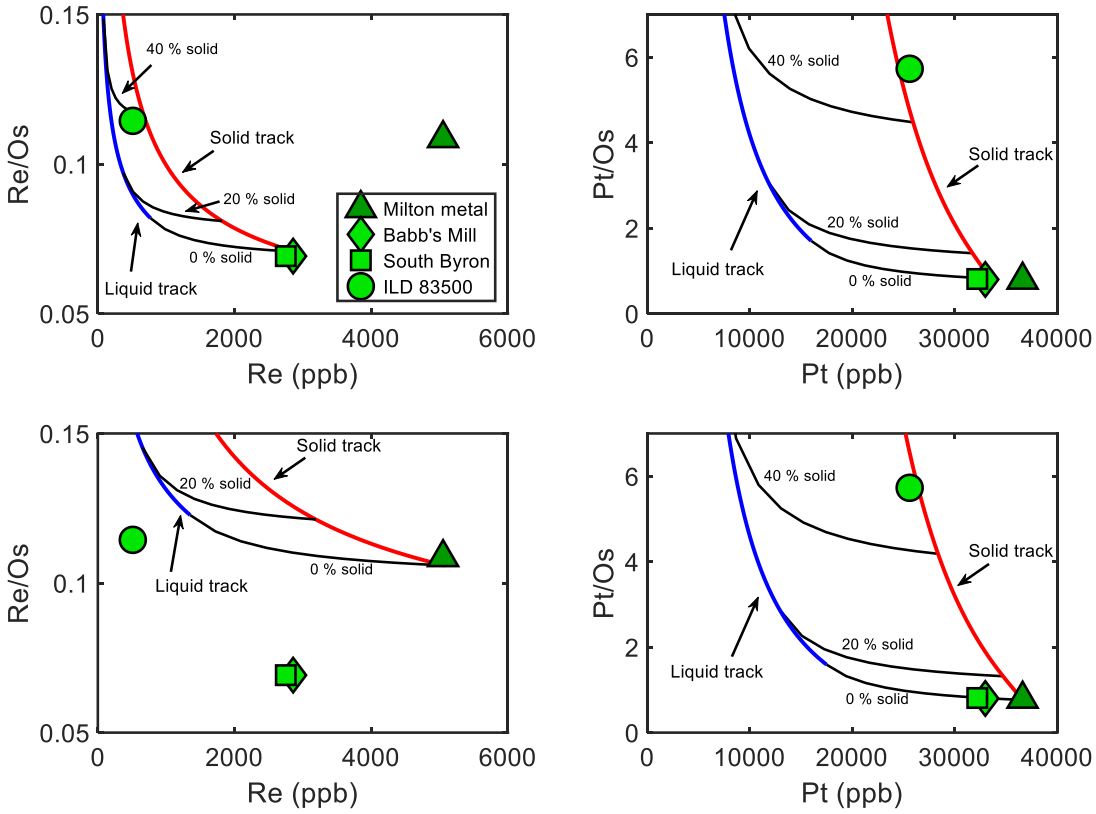

Fig. A2.4. Fractional crystallization models for Re (ppb) *vs*. Re/Os and Pt (ppb) *vs.* Pt/Os for two pairs of parental melt compositions. Black lines represent mixing between solid and liquid, at 0 % solid-100 % liquid, 20 % solid-80 % liquid, and 40 % solid-60 % liquid. (*Upper left and right*) Fractional crystallization model, which reproduce the HSE patterns observed for the SBT, calculated for the initial parameters listed in Table 2.4. (*Bottom left and right*) Fractional crystallization model with 7 wt. % S and 1 wt. % P, which can reproduce the observed HSE patterns for Milton metal. This model requires a starting liquid composition of Re = 1,350 ppb, Os = 11,000 ppb, and Pt = 17,500 ppb. Neither model can reproduce both Re/Os and Pt/Os observed in Milton metal and the SBT through solid metal-liquid metal mixing.

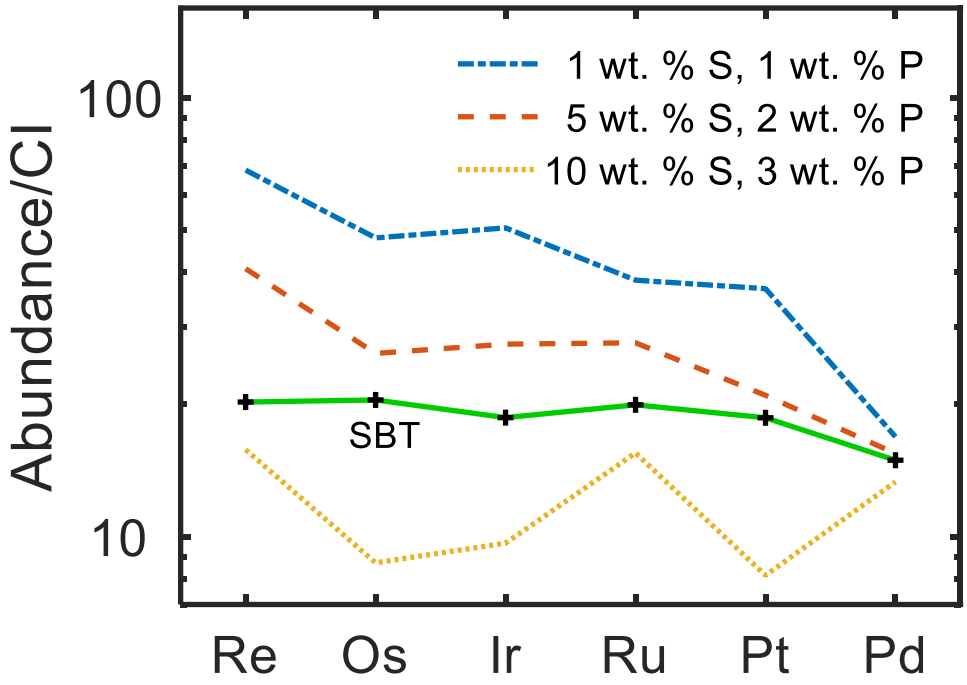

Fig. A2.5. CI-normalized HSE parental melt compositions, with varying S and P contents, which reproduce the Milton HSE pattern as an early (<10 %) fractional crystallizing metal. The parental melt composition of the SBT is shown for comparison.

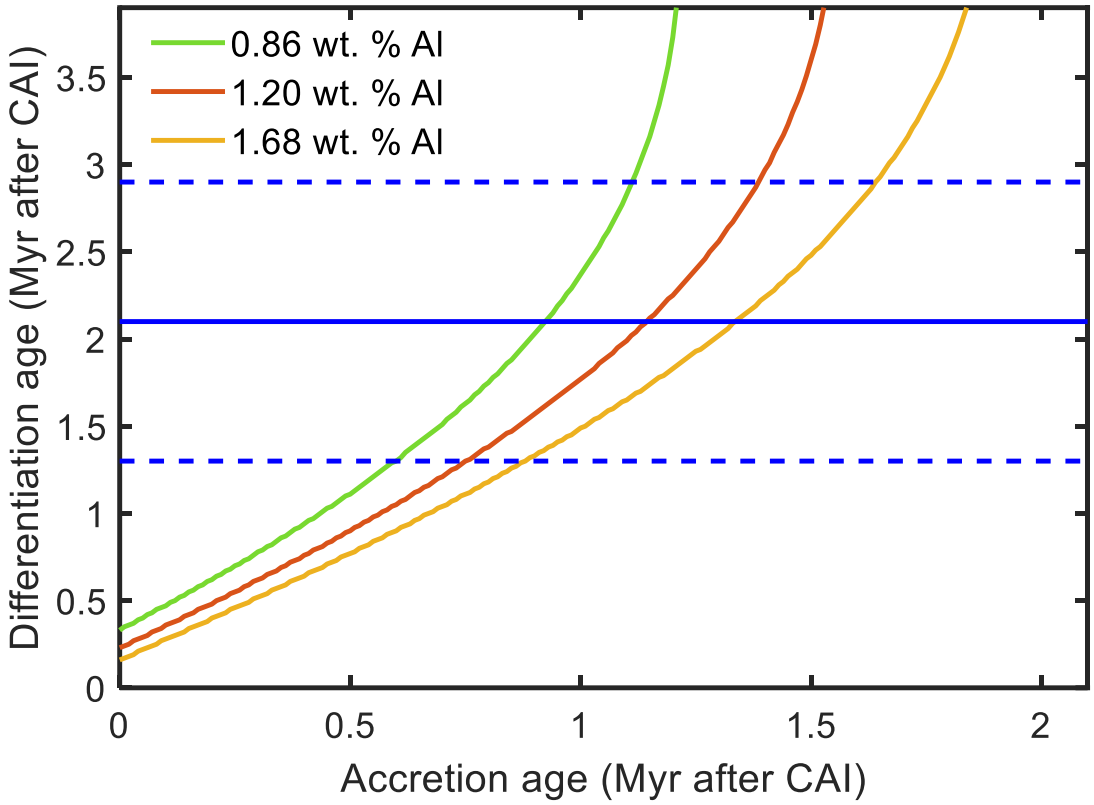

Fig. A2.6. Thermal model results for a 40 km radius body when evaluating the temperature midway to the center of the body (r = 20 km). The model is based on an assumption of instantaneous differentiation when the temperature reaches 1600 K. Thermal model results are shown for Al concentrations of 0.86, 1.20, and 1.68 wt. %. The differentiation age of the SBT (2.1 ± 0.8 Myr after CAI formation; blue solid line ± blue dashed lines) fits an accretion age range of 1.1 ± 0.5 Myr after CAI formation.

Chapter 3: New implications for the origin of the IAB main group iron meteorites and the isotopic evolution of the noncarbonaceous (NC) reservoir

Note: This chapter has been previously published in the following publication:

Hilton C.D. and Walker R.J. (2020) New implications for the origin of the IAB main group iron meteorites and the isotopic evolution of the noncarbonaceous (NC) reservoir. *Earth Planet. Sci. Lett.* **540**, 116248.

3.1 Abstract

The origin of the IAB main group (MG) iron meteorites is explored through consideration of ^{182}W isotopic compositions, thermal modeling of ^{26}Al decay, and mass independent (nucleosynthetic) Mo isotopic compositions of planetesimals formed in the noncarbonaceous (NC) protosolar isotopic reservoir. A refined ^{182}W model age for the meteorites Campo del Cielo, Canyon Diablo, and Nantan suggests that the IAB-MG parent body underwent some form of metal-silicate segregation as early as 5.3 ± 0.4 Myr after calcium-aluminum rich inclusion (CAI) formation or as late as 13.8 ± 1.4 Myr after CAI formation. If melting of the IAB-MG occurred prior to 7 Myr after CAI formation, it was likely driven by ^{26}Al decay for a parent body radius >40 km. Otherwise, additional heat from impact is required for melting metal this late in Solar System history. If melting was partially or wholly the result of internal heating, a thermal model of ^{26}Al decay heat production constrains the accretion age of the IAB-MG parent body to ~1.7 ± 0.4 Myr after CAI formation. If melting was, instead, dominantly caused by impact heating, thermal modeling suggests the parent body accreted more than 2 Myr after CAI formation. Comparison of Mo mass independent isotopic compositions of the IAB-MG to other NC bodies with constrained accretion ages suggests that the Mo isotopic

composition of the NC reservoir changed with time, and that the IAB-MG parent body accreted between 2 to 3 Myr after CAI formation, thus requiring an origin by impact. The relationship between nucleosynthetic Mo isotopic compositions and accretion ages of planetesimals from the NC reservoir suggests that isotopic heterogeneity developed from either addition of *s*-process material to, or removal of coupled *r*-/*p*-process material from the NC reservoir.

3.2 Introduction

"Nonmagmatic" iron meteorite groups (e.g., IAB complex, IIE) are so termed due to their chemical and textural differences compared to "magmatic" irons (e.g., IIAB, IIIAB, IVA) (e.g., Willis, 1981; Wasson and Kallemeyn, 2002). Magmatic iron meteorites consist of members that have chemical compositions that can largely be related to one another through fractional crystallization of liquid metal (e.g., Scott, 1972). As such, they are widely interpreted to sample planetary cores. By contrast, nonmagmatic irons are characterized by chemical compositions that cannot be accounted for by simple fractional crystallization (e.g., Wasson and Kallemeyn, 2002; Worsham et al., 2016a). Many are also silicate-bearing (Benedix et al., 2000; Hunt et al., 2017a), leading to proposals that nonmagmatic irons represent partially differentiated bodies and/or bodies partially melted by impact. While the term "nonmagmatic" is intended to highlight differences with "magmatic" irons, this title is somewhat of a misnomer, as the metal initially crystallized from a molten state.

The IAB main group (MG), which is the largest nonmagmatic iron group, is characterized by variations in siderophile element abundances that reflect the dominant effects of physical mixing processes rather than simple fractional crystallization (Wasson

and Kallemeyn, 2002; Worsham et al., 2016a). As with other nonmagmatic iron meteorites, many IAB-MG metals also contain trapped silicate and graphite inclusions, despite their strong density contrasts with metal, consistent with the interpretation of formation by physical mixing (Wasson and Kallemeyn, 2002). Some studies have sought to explain the chemical and mineralogical characteristics of the IAB-MG irons as a result of partial differentiation of a planetesimal driven by internal heating (e.g., Kratcher, 1985). Other studies have called for an impact-related origin (e.g., Wasson and Kallemeyn, 2002), or have argued for hybrid models, which combine partial differentiation with a subsequent impact (e.g., Benedix et al., 2000). Keys to discerning between these models include the interpretation of age constraints. If metal melting and metal-silicate segregation on the IAB-MG parent body occurred sufficiently early that ^{26}Al decay would contribute significant heat to the body, then internal heating was likely involved in the process. If instead, melting occurred after the viability of ^{26}Al internal heating, impact related heating of an undifferentiated body must be involved.

The extent of ^{26}Al internal heating is related to the accretion age of a planetary body (e.g., Kruijer et al., 2014a; Hunt et al., 2018). This age, in some cases, can be constrained using thermal models of ^{26}Al decay with a calculated age of metal-silicate segregation for an iron meteorite (e.g., Hilton et al., 2019). The segregation age, in turn, can be constrained by application of the Hf-W chronometer ($^{182}Hf \rightarrow {}^{182}W + 2\beta^-$, $T_{1/2}$ = 8.9 Myr; Vockenhuber et al., 2004). Despite its importance, however, the metal-silicate segregation age of the IAB-MG is debated, with different studies reporting different ages. One problem encountered by earlier studies is the effect of meteorite exposure to galactic cosmic rays, which can induce nuclear reactions within meteorites and cause burnout of

some W isotopes (e.g., Masarik, 1997; Leya et al., 2003). Initial studies of ^{182}W isotopic compositions of IAB-MG irons reported model metal-silicate segregation ages ranging from 1.2 ± 1.8 to 9.1 ± 3.6 Myr after calcium-aluminum rich inclusion (CAI) formation, possibly reflecting cosmic ray exposure (CRE) effects that were uncorrected or inadequately corrected for (Markowski et al, 2006; Qin et al., 2008; Schulz et al., 2009, 2012). Methods to monitor and correct siderophile elements for CRE were subsequently developed, involving measurement of Os or Pt isotopes in the same meteorite chunk being analyzed for ^{182}W isotopic composition (e.g., Walker, 2012; Kruijer et al., 2013; Wittig et al., 2013). Both of these methods have been applied to IAB-MG irons, yet somewhat discrepant ages of 3.4 ± 0.7 (Worsham et al., 2017) and 5.3 ± 0.5 (Hunt et al., 2018) Myr after CAI formation have been most recently reported. Assuming a maximum expansion of errors, these values differ by as little as 0.7 Myr, or as much as 3.1 Myr. The differences have implications for how the IAB-MG irons formed.

Potentially useful in the interpretation of the IAB-MG origin is their "genetic" isotopic compositions. Past studies have proposed that variations in mass independent, nucleosynthetic Cr and Ca isotopic compositions of bulk meteorites are related to the accretion ages of their parent bodies (Sugiura and Fujiya, 2014; Schiller et al., 2018). This relationship for the IAB-MG can instead be assessed using mass independent isotopic compositions of some siderophile elements (Mo, Ru, Pd) (Dauphas et al., 2004; Burkhardt et al., 2011; Fischer-Gödde et al., 2015; Budde et al., 2016a, 2019; Poole et al., 2017; Worsham et al., 2017; Bermingham et al., 2018; Ek et al., 2019). Overall, the nucleosynthetic isotopic heterogeneity observed for these elements (as well as Ti, Ni; Trinquier et al., 2007, 2009; Regelous et al., 2008; Nanne et al., 2019) reveal the

existence of at least two isotopically distinct nebular reservoirs during the first few millions of years of Solar System history, that have been termed “noncarbonaceous” (NC) and “carbonaceous” (CC) (e.g., Trinquier et al., 2007; Warren, 2011; Kruijer et al., 2017). The NC reservoir, in which the IAB-MG irons formed, was characterized by variable *s*-process depletions and/or coupled *r*-/*p*-process enrichments for certain elements, relative to terrestrial materials (e.g., Dauphas et al., 2004; Fisher-Gödde et al., 2015; Budde et al., 2016a, 2019; Kruijer et al., 2017; Poole et al., 2017; Worsham et al., 2017; Bermingham et al., 2018; Ek et al., 2019). The CC reservoir was characterized by an additional enrichment of *r*- and possibly *p*-process material compared to the NC reservoir, as well as also having its own variable *s*-process depletions and/or coupled *r*-/*p*-process enrichments (e.g., Dauphas et al., 2004; Fisher-Gödde et al., 2015; Budde et al., 2016a, 2019; Kruijer et al., 2017; Poole et al., 2017; Worsham et al., 2017; Bermingham et al., 2018; Ek et al., 2019). If isotopic compositions of siderophile elements in meteorites reflect accretion ages as well, it has important implications for the origins of the NC and CC reservoirs.

For this study, we analyzed the IAB-MG meteorites Campo del Cielo, Canyon Diablo, and Nantan for W isotopic compositions. These meteorites were classified as IAB-MG irons by Wasson and Kallemeyn (2002) based on relatable chemical compositions, and were chosen for intensive study here because Campo del Cielo and Nantan have young CRE ages (Nagai et al., 1993; Nishiizumi et al., 1995), and prior applications of CRE dosimeters to Campo del Cielo and Canyon Diablo showed minimal effects from cosmic rays (Worsham et al., 2017; Hunt et al., 2018). One possible cause of prior differences in reported segregation ages could be the calibration of the dosimeters

used to correct for CRE. Worsham et al. (2017) applied Os isotopes while Hunt et al. (2018) applied Pt. Consequently, for comparison purposes, here we assess CRE applying both Os and Pt dosimeters.

3.3 Methods

3.3.1 Sample preparation

A ~5 g chunk of Campo del Cielo (USNM 5615) was obtained from the Division of Meteorites, Department of Mineral Sciences, Smithsonian Institution. Chunks of Canyon Diablo (~6 g) and Nantan (~7 g) were obtained from private collectors. These meteorite chunks were cut into smaller pieces, using a water-cooled *Leco Vari-cut* saw and a 12.7 cm diamond-wafering blade, to be processed through chemical purification procedures for Os, Pt and W. The blade was cleaned with carborundum prior to cutting each meteorite piece. The surface of each cut piece was polished to remove sawblade marks using a range of coarse- to fine-grit sandpaper, then each meteorite piece was sonicated multiple times in ethanol, prior to dissolution, to remove adhering particles formed by sanding.

3.3.2 Osmium, Pt and W isotopic measurements

Cleaned pieces of Campo del Cielo, Canyon Diablo and Nantan were dissolved in 40 mL 8 M HCl at 120 °C for 72 hours in Teflon beakers. The resulting solutions were then centrifuged and the supernatants were divided into two aliquots to be separately processed for Os and Pt/W isotopic measurements. Aliquots for Os isotopic analyses were added into chilled Pyrex® Carius tubes, along with 4 ml of concentrated HNO_3 and

1.5 ml of concentrated HCl. The Carius tubes were sealed and then heated for 72 h at 240 °C (Shirey and Walker, 1995). Additional solid metal pieces of each meteorite, which were adjacent to the pieces dissolved in Teflon beakers, were also separately dissolved in Carius tubes in the same way. Solutions were removed from the Carius tubes and Os was then extracted from the solutions using CCl_4 solvent-extraction methods (Cohen and Waters, 1996), and purified using microdistillation techniques (Birck et al., 1997). Purified Os samples were loaded onto outgassed Pt filaments in concentrated HBr, activated with $Ba(OH)_2$, and analyzed as OsO_3^- using a *Thermo-Fisher Triton* thermal ionization mass spectrometer (TIMS) at the University of Maryland (UMd) (Walker et al., 2008). Osmium isotopic data were corrected for instrumental and natural mass-fractionation by normalizing $^{192}Os/^{188}Os$ to 3.08271 (Allègre and Luck, 1980). Isobaric interferences from OsO_3^- species with ^{17}O or ^{18}O were corrected using the oxygen isotopic composition reported by Nier (1950). The typical blanks for this procedure were <10 pg Os. The two-standard deviation (2SD) values for multiple analyses of the Johnson Matthey Os standard analyzed during two analytical campaigns (n = 9 and 12, respectively) were $\mu^{189}Os$ = 3 and 5 ppm (μ represents the part per million deviation of an isotopic ratio of a sample compared to a standard). The Os standard was not processed by the described microdistillation procedure.

The aliquots for Pt/W isotopic measurements were dried, dissolved in 1 M HCl-0.1 M HF, and eluted through a cation column of AG50-X8 (200-400 mesh) resin with 1 M HCl-0.1 M HF. This step was repeated until sufficient amounts of Fe were removed from the solutions so as not to overload secondary columns. Solutions were then dried, dissolved in 0.5 M HCl-0.5 M HF, loaded onto an anion column of AG1-X8 (100-200

mesh) resin, W was eluted with 6 M HCl-1 M HF, and Pt was eluted with concentrated HNO_3.

The Pt elution was dried, refluxed in 2:1 concentrated HNO_3:HCl, then dried in concentrated HCl, and finally dissolved in 0.5 M HCl. Samples were loaded onto an anion column with AG1-X8 (200-400 mesh) resin and eluted with concentrated HNO_3 (Method 2 - Hunt et al., 2017b). Solutions were dried, treated with 2:1 concentrated HNO_3:HCl, dried, and dissolved in 5 % HNO_3 for analysis, using Faraday cups on a *Thermo-Fisher Neptune Plus* MC-ICP-MS at UMd. Platinum isotopic data were corrected for instrumental and natural mass-fractionation by normalizing $^{198}Pt/^{195}Pt$ to 0.2145 (Kruijer et al., 2013). External reproducibility (2SD) of a Pt standard (made from high purity Pt ribbon, and not processed by the described chemical procedure), for $^{196}Pt/^{195}Pt$ was 12 ppm (n = 10). No systematic drift in the measured standard composition was observed over the duration of the measurement campaign. The typical blanks for these procedures were <40 pg Pt, which is negligible for the purposes of Pt isotopes in this study. Additional information about the Pt measurement routine is provided in Appendix 3.

The W eluant was dried and the column procedure was repeated two more times with sequentially less resin and acid (Touboul and Walker, 2012). Organics accrued during the W column chemistry were removed by drying the sample multiple times in concentrated HCl and HNO_3. About 600-1000 ng of purified W were then dissolved in 1 M HCl-0.01 M HF, loaded onto outgassed Re filaments, activated with 1 µL of a 5 µg/µL La-5 µg/µL Gd solution, and measured as WO_3^- using a *Thermo-Fisher Triton* TIMS, at UMd, following the method of Archer et al. (2017). Tungsten isotopic data were corrected for

instrumental and natural mass-fractionation by normalizing $^{186}W/^{184}W$ to 0.92767 (Volkening et al., 1991). The reproducibility (2SD) of the *Alfa Aesar Specpure*® W standard from three analytical campaigns (n = 9, 10 and 6, respectively) was 8 ppm for $^{182}W/^{184}W$ (all campaigns) and 7, 4, and 8 ppm for $^{183}W/^{184}W$. The typical blanks for this procedure were <1 ng W, which constituted an inconsequential <0.2 % of total W analyzed per sample.

3.4 Results

3.4.1 Assessment of CRE

Cosmic ray exposure effects on W isotopic compositions were monitored by measuring the $^{189}Os/^{188}Os$ and $^{196}Pt/^{195}Pt$ ratios of each meteorite chunk. Increasingly greater CRE effects result in increasingly negative $\mu^{189}Os$ and increasingly positive $\mu^{196}Pt$ values. Campo del Cielo (n = 4), Canyon Diablo (n = 4), and Nantan (n = 5) have $\mu^{189}Os$ values (± 2 SE of sample values) of +3 ± 1, +1 ± 1, and +2 ± 2, respectively, which are not resolved from the Os terrestrial standard analyzed with the samples, indicating that the meteorite chunks examined were not measurably modified by CRE (**Table 3.1**). The average $\mu^{189}Os$ values include the additional metal pieces that were digested separately in Carius Tubes. No isotopic differences between these pieces and those dissolved in Teflon beakers were observed. Consistent with minimal CRE modification, Campo del Cielo, Canyon Diablo, and Nantan (n = 1 for each) have $\mu^{196}Pt$ values (± 2 SD of standard values) of +1 ± 12, +7 ± 12, and -3 ± 12, respectively, which are also not resolved from the Pt terrestrial standard analyzed with the samples, and

indicate no corrections for CRE to the W isotopic compositions of these meteorites are warranted.

Table 3.1. Osmium, Pt and W isotopic compositions of Campo del Cielo, Canyon Diablo and Nantan.

Sample	n_{Os}	$\mu^{189}Os$	±	n_{Pt}	$\mu^{196}Pt$	±	n_{W}	$\mu^{182}W_{Measured}$	±	$\mu^{183}W$	±	ΔT_{CAI}	±
Campo del Cielo	4	+3	1	1	+1	12	1	-297	8	-5	4	5.1	1.0
Canyon Diablo	4	+1	1	1	+7	12	2	-294	8	-6	8	5.4	1.0
Nantan	5	+2	2	1	-3	12	3	-296	8	+0	8	5.2	1.0
IAB-MG Average							6	-295	3	-3	3	5.3	0.4

The number of measurements per sample is represented as n. For n<4, uncertainties reflect the largest of the 2SD of the standards run during an analytical campaign or 2SE of individual sample analyses. For n≥4, the 2SE of the average sample values are reported. Values of ΔT_{CAI} are reported assuming $\mu^{182}W_{Chondrite} = -190 \pm 10$ (Kleine et al., 2004).

3.4.2 Tungsten isotopic composition of IAB-MG

Campo del Cielo (n = 1), Canyon Diablo (n = 2), and Nantan (n = 3) have $\mu^{182}W$ values of -297 ± 8, -294 ± 8, and -296 ± 8, respectively, as well as corresponding $\mu^{183}W$ values of -5 ± 4, -6 ± 8, and +0 ± 8, respectively (**Table 3.1**). Combining data for all three meteorites, the average $\mu^{183}W$ value (± 2SE of sample values, n = 6) of -3 ± 3 is not resolved from the terrestrial W standard, indicating that no detectible nucleosynthetic variations or effects from nuclear field shift (e.g., Cook and Schönbächler, 2016; Kruijer et al., 2017; Kruijer and Kleine, 2019) are observed. Combining data for all three meteorites, an average $\mu^{182}W$ value of -295 ± 3 (± 2SE of sample values, n = 6) is obtained and presumed to be representative of the IAB-MG.

3.5 Discussion

3.5.1 $\mu^{182}W$ of the IAB-MG

The $\mu^{182}W$ values of Campo del Cielo, Canyon Diablo, Nantan, and the average IAB-MG are compared to results of past studies in **Fig. 3.1**. The $\mu^{182}W$ values of individual iron meteorites typically agree within analytical uncertainties, with measurements by Markowski et al. (2006), Qin et al. (2008), Schulz et al. (2012), Worsham et al. (2017), and Hunt et al. (2018). There is less agreement among the group averages, however. The average value of -295 ± 3 from this study is resolved from the average values of -283 ± 3 reported by Schulz et al. (2012) and -312 ± 6 reported by Worsham et al. (2017). The value is identical to the value of -295 ± 4 reported by Hunt et al. (2018).

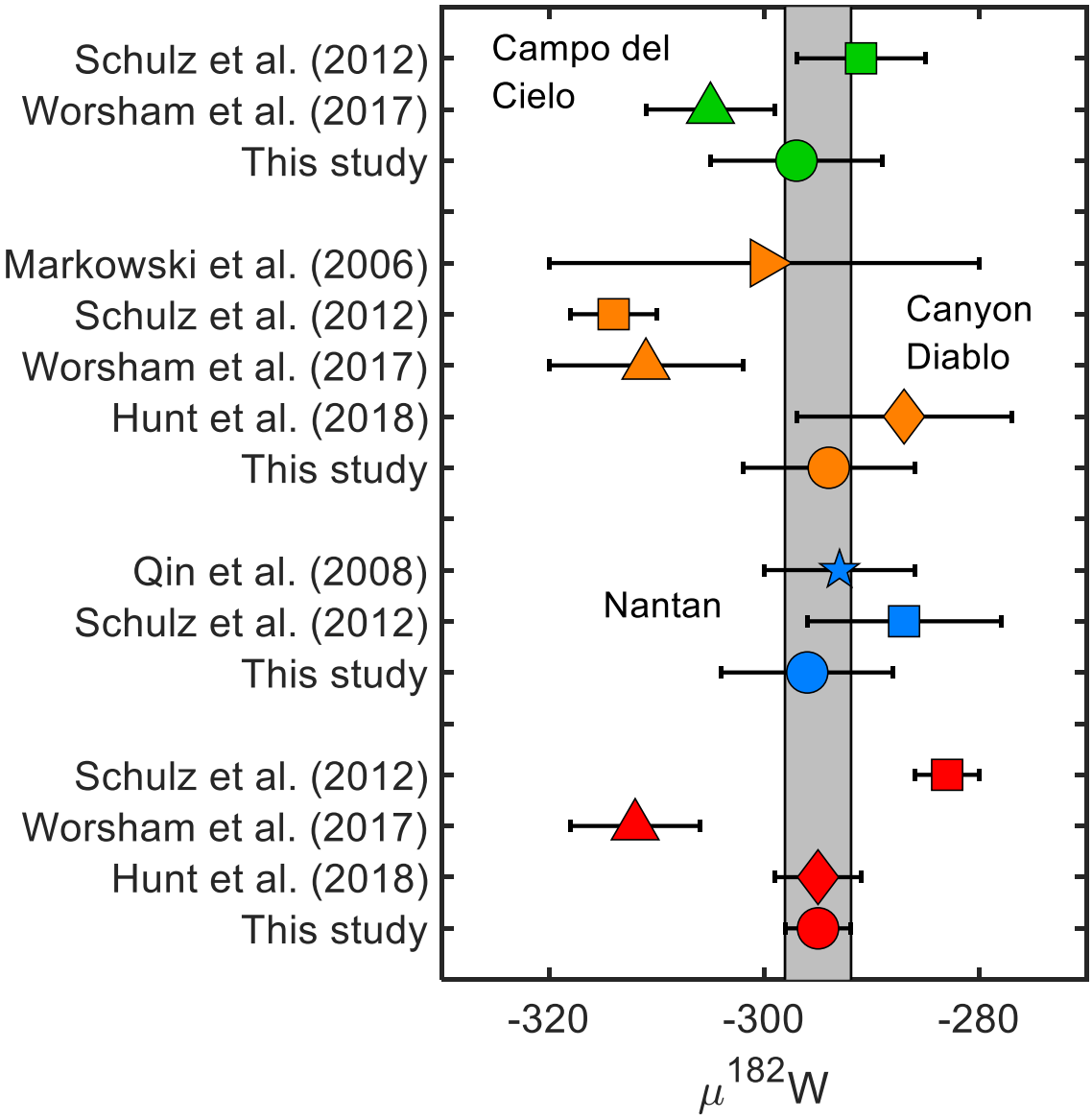

Fig. 3.1. Comparison of $\mu^{182}W$ values for Campo del Cielo, Canyon Diablo and Nantan from this study to past studies. The gray box represents the 2SE (n=6) uncertainty field for the average $\mu^{182}W$ value for the IAB-MG from this study. This average value is compared to the group average values (red symbols), which include $\mu^{182}W$ values for some IAB-MG irons not analyzed in this study, from past studies.

The origins behind the discrepant $\mu^{182}W$ values of Schulz et al. (2012) and Worsham et al. (2017) to the $\mu^{182}W$ values of this study and Hunt et al. (2018) are unknown. Schulz et al. (2012) monitored and corrected for CRE using ages determined from cosmogenic

noble gases. As discussed by Hunt et al. (2018), this approach is inadequate for correcting $\mu^{182}W$ values modified by CRE, possibly accounting for the discrepant $\mu^{182}W$ value from that study. Worsham et al. (2017) monitored and corrected for CRE using Os isotopes, which has been shown to be a viable method (e.g., Wittig et al., 2013) and is confirmed as applicable in this study. As the $\mu^{182}W$ values from this study and Worsham et al. (2017) were determined from the same laboratory using the same mass spectrometer, the discrepant $\mu^{182}W$ value from that study may be a result of the measurement routine used, which applied a secondary oxide correction (Touboul and Walker, 2012) to the measured W isotopic composition as opposed to a line-by-line correction used by the current study (Archer et al., 2017). The only IAB-MG iron measured by Worsham et al. (2017) using the line-by-line oxide correction method was modified by CRE, inhibiting a definitive assessment of this possibility. Despite discrepancies with past studies, the agreement of the $\mu^{182}W$ value from this study with the value from Hunt et al. (2018) suggests that the correct $\mu^{182}W$ value for the IAB-MG is -295 ± 3.

3.5.2 Metal-silicate segregation age

Calcium-aluminum rich inclusions, considered the earliest objects to form in the Solar System, have been examined in order to constrain the initial Solar System $\mu^{182}W$ value to -349 ± 7 (Kruijer et al., 2014b). Iron meteorites with $\mu^{182}W$ values that are greater than the CAI value dominantly reflect addition of ^{182}W from the decay of ^{182}Hf subsequent to CAI formation. Assuming that the Solar System at its inception had a uniform W isotopic

composition, variations in $\mu^{182}W$ values among iron meteorites can represent differences in timing of Hf/W fractionation and/or differences in parental Hf/W ratios.

If the parental Hf/W ratios of NC bodies are assumed to be constant, a relative model age of metal-silicate segregation can be calculated for an iron meteorite assuming separation of metal and silicate in a single event from a reservoir with a "chondritic" composition. A model age is determined relative to CAI formation using Eq. 1, where λ = 0.078 ± 0.002 Myr^{-1} (Vockenhuber et al., 2004), and $\mu^{182}W_{Chondrite}$ is the modern-day composition of chondrites reflecting the Hf/W ratio of the parent body (Kleine et al., 2004).

$$\text{Eq. 1: } \Delta t_{CAI} = -\frac{1}{\lambda} \ln \left[\frac{\mu^{182}W_{Sample} - \mu^{182}W_{Chondrite}}{\mu^{182}W_{CAI} - \mu^{182}W_{Chondrite}} \right]$$

Model ^{182}W ages are commonly calculated using a $\mu^{182}W_{Chondrite}$ value of -190 ± 10 (Kleine et al., 2004), obtained from bulk carbonaceous chondrites, which have an average $^{180}Hf/^{184}W$ ratio of 1.37 ± 0.11 (Kruijer et al., 2014b; Budde et al., 2016b, 2018). A model metal-silicate segregation age of 5.3 ± 0.4 Myr after CAI formation for the IAB-MG is obtained assuming that the parent body of the IAB-MG formed with this $^{180}Hf/^{184}W$ ratio. This age is substantially younger than most magmatic NC iron meteorites, which have model ages between 0 and 3 Myr after CAI formation (Kruijer et al., 2014a, 2017), but is similar to IAB subgroups sLL and sLM, and IIE iron meteorites, which have model ages between ~4 and 5 Myr after CAI formation (Worsham et al., 2017; Kruijer and Kleine, 2019).

One potential complication with the calculation of a model ^{182}W age of metal-silicate segregation is the assumption that the bulk parent body had a $^{180}Hf/^{184}W$ ratio similar to

carbonaceous chondrites. Carbonaceous chondrites formed in the CC reservoir from isotopically distinct material from the IAB-MG iron meteorites (e.g., Burkhardt et al., 2011). As such, if chemical compositions of parent bodies varied with isotopic composition, the carbonaceous chondrite average $^{180}Hf/^{184}W$ may be unsuitable for NC-type iron meteorites (Hellmann et al., 2019). Of the chondrites that formed in the NC reservoir (e.g., enstatite, ordinary, rumuruti; Budde et al., 2019), enstatite chondrites are genetically most similar to the IAB-MG (Fischer-Gödde et al., 2017; Budde et al., 2019), suggesting that the $^{180}Hf/^{184}W$ ratio of bulk enstatite chondrites may be most appropriate for the IAB-MG parent body. Lee and Halliday (2000) reported a range of $^{180}Hf/^{184}W$ ratios in bulk enstatite chondrites from 0.7156 ± 0.0036 to 1.344 ± 0.007. A ratio of 0.7156 would lead to a present-day chondritic $\mu^{182}W$ value of -267, which in turn results in a model age of metal-silicate segregation of 13.8 ± 1.4 Myr after CAI formation for the IAB-MG. By contrast, a ratio of 1.344 is unresolved from the $^{180}Hf/^{184}W$ ratio of the carbonaceous chondrite average and, thus, results in an unresolved model age of 5.3 ± 0.4 Myr after CAI formation. Discerning between these possible ages without further constraints on the Hf/W ratio of the IAB-MG parent body is currently impossible. Support for a Hf/W ratio lower than carbonaceous chondrites includes proposals for lower ratios for the NC-type acapulcoites-lodranites, and ordinary chondrites (Touboul et al., 2009; Hellmann et al., 2019). Additionally, it is noteworthy that the younger model age is similar to the age of ~12 Myr after CAI formation of a potential impact event to the IAB-MG parent body obtained by Pd-Ag, Pb-Tl, and Ar-Ar chronometers (Vogel and Renne, 2008; Baker et al., 2010; Theis et al., 2013).

3.5.3 Accretion age

An assessment of whether metal-silicate segregation ages of 5.3 ± 0.4 or 13.8 ± 1.4 Myr after CAI formation could reflect metal melting driven by internal heating or require additional external heat from impact can be made using a thermal model of heat production from ^{26}Al decay, and heat loss by conduction for a planetary body (**Fig. 3.2**). The thermal model is described in detail by Hilton et al. (2019). In brief, metal-silicate segregation is assumed to occur when the midpoint to the center of a planetary body reaches a temperature of 1470 K, based on the peak temperatures recorded by IAB-MG meteorites (Benedix et al., 2000; Hunt et al., 2018). The effect of different Al concentrations for the parent body on the thermal model are also assessed, with consideration to the range of Al concentrations observed in chondrites. We use a minimum Al content of 0.82 wt. % from EH chondrites and a maximum of 1.68 wt. % from CV chondrites (Lodders and Fegley, 1998).

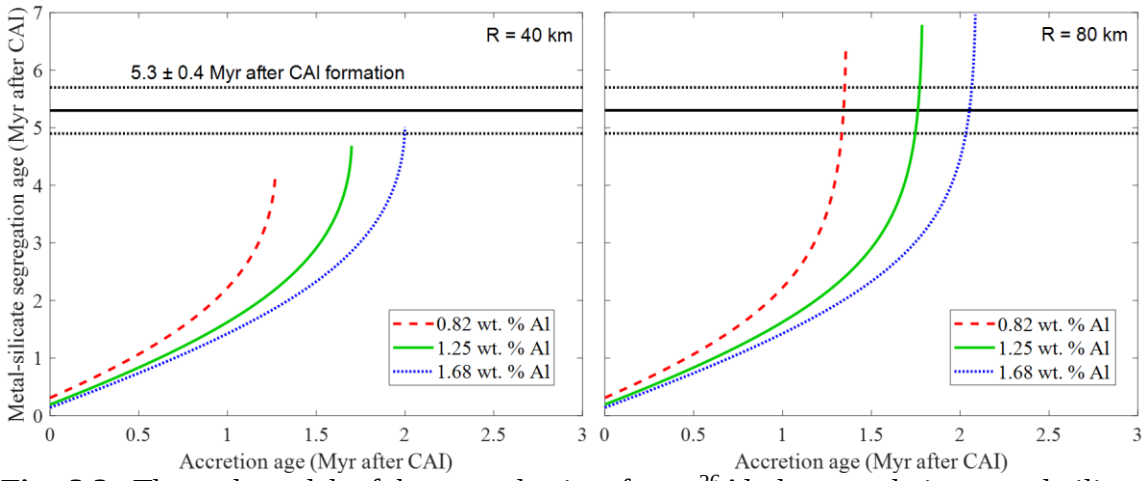

Fig. 3.2. Thermal model of heat production from ^{26}Al decay, relating metal-silicate segregation ages (assumed to occur at 1470 K) to accretion ages. The range of Al concentrations reflects the range observed in chondrites (Lodders and Fegley, 1998). The value of 0.82 wt. % is from EH chondrites, while the value of 1.68 wt. % is from CV chondrites. Also shown is the metal-silicate segregation age of the IAB-MG assuming Hf/W of carbonaceous chondrites. Models of two bodies with radii of 40 km (left) and 80 km (right) are shown.

The results of the thermal model show that internal heating, driven by ^{26}Al decay, cannot cause metal-silicate segregation at 13.8 ± 1.4 Myr after CAI formation for a body of any size, or 5.3 ± 0.4 Myr after CAI formation for bodies with a radius ≤40 km. Therefore, these scenarios require additional external heat by impact to an undifferentiated body to cause metal-silicate segregation. Model results reported by Davison et al. (2012) suggest that impacts can generate sufficient heat to cause localized melting, making this process a plausible scenario in the case of the IAB-MG. For a planetesimal to remain undifferentiated by the time of impact, it likely would have accreted >2 Myr after CAI formation (**Fig. 3.2**). Internal heat from ^{26}Al decay, on the other hand, can cause metal-silicate segregation up to 7 Myr after CAI formation for bodies with a radius >40 km. For example, an accretion age of 1.7 ± 0.4 Myr after CAI formation is predicted for a parent body with a radius of 80 km, and a metal-silicate segregation age of 5.3 ± 0.4 Myr after CAI formation (**Fig. 3.2**). This result is in

agreement with the thermal model results of Hunt et al. (2018), in which the authors proposed that metal-silicate segregation as late as 6.0 ± 0.8 Myr after CAI formation could be driven by internal heating from ^{26}Al decay if the IAB-MG parent body had a radius ≥60 km and accreted by ~1.4 Myr after CAI formation. For this interpretation, the IAB-MG could represent a partially formed planetesimal core modified by a subsequent impact that resulted in core disruption and metal-silicate mixing (Benedix et al., 2000; Hunt et al., 2017a, 2018). Due to the present uncertainty in the Hf/W ratio and radius of the IAB-MG parent body, we find that neither model can be ruled out from μ^{182}W alone.

3.5.4 Accretion age inferred from nucleosynthetic isotopic compositions

Since the accretion age of the IAB-MG inferred from the μ^{182}W value is ambiguous, it may be possible to add additional constraints by comparison of mass independent isotopic compositions of the IAB-MG to other NC bodies. Some past studies have proposed that mass independent isotopic compositions for Cr and Ca of planetary bodies vary as per their accretion ages (Sugiura and Fujiya, 2014; Schiller et al., 2018). Sagiura and Fujiya (2014) determined accretion ages for numerous parent bodies using thermal models of ^{26}Al decay coupled with estimates of the maximum temperatures recorded by different meteorite groups while Shiller et al. (2018) used estimates of the masses of planetary bodies to infer accretion age. If Cr and Ca isotopic compositions of planetary bodies did vary with accretion ages, isotopic compositions of other elements, such as Mo, Ru, and Pd, may have varied with accretion age as well. Given that more meteorites have been characterized for Mo isotopic compositions compared to Ru and Pd, comparison of mass independent Mo isotopic compositions of the IAB-MG to other NC meteorites

interpreted to form from fully differentiated, partially differentiated, and undifferentiated bodies may prove useful.

The mass independent μ^{97}Mo isotopic compositions (Burkhardt et al., 2011; Budde et al., 2016a, 2019; Poole et al., 2017; Worsham et al., 2017; Bermingham et al., 2018) and accretion ages (Sugiura and Fujiya, 2014) of NC meteorites (magmatic iron meteorites, primitive achondrites, achondrites, and chondrites) are compared in **Fig. 3.3a** (also see **Fig. A3.1**). Although uncertainties associated with Mo isotopic compositions and accretion ages are significant, meteorites from planetesimals with younger accretion ages, as a whole, are characterized by less Mo *s*-process depletions. The IAB-MG has a μ^{97}Mo value that is *s*-process un-depleted while enstatite, ordinary, and rumuruti chondrites have modest *s*-process depletions (Worsham et al., 2017; Budde et al., 2019). The shift of *s*-process depleted μ^{97}Mo values toward *s*-process un-depleted μ^{97}Mo values with younger accretion age is suggestive of the IAB-MG parent body accreting after the enstatite, ordinary, and rumuruti chondrite parent bodies. If this interpretation is accurate, the IAB-MG parent body may have accreted between 2 to 3 Myr after CAI formation. Since results of thermal models indicate ^{26}Al decay alone is not an effective heat source to cause metal melting after 2 Myr, impact is required to add the additional heat required to melt metal in the IAB-MG parent body.

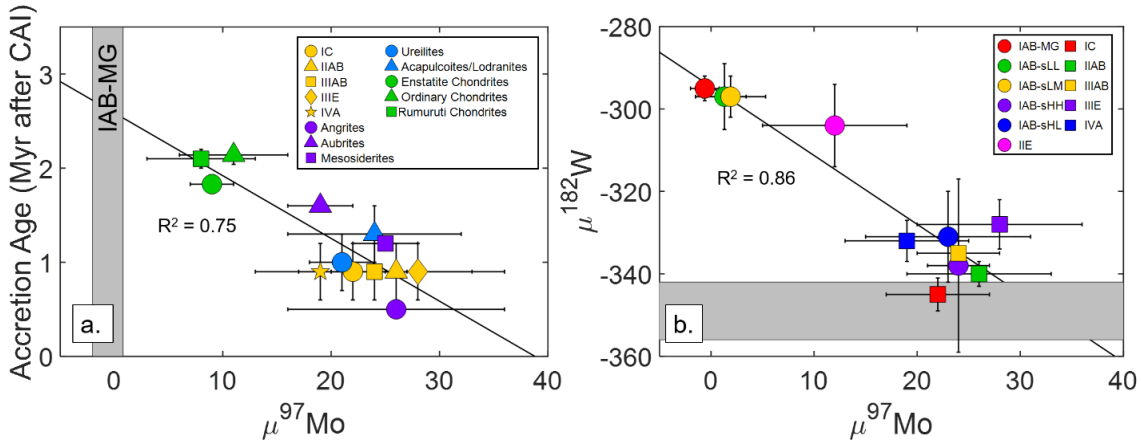

Fig. 3.3. (a) Accretion ages *vs.* μ^{97}Mo of magmatic iron meteorites (yellow symbols), primitive achondrites (light blue symbols), achondrites (purple symbols), and chondrites (green symbols) from the NC reservoir. The gray box represents the μ^{97}Mo value of the IAB-MG (Worsham et al., 2017). Accretion ages are from Sugiura and Fujiya (2014). (b) μ^{182}W *vs.* μ^{97}Mo of magmatic (square symbols) and nonmagmatic (circle symbols) iron meteorites from the NC reservoir. The gray box represents the initial μ^{182}W value of CAI (Kruijer et al., 2014b). Tungsten isotope data are from Kruijer et al. (2017), Worsham et al. (2017) and Kruijer and Kleine (2019). The μ^{97}Mo values for (a) and (b) are from Burkhardt et al. (2011), Budde et al., (2016a, 2019), Poole et al. (2017), Worsham et al. (2017), and Bermingham et al. (2018). Linear regressions for both data sets are shown with corresponding R^2 values, although linear fits are not required.

A corollary of this relationship is that μ^{97}Mo and μ^{182}W values (Burkhardt et al., 2011; Budde et al., 2016a, 2019; Kruijer et al., 2017; Poole et al., 2017; Worsham et al., 2017; Bermingham et al., 2018; Kruijer and Kleine, 2019) of metals formed in single-stage melting events are also linked (**Figs. 3.3b, A3.2**). The μ^{182}W and μ^{97}Mo values of NC iron meteorites define two distinct clusters, possibly indicating a relationship between radiogenic and nucleosynthetic isotopic compositions. If so, this is likely a reflection of the relationship between Mo nucleosynthetic isotopic compositions and accretion ages. The isotopically similar IAB-sLL and IAB-sLM groups to the IAB-MG are chemically distinct from the IAB-MG, suggesting this cluster may represent three separate bodies (Worsham et al., 2016a). The IIE iron meteorites, which fall in the middle of both

clusters, are isotopically unresolved from either cluster making identification of any clear trend difficult. Similar clusters are also observed for Ru and Pd isotopes, although these data sets are more limited by number of samples and, for Pd, associated uncertainties (Bermingham et al, 2018; Ek et al., 2019).

3.5.5 Implications for NC reservoir

Correlations between some isotopic compositions reflecting distinct nucleosynthetic origins in meteorites (Trinquier et al., 2009), coupled with the lack of isotopic anomalies for certain elements observed for bulk meteorites (e.g., Os, Pt) (Walker, 2012; Kruijer et al., 2013; Worsham et al., 2019) provide strong evidence that the protoplanetary disk was initially well-mixed. Consequently, some studies have sought to explain the isotopic heterogeneity observed among bulk meteorites for some elements by the subsequent addition/removal of certain materials to/from parts of the Solar System (e.g., Trinquier et al., 2007, 2009; Regelous et al., 2008; Dauphas et al., 2010; Burkhardt et al., 2012; Brennecka et al., 2013).

The observation that Mo nucleosynthetic isotopic compositions of NC bodies may vary with accretion ages has important implications for the formation of isotopic heterogeneity in the NC reservoir. Specifically, the data suggest that the oldest planetesimals formed from more *s*-process depleted materials, while younger planetesimals formed from increasingly less *s*-process depleted materials. Correlations between Mo isotopic compositions with Ru and Pd isotopic compositions for NC materials suggest that this observation may apply to these elements as well (Bermingham et al, 2018; Ek et al., 2019). As such, this indicates that there was an addition of *s*-process

rich material to the NC reservoir, and/or destruction and removal of a coupled *r*-/*p*-process rich component. Models calling for adding a coupled *r*-/*p*-process rich component or removing a *s*-process rich component can likely be excluded.

Whether this apparent relationship indicates a rapid or gradual addition/removal of isotopically distinct materials cannot presently be constrained. For example, if mixing of the NC reservoir was relatively rapid, variations in isotopic compositions for bodies that accreted over 2 Myr may indicate a gradual addition/removal of material. If, instead, mixing was relatively slow, addition/removal of material to part of the NC reservoir may have been rapid and isotopic compositions for bodies that accreted over 2 Myr may reflect spatial heterogeneities (e.g., Yamakawa et al., 2010). While accretion ages represent at least a 2 Myr range, this is not necessarily the timeline of isotopic heterogeneity in the NC reservoir as accretion ages provide only an upper limit of when isotopically variable precursor materials existed in the protoplanetary disk. One possible avenue of adding material to the reservoir could be by late infalling of material from the parental molecular cloud (Burkhardt et al., 2019; Nanne et al., 2019; Kruijer et al., 2019). If correct, new constraints indicate this material was *s*-process rich. It is also possible that thermal processing (e.g., Trinquier et al., 2009; Burkhardt et a., 2012; Poole et al., 2017; Worsham et al., 2019) may have removed certain materials from the reservoir. If so, this material was likely coupled *r*-/*p*-process rich.

3.6 Conclusions

Study of the IAB-MG iron meteorites Campo del Cielo, Canyon Diablo, and Nantan indicate that the IAB-MG iron meteorites have mass independent $\mu^{189}Os$ and $\mu^{196}Pt$

values that are unresolved from terrestrial standards. The IAB-MG iron meteorites have a $\mu^{182}W$ value of -295 ± 3, which results in a W model age of metal-silicate segregation between 5.3 ± 0.4 and 13.8 ± 1.4 Myr after CAI formation, based on the range of $^{180}Hf/^{184}W$ observed in enstatite chondrites. Results of a thermal model of ^{26}Al decay heat production indicate that the IAB-MG iron meteorites could have formed by impact heating or internal heating, depending on the size of the parent body and the true age of metal-silicate segregation. The IAB-MG origin is constrained to impact heating, however, if nucleosynthetic Mo isotopic compositions of NC meteorites are linked to accretion ages. This relationship suggests that *s*-process isotopic variation in the NC reservoir occurred from addition of *s*-process rich material and/or removal of coupled *r*-/*p*-process rich material.

3.7 Acknowledgements

We gratefully acknowledge the Division of Meteorites, Department of Mineral Sciences, Smithsonian Institution for providing access to a sample for this study. We also thank Richard Ash for helpful discussions. Frederic Moynier, Emily Worsham, and Alison Hunt are thanked for their helpful comments that improved the quality of this manuscript. This study was supported by NASA Emerging Worlds grant NNX16AN07G (to RJW).

3.8 Appendix 3

3.8.1 Platinum methods

Platinum isotopic compositions of Campo del Cielo, Canyon Diablo, and Nantan were determined using a *Neptune Plus* MC-ICPMS at UMd using the cup configuration in **Table A3.1**. A gain calibration was made prior to an analysis. Samples and standards were prepared as 200 ppb solutions using 5 % HNO_3. Solutions were introduced to the mass spectrometer using an Aridus 3, Ar sweep gas, and N_2 gas to stabilize the signal. A solution baseline was taken at the start of an analytical session and subtracted from all subsequent measurements. Every measurement included a peak center on ^{194}Pt. Measurements were made for 1 block with 30 cycles, with an integration time of 16.777 seconds and a 7 second idle time.

Table A3.1. Cup configuration of the *Neptune Plus* MC-ICPMS for Pt isotope analysis.

Cup	L4	L3	L2	L1	C	H1	H2	H3	H4
Resistor	10^{13}	10^{11}	10^{13}	10^{11}	10^{11}	10^{11}	10^{11}	10^{11}	10^{13}
Mass	^{189}Os	^{191}Ir	^{192}Pt	^{193}Ir	^{194}Pt	^{195}Pt	^{196}Pt	^{198}Pt	^{200}Hg

3.8.2 Supplemental figures

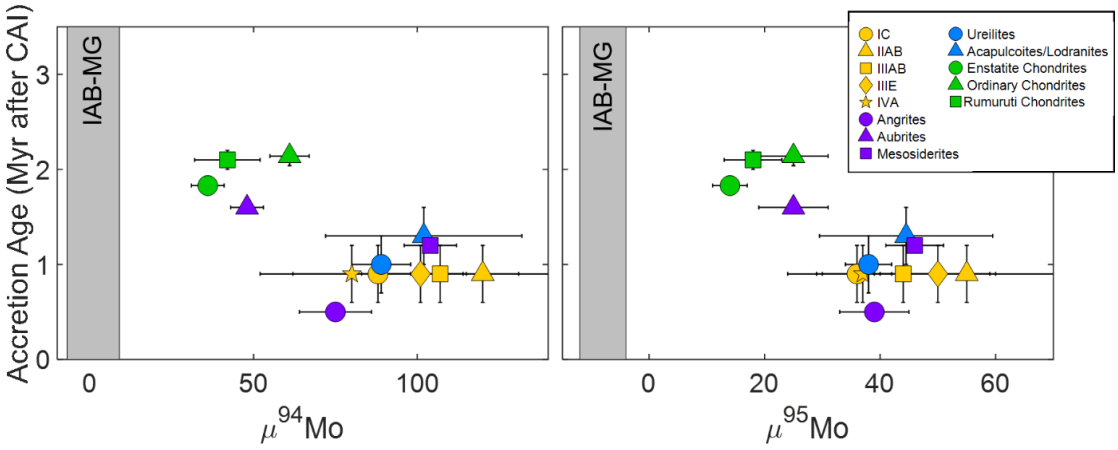

Fig. A3.1. Accretion ages *vs.* $\mu^{94,95}$Mo of magmatic iron meteorites (yellow symbols), primitive achondrites (light blue symbols), achondrites (purple symbols), and chondrites (green symbols) from the NC reservoir. The gray box represents the $\mu^{94,95}$Mo value of the IAB-MG (Worsham et al., 2017). Accretion ages are from Sugiura and Fujiya (2014). The $\mu^{94,95}$Mo values are from Burkhardt et al. (2011), Budde et al. (2016a, 2019), Poole et al. (2017), Worsham et al. (2017), and Bermingham et al. (2018).

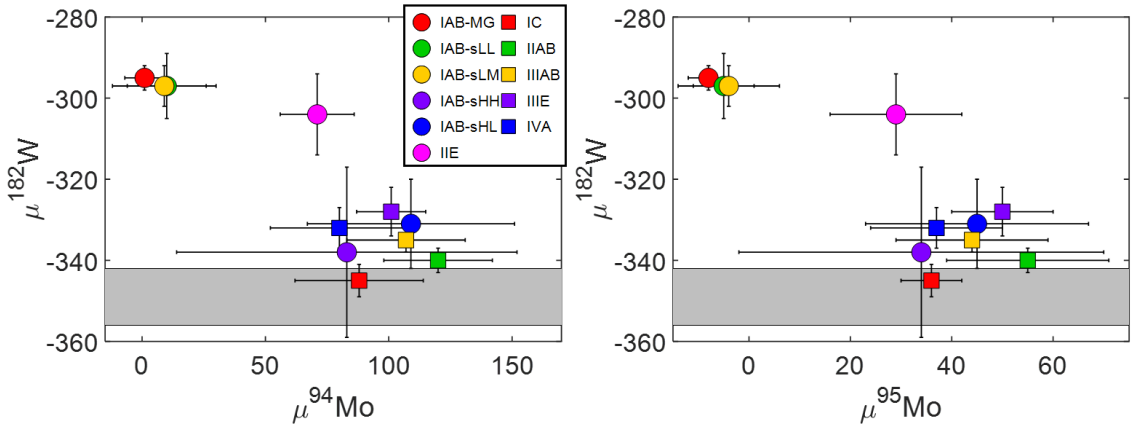

Fig. A3.2. μ^{182}W *vs.* $\mu^{94,95}$Mo of magmatic (square symbols) and nonmagmatic (circle symbols) iron meteorites from the NC reservoir. The gray box represents the initial μ^{182}W value of CAI (Kruijer et al., 2014b). Tungsten isotope data are from Kruijer et al. (2017), Worsham et al. (2017) and Kruijer and Kleine (2019). The $\mu^{94,95}$Mo values are from Burkhardt et al. (2011), Budde et al., (2016a, 2019), Poole et al. (2017), Worsham et al. (2017), and Bermingham et al. (2018).

Chapter 4: Origin of the Eagle Station Pallasites from the IIF iron meteorite core

Note: This chapter is currently in revision with *Meteoritics and Planetary Science*.

4.1 Abstract

The group IIF iron meteorites and Eagle Station Pallasites (PES) have siderophile element abundances that are permissive of derivation of all from the same parental metal liquid. Previously published genetic Mo isotopic compositions and cooling rates of these meteorites also support a common parent body origin. Modeling of highly siderophile element (Re, Os, Ir, Ru, Pt, Pd) abundances of IIF and PES metal suggests these meteorites formed mainly by mixing of primitive and evolved solid metals and liquid metals during a fractional crystallization sequence, rather than simple fractional crystallization. This type of process can be most parsimoniously explained as a result of impact induced core disruption and mixing.

4.2 Introduction

Some past studies have sought to explain the silicate and metal textures of pallasites by formation at the core-mantle boundary of planetesimals (Anders, 1964; Scott, 1977a; Wood, 1978). Other studies have called for pallasite origins by mixing of core metal and mantle materials through impact (Wasson and Choi, 2003; Yang et al., 2010), or mixing of mantle-derived metal and silicate above the core-mantle boundary (Urey, 1966; Mittlefehldt, 1980; Malvin et al., 1985; Davis and Olsen, 1991; Boesenberg et al., 2012). A key issue with most models of pallasite formation is the requirement for co-mingling silicate and liquid metal which, because of density differences, is difficult to achieve,

even in low gravity environments. Nevertheless, density separation of tightly-packed liquid metal and silicates may have been prevented in some circumstances by the high pressure of overlying materials, or rapid crystallization of the metal (Rayleigh, 1942; Scott, 1977c).

One potential key to discerning between different pallasite origin scenarios is to assess whether or not metal in pallasites share a relation to any of the planetesimal cores sampled by magmatic iron meteorites (Lovering et al., 1957). Most attention relating to pallasite-iron relations has been focused on main group pallasites (PMG) and the group IIIAB iron meteorites. The PMG and IIIAB irons share similar "genetic" O, Mo, and S isotopic compositions, supporting an origin on the same parent body (Clayton and Mayeda, 1996; Burkhardt et al., 2011; Dottin et al., 2018). In addition, the metal in PMG is compositionally similar to that in IIIAB iron meteorites, allowing for the possibility that the pallasite metal formed from the parental melt to the IIIAB iron meteorites (Scott, 1977a; Wasson and Choi, 2003). However, differences in the measured cooling rates of IIIAB irons (50-350 K/Myr) and PMG metal (2.5-18 K/Myr) are difficult to explain in a common core scenario, and have been interpreted by some to suggest that the IIIAB irons and PMG ultimately formed on separate parent bodies (Yang et al., 2010). A pallasite-iron relationship may also exist for the ungrouped Milton pallasite and South Byron Trio (SBT) iron meteorites, which share identical genetic isotope signatures, although it is problematic to chemically relate them to the same parental melt (Hilton et al., 2019; McCoy et al., 2019).

A potential iron-pallasite relationship for the IIF iron meteorites and Eagle Station Pallasites (PES) was suggested by Kracher et al. (1980), based on similar, elevated Ge/Ga

ratios of metal. Iron meteorites typically have Ge/Ga ratios of <4 (Lovering et al., 1957), while the IIF irons and PES metal have unusually high ratios near 14 (Kracher et al., 1980). However, these authors ultimately ruled out any petrogenetic relationship due to the lack of any clear relationships in the limited suite of measured siderophile element/Ni plots. As such, this potential relationship has not been further explored in much depth. The PES now ostensibly consists of five pallasites (Eagle Station, Cold Bay, Itzawisis, Karavannoe and Oued Bourdim 001) that have been grouped based on chemical compositions of metal and the unusual ^{16}O-rich oxygen isotopic compositions ($\Delta^{17}O$ = -4.68 ‰) of olivines (Scott, 1977d; Clayton and Mayeda, 1996; Korochantsev et al., 2013; Humayun et al., 2014; Bouvier et al., 2017). The IIF iron meteorite group currently consists of six members (Dorofeevka, Del Rio, Monahans (1938), Repeev Khutor, Corowa, and Purmela), which are grouped based on similar chemical compositions of some siderophile elements (Kracher et al., 1980; Connolly, Jr. et al., 2006). In this study, we analyze all six IIF irons and four PES for siderophile element abundances and Re-Os isotope systematics to re-assess a common parent body origin.

4.3 Materials and methods

Chunks of Eagle Station, Cold Bay, Corowa, and Del Rio, and a polished section of Itzawisis (USNM 7796a) were obtained from the Division of Meteorites, Department of Mineral Sciences, Smithsonian Institution. Chunks of Dorofeevka and Repeev Khutor were obtained from the Committee on Meteorites at the Russian Academy of Sciences, and Oued Bourdim 001, Monahans (1938) and Purmela were obtained from the Center of Meteorite Studies at Arizona State University. Smaller metal pieces were cut from the

meteorite chunks, when necessary, using a water-cooled *Leco Vari-cut* saw and a 12.7 cm diamond-wafering blade. Carborundum was used to clean the blade prior to cutting each meteorite. Each cut meteorite piece was polished using a range of coarse- to fine-grit SiC sandpaper to remove sawblade marks, then sonicated in ethanol to remove sawing and polishing residue.

All six IIF irons and two PES were analyzed for siderophile element abundances *in situ* using laser-ablation inductively coupled plasma mass spectrometry (LA-ICP-MS). A *New Wave UP213* ultraviolet laser was used, coupled to a *Thermo Finnigan Element 2* at the University of Maryland (UMd), following similar methods reported by Walker et al. (2008). Absolute concentrations were obtained from comparison with in-house laboratory reference iron meteorites Coahuila, North Chile, and Hoba. Data normalization was achieved using Ni concentrations reported by Wasson (1969), Scott and Wasson (1976), Scott (1977d), Connolly, Jr. et al. (2006), and Bouvier et al. (2017). Concentrations of Fe, Ni, and Co were then totaled to 100 % and concentrations of other siderophile elements were calculated relative to this total. Average concentrations and 1SD uncertainties for two to eight laser ablation tracks from each meteorite were determined. Eagle Station and Cold Bay were not analyzed by LA-ICP-MS.

With the exception of Itzawisis, concentrations of highly siderophile elements (HSE; Re, Os, Ir, Ru, Pt, Pd) and ^{187}Re-^{187}Os isotopic data were determined using the isotope dilution method used by Walker et al. (2008). About 40 to 90 mg metal pieces of each meteorite were combined in a Pyrex® Carius tube with 5 ml of concentrated HNO_3, 2.5 ml of concentrated HCl, a platinum-group element spike (^{191}Ir, ^{99}Ru, ^{194}Pt, and ^{105}Pd), and a Re-Os spike (^{185}Re and ^{190}Os). Tubes were sealed and heated for at least 24 h at

240 °C (Shirey and Walker, 1995). The tubes were allowed to cool, opened and solutions were transferred to centrifuge tubes, containing CCl_4. Osmium was extracted using the CCl_4 solvent-extraction method of Cohen and Waters (1996) and then Os was purified using a microdistillation procedure (Birck et al., 1997). Spiked Os samples were analyzed by a *Thermo-Fisher Triton* thermal ionization mass spectrometer to determine Os concentrations and $^{187}Os/^{188}Os$ ratios (Walker et al., 2008). Osmium isotopic data were corrected for instrumental and natural mass-fractionation by normalizing $^{192}Os/^{188}Os$ to 3.08271 (Allègre and Luck, 1980).

The other HSE were separated and purified using an anion column procedure, then Re and Ru separates were further purified using an additional anion column (Walker et al., 2008). The HSE solutions were evaporated to dryness and dissolved in 0.8 N HNO_3. Aliquots for Re analyses were doped with W in order to correct for instrumental mass bias. Final solutions were measured using a *Thermo-Fisher Neptune Plus* multi-collector inductively-coupled plasma mass spectrometer at UMd, except for Eagle Station and Cold Bay, which were analyzed using a *Nu Plasma* multi-collector inductively-coupled plasma mass spectrometer, also at UMd. The blanks (n = 3) for these methods ranged from 1 to 3, 3 to 5, 1 to 2, 3 to 80, 5 to 6, and 2 to 500 pg Re, Os, Ir, Ru, Pt, and Pd, respectively, which have an inconsequential effect on the reported concentrations. The uncertainties for Re, Os, Ir, Ru, Pt, and Pd abundances were estimated to be ±0.2 %, ±0.3 %, ±0.2 %, ±0.08 %, ±0.4 %, and ±0.2 %, respectively, based on the reproducibility of two separately prepared samples of Monahans (1938). Uncertainties for $^{187}Os/^{188}Os$ ratios were estimated to be ±0.1 %, and the uncertainties for $^{187}Re/^{188}Os$ ratios were estimated to be ±0.2 %.

4.4 Results

Siderophile element abundances determined by LA-ICP-MS for the IIF irons and two PES are reported in **Table 4.1**. Average concentrations generally agree with those reported by past studies within 20 %, with a few values differing as much as 150 % (the three greatest deviations are 150 %, 83 % and 44 %, observed for W – Corowa, Re – Corowa, and As – Itzawisis, respectively) (Wasson, 1969; Scott and Wasson, 1976; Scott, 1977d; Connolly, Jr. et al., 2006; Bouvier et al., 2017). Highly siderophile element abundances, determined by isotope dilution, are reported in **Table 4.2**. Abundances of HSE agree with those determined by LA-ICP-MS within 34 %. The Re-Os isotopic data are also reported in **Table 4.2**. The IIF irons are characterized by a moderate range of $^{187}Re/^{188}Os$ and $^{187}Os/^{188}Os$ ratios of 0.3675 to 0.5901 and 0.12444 to 0.14315, respectively. The PES are characterized by a lesser range in $^{187}Re/^{188}Os$ and $^{187}Os/^{188}Os$ ratios of 0.3654 to 0.4836 and 0.12477 to 0.13456, respectively. The IIF irons and PES have E_{Os} values ranging from +1 ± 1 to +25 ± 1, calculated as the part per 10,000 deviation from the $^{187}Os/^{188}Os$ ratio of a sample to a 4.568 Ga reference isochron, assuming an initial Solar System $^{187}Os/^{188}Os = 0.09517$ and $\lambda = 1.666 \times 10^{-11}$ yr^{-1} (Smoliar et al., 1996; Archer et al., 2014) (**Fig. 4.1**). The largest deviation of +25 ± 1 was determined for Cold Bay, of which our piece was highly rusted (Scott, 1977d). Nevertheless, these E_{Os} values are consistent with these meteorites experiencing limited open-system behavior for the HSE since metal crystallization in the early Solar System.

Table 4.1. Average siderophile element abundances of IIF iron meteorites and two Eagle Station Pallasites (PES) determined by LA-ICP-MS.

	Dorofeevka	Del Rio	Monahans (1938)	Purmela	Repeev Khutor	Corowa	Itzawisis	Oued Bourdim 001
Re	2.04 ± 0.03	1.60 ± 0.07	1.06 ± 0.05	0.74 ± 0.05	0.19 ± 0.04	0.06 ± 0.01	1.7 ± 0.2	0.35 ± 0.02
Os	27 ± 1	21 ± 1	11.5 ± 0.2	9.6 ± 0.4	1.33 ± 0.08	0.64 ± 0.04	24 ± 2	3.5 ± 0.2
W	1.26 ± 0.07	1.2 ± 0.1	2.6 ± 0.5	0.76 ± 0.05	0.72 ± 0.04	0.21 ± 0.03	0.3 ± 0.1	0.33 ± 0.05
Ir	23 ± 1	19.6 ± 0.8	13.8 ± 0.2	9.8 ± 0.4	2.8 ± 0.2	0.80 ± 0.04	21 ± 1	5.7 ± 0.1
Mo	11.4 ± 0.6	11.9 ± 0.7	13 ± 2	10.4 ± 0.4	13.1 ± 0.9	17 ± 2	13 ± 1	14.4 ± 0.7
Ru	21.7 ± 0.7	19.2 ± 0.8	18.6 ± 0.4	12.0 ± 0.4	11.0 ± 0.3	3.8 ± 0.5	19 ± 1	11.3 ± 0.8
Pt	27.3 ± 0.7	24 ± 1	25.4 ± 0.4	15.3 ± 0.4	16.1 ± 0.5	4.6 ± 0.1	24 ± 1	17.0 ± 0.5
Rh	2.55 ± 0.09	2.2 ± 0.1	2.34 ± 0.08	1.60 ± 0.02	2.12 ± 0.05	1.48 ± 0.03	2.4 ± 0.2	2.0 ± 0.1
Ni	11.3 ± 0.2	11.6 ± 0.5	9.9 ± 0.3	11.1 ± 0.3	12.2 ± 0.1	13.2 ± 0.6	15 ± 2	16 ± 1
Co	6690 ± 60	6900 ± 100	6200 ± 100	6000 ± 100	7030 ± 60	6900 ± 200	8400 ± 600	9400 ± 500
Fe	88.0 ± 0.2	87.7 ± 0.5	89.5 ± 0.3	88.3 ± 0.3	87.1 ± 0.2	86.1 ± 0.6	84 ± 2	83.2 ± 0.9
Pd	3.0 ± 0.2	2.7 ± 0.1	2.8 ± 0.2	2.6 ± 0.2	4.3 ± 0.2	5.0 ± 0.1	4.2 ± 0.7	5.4 ± 0.7
As	5.5 ± 0.4	4.9 ± 0.1	5.0 ± 0.2	5.1 ± 0.1	11.9 ± 0.2	17 ± 1	11 ± 2	11.6 ± 0.8
Au	0.80 ± 0.04	0.69 ± 0.3	0.69 ± 0.05	0.62 ± 0.01	1.4 ± 0.1	2.06 ± 0.03	1.4 ± 0.3	1.6 ± 0.1
Cu	320 ± 20	336 ± 3	240 ± 10	307 ± 1	293 ± 7	250 ± 9	330 ± 50	230 ± 10
Ga	10.0 ± 0.5	9.4 ± 0.2	9.3 ± 0.6	12.7 ± 0.5	10.4 ± 0.2	10.3 ± 0.3	5.9 ± 0.5	7.8 ± 0.2
Ge	132 ± 4	100 ± 2	123 ± 2	32 ± 1	159 ± 3	165 ± 4	90 ± 10	118 ± 2

Abundances are reported in ppm and wt. % (Ni and Fe). 1SD uncertainties are also reported.

Table 4.2. Highly siderophile element abundances and Re-Os isotope systematics of PES and IIF iron meteorites determined by isotope dilution.

Meteorite	Catalog	Mass	Re	Os	Ir	Ru	Pt	Pd	$^{187}Re/^{188}Os$	$^{187}Os/^{188}Os$	E_{Os}
IIF											
Dorofeevka	KMAN	0.0735	2275	29818	24610	23750	27770	3494	0.3675	0.12444	+2 ± 1
Del Rio	USNM 6160	0.0415	1832	23474	20560	21490	25880	3282	0.3760	0.12505	+2 ± 1
Monahans (1938)	ASU 256	0.0630	1103	12037	14100	20770	25520	3231	0.4415	0.13119	+11 ± 1
Monahans (1983) *rep*	ASU 256	0.0824	1100	12007	14080	20760	25620	3226	0.4418	0.13118	+11 ± 1
Purmela	ASU 1515	0.0954	863.6	10988	10730	13850	17220	3484	0.3786	0.12519	+1 ± 1
Repeev Khutor	KMAN	0.0405	186.4	1524.5	2867	11880	16860	4997	0.5901	0.14315	+13 ± 2
Corowa	USNM 7230	0.0751	75.69	795.62	868.2	3330	4931	6339	0.4585	0.13155	+1 ± 2
PES											
Eagle Station	USNM	0.0386	1167	15099	12310	17910	22240	4534	0.3723	0.12477	+2 ± 1
Cold Bay	USNM	0.0452	638.2	8413.1	7705	14310	20030	6497	0.3654	0.12656	+25 ± 1
Oued Bourdim 001	ASU 1860	0.0643	369.7	3687.0	5819	12400	17060	6066	0.4836	0.13456	+12 ± 1

Values are reported in grams for mass and ppb for HSE. E_{Os} is the part per 10,000 deviation of the $^{187}Os/^{188}Os$ ratio of a meteorite from a 4.568 Ga reference isochron, calculated from an initial Solar System $^{187}Os/^{188}Os$ = 0.09517 and $\lambda = 1.666 \times 10^{-11}$ yr^{-1} (Smoliar et al., 1996; Archer et al., 2014). KMAN = Committee on Meteorites, Academy of Sciences, Russia. USNM = Division of Meteorites, Department of Mineral Sciences, Smithsonian Institution. ASU = Center for Meteorite Studies at Arizona State University.

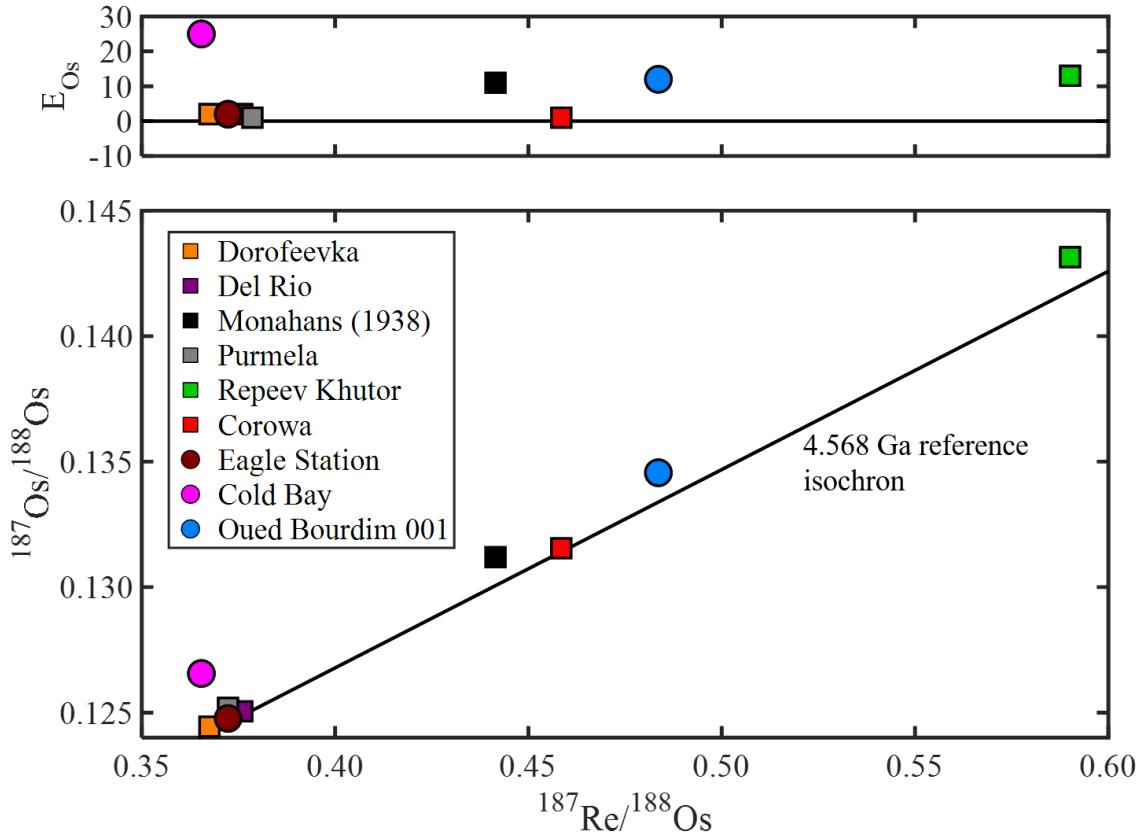

Fig. 4.1. (*top*) $^{187}Re/^{188}Os$ *vs*. E_{Os} plot for the iron meteorites and pallasites from this study. E_{Os} is the parts per 10,000 deviation of the $^{187}Os/^{188}Os$ ratio of a sample from the 4.568 Ga reference isochron in the bottom figure. (*bottom*) $^{187}Re/^{188}Os$ *vs*. $^{187}Os/^{188}Os$ plotted with a 4.568 Ga reference isochron, calculated from an initial Solar System $^{187}Os/^{188}Os = 0.09517$ and $\lambda = 1.666 \times 10^{-11}$ yr^{-1} (Smoliar et al., 1996; Archer et al., 2014).

4.5 Discussion

4.5.1 IIF iron meteorites

Wasson (1969) reported similar Ni, Ga, Ge, and Ir abundances for Corowa and Monahans (1938), leading to the suggestion that the two may be related. Publication of Ni, Ga, Ge, and Ir abundances for Dorofeevka, Del Rio, and Repeev Khutor by Scott and Wasson (1976) led to a new interpretation that Dorofeevka, Del Rio, and Monahans (1938) should be considered an iron trio, and that Repeev Khutor and Corowa may be a

possible iron duo. This idea was then modified by Kracher et al. (1980) after measuring these five irons for abundances of additional siderophile elements, including Co, Cu, As, W, Re, and Au. Kracher et al. (1980) concluded that these irons should be designated as a new iron meteorite group they termed the IIF irons. Purmela was later analyzed for Ni, Co, Ga, As, and Ir abundances (Connolly et al., 2006), and classified as the sixth member of this group.

Siderophile element abundances determined by LA-ICP-MS for the six IIF irons are compared in **Fig. 4.2**. Major variations (200 to 4,000 %) are observed in the abundances of Re, Os, W, Ir, Ru, Pt, As, Au, and Ge among the IIF irons, while moderate variations (4 to 100 %) are observed for Mo, Rh, Ni, Co, Fe, Pd, Cu, and Ga. Kracher et al. (1980) interpreted the variations in siderophile element abundances in IIF irons to be a result of fractional crystallization in a common core. The variations observed here are broadly consistent with those observed for other iron groups interpreted to be products of fractional crystallization (SBT, IVA, IVB), measured using similar techniques (Walker et al., 2008; McCoy et al., 2011, 2019), supporting this idea. If true, the degree of variations for the element concentrations of IIF irons likely reflect the partition coefficients (D values) of these elements between solid metal and liquid metal during fractional crystallization. Major variations of certain element abundances may be explained by highly compatible (D values >> 1) or incompatible behavior (D values << 1) during fractional crystallization, while moderate variations of certain elements suggest D values closer to 1.

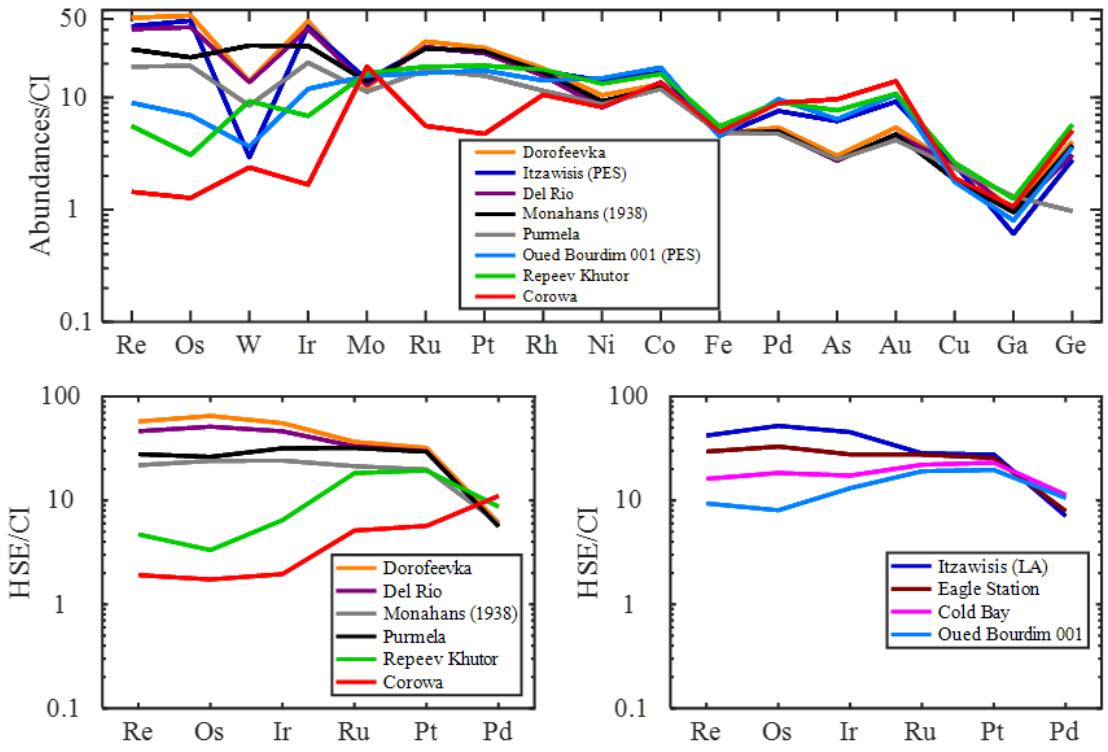

Fig. 4.2. (*top*) Siderophile element abundances, normalized to CI chondrites (Lodders, 2003), for six IIF irons and metal for two PES obtained by LA-ICP-MS. (*bottom*) Highly siderophile element abundances, normalized to CI chondrites (Horan et al., 2003), for the IIF irons (*left*) and PES (*right*). Data were obtained by isotope dilution except for Itzawisis (LA-ICP-MS).

An origin of the IIF irons by fractional crystallization can be further evaluated by comparison of the high-precision HSE concentration data (**Fig. 4.2**), obtained by isotope dilution, to fractional crystallization models (e.g., Walker et al., 2008; McCoy et al., 2011; Hilton et al., 2019). To do this, we use the parameterization method most recently discussed by Chabot et al. (2017) for calculating solid metal-liquid metal D values during fractional crystallization. This approach is necessary as D values of siderophile elements typically vary depending on the S, P, and/or C content of a liquid (e.g., Jones and Malvin, 1990, Chabot and Jones, 2003; Worsham et al., 2016a). The approach used here treats the initial S content of a liquid as the only free parameter, and the D values of P and C are

calculated as the initial S content is varied, based on experimentally-derived S *vs*. D value relationships (Chabot et al., 2017). The corresponding initial P and C contents for each initial S content model are then calculated by applying the calculated P and C D values to the P and C contents of the first iron assumed to have formed by "simple" fractional crystallization. The D values for the HSE and their initial concentrations are then determined in a similar way, but with consideration to the combined effect of the liquid S, P, and C content on HSE D values. Element D values are then calculated at each 0.1 % of fractional crystallization, while calculating the change in S, P, and C content of the liquid as fractional crystallization progresses. Additional details about these calculations are provided in Appendix 4.

For iron meteorites that form as a result of simple fractional crystallization, abundances of compatible (Re, Os, Ir, Ru, Pt) and incompatible (Pd) HSE typically produce well correlated trends. This is not observed for the IIF irons (**Fig. 4.2**), however, indicating that the IIF irons are either not all related to the same parental melt as envisioned by Kracher et al. (1980), or require an additional process(es) to account for deviations from a simple fractional crystallization model. This is highlighted in **Fig. A4.1**, which shows that no simple fractional crystallization model can account for the HSE abundances of more than one IIF iron at a time. Therefore, to further examine their possible origin by fractional crystallization, we consider the effects of mixing solids with equilibrium or non-equilibrium melts, which are scenarios that have been applied to other iron meteorite groups with complex chemical compositions (e.g., IIIAB; Smoliar, 1999; Wasson, 1999; Cook et al., 2004). If, for example, crystallizing solid traps liquid that it crystallized from, subsequent diffusion may result in equilibrium solid metal-liquid metal

mixing (Wasson, 1999). Alternatively, solid metal and liquid metal produced at different intervals of a crystallization sequence (i.e., non-equilibrium) may mix if a solid portion of a partially crystallized core is fractured, evolved liquid infiltrates the fractures, and the primitive solid and evolved liquid equilibrate by diffusion (Smoliar, 1996; Cook et al., 2004). The additional details of equilibrium and non-equilibrium mixing calculations are provided in Appendix 4 (Chabot, 2019).

Since the IIF irons cannot be related by simple fractional crystallization, we constrain our model by assuming Monahans (1938), which has the lowest abundance of Pd, is the only "simple" solid. The HSE abundances of the other IIF irons can then be accounted for by invoking non-equilibrium solid metal-liquid metal mixing (**Fig. 4.3**). If most IIF irons are the products of non-equilibrium solid metal-liquid metal mixing, there are potentially endless parental melt compositions that the IIF irons could have crystallized from. This is because multiple combinations of solid metal-liquid metal mixing, including between three or more endmember compositions, can produce the same HSE compositions (e.g., **Fig. A4.2**: Re *vs*. Pd systematics between the three models of **Table 4.3**). Given this, we restrict the possible parental melt compositions for the IIF irons to those with relative abundances of HSE that are within the ranges observed in chondrites (Horan et al., 2003; Fischer-Gödde et al., 2010). Possible compositions are listed in **Table 4.3** and shown in **Fig. 4.4**, with Model 1 (S = 14 wt. %) having relative abundances of HSE in the middle of the range observed in chondrites, while Model 2 (S = 11 wt. %) and Model 3 (S = 17 wt. %) have relative abundances of HSE that are at the extremes observed in chondrites. Changing the S content >17 wt. % or <11 wt. % requires parental melts with relative abundances of Pd, compared to the other HSE, that are outside the ranges observed in

chondrites (Pd depleted and Pd enriched, respectively). A Pd depletion relative to the other HSE was observed for the IVB iron meteorite parental melt (Campbell and Humayun, 2005; Walker et al., 2008), but it was coupled with depletions for volatile elements. The IIF irons are volatile-rich compared to the IVB irons, making a relative depletion in Pd composition due to volatility unlikely. Worsham et al. (2016a) observed, for the parental melt of the IAB-sLM iron meteorite subgroup, a Pd enrichment relative to other HSE, which was suggested to reflect fractionation of refractory elements by a volatility-driven process. However, the IIF irons do not exhibit depletions in other refractory elements (e.g., Mo), making this explanation for the IIF irons also unlikely (**Fig. 4.2**).

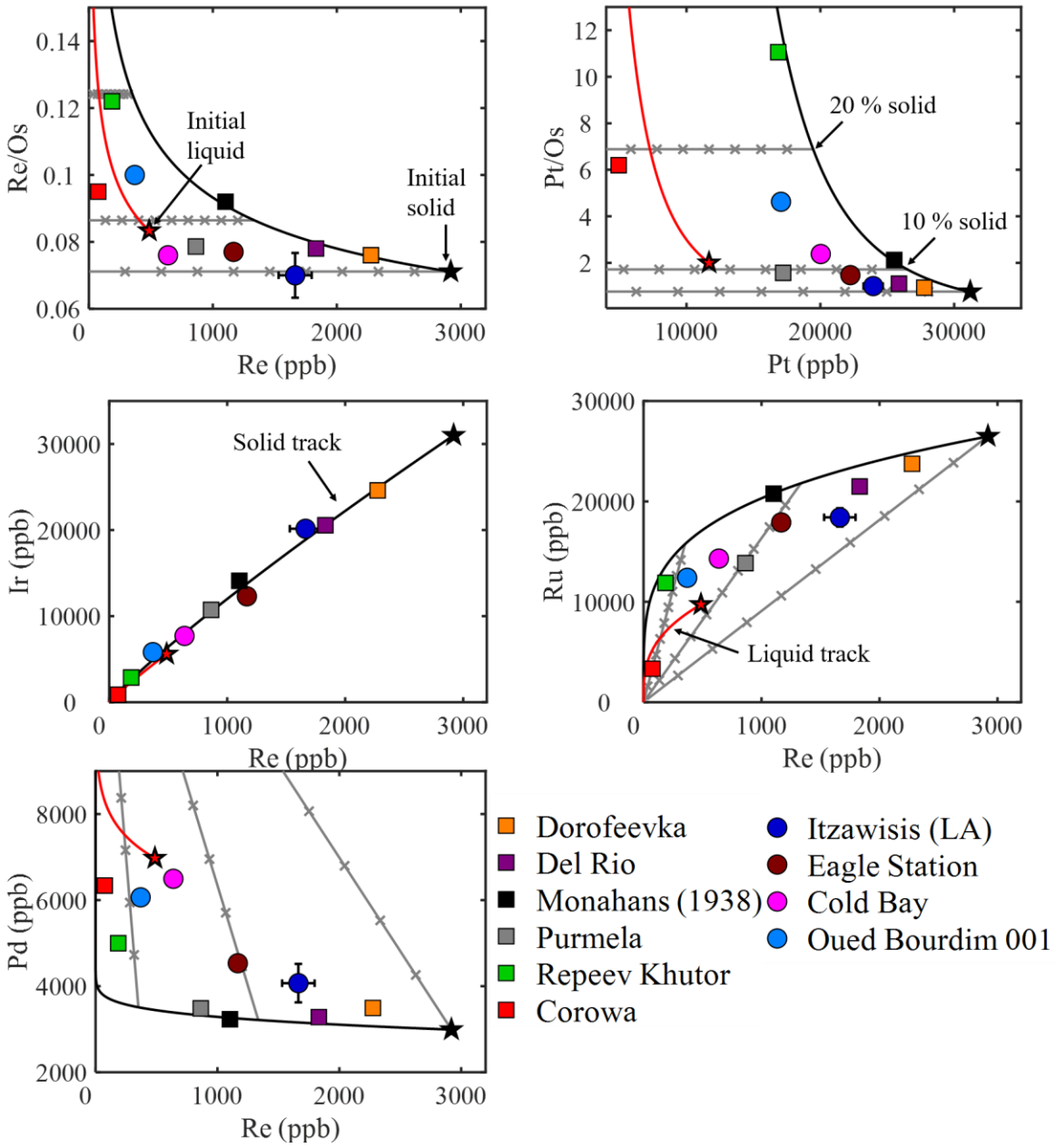

Fig. 4.3. Fractional crystallization model of Model 1 from Table 3. This model can account for the HSE compositions of the IIF irons and PES through various degrees of solid metal-liquid metal mixing. Solid metal and liquid metal evolution lines are shown in black and red, respectively. Initial solid and liquid compositions are shown as black and red stars, respectively. Grey lines reflect mixing of solid at initial, 10 %, and 20 % fractional crystallization with a liquid after 45 % crystallization. Tick marks on mixing lines reflect 10 % increments.

Table 4.3. Projected parental melt compositions of the IIF-PES parental core based on three models discussed in the text.

	Re	Os	Ir	Ru	Pt	Pd	S	P	C
Model 1	300	3600	3450	6000	7200	4300	14	0.4	<0.05
Model 2	480	5800	5500	8500	10300	4300	11	0.5	<0.05
Model 3	175	2050	2100	3950	4750	4050	17	0.3	<0.05

Values are in ppb for HSE and wt. % for S, P, and C. Models 2 and 3 define the endmembers of the possible parental melt compositions with chondritic relative abundances of HSE. Model 1 is the middle solution in this range.

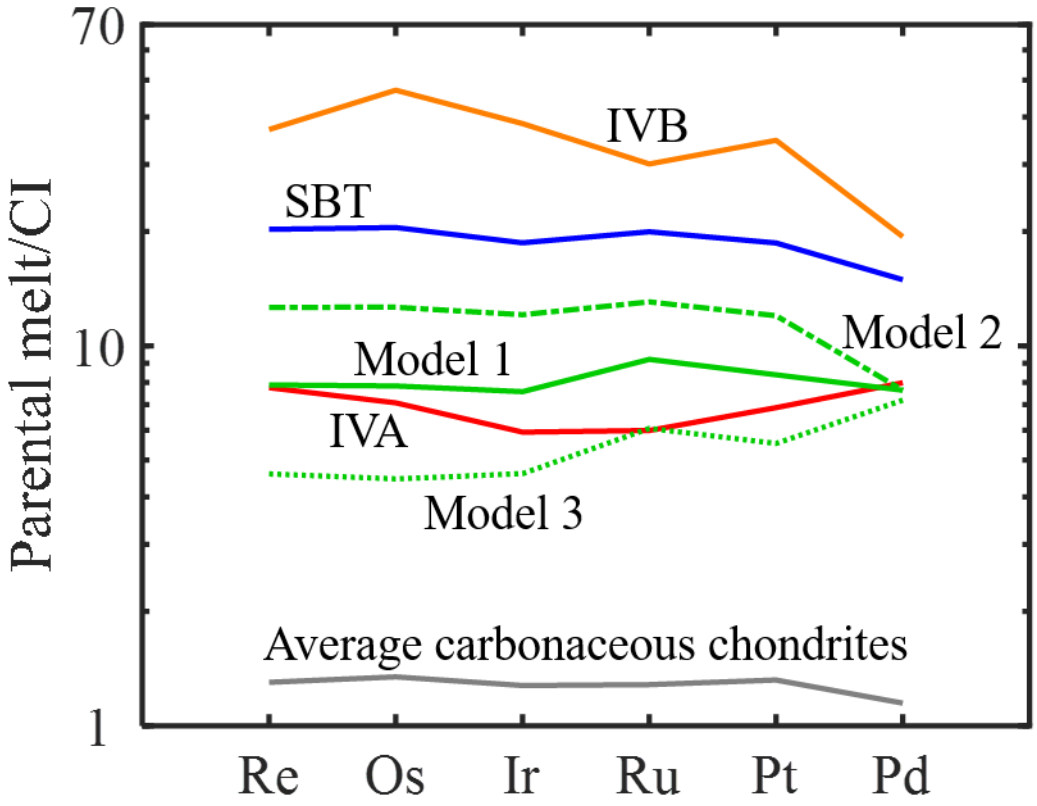

Fig. 4.4. Calculated HSE parental melt compositions, normalized to CI chondrites (Horan et al., 2003), of the IIF-PES for Models 1, 2, and 3 compared to parental melt compositions of the IVB (Walker et al., 2008), IVA (McCoy et al., 2011), and SBT irons (Hilton et al., 2019). The average HSE composition of carbonaceous chondrites is also shown (Horan et al., 2003; Fischer-Gödde et al., 2010).

Using composition Model 1, Monahans (1938) is accounted for as a solid produced after 13 % fractional crystallization (**Fig. 4.3**). The compositions of Dorofeevka and Del

Rio can be accounted for by mixing solids formed after 3 % and 5 % crystallization, respectively, with evolved liquid present after ~45 % crystallization. The HSE abundances of Repeev Khutor can be broadly re-created by mixing a solid formed from 23 % fractional crystallization with a liquid present after ~45 % fractional crystallization. This non-equilibrium mixing of evolved liquid with earlier formed solids may have been achieved by fracturing of the crystallizing core, followed by mobilization of the evolved melt throughout the fractures (Smoliar, 1996). One way to fracture a crystallizing core may be through impact.

The composition of Corowa is more difficult to reproduce by mixing of primitive solids and evolved liquids. It is best accounted for by mixing evolved solid and primitive liquid, such as solid formed after ~45 % fractional crystallization with liquid formed after ~13 % fractional crystallization. This scenario is difficult to envision, however. One possible mechanism leading to the mixing of an evolved solid and primitive liquid may be in an inward-out crystallizing core coupled with late segregation of primitive metal from the mantle. Addition of primitive, residual liquid from the mantle may have caused the evolved composition of the liquid outer core to shift toward a more primitive composition. Subsequent non-equilibrium solid metal-liquid metal mixing may then appear as mixing between evolved solid and primitive liquid (Smoliar, 1996). Alternatively, Corowa may sample the same IIF core but formed in a magma chamber that was isolated from the domain in which the other IIF irons crystallized. Separate magma chambers in the IIF core may have been produced by inward dendritic crystallization, which could have resulted in slightly chemically variable magma chambers that ultimately crystallized somewhat different solid compositions (Haack and

Scott, 1992). This possibility has been envisioned to explain the deviations of some IIIAB iron meteorites chemical compositions from simple fractional crystallization models (Haack and Scott, 1993).

While all other IIF irons can be produced by invoking solid metal-liquid mixing, Purmela is the exception. For example, as shown in **Fig. 4.3**, mixing is needed to explain abundances of Re, Os, Ru, and Pt, but not Pd. In addition, while our new Ge/Ga ratios for the IIF irons of between 11 to 16 are consistent with the ratios of 11 to 17 reported by Kracher et al. (1980), Purmela has a Ge/Ga ratio of 3. This lower ratio is due to a lower Ge abundance than observed for any other IIF iron. Fractionating Ge from Ga in order to obtain this ratio is difficult to envision by fractional crystallization since Ge and Ga have similar partitioning behaviors (Chabot et al., 2017). As such, these chemical differences together suggest that Purmela may not be a IIF iron and may instead derive from a parent body with a similar, but different bulk chemistry. As such, we question Purmela's current status as a IIF iron and submit that further study of this meteorite is warranted.

4.5.2 Eagle Station Pallasites

Itzawisis, Eagle Station and Cold Bay were designated the Eagle Station Trio by Scott (1977d). Karavannoe and Oued Bourdim 001 have since been added to this trio (Korochantsev et al., 2013; Humayun et al., 2014; Bouvier et al., 2017), bringing the total number of PES members to five. Highly siderophile element abundances of four PES are compared in **Fig. 4.2**. Like the IIF irons, the PES metal do not form well correlated trends for compatible and incompatible HSE abundances. For example, Cold Bay is enriched in compatible and incompatible HSE compared to Oued Bourdim 001. As a result, the metal

in these pallasites cannot be produced by simple fractional crystallization from a common liquid. This is also highlighted in **Fig. A4.1**, which shows that the PES metals match solid compositions for Re *vs.* Pd with 6 wt. % S, but Pt *vs.* Pt/Os compositions require 14 wt. % S. These chemical trends suggest PES metal formation from solid metal-liquid metal mixing, as discussed for the IIF irons.

4.5.3 Common IIF-PES core

The limited data sets of Kracher et al. (1980) were used to suggest that the IIF irons and PES share chemical similarities, although not enough to indicate derivation from the same body. We find that the new siderophile element abundances of Itzawisis and Oued Bourdim 001 fall near the siderophile element ranges observed among the IIF irons and are permissive of a common parent body origin (**Fig. 4.2**). The PES also have HSE abundances that fall within the ranges observed for the IIF irons (**Fig. 4.2**). For example, the PES form a striking trend with Del Rio and Dorofeevka for Pt *vs.* Pt/Os (**Fig. 4.3**). The HSE compositions in PES metal are compared to the fractional crystallization Model 1 of the IIF irons in **Fig. 4.3**. The HSE abundances of the PES fall within the ranges permitted by mixing of initial solid and solid produced after ~20 % crystallization with a liquid produced following 25 % to 45 % crystallization. Invoking two endmember mixing between these solid and liquid ranges can broadly reproduce the HSE compositions of the PES (**Fig. 4.3**). As such, it is plausible that the IIF irons and PES formed from a common liquid and, consequently, a common core.

Proposed origins for the PES include formation at the core-mantle boundary, based on the concentrations of rare earth elements in phosphates present in Eagle Station (Davis

and Olsen, 1991), and formation through two impacts, the first of which caused metal-silicate melting and the second of which caused metal intrusion into olivine (Malvin et al., 1985). Contrary to the model by Malvin et al. (1985), an origin of PES metal in association with the IIF core suggests formation near the core-mantle boundary on a differentiated body that was melted by internal heating. However, as proposed by Malvin et al. (1985), an impact may have caused metal intrusion into olivine. An impact could also explain the non-equilibrium mixing required for IIF and PES metal HSE compositions. For example, an impact could have fractured a partially crystallized core, causing multiple endmember mixing of solids with liquids, in addition to mixing between metal and olivine (**Fig. 4.5**). Impact is also consistent with the highly angular (and likely fractured) olivines in the PES (Scott, 1997c; Scott and Taylor, 1990).

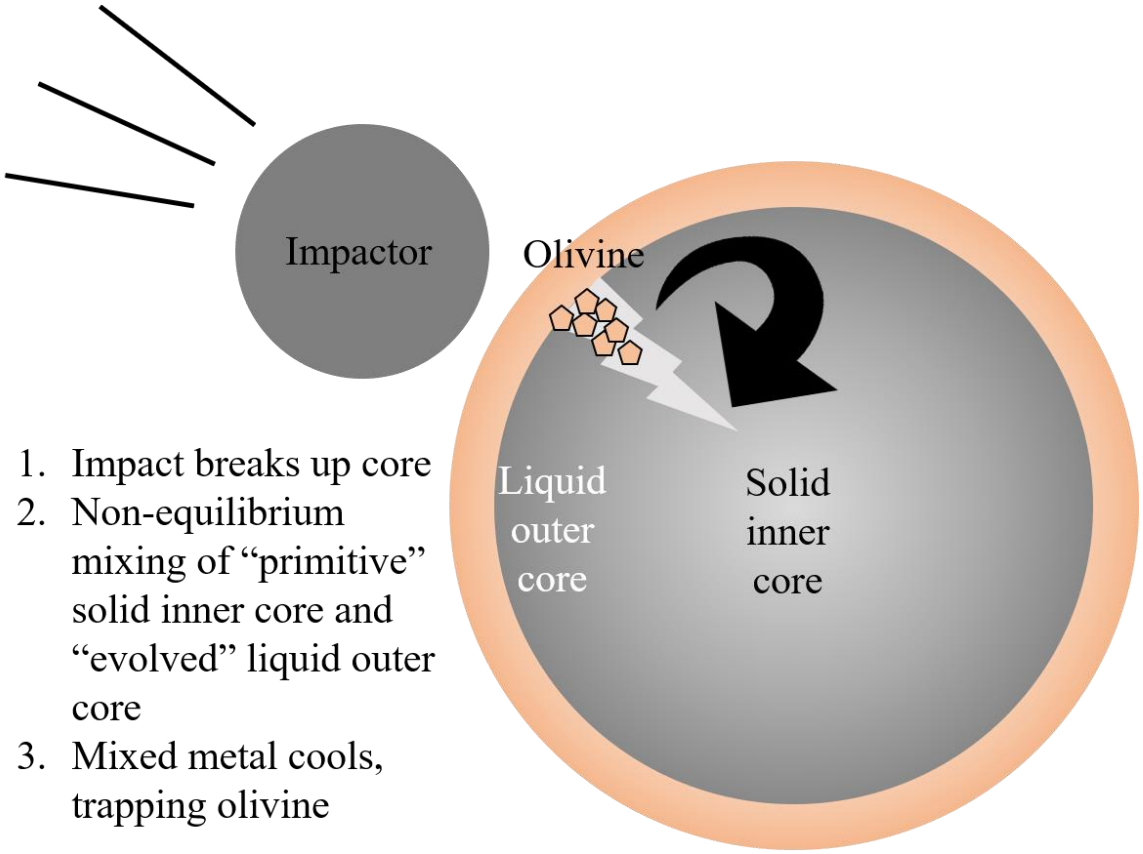

Fig. 4.5. Cartoon depicting the preferred scenario for forming the PES. An impactor disrupts a partially crystallized IIF core, resulting in the non-equilibrium mixing of "primitive" solid and "evolved" liquid. Silicates are mixed into the metal and the metal rapidly cools. Cartoon is not to scale.

Mixing of primitive solids and evolved liquids, as proposed here for most IIF irons and all PES, was also invoked for the IIIAB-PMG (Scott, 1977a; Wasson and Choi, 2003). However, this scenario was discounted by Yang et al. (2010), in which the authors noted faster cooling rates for IIIAB irons (50-350 K/Myr) compared to PMG (2.5-18 K/Myr). These authors interpreted the cooling rate differences to reflect that the IIIAB irons and PMG did not form on the same parent body. In comparison, the IIF irons and PES have more consistent cooling rates of 1-5 K/Myr (Rasmussen et al., 2001) and 15 K/Myr (Yang et al., 2010), respectively, permissive of a common core origin. In addition,

the potential iron-pallasite relationship is also supported by identical genetic Mo isotopic compositions reported for the PES (Burkhardt et al., 2011) and IIF irons (Kruijer et al., 2017; Worsham et al., 2019). Due to these consistencies in chemical compositions, cooling rates, and genetic isotopic compositions between the IIF irons and PES, this may be the most promising iron-pallasite relationship yet discovered.

4.6 Conclusions

Study of the siderophile element abundances present in metal in IIF irons and PES provides permissive evidence for derivation from a common planetesimal core. The HSE compositions of neither group can be explained solely by simple fractional crystallization and require substantial solid metal-liquid metal mixing. As such, these meteorites most likely formed as a result of mixing of various components of a partially crystallized core, disrupted by an impact.

4.7 Acknowledgements

We gratefully acknowledge the Division of Meteorites, Department of Mineral Sciences, Smithsonian Institution, the Center for Meteorite Studies at Arizona State University, and the Committee on Meteorites, Academy of Sciences, Russia for providing access to the samples for this study. This study was supported by NASA Emerging Worlds grant NNX16AN07G (to RJW).

4.8 Appendix 4

4.8.1 Fractional crystallization modeling

The concentrations of S, P, C, and HSE in liquid during fractional crystallization were determined using Eq. S1. In this equation, F_n is the fraction of liquid (n = 100 is pure liquid), C_{Ln} is the concentration of an element in the liquid phase at F_n, and D_n is the partition coefficient of an element. The concentrations of these elements were calculated at each 0.1 % of crystallization. A constant partition coefficient of 0.001 was used for S (Walker et al., 2008). The partition coefficients for P and C were determined at each F_n by considering the concentration of S and P or S and C, respectively, in the liquid at F_{n+1}. Equation S2 is used to account for the effects of S on P and C partitioning behavior (Chabot and Jones, 2003).

Values of D_o for P and C are taken from Chabot et al. (2017) and Worsham et al. (2016a), respectively. The β_{SPC} variable is determined using Eq. S3 (Jones and Malvin, 1990), in which β_S and β_P are taken from Chabot et al. (2017) and β_C is taken from Worsham et al. (2016a). For P, the effects of C are not considered and for C, the effects of P are not considered. The β_{SPC} and "Fe domains" (Eq. S4; Chabot et al., 2017) variables are calculated at each F_n, where X_i is the mole fraction of an element. The initial P content of the IIF parental melt was constrained by considering the P content of Monahans (1938), 0.09 wt. % (Buchwald, 1975). Initial S and C contents were determined iteratively.

After determining the concentration of S, P, and C at each F_n, the D values for the HSE are calculated at each F_n using Eq. S2-S4 by collectively considering the changes in S, P, and C content in the liquid (Jones and Malvin, 1990; Chabot and Jones, 2003; Worsham et al., 2016a; Chabot et al., 2017). The concentration of HSE in the liquid at each F_n is then determined using Eq. S1 and the solid composition (C_{Sn}) at each F_n is

determined using Eq. S5. For solid metal-liquid metal mixing, the composition of the liquid endmember ("trapped melt") was determined from C_{Ln} following the approach of Chabot (2019). The concentration of S in the liquid at each F_n was divided by 36.5 to determine the "x" value. The HSE concentrations of the trapped melt were determined by Eq. S6.

$$\text{Eq. S1: } C_{Ln-1} = \frac{C_{Ln}}{(F_{n-1} + 1 - F_{n-1}D_{n-1})}$$

$$\text{Eq. S2: } \frac{1}{D} = \frac{[\text{Fe domains}]^{\beta_{SPC}}}{D_o}$$

$$\text{Eq. S3: } \beta_{SPC} = \left[\frac{2X_S}{2X_S + 4X_P + 4X_C}\right]\beta_S + \left[\frac{4X_P}{2X_S + 4X_P + 4X_C}\right]\beta_P + \left[\frac{4X_C}{2X_S + 4X_P + 4X_C}\right]\beta_C$$

$$\text{Eq. S4: Fe domains} = \frac{1 - 2X_s - 4X_P - 4X_C}{1 - X_s - 3X_P - 3X_C}$$

$$\text{Eq. S5: } C_{Sn} = C_{Ln}D_n$$

$$\text{Eq. S6: } C_{\text{trapped melt}} = \frac{C_{Ln}}{(1-x)}$$

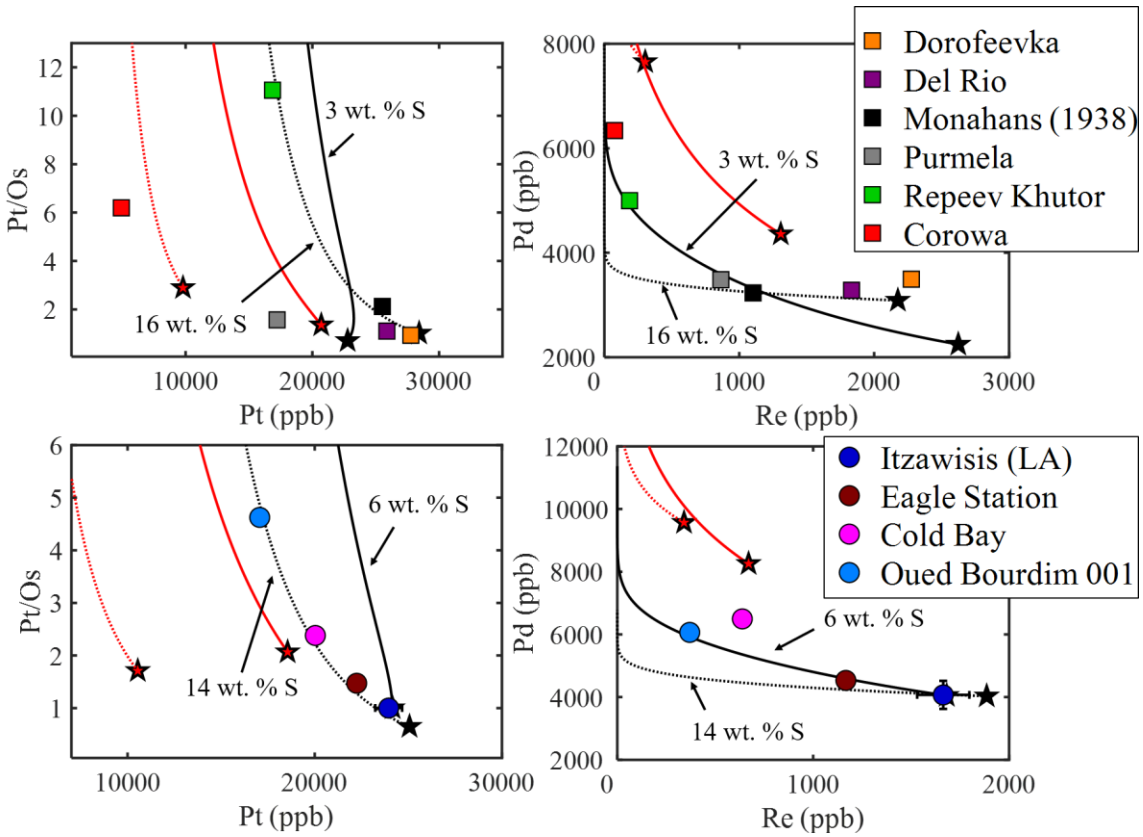

Fig. A4.1. Fractional crystallization models compared to IIF irons (*top*) and PES (*bottom*). (*top*) The Pt *vs*. Pt/Os compositions of IIF irons can be explained as metal from simple fractional crystallization for a system with 16 wt. % S, but Re *vs*. Pd compositions require 3 wt. % S. Corowa cannot be related to the other IIF irons as a simple fractionally crystallized solid in any model. (*bottom*) The Pt *vs*. Pt/Os compositions of PES can be explained as metal from simple fractional crystallization for a system with 14 wt. % S, but Re *vs*. Pd compositions require 6 wt. % S.

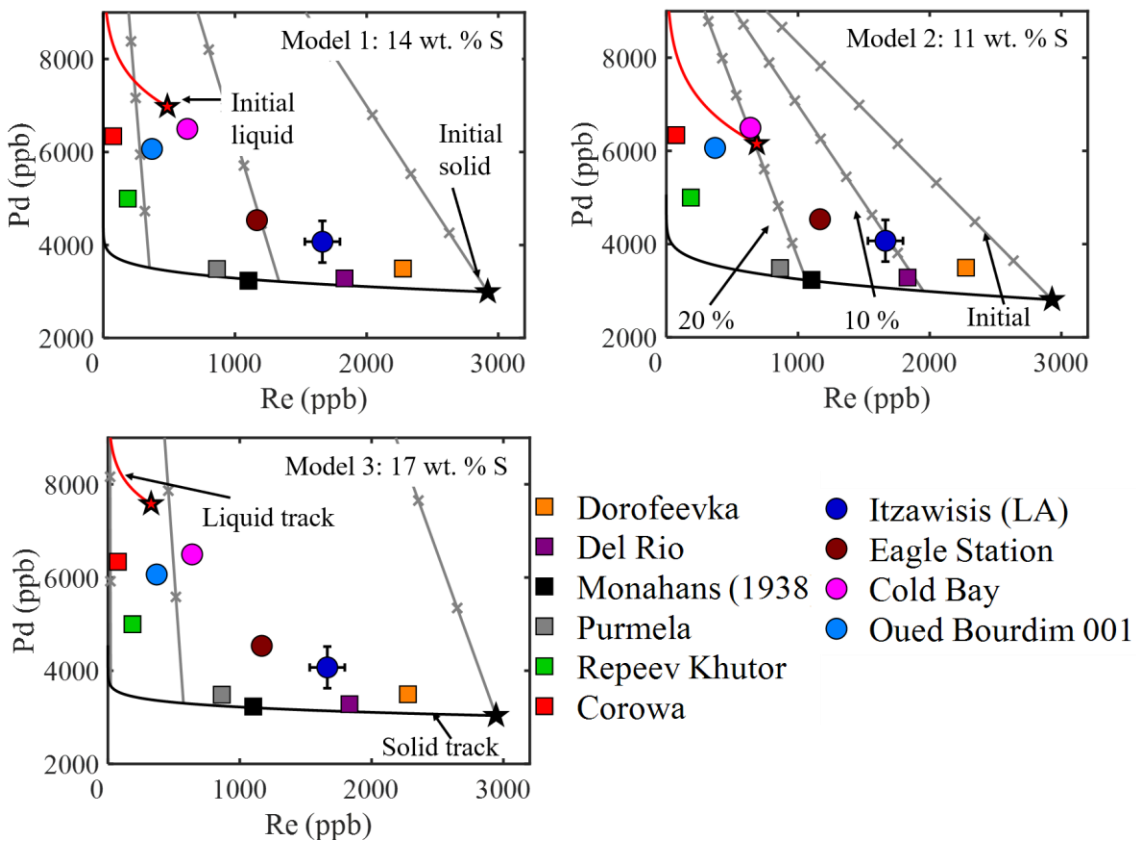

Fig. A4.2. Re *vs*. Pd compositions of the IIF irons and PES metal compared to fractional crystallization models using parental melt compositions of Model 1, Model 2, and Model 3. Solid metal and liquid metal evolution lines are shown in black and red, respectively. Initial solid and liquid compositions are shown as black and red stars, respectively. Grey lines reflect mixing of solid at initial, 10 %, and 20 % fractional crystallization with a liquid after 45 % crystallization. Tick marks on mixing lines reflect 10 % increments.

Chapter 5: Constraints on the chemical characteristics of the noncarbonaceous (NC) and carbonaceous (CC) nebular reservoirs

5.1 Abstract

The projected bulk highly siderophile element (HSE; Re, Os, Ir, Ru, Pt, and Pd) characteristics of the parent bodies of ten magmatic iron meteorite groups/grouplet (IC, IIAB, IIC, IID, IIF, IIIAB, IIIF, IVA, IVB, and South Byron Trio) are compared in order to assess whether there are chemical differences between the isotopically distinct noncarbonaceous (NC) and carbonaceous (CC) nebular reservoirs. With few exceptions, the relative abundances of HSE inferred for each of the parent bodies are similar and show no resolvable difference between NC and CC heritage. Thus, the processes driving genetic isotopic heterogeneity in the early Solar System evidently did not leave discernable chemical fingerprints, with respect to processing of HSE, on the bulk planetesimal scale. By contrast, the absolute abundances of HSE projected for parent body cores, on average, are higher in the CC bodies compared to the NC bodies. This most likely reflects proportionally smaller cores, on average, which in turn may indicate that at least some CC parent bodies were more oxidized than NC parent bodies. The distribution of Fe inferred between the core and mantle of these planetary bodies shows a weak correlation with model core segregation ages, suggesting that the timing of planetary differentiation may have been affected by the oxidation state of the body.

5.2 Introduction

It is well established from the nucleosynthetic, “genetic”, isotopic compositions of certain elements (e.g., Cr, Ti and Ni) in bulk meteorites that parent bodies accreted from

differing proportions of precursor materials with diverse isotopic compositions (e.g., Trinquier et al., 2007, 2009; Leya et al., 2008; Regelous et al., 2008). Further, studies comparing genetic isotopic compositions of bulk meteorites have shown that two isotopically distinct reservoirs, referred to as the noncarbonaceous (NC) and carbonaceous (CC) reservoirs, were present in the early Solar System (e.g., Warren, 2011). This division is especially well documented with respect to nucleosynthetic anomalies present for certain siderophile elements (e.g., Ni, Mo, W, Ru, and Pd) in iron meteorites and pallasites (e.g., Budde et al., 2016a; Kruijer et al., 2017; Bermingham et al., 2018; Ek et al., 2019; Nanne et al., 2019).

The process(es) resulting in the heterogeneous accretion of isotopically diverse presolar materials to parent bodies accreting within and between the NC and CC reservoirs remains unconstrained. Numerous ideas have been proposed, including that the heterogeneous accretion of isotopically diverse materials reflects the initially heterogeneous distribution of these materials in the parental molecular cloud (e.g., Dauphas et al., 2002). It has also been suggested that the heterogenous distribution of isotopically distinct materials was due to the physical sorting of materials by size or type (e.g., Regelous et al., 2008) or the thermal processing of materials (e.g., Trinquier et al., 2009). The heterogenous distribution of isotopically distinct materials may also result from the late addition of isotopically distinct materials (e.g., Brennecka et al., 2013).

To complement genetic information, the ^{182}Hf-^{182}W isotopic systematics of iron meteorites have been used to provide constraints on the relative timing of metal-silicate segregation of parent bodies (e.g., Kleine et al., 2009; Kruijer et al., 2014a, 2017). In certain instances, model ^{182}W ages can be combined with thermal models of heat

production in a planetesimal to constrain parent body accretion ages (e.g., Kruijer et al., 2014a, 2017; Hilton et al., 2019). Such ages may be important for understanding the origins of the NC and CC domains (e.g., Kruijer et al., 2017).

One aspect of the NC-CC dichotomy that has been pursued less vigorously than genetic and chronologic differences is the exploration of potential chemical differences between the two nebular reservoirs. So-called "magmatic" iron meteorite groups and grouplets (defined as having 5 or more, and 3 or more members, respectively; Wasson, 1974) are particularly valuable for comparing the siderophile element compositions of individual parent bodies from these reservoirs, as they are commonly interpreted to be fragments of planetesimal cores, dominantly related by fractional crystallization (e.g., Scott, 1972). As such, the siderophile element content for group/grouplet members can be used to determine the fractional crystallization and mixing sequence involved in the generation of the group/grouplet, and viable crystallization models can be projected back to a parental melt composition. This composition is normally presumed to represent the composition of the bulk core. This method can additionally provide constraints on the parental melt S, P, and C concentrations as these elements can strongly affect siderophile element solid metal-liquid metal partition coefficients (D values) (e.g., Jones and Malvin, 1990; Chabot and Jones, 2003; Chabot et al., 2017). For highly siderophile elements (HSE; Re, Os, Ir, Ru, Pt, and Pd), a bulk core composition may reflect the relative abundances of the bulk planetesimal, whereas for moderately and/or multivalent elements (e.g., Fe, Ni, and S), constraints on the bulk core composition can, in turn, be used to constrain the distribution of these elements between the core and mantle, assuming chondritic absolute abundances for the bulk planetesimal.

Prior studies have focused most attention on modeling HSE, given their well constrained, absolute and relative liquid metal-solid metal partitioning characteristics with varying S, P, and C contents (Chabot et al., 2017). Such models have been previously reported for the NC-type IC and IVA and CC-type IIC, IIF, IVB, and South Byron Trio (SBT) magmatic iron meteorite groups/grouplet (Walker et al., 2008; McCoy et al., 2011; Hilton et al., 2019, in revision; Tornabene, 2020; Tornabene et al., 2020). Here, additional HSE parental melt compositions are constrained by modeling for NC-type IIAB and IIIAB and CC-type IID and IIIF magmatic iron meteorite groups. The chemical characteristics of ten magmatic iron meteorite parent bodies are then compared within the framework of their corresponding genetic isotopic compositions and metal-silicate segregation ages.

5.3 Materials and methods

Chunks of IIAB, IID, IIIAB, and IIIF iron meteorites were obtained from the Division of Meteorites, Department of Mineral Sciences, Smithsonian Institution, and a sample of Northeast Africa (NEA) 002 (IID) was obtained from the University of California, Los Angeles (UCLA) meteorite collection. Emphasis was placed on obtaining samples representing the earliest stages of fractional crystallization, i.e., those with the least fractionated HSE patterns. Bulk pieces of all iron meteorites examined were measured for HSE abundances and ^{187}Re-^{187}Os isotopic compositions using isotope dilution methods (e.g., Walker et al., 2008). Between 25 to 300 mg pieces of metal were cut from each meteorite chunk using a water-cooled *Leco Vari-cut* saw and a 12.7 cm diamond-wafering blade, which was cleaned with SiC blocks prior to cutting each meteorite. Cut

meteorite pieces were polished using a range of coarse- to fine-grit SiC sandpaper to remove sawblade marks, then sonicated in ethanol to remove sawing residue. Cut and polished metal chunks of each meteorite were combined in a Pyrex® Carius tube with a platinum-group element spike (^{191}Ir, ^{99}Ru, ^{194}Pt, and ^{105}Pd), a Re-Os spike (^{185}Re and ^{190}Os), 5 ml of concentrated HNO_3, and 2.5 ml of concentrated HCl. Tubes were sealed and heated for a minimum of 24 h at 240 °C (Shirey and Walker, 1995). The tubes were then opened and solutions were transferred to centrifuge tubes and mixed with CCl_4 in order to extract Os (Cohen and Waters, 1996). Osmium was further purified using the microdistillation procedure of Birck et al. (1997).

Spiked Os samples for the IIIAB irons were analyzed by a *VG Sector 54* thermal ionization mass spectrometer (TIMS), while those for the IIAB, IID, and IIIF irons were analyzed using a *Thermo-Fisher Triton* or *Triton Plus* TIMS to determine Os concentrations and ^{187}Os/^{188}Os ratios (Walker et al., 2008). Osmium isotopic data were corrected for instrumental and natural mass-fractionation by normalizing ^{192}Os/^{188}Os to 3.08271 (Allègre and Luck, 1980). The other HSE were separated and purified using an anion column procedure, and then Re and Ru separates were further purified using an additional miniature anion column (Walker et al., 2008). The Re and Ru aliquot was split and HSE fractions were evaporated to dryness and dissolved in 0.8 N HNO_3. Aliquots for Re analyses were doped with natural W in order to correct for instrumental mass bias. Final solutions were measured using a *Neptune Plus* multi-collector ICP-MS at UMd for all IID and IIIF irons, as well as the Re, Ir, and Pt fractions for IIAB irons. Solutions of all IIIAB irons were analyzed using a *Nu Plasma* multi-collector ICP-MS, also at UMd.

Finally, Ru and Pd abundances of the IIAB irons were analyzed using a *Thermo Finnigan Element 2* ICP-MS.

The blanks for these methods (n = 6) ranged from 0.4 to 3, 1 to 5, 0.4 to 2, 3 to 80, 4 to 30, and 2 to 500 pg for Re, Os, Ir, Ru, Pt, and Pd, respectively, which are sufficiently low (<0.1%) to have an inconsequential effect on the reported concentrations, except for Klamath Falls (IIIF). The external reproducibility of Re and Os abundances, estimated based on the reproducibility of similar samples analyzed using identical techniques (Walker et al., 2008), were ≤0.2 % and ≤0.1 %, respectively, and <3 % for the other HSE. Measurement uncertainties for $^{187}Os/^{188}Os$ ratios were estimated to be ≤0.1 % and the uncertainties for $^{187}Re/^{188}Os$ ratios were estimated to be ≤0.2 %.

5.4 Results

The Re-Os isotopic data and HSE abundances of the IIAB, IID, IIIAB, and IIIF iron meteorites are provided in **Table 5.1**. Meteorites from these groups span a large range of $^{187}Re/^{188}Os$ ratios from 0.3196 to 1.152 and $^{187}Os/^{188}Os$ ratios from 0.12057 to 0.18766. Values of E_{Os}, representing the part per 10,000 deviation of each meteorite's Re-Os systematics from a 4.568 Ga reference Re-Os isochron, calculated with a Solar System initial $^{187}Os/^{188}Os = 0.09517$ and slope = 0.07908 (Archer et al., 2014), are also reported in **Table 5.1**. These values range from -11 ± 2 to +40 ± 2.

The abundances of HSE in the IIAB, IID, IIIAB, and IIIF iron meteorites examined are typically within ±20 % of values reported by Schaudy et al. (1972), Scott and Wasson (1976), Pernicka and Wasson (1987), Wasson (1999), Grossman (2000), Cook et al.

(2004), Wasson and Huber (2006), and Wasson et al. (2007). The concentrations reported here are compared to literature values in **Table A5.1** of Appendix 5.

Table 5.1. Highly siderophile element concentrations and ^{187}Re-^{187}Os isotopic data for members of the IIAB, IID, IIIAB, and IIIF iron meteorites groups.

Sample	ID	Wt. (g)	Re	Os	Ir	Ru	Pt	Pd	$^{187}Re/^{188}Os$	$^{187}Os/^{188}Os$	E_{Os}
IIAB irons											
Forsyth County	USNM	0.0681	3700	44554	39270	27300	37610	1754	0.4000	0.12665	-1 ± 1
Cincinnati	USNM	0.0436	1530	13199	19940	24070	33330	1757	0.5671	0.13915	-9 ± 2
Braunau	USNM	0.0650	772.5	5445.9	11020	17680	30080	1820	0.6849	0.14900	-3 ± 2
North Chile	USNM	0.0482	208.8	1067.5	3585	15810	26590	2006	0.9473	0.16956	-5 ± 2
Sikhote-Alin	USNM	0.1338	1.528	12.110	23.08	4862	5377	2449	0.6079	0.14242	-8 ± 2
IID irons											
NEA 002	UCLA	0.0276	1960	28741	21480	16990	22310	2774	0.3284	0.12210	+10 ± 1
Arltunga	USNM 2467	0.2297	1914	26255	20540	17220	23180	2868	0.3510	0.12311	+2 ± 1
Losttown	USNM 1071	0.0408	1912	26303	20490	17340	22660	2988	0.3500	0.12295	+1 ± 1
N'Kandhla	USNM 2397	0.1912	1779	23869	19160	16970	22780	2959	0.3589	0.12371	+2 ± 1
Bridgewater	USNM	0.1645	1767	23628	19100	17000	22880	2950	0.3602	0.12386	+2 ± 1
Mount Ouray	USNM 777	0.0986	1586	20594	17240	16510	22550	3280	0.3710	0.12464	+1 ± 1
Elbogen	USNM 309	0.0490	1415	18114	15570	15080	20700	2890	0.3763	0.12508	+2 ± 1
Carbo	USNM 838	0.2951	1292	15544	14080	16030	22080	3097	0.4004	0.12698	+1 ± 1
Puquios	USNM 3008	0.0994	1263	16060	14190	15550	20500	3185	0.3788	0.12613	+10 ± 1
Rodeo	USNM 3016	0.0438	754.1	9383.0	8726	12180	16690	3930	0.3872	0.12683	+10 ± 1
Needles	USNM 3533	0.2222	453.8	5056.0	5139	10200	14610	4935	0.4326	0.12945	+1 ± 1
Wallapai	USNM 788	0.0473	343.7	3532.0	3830	9449	12530	5133	0.4693	0.13348	+12 ± 2
IIIAB irons											
Costilla Peak	USNM 702	0.1190	1421	18319	13750	12740	15870	3349	0.3780	0.12428	-8 ± 1
Henbury	-	0.1015	1287	15053	13630	13180	16670	2127	0.4121	0.12796	+2 ± 1
Charcas	USNM 467A	0.1302	150.8	1082.3	2240	8411	12110	2619	0.6781	0.14767	-11 ± 2
Tamarugal	USNM 6680	0.1064	33.88	235.30	562.6	4854	7624	3336	0.6939	0.14961	-4 ± 2
Maldyak	KMAN 1402	0.1444	25.37	167.01	462.5	4602	7148	4325	0.7397	0.15311	-6 ± 2
IIIF irons											
Nelson County	USNM 2951	0.1073	794.8	11970	8650	7064	10310	2517	0.3196	0.12057	+1 ± 1
Clark County	USNM 1304	0.0899	665.1	9271.0	7240	6747	10150	2681	0.3454	0.12222	-3 ± 1
Oakley	USNM 780	0.0381	507.2	6500.8	5529	6307	9635	3016	0.3758	0.12505	+2 ± 1
Cerro del Inca	USNM 7062	0.0735	282.9	2873.2	3251	6348	8719	3298	0.4747	0.13327	+6 ± 2
St. Genevieve County	USNM 454	0.1373	159.8	1345.7	1950	5651	8315	3554	0.5732	0.14051	+0 ± 2

Moonbi	USNM 1467	0.0397	110.2	854.60	1398	5126	7611	3782	0.6225	0.14586	+15 ± 2
Klamath Falls	USNM 7008	0.3060	0.2787	1.3166	3.229	1033	1455	5702	0.9994	0.17821	+40 ± 2

Samples are listed by decreasing Re concentrations for each group and concentrations are reported in ppb. E_{Os} represents the part per 10,000 deviation from a 4.568 Ga reference Re-Os isochron, calculated with a Solar System initial $^{187}Os/^{188}Os$ = 0.09517 and slope = 0.07908 (Archer et al., 2014). KMAN = Committee on Meteorites, Academy of Sciences, Russia. USNM = Division of Meteorites, Department of Mineral Sciences, Smithsonian Institution. UCLA = University of California, Los Angeles meteorite collection.

5.5 Discussion

5.5.1 Chemical characteristics vs. genetics

5.5.1.1 Modeling HSE abundances of magmatic iron meteorite groups

The ^{187}Re-^{187}Os system, when applied to magmatic iron meteorites, can be used to date the absolute timing of core crystallization, albeit with relatively low resolution of typically >±5 Ma (e.g., Smoliar et al., 1996). The system has been used to assess whether iron meteorites have maintained closed-system behavior since crystallization. The Re-Os isotope systematics of the IIAB, IID, IIIAB, and IIIF iron meteorites fall within the ranges previously observed for other magmatic iron meteorite groups (IC, IIC, IIF, IVA, IVB, and SBT) (**Fig. 5.1**), indicating that the range of Re-Os fractionation during core crystallization was similar among these parent bodies. The IIAB, IID, IIIAB, and IIIF irons dominantly fall within ±10 part per 10,000 of a 4.568 Ga reference isochron, indicating that most of the iron meteorites from these groups maintained closed-system behavior of Re and Os, and presumably the other HSE, since crystallization.

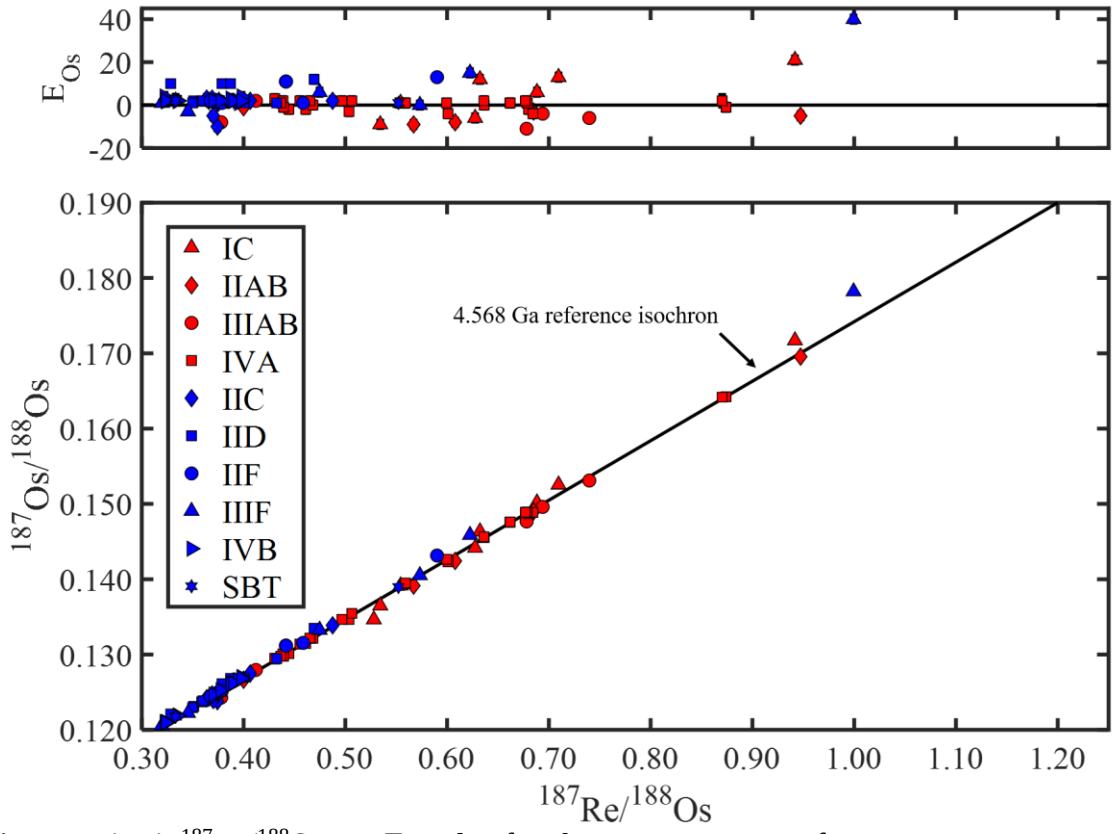

Fig. 5.1. (*top*) $^{187}Re/^{188}Os$ *vs*. E_{Os} plot for the iron meteorites from ten magmatic iron meteorite groups. E_{Os} is the parts per 10,000 deviation of the $^{187}Os/^{188}Os$ ratio of a sample from the 4.568 Ga reference isochron in the bottom figure. (*bottom*) $^{187}Re/^{188}Os$ *vs*. $^{187}Os/^{188}Os$ plotted with a 4.568 Ga reference isochron, calculated from an initial Solar System $^{187}Os/^{188}Os = 0.09517$ and $\lambda = 1.666 \times 10^{-11}$ yr^{-1} (Smoliar et al., 1996; Archer et al., 2014). Data are from Walker et al. (2008), McCoy et al. (2011), Hilton et al. (2019, in revision), Tornabene (2020), and Tornabene et al. (2020).

The CI chondrite normalized HSE patterns of iron meteorites from the IIAB, IID, IIIAB, and IIIF iron meteorite groups display similar relative and absolute variations to other magmatic iron meteorites (**Figs. 5.2** and **5.3**). For example, the abundance of the incompatible element Pd typically increases within an iron meteorite group with decreasing abundances of the compatible elements Re, Os, Ir, Ru, and Pt. These variations have typically been interpreted to be products of fractional crystallization with the degree of absolute and relative variations in HSE reflecting the abundances of S, P,

and C in the parental melt. Variations in the absolute abundances of HSE of iron meteorites between groups may also reflect variations in the HSE parental melt composition.

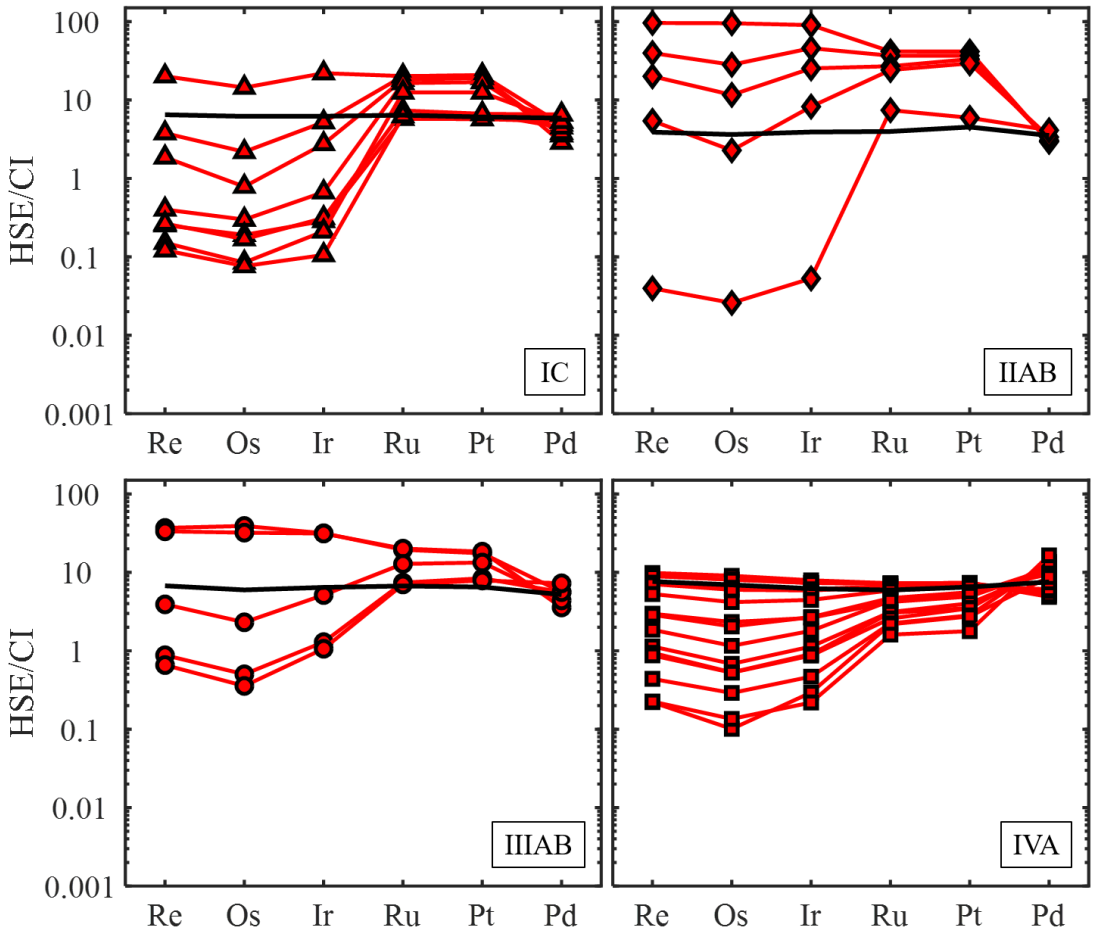

Fig. 5.2. Highly siderophile element abundances, normalized to CI chondrites (Horan et al., 2003), of NC-type IC, IIAB, IIIAB, and IVA iron meteorites (McCoy et al., 2011; Tornabene, 2020). Calculated parental melt compositions are shown as black lines.

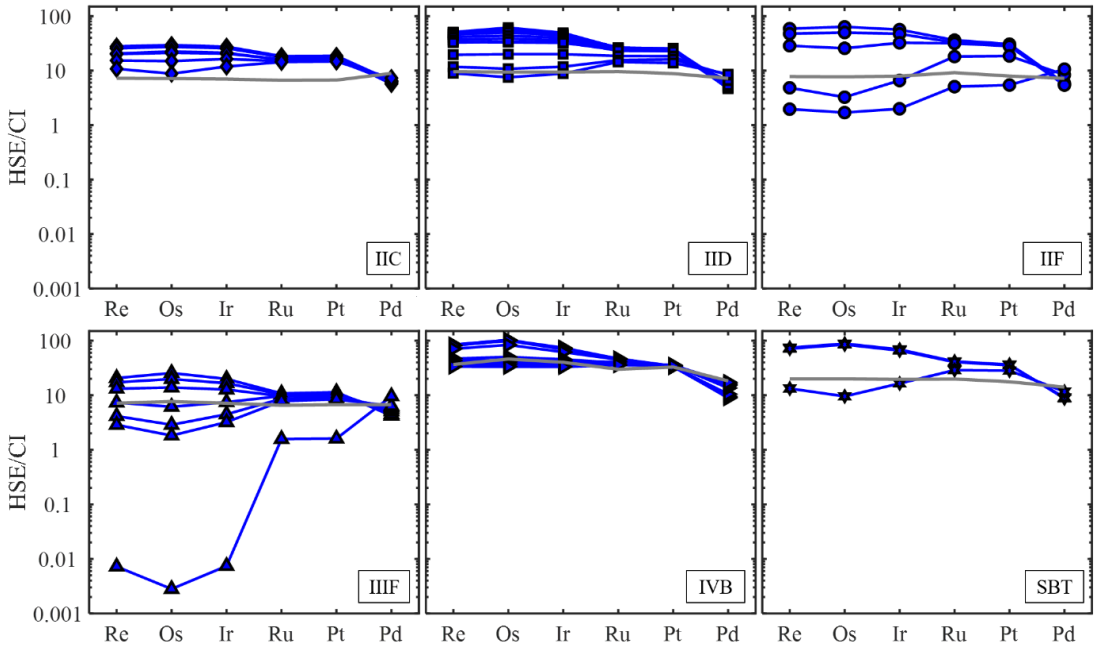

Fig. 5.3. Highly siderophile element abundances, normalized to CI chondrites (Horan et al., 2003), of the CC-type IIC, IID, IIF, IIIF, IVB, and SBT iron meteorites (Walker et al., 2008; Hilton et al., 2019, in revision; Tornabene et al., 2020). Calculated parental melt compositions are shown as grey lines.

Comparisons of measured HSE abundances of IIAB, IID, IIIAB, and IIIF iron meteorites with those predicted by liquid-crystal fractionation models, in order to assess their adherence to simple fractional crystallization and constrain parental melt compositions, were made following the approach initially discussed by Walker et al. (2008). In this approach, initial S, P, C, and HSE contents are treated as free parameters and all D values (solid metal-liquid metal partition coefficients) are calculated relative to experimentally-derived S, P, and C abundances *vs*. D value relationships (e.g., Jones and Drake, 1983; Jones and Malvin, 1990; Chabot and Jones, 2003; Chabot et al., 2017). Here, the parameterization method outlined by Jones and Malvin (1990), and modified by Chabot and Jones (2003), Worsham et al (2016a), and Chabot et al. (2017), is used to integrate the effects of S, P, and C abundances on HSE partitioning behavior. Additional

details and figures related to the modeling of bulk core HSE, S, P, and C contents, including assessment of uncertainties, for the IIAB, IID, IIIAB, and IIIF iron meteorites are discussed in Appendix 5. Initial composition data for all iron systems examined are provided in **Table 5.2**.

Table 5.2. Compositions of bulk cores of ten magmatic iron meteorites.

	Re	Os	Ir	Ru	Pt	Pd	S	P	Ni	Fe	FeS/Fe ratio of core	Relative mass of core (%)	% of Fe in core	% of Ni in core
NC-type														
IC[a]	250	2900	2700	4200	5500	3500	19	0.1	6	75	1.24 ± 0.12	21 ± 1	63^{+17}_{-11}	82^{+30}_{-17}
IIAB	150	1700	1700	2600	4100	2100	20	0.5	4	75	1.36 ± 0.14	34 ± 7	101^{+27}_{-18}	104^{+38}_{-22}
IIIAB	260	2800	2800	4400	5900	3100	12	0.2	7	80	0.55 ± 0.06	21 ± 3	67^{+18}_{-12}	107^{+40}_{-23}
IVA[b]	295	3250	2700	3900	5900	4500	6	0.1	8	86	0.22 ± 0.04	19 ± 4	66^{+18}_{-12}	108^{+40}_{-23}
Average	240	2700	2500	3800	5400	3300	14	0.2	6	79	0.84	24	75	100
CC-type														
IIC[c]	280	3350	3050	4340	6070	5300	8	3	11	78	0.34 ± 0.05	18 ± 5	49^{+27}_{-13}	102^{+68}_{-29}
IID	370	4400	4100	6300	8000	4300	10	1	10	79	0.45 ± 0.06	14 ± 1	39^{+21}_{-10}	76^{+53}_{-23}
IIF[d]	300	3600	3450	6000	7200	4300	14	0.4	10	75	0.75 ± 0.08	16 ± 2	43^{+23}_{-11}	89^{+60}_{-26}
IIIF	275	3600	3100	4300	6100	4000	5	1	8	86	0.18 ± 0.04	18 ± 2	55^{+30}_{-14}	75^{+50}_{-21}
IVB[e]	1410	21600	17500	19600	29800	10900	1	0.65	19	80	0.04 ± 0.04	4 ± 2	11^{+6}_{-3}	40^{+27}_{-11}
SBT[f]	770	9400	8500	13000	16000	8400	7	1	19	73	0.31 ± 0.05	7 ± 1	18^{+10}_{-5}	70^{+47}_{-20}
Average	570	7700	6600	8900	12000	6200	8	1.2	13	79	0.34	13	36	76

Concentrations are in ppb for HSE and wt. % for S, P, Ni, and Fe. Carbon contents are estimated to be <0.05 wt. % and are not listed. Bulk core HSE, S, and P data are from [a]Tornabene (2020), [b]McCoy et al. (2011), [c]Tornabene et al. (2020), [d]Hilton et al. (in revision), [e]Walker et al. (2008), and [f]Hilton et al. (2019). Uncertainties on FeS/Fe ratio of core values reflect the ±1.5 wt. % uncertainties on bulk core S and Fe values. The relative mass of core values reflect the average ± 2SD enrichment factors of HSE compared to NC- or CC-type chondrites. Percent of Fe and Ni in core values were calculated using the median Fe or Ni content of NC- or CC-type chondrites and uncertainties reflect the min and max contents. Values >100 may indicate these parent bodies had Fe or Ni contents lower than the median Fe or Ni content of chondrites used in the calculation.

For the IIAB iron meteorites, HSE abundances are best explained by an initial melt composition of ~ 20 wt. % S, 0.5 wt. % P, <0.05 wt. % C. Using these parameters, the IIAB irons can be accounted for as solids produced as a result of fractional crystallization from a primary initial melt characterized by Re, Os, Ir, Ru, Pt, and Pd abundances of 150, 1700, 1700, 2600, 4100, and 2100 ppb, respectively. The IID iron meteorites, by contrast, have HSE abundances that are most consistent with crystallization from a melt with ~ 10 wt. % S, 1 wt. % P, <0.05 wt. % C, and Re, Os, Ir, Ru, Pt, and Pd abundances of 370, 4400, 4100, 6300, 8000 and 4300 ppb, respectively. For this composition, five of the 12 studied IID irons can be accounted for as solids formed directly by fractional crystallization while the other seven irons require various amounts of equilibrium solid metal-liquid metal mixing, ranging from mixing of initial solid and liquid, to mixing of solid and liquid produced after 25 % of crystallization.

The HSE abundances of five IIIAB irons with limited fractionations of HSE were successfully modeled using initial parameters of ~ 12 wt. % S, 0.2 wt. % P, <0.05 wt. % C, and Re, Os, Ir, Ru, Pt, and Pd abundances of 260, 2800, 2800, 4400, 5900, and 3100 ppb, respectively. Using this parental melt composition, two of the five examined IIIAB irons can be explained as direct products of fractional crystallization while the others likely required additional processes, such as equilibrium solid metal-liquid metal mixing. For the IIIF iron meteorites, the HSE abundances can largely be accounted for by a simple fractional crystallization model, with most representing equilibrium solids. The best fit model is characterized by initial parameters of ~ 5 wt. % S, 1 wt. % P, and <0.05

wt. % C, as well as Re, Os, Ir, Ru, Pt, and Pd abundances of 275, 3600, 3100, 4300, 6100, and 4000 ppb, respectively.

Using the parental melt S contents constrained by HSE modeling and the corresponding D values for Ni, the parental melt Ni abundance of each iron meteorite group can be determined from the Ni content of the least evolved group member. For example, a parental melt content of 20 wt. % S (IIAB) results in a Ni D value of 1.18, whereas a content of 1 wt. % S (IVB) results in a Ni D value of 0.88 (Chabot et al., 2019). This range of Ni D values results in parental melt Ni contents within 0 to 2 wt. % of the least evolved member. The Fe content of the core can then be calculated by mass balance. Results of these calculations, applied to all ten magmatic iron meteorite groups, are provided in **Table 5.2** and **Fig. 5.4**.

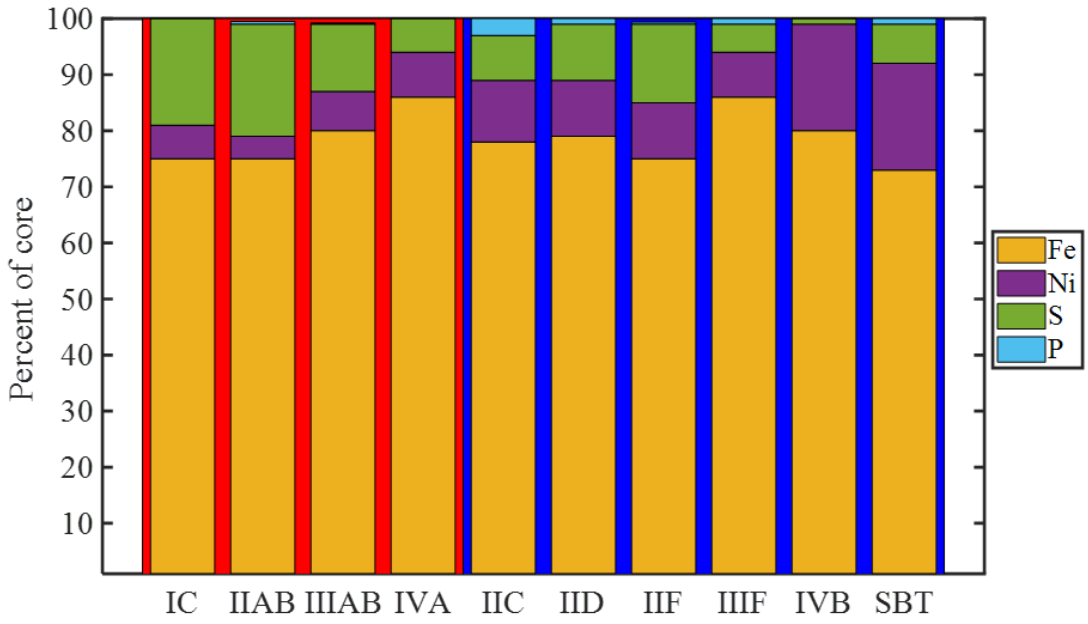

Fig. 5.4. The proportions of Fe, Ni, S, and P determined for bulk cores from ten magmatic iron meteorite parent bodies (Walker et al., 2008; McCoy et al., 2011; Hilton et al., 2019, in revision; Tornabene, 2020; Tornabene et al., 2020). The NC-type parent bodies are identified with a red background while CC-type parent bodies are identified with a blue background.

5.5.1.2 Accretion of HSE

Since ~99 % of the HSE in a planetesimal likely reside in its core, the relative abundances of these elements in a bulk core presumably reflect the relative abundances of these elements in the entire body. Most of the HSE ratios inferred for NC-type iron meteorite parent bodies are similar to one another, and within the average ± 2SD range of ratios defined by bulk enstatite and ordinary (NC-type) chondrites (Horan et al., 2003; Fischer-Gödde et al., 2010) (**Fig. 5.5**). Most of the HSE ratios inferred for CC-type iron meteorite parent bodies, except the IVB, are also similar to one another, and within the average ± 2SD range of ratios defined by bulk carbonaceous (CC-type) chondrites (Horan et al., 2003; Fischer-Gödde et al., 2010) (**Fig. 5.6**). Furthermore, the iron meteorite and chondrite parent bodies do not show appreciable differences in HSE/Ir ratios between the

NC and CC reservoirs (**Fig. 5.6**). Given that Re, Os, Ir, Ru, and Pt condense out of a solar nebular gas into an assortment of refractory metal phases, while Pd condenses at lower temperatures into a Fe alloy (Lodders, 2003), the similar HSE/Ir ratios among these examined iron meteorite and chondrite parent bodies suggest that most of them accreted similar proportions of these different phases.

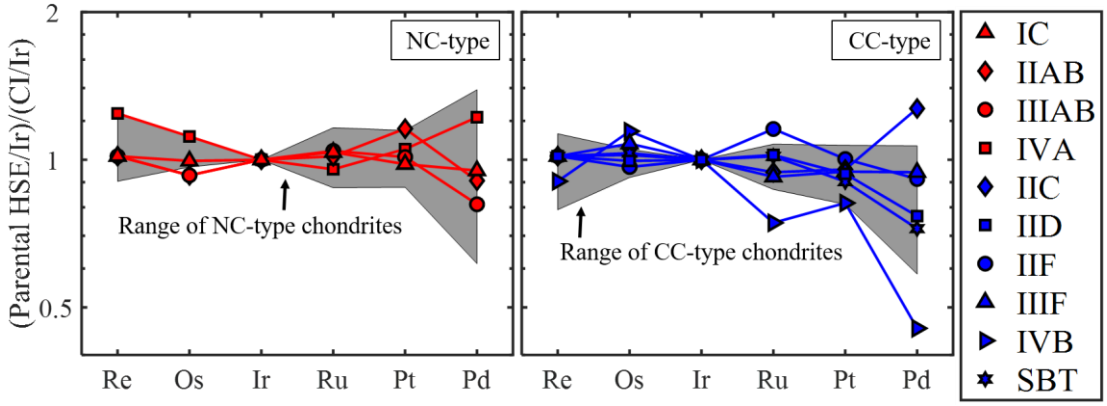

Fig. 5.5. Ir- and CI-normalized parental melt HSE abundances of ten iron meteorite parent bodies (Walker et al., 2008; McCoy et al., 2011; Hilton et al., 2019, in revision; Tornabene, 2020; Tornabene et al., 2020) compared to the average ± 2SD ranges observed in NC-type ordinary and enstatite chondrites, as well as CC-type carbonaceous chondrites (grey fields) (Horan et al., 2003; Fischer-Gödde et al., 2010).

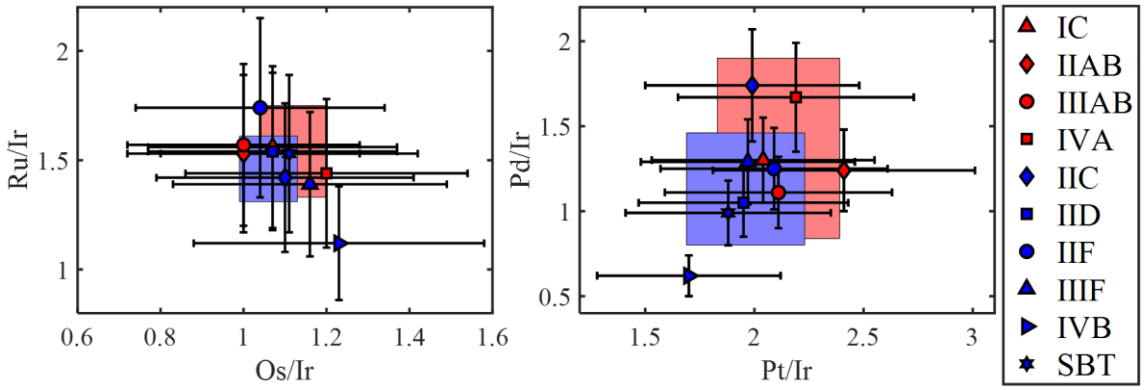

Fig. 5.6. The Ru/Ir *vs*. Os/Ir and Pd/Ir *vs*. Pt/Ir ratios of NC- and CC-type iron meteorite parent bodies compared to the average ± 2SD ratios of NC-type enstatite and ordinary chondrites (red box) and CC-type carbonaceous chondrites (blue box) (Horan et al., 2003; Fischer-Gödde et al., 2010).

The IVB iron meteorites are the only core materials considered here that were evidently not derived from a parental melt with relative abundances of some HSE in the ranges observed for other iron meteorite or chondrite parent bodies (Campbell and Humayun, 2005; Walker et al., 2008). This indicates that the IVB iron meteorite parent body, or precursor materials, had a distinctly different formation history compared to other magmatic irons considered. Past studies have suggested that this may be due to high temperature processing event, which fractionated elements by volatilization during the condensation of precursor materials (Campbell and Humayun, 2005; Walker et al., 2008). The fractionated abundances of HSE appear unrelated to the genetic isotopic compositions of this parent body, however, as it is isotopically identical to other CC-type planetesimals without fractionated Pd/Ir.

Of the six HSE considered in this study, nucleosynthetic isotopic variations between NC- and CC-type magmatic iron meteorite groups are observed for Ru (e.g., Bermingham et al., 2018) and Pd (Ek et al., 2019) but absent for Os (Walker, 2012) and

Pt (Kruijer et al., 2013). Past studies have proposed that the isotopic variations that are observed between NC and CC materials were a product of variable thermal processing (e.g., Trinquier et al., 2009; Poole et al., 2017; Ek et al., 2019; Worsham et al., 2019). Specifically, these studies have envisioned that unstable presolar carriers with a certain isotopic composition were variably destroyed based on heliocentric distance in the solar nebula prior to planetesimal accretion or otherwise excluded from the accretionary processes leading to planetesimal formation. If so, the selective loss of Ru and Pd from certain planetary precursor materials did not fractionate these elements relative to Os and Pt on the bulk planetary scale to the level that is resolvable by this kind of approach. There are no systematic variations in Ru/Ir or Pd/Ir ratios of iron meteorite or chondrite parent bodies from Os/Ir or Pt/Ir ratios with genetic isotopic composition (**Fig. 5.6**).

It has also been proposed that the genetic isotopic compositions of CC-type materials reflect a potential mixing of NC-type materials with materials that are isotopically similar to Ca-Al-rich inclusions (CAIs) (Burkhardt et al., 2019; Nanne et al., 2019). This idea is supported by the conclusions of Rubin (2018), in which it was proposed that CC-type planetesimals accreted more CAIs than NC-type planetesimals based on an observation that CC-type iron meteorites are enriched in refractory siderophile elements (Re, Os, Ir, Ru, and Pt), of which most CAIs are strongly enriched relative to bulk chondrites. This idea can be further evaluated by considering the abundance of Pd relative to the other HSE, since Pd is not a refractory siderophile element and condenses into Fe alloys rather than refractory metal phases (Lodders, 2003). As such, most CAIs have depletions in Pd relative to Re, Os, Ir, Ru, and Pt (Campbell et al., 2003; Archer et al., 2014). Only Group 2 CAIs have no systematic relative depletions in Pd compared to Re, Os, Ir, Ru, and Pt,

but they are not strongly enriched in HSE (0.1 to 1xCI) and, therefore, unlikely to enrich the refractory siderophile element content of a planetary body relative to another (Archer et al., 2014).

If differences in the bulk core refractory siderophile element abundances of NC- and CC-type bodies were the result of variable accretion of CAIs, this would likely present itself with bulk core compositions characterized by relative Pd depletions. However, this is not observed (**Fig. 5.6**) among most NC- and CC-type iron meteorite parent bodies and, therefore, no chemical indication from siderophile elements for the heterogeneous accretion of CAIs is apparent. Only the projected bulk core composition for the IVB irons has a sub-chondritic Pd/Ir ratio (**Fig. 5.6**), permissive of accreting more refractory metal phases and CAIs (Rubin, 2018). However, this characteristic at present cannot be related to genetic isotopic composition.

5.5.1.3 Relative masses of NC vs. CC cores

Past studies have commonly interpreted the range of Ni contents among magmatic iron meteorite groups to reflect the relative distribution of Fe between the core and mantle of a planetary body and thus, the mass of the core relative to the mantle (e.g., Kelly and Larimer, 1977). Consequently, as CC-type magmatic iron meteorites in most instances have higher Ni/Fe ratios relative to NC-type magmatic iron meteorites, their parent bodies have been interpreted to have a lower proportion of metallic Fe and relatively smaller cores (Rubin, 2018).

The relative mass of a planetary core compared to the mantle can be quantitatively constrained from the bulk core HSE abundances compared in this study. This is made

possible by assuming ~99 % of HSE partition into the core and that NC- and CC-type iron meteorite parent bodies had bulk HSE compositions of NC- and CC-type chondrites, respectively. Of the projected abundances of HSE in the parental melts of the four NC-type parent bodies, bulk core HSE abundances are concentrated by factors of 3 to 5 compared to the average HSE composition of the NC-type enstatite and ordinary chondrites (Horan et al., 2003; Fischer-Gödde et al., 2010). These enrichment factors suggest that these parent bodies had cores consisting of 19 to 34 % the mass of the whole asteroid (**Fig. 5.7**). For the six CC-type parent bodies, bulk core HSE abundances are enriched compared to the average abundance of CC-type carbonaceous chondrites by factors of 6 to 27, which correspond to parent bodies with cores consisting of 4 to 18 % the mass of the whole asteroid (**Fig. 5.7**). Overall, these core sizes are grouped with genetic isotopic compositions, with CC-type bodies typically having proportionally smaller cores than NC-type bodies. However, within a single reservoir, bodies with identical genetic isotopic compositions formed cores with variable sizes.

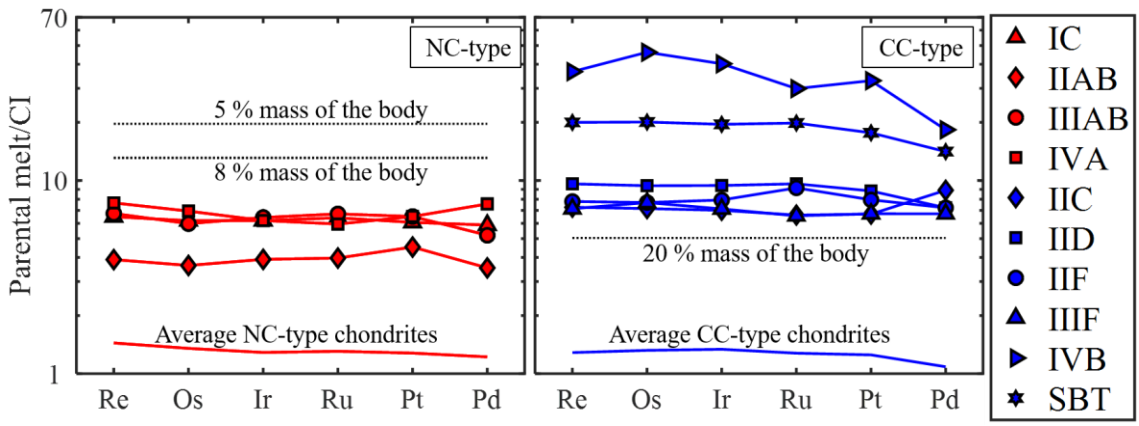

Fig. 5.7. Parental melt HSE abundances, normalized to CI chondrites (Horan et al., 2003), of ten iron meteorite parent bodies (Walker et al., 2008; McCoy et al., 2011; Hilton et al., 2019, in review; Tornabene, 2020; Tornabene et al., 2020). Average HSE abundances of NC-type ordinary and enstatite chondrites and CC-type carbonaceous chondrites are shown for reference (Horan et al., 2003; Fischer-Gödde et al., 2010) as well as lines representing the HSE content of a bulk core that is 5, 8, and 20 % the mass of a planetary body.

5.5.1.4 Oxidation

Upon recognizing the existence of the NC and CC reservoirs, Warren (2011) posited that these reservoirs may represent the inner and outer Solar System, respectively, relative to Jupiter. This argument was based on the limited number (at the time) of CC-type samples derived from differentiated bodies, which was interpreted to indicate that CC-type planetesimals were less likely to undergo major heating, coupled with the widespread hypothesis that carbonaceous chondrites, some of which bear hydrous minerals, likely formed at greater radial distances from the Sun than NC chondrites (e.g., Wood, 2005). While numerous CC-type differentiated meteorites, such as the IIC, IID, IIF, IIIF, IVB, and SBT iron meteorites, have since been identified (Kruijer et al., 2017; Hilton et al., 2019), indicating that NC- and CC-type planetesimals both underwent major heating sufficient for core segregation, the locations of the NC and CC reservoirs as the inner and outer Solar System, relative to Jupiter, continue to be favored by many

subsequent studies (e.g., Budde et al., 2016a; Kruijer et al., 2017; Burkhardt et al., 2019; Nanne et al., 2019; Worsham et al., 2019). For example, Worsham et al. (2019) built upon an inner and outer Solar System divide to propose that the variable isotopic compositions observed for Mo, Ru, and W among NC- and CC-type iron meteorites were consistent with these reservoirs evolving under distinct redox conditions, specifically reduced conditions for NC-type materials as envisioned for the inner Solar System and oxidized conditions for CC-type materials as expected for the outer Solar System.

While the oxidation conditions of the four NC-type parent bodies and the six CC-type parent bodies considered here can be indirectly inferred from the relative mass of their cores, a more direct comparison can be made by constraining the distribution of Fe and Ni in these planetary bodies between the core and mantle (Kelly and Larimer, 1977). Quantitative Fe_{core}/Fe_{total} and Ni_{core}/Ni_{total} ratios can be determined from the bulk Fe and Ni contents of each core, coupled with the mass proportion of each parent body residing in a core, and using the Fe and Ni contents of NC- and CC-type chondrites (Lodders and Fegley, 1998) as a proxy for the bulk Fe and Ni compositions of NC- and CC-type iron meteorite parent bodies (**Table 5.2**).

The CC-type planetesimals, on average, have a smaller proportion of total Fe in their cores, compared to NC-type planetesimals, permissive of the CC reservoir being a more oxidized environment, such as the outer Solar System (**Fig. 5.8**). However, this environment was not oxidizing to the extent that it affected the distribution of Ni between the core and mantle. Additionally, significant overlap in the inferred oxidation state of NC- and CC-type iron meteorite parent bodies is observed, making any distinction between the oxidation state of individual planetary bodies with genetic isotopic

composition ambiguous. If the NC and CC reservoirs represent the inner and outer Solar System, respectively, relative to Jupiter, one possible explanation for the overlap in oxidation conditions is if the snow line was located sunward of Jupiter (Lacar et al., 2006; Garaud and Lin, 2007; Kennedy and Kenyon, 2008). If so, this could explain why some NC-type bodies have similar oxidation states to some CC-type bodies.

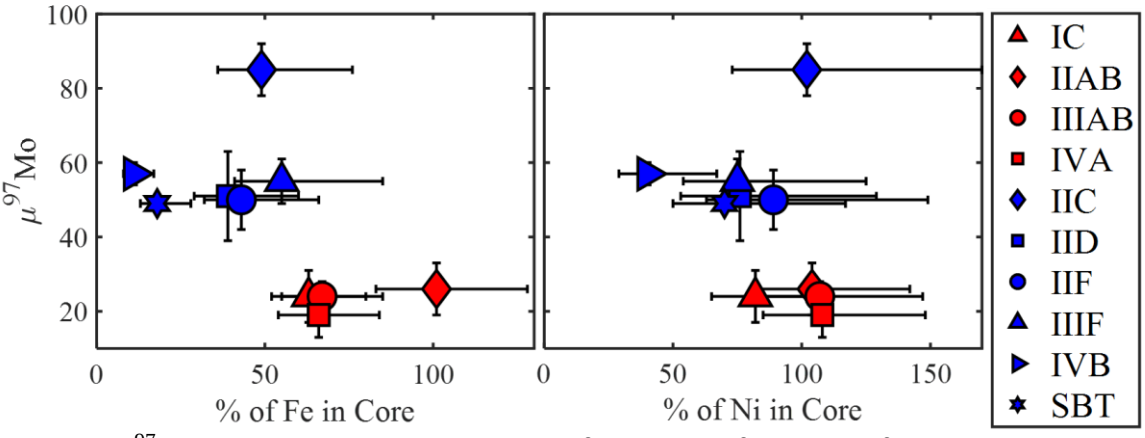

Fig. 5.8. μ^{97}Mo isotopic compositions *vs*. (*left*) percent of total Fe of a planetary body in the core and (*right*) percent of total Ni of a planetary body in the core for ten iron meteorite parent bodies. Isotopic compositions are from Kruijer et al. (2017), Worsham et al. (2017), Bermingham et al. (2018), and Hilton et al. (2019). Error bars for percent of total Fe and Ni in the core represent the range of Fe and Ni contents observed in NC- and CC-type chondrites (Lodders and Fegley, 1998).

As noted for core size, there is no relationship between projected oxidation conditions and genetic isotopic compositions for parent bodies that formed within the same reservoir (**Fig. 5.8**). For example, the CC-type IIC iron meteorites have a distinct Mo isotopic composition from the other CC-type iron meteorites considered in this study (Kruijer et al., 2017; Tornabene et al., 2020), yet an indistinguishable relative oxidation state. As such, if the distinct isotopic composition of the IIC irons compared to other CC-type iron meteorites is related to oxidation conditions, this is not reflected in the chemical

characteristics of bulk planetary bodies. Whether or not oxidation states of NC-type bodies vary with genetic isotopic compositions cannot currently be constrained since the IC, IIAB, IIIAB, and IVA irons have similar genetic isotopic compositions (e.g., Bermingham et al., 2018). Only some non-magmatic (e.g., IAB main group) and ungrouped (e.g., Gebel Kamil) iron meteorites have been reported to have Mo and Ru genetic isotopic compositions that differ from the IC, IIAB, IIIAB, and IVA iron meteorites (Bermingham et al., 2018). Unlike for magmatic irons, however, the origins of these types of iron meteorites remain uncertain (e.g., Hilton and Walker, 2020), making a comparison of their chemical compositions to those of magmatic iron meteorite groups ambiguous.

5.5.1.5 Volatility

Bulk core S contents vary among NC-type asteroids from 6 wt. % (IVA) to 20 wt. % (IIAB) and among CC-type asteroids from 1 wt. % (IVB) to 14 wt. % (IIF). These variations may be the result of pre- and/or post-accretion processes. For example, pre-accretion, the S content of precursor materials is set by the formation of FeS through the reaction of Fe metal with H_2S (Kelly and Larimer, 1977). As such, FeS formation can vary with the temperature at which an asteroid's precursor materials condensed. Post-accretion, it may be possible to lose S through planetary outgassing (e.g., Rasmussen et al., 1984). Secondary processes, such as aqueous alteration, metamorphic process, and/or oxidation, may also transport S between different phases, such as sulfides, sulfates, S^0, and organic compounds, as evidenced in carbonaceous chondrites (Gao and Thiemens,

1993). Finally, the bulk core S content is set by the efficiency of the segregation of remaining FeS to the core (e.g., Kruijer et al., 2014a).

Since S, which has a 50 % condensation temperature (T_{50}) of 664 K (Lodders, 2003), is the most volatile element considered in this study, possible S variations by volatile-related processes, such as condensation or outgassing, may be assessed through comparison to other elements with similar condensation temperatures. These include Ga and Ge, which have 50 % condensation temperatures of 968 K and 883 K, respectively (Lodders, 2003). Since Ga and Ge typically have solid metal-liquid metal partition coefficients near 1 regardless of initial S content (Chabot et al., 2017), the average iron meteorite group Ga and Ge abundances provide first-order constraints on bulk core compositions. Bulk core S contents form broad positive relationships between Ga and Ge average group abundances, suggesting that at least some variations in bulk core S contents are likely volatility-related (**Fig. 5.9**). The variations are decoupled from genetic isotopic compositions, however, indicating both NC- and CC-type asteroids were variably affected by volatility-related processes, such as processes affecting precursor materials (i.e., inductive heating of nebular materials) and/or parent body processes (i.e., impacts). Since the bulk core content of volatile siderophile elements is not diagnostic of which volatility-related processes were occurring, NC- and CC-type iron meteorite parent bodies may have been affected by both processes similarly or variably.

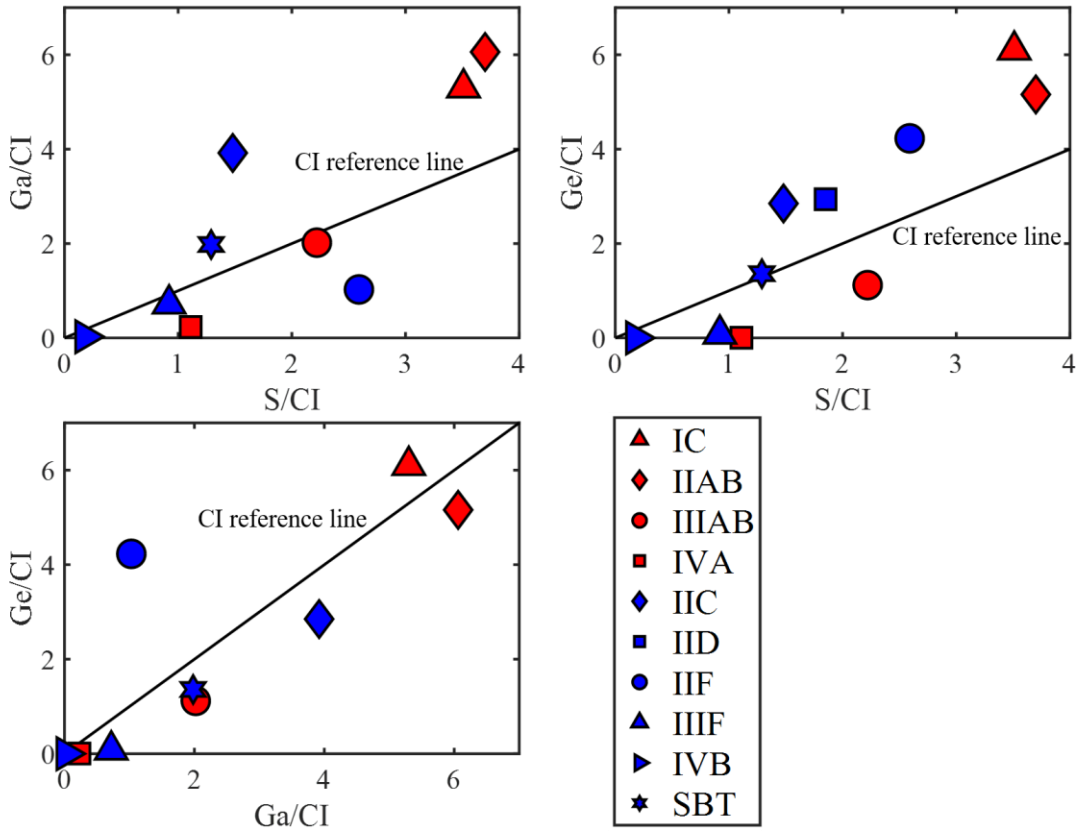

Fig. 5.9. Comparisons of Ga/CI, Ge/CI, and S/CI abundances of bulk cores from ten magmatic iron meteorite parent bodies (Walker et al., 2008; McCoy et al., 2011; Hilton et al., 2019, in revision; Tornabene, 2020; Tornabene et al., 2020). CI-chondrite reference lines are also shown (Lodders and Fegley, 1998). Average group Ga and Ge abundances are compiled from the literature.

5.5.2 Chemical characteristics vs. ages

One aspect concerning the origins of the NC and CC reservoirs that remains uncertain is the relative timing of the introduction of the isotopically distinct materials of these reservoirs to the early Solar System. Kruijer et al. (2017) proposed that CC-type materials were added to the Solar System after NC-type materials, due to differences in model ^{182}W ages of some NC- and CC-type iron meteorites. That study noted that NC-type magmatic iron meteorites, compared to CC-type irons, tend to have μ^{182}W isotopic compositions more similar to CAIs, which are interpreted as the first materials to condense in the Solar

System (e.g., Amelin et al., 2002). This observation was interpreted to indicate that NC-type bodies began forming cores, on average, about 1 Myr earlier than CC-type iron meteorite parent bodies. Thermal modeling conducted by Kruijer et al. (2017) also suggested the NC parent bodies accreted about 0.5 Myr, on average, earlier than CC parent bodies.

By contrast, more recent studies have proposed that CC-type materials were present in the Solar System prior to NC materials, based on the genetic isotopic similarities of CC-type materials to CAIs (Burkhardt et al., 2019; Kruijer et al., 2019; Nanne et al., 2019). If so, then the observed offset in $\mu^{182}W$ values between some NC- and CC-type bodies warrants explanation. Some past studies have proposed that factors other than accretion ages, such as chemical compositions, may account for differences in initial $\mu^{182}W$ values. For example, Hellmann et al. (2019) proposed that differences in $\mu^{182}W$ values between NC and CC bodies may reflect differences in the bulk Hf/W ratios of precursor materials and parent bodies. Hilton et al. (2019) proposed that differences in $\mu^{182}W$ values could represent differences in the FeS *vs*. Fe content of NC- *vs*. CC-type planetary cores. If either is true, then the interpretation of W model ages, and thus the current interpretations regarding the timing of core formation on NC- and CC-type bodies, may be problematic.

Whether the FeS *vs*. Fe content of a planetary core can account for differences in the $\mu^{182}W$ isotopic composition of NC- and CC-type magmatic iron meteorites can be further assessed using the additional chemical constraints compiled by this study. Kruijer et al. (2014a) initially proposed that differences in core formation ages could reflect differences in the relative proportions of FeS *vs*. Fe in planetary cores since FeS and Fe

melt at different temperatures and, therefore, FeS and Fe liquids may evolve distinct $\mu^{182}W$ isotopic compositions. As such, a bulk core $\mu^{182}W$ isotopic composition could be the product of mixing variable proportions of FeS and Fe. This idea was then applied by Hilton et al. (2019) to explain the core formation age dichotomy observed for some NC- and CC-type parent bodies using bulk core S contents for three NC-type and three CC-type iron meteorite parent bodies. With the new constraints provided by this study on the Fe and S contents of bulk cores, it is possible to calculate the FeS/Fe ratio of bulk cores for ten magmatic iron meteorite parent bodies (**Table 5.2**). These calculations are based on the assumptions that all S in the core is sourced from FeS and no S was lost from the core following differentiation. Overall, there is a tendency for FeS-rich cores to have more negative $\mu^{182}W$ isotopic compositions (**Fig. 5.10**). However, highlighting a clear relationship is problematic since CC-type irons, which have a 14 wt. % range in bulk core S contents, have no resolved differences in $\mu^{182}W$ isotopic compositions.

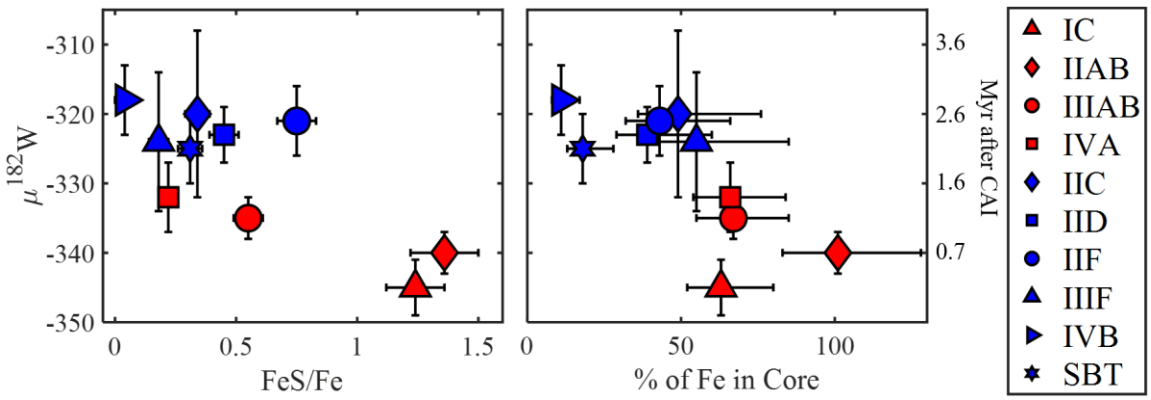

Fig. 5.10. Radiogenic $\mu^{182}W$ isotopic compositions *vs*. (*left*) bulk core FeS/Fe ratio and (*right*) percent of the planetary body Fe content in the core. Radiogenic $\mu^{182}W$ isotopic compositions are from Kruijer et al. (2017) and Hilton et al. (2019).

The $\mu^{182}W$ values of NC- and CC-type magmatic iron meteorites also do not correlate with percent of Fe of a planetary body in the core (**Fig. 5.10**) since many of these values are not resolved among parent bodies. Since the distribution of Fe in a planetary body serves as a proxy for oxidation state, a relationship could suggest that more oxidized bodies form cores at slower rates than reduced bodies, possibly by the heterogeneous accretion of ice. Ice can increase the oxidation state of a planetary body as well as vary the planetesimal's density and concentration of ^{26}Al, the dominant heat-producing radionuclide in the early Solar System. As a result, the overall power per unit volume from ^{26}Al decay for melting planetary bodies could be reduced (e.g., Hilton et al., 2019). Additionally, if any ice melted and then evaporated during planetary processing, it is plausible that there could be a loss of energy from the system and, thus, a slowing and prolonging of core formation. It is also possible that a relationship between the distribution of Fe in a planetary body and the timing of core formation simply reflects the relative proportions of FeS *vs.* Fe in the core since less Fe will segregate into the core of an oxidized body. Overall, since the FeS/Fe content of a core and the oxidation state of a body do not form definitive relationships with timing of core formation, the observed offset in $\mu^{182}W$ values between some NC- and CC-type bodies may still reflect differences in accretion ages (Kruijer et al., 2017) or bulk planetesimal Hf/W ratios (Hellmann et al., 2019). Further work is needed to discriminate between these possibilities.

5.5.3 Isotopic heterogeneity of the NC and CC reservoirs

A common explanation for the isotopic heterogeneity of the NC and CC reservoirs is the inheritance of isotopic heterogeneities to planetary bodies based on the initial heterogeneous distribution of isotopically distinct precursor materials in the parental molecular cloud (Dauphas et al., 2002; Burkhart et al., 2019; Nanne et al., 2019). A shortcoming of this model, however, is that it fails to account for the apparent homogenous distribution of certain precursor materials, such as those hosting Hf, Os, and Pt (Sprung et al., 2010; Walker, 2012; Kruijer et al., 2013). Other studies, therefore, have argued for an isotopically homogenized molecular cloud, which then developed certain isotopic heterogeneities due to a specific process, including sorting of materials by type (Regelous et al., 2008) or size (Dauphas et al., 2010), thermal processing of materials under variable oxidation conditions (Poole et al., 2017; Worsham et al., 2019), or the late injection of isotopically distinct materials (Brennecka et al., 2013; Sugiura and Fujiya, 2014; Kruijer et al., 2017).

We find that the chemical characteristics of the studied iron meteorite parent bodies neither support nor disprove the previously proposed mechanisms. For example, Regelous et al. (2008) proposed that phases of metal, sulfides, and silicates, which had distinct genetic Ni isotopic compositions, were physically separated (further details were not provided) in the Solar System and, therefore, heterogeneously accreted by planetary bodies. In this study, we find that the FeS/Fe ratio of magmatic iron meteorite cores, while variable, do not vary with genetic isotopic composition. This lack of relationship does not disprove the proposed idea of Regelous et al. (2008), however, as the FeS/Fe ratio of the core does not constrain the FeS/Fe ratio of the parent body.

The abundance of volatile elements in the cores of the examined magmatic iron meteorites does not provide a clear assessment of the possible effects of thermal processing. Trinquier et al. (2009) argued for the thermal processing of materials to explain the correlated variations in isotopes of Ti derived from different nucleosynthetic processes. In this scenario, certain precursor materials were destroyed by sublimation, separated from other materials as a gas, and re-condensed elsewhere in the Solar System. This idea was expanded by Poole et al. (2017) to also account for Mo and further expanded by Worsham et al. (2019) to account for decoupled variations for Mo and ^{183}W among CC-type materials and Mo and Ru among NC-type materials. If thermal processing was occurring at relatively high temperatures (~ >700 K), volatile siderophile elements may also have sublimated and abundances of these elements in a parent body may correlate with degree of isotopic heterogeneity. Yet no variations among Ga, Ge, and S abundances with genetic isotopic composition are observed for the cores of iron meteorite parent bodies, suggesting thermal processing at high temperatures did not dominantly cause the isotopic heterogeneity among asteroids. This observation does not fully exclude this idea, however, as the Ga, Ge, and S content of a core may also be set by processes occurring after planetary accretion. Overall, if thermal processing did produce isotopic heterogeneities, it may have been a relatively lower temperature process.

Poole et al. (2017) and Worsham et al. (2019) argued for additional affects of oxidation to the thermal processing of precursor materials. Specifically, Poole et al. (2017) noted that decoupled isotopic variations of Mo and W for some meteorites, despite the hosting of these elements in the same carriers (Burkhardt et al., 2012), indicated Mo

was volatilized under oxidizing conditions. Worsham et al. (2019) applied this logic further to account for correlated variations for isotopic compositions of Mo and Ru among NC-type iron meteorites and correlated variations for isotopic compositions of Mo and ^{183}W among CC-type iron meteorites, calling upon thermal processing of Mo and Ru carriers in the NC reservoir under reduced conditions and thermal processing of Mo and ^{183}W carriers in the CC reservoir under oxidizing conditions. If true, it may be expected that the IIC iron meteorite parent body, which has the greatest *s*-process Mo deficits relative to terrestrial materials of the examined iron meteorite parent bodies, would be the most oxidized body. However, that is not observed, with the IIC iron meteorite parent body having an oxidation state similar to isotopically distinct CC and NC iron meteorites. Yet, it remains possible that additional oxidation processes overprinted those involved in generating isotopic heterogeneities on the parent body scale.

Late injection of isotopically distinct materials remains a possible mechanism to explain the isotopic variability of the NC and CC reservoirs. While there are no clear differences in the accretion ages of NC- and CC-type parent bodies that would indicate differences in the relative timing of the addition of NC- or CC-type materials to the Solar System (Hilton et al., 2019; Kaminski et al., 2020), there may be evidence for the late injection of isotopically distinct materials (or removal of isotopically distinct materials) to just the NC reservoir. Hilton and Walker (2020) observed a relationship between genetic isotopic composition and age of iron meteorite formation for NC-type irons. By contrast, no such relationship is observed for CC-type materials (Kruijer et al., 2017). These observations may indicate that the causes of isotopic heterogeneity varied between the two reservoirs. If true and the cause of isotopic heterogeneity of the CC reservoir was

not time related, the cause is not apparent when comparing the chemical characteristics of CC-type iron meteorite parent bodies.

Overall, the chemical characteristics of NC- and CC-type magmatic iron meteorite parent bodies do not form clear relationships with genetic isotopic compositions in ways that indicate the cause of isotopic heterogeneity to the early Solar System. This may be due to the overwriting of signatures by the process of planetary formation and differentiation. Alternatively, this may indicate that the cause of isotopic heterogeneity on the planetary scale was due to the minor heterogeneous accretion of materials with major isotopic anomalies. As such, isotopic anomalies on the parent body scale would be observed without any clear variations in the chemical characteristics of a bulk body. If true, more insights to the cause of isotopic heterogeneity may be gained by studying the isotopic and chemical compositions of planetary precursor materials, such as through leachate analyses of chondrites and studies of presolar grains, CAI, chondrule, and matrix separates. Both of these applications have shown distinct isotopic compositions exist among the individual components of a parent body (e.g., Burkhardt et al., 2011, 2019; Budde et al., 2016a, 2018, 2019). By improving our understanding of the degree of isotopic anomalies present in different host phases, host phases with the largest isotopic anomalies can be further studied to determine their stabilities under different nebular conditions. It may then be possible to identify the specific precursor material(s) varying in abundance among planetary bodies.

5.6 Conclusions

Through the study of HSE abundances in magmatic iron meteorites, we draw the following conclusions:

1. Comparison of the parent body HSE/Ir ratios and bulk core inventories of volatile elements (i.e. Ga, Ge, and S) of NC- and CC-type iron meteorite parent bodies indicate that the processes setting planetesimal genetic isotopic compositions and these chemical characteristics in early formed iron meteorite parent bodies are largely decoupled.
2. The bulk core chemical compositions (HSE, S, P, C, Ni, and Fe) and core-mantle distribution of Fe of NC- and CC-type iron meteorite parent bodies are permissive of CC-type bodies typically having smaller relative cores and accreting in more oxidized environments.
3. Comparison of the chemical characteristics of NC- and CC-type iron meteorite parent bodies with radiogenic $\mu^{182}W$ isotopic compositions suggest that a model ^{182}W age may be partially controlled by the core FeS/Fe content and/or oxidation state of a planetary body, although there is no clear relationship. As such, the differences in $\mu^{182}W$ values among some NC- and CC-type magmatic iron meteorites remain largely unaccounted for.

5.7 Appendix 5

5.7.1 Fractional crystallization modeling overview

The concentration of S (and eventually the other elements) is calculated throughout the evolution of a liquid melt using Eq. 1, in which F_n is the fraction of liquid (n = 100 is

pure liquid), C_{Ln} is the concentration of an element in the liquid phase at F_n, and D_n is the partition coefficient of an element. A constant partition coefficient of 0.001 is used for S (Walker et al., 2008). The partition coefficients for P and C are determined at each F_n by considering the concentration of S and P or S and C, respectively, in the liquid at F_{n+1}. Equation 2 is used to account for the effects of S on P and C partitioning behavior (Chabot and Jones, 2003), where values of D_o for P and C are taken from Chabot et al. (2017) and Worsham et al. (2016a), respectively. The "Fe domains" value, where X_i is the mole fraction of an element in the liquid, represents the conceptual combination of Fe metal, FeS, Fe_3P, and Fe_3C components in the liquid (Eq. 3; Chabot et al., 2017). This term is used with β, which represents the correlation between Fe domains and D values. The β_{SPC} variable is determined using Eq. 4 (Jones and Malvin, 1990), in which β_S and β_P are taken from Chabot et al. (2017) and β_C is taken from Worsham et al. (2016a). For P, the effects of C are not considered and for C, the effects of P are not considered. The β_{SPC} and "Fe domains" variables are calculated at each F_n.

After determining the concentration of S, P, and C at each F_n for a given initial S, P, and C content, the corresponding D values for the HSE are calculated using Eq. 2-4 (Jones and Malvin, 1990; Chabot and Jones, 2003; Worsham et al., 2016a; Chabot et al., 2017). After assuming an initial HSE composition, the concentration of HSE in the liquid at each F_n is then determined using Eq. 1 and the solid composition (C_{Sn}) crystallizing at each F_n is determined using Eq. 5. The composition of trapped melt (the liquid endmember in sold metal-liquid metal mixing) is then determined from C_{Ln} following the approach of Chabot (2019) for considering the effects of troilite formation. The

concentration of S in the liquid at each F_n is divided by 36.5 to determine the "x" value. The HSE concentrations of the trapped melt are determined by Eq. 6.

$$\text{Eq. 1: } C_{Ln-1} = \frac{C_{Ln}}{(F_{n-1} + 1 - F_{n-1}D_{n-1})}$$

$$\text{Eq. 2: } \frac{1}{D} = \frac{[\text{Fe domains}]^{\beta_{SPC}}}{D_o}$$

$$\text{Eq. 3: Fe domains} = \frac{1 - 2X_s - 4X_p - 4X_C}{1 - X_s - 3X_p - 3X_C}$$

$$\text{Eq. 4: } \beta_{SPC} = \left[\frac{2X_S}{2X_S + 4X_p + 4X_C}\right]\beta_S + \left[\frac{4X_p}{2X_S + 4X_p + 4X_C}\right]\beta_p + \left[\frac{4X_C}{2X_S + 4X_p + 4X_C}\right]\beta_C$$

$$\text{Eq. 5: } C_{Sn} = C_{Ln}D_n$$

$$\text{Eq. 6: } C_{\text{trapped melt}} = \frac{C_{Ln}}{(1 - x)}$$

These calculations are performed iteratively as the initial S, P, C, and HSE abundances are adjusted. The initial P and C contents are, to a first-order, constrained by applying the calculated D values for a given initial S content to the P and C contents, determined from modal analysis of phosphide and carbide inclusions (Buchwald, 1975), of the most primitive irons, which are assumed to crystallize within the first ~10 % of factional crystallization. Initial HSE abundances are then determined in a similar way by applying calculated D values for a given initial S, P, and C content to the HSE abundances of the same primitive irons. Ultimately, the initial S, P, C, and HSE parental melt contents are varied until a best fit to the measured HSE abundances is identified. Values for D_o, β_S, β_P, and β_C are allowed to vary within the 2σ uncertainties provided by Chabot et al (2017) in order to achieve the best model fit. In the event that there are multiple parental melt compositions that can account for the HSE data, the parental melt composition with relative abundances of HSE closest to the ranges observed in chondrites

is reported as the best-fit model (e.g., Hilton et al., in revision). Examples of predicted HSE patterns for solids and liquids produced during fractional crystallization with various initial S and P contents are shown in **Figs. A5.1** and **A5.2**).

5.7.2 Fractional crystallization modeling of IIAB irons

Conflicting initial S, P, and C contents of the IIAB liquid have been previously proposed, ranging from as low as 6 wt. % S and 1.5 wt. % P, to as great as 16 to 18 wt. % S and 1 wt. % P (Chabot, 2004; Wasson et al., 2007; Goldstein et al., 2009). We find that the HSE abundances of the IIAB irons are best explained by an initial parental melt composition of 20 wt. % S, 0.5 wt. % P, <0.05 wt. % C. Using these initial parameters, the IIAB irons can be accounted for as solids produced as a result of fractional crystallization from a primary initial melt characterized by Re, Os, Ir, Ru, Pt, and Pd abundances of 150, 1700, 1700, 2600, 4100, and 2100 ppb, respectively (**Fig. A5.3**). Comparisons of the HSE abundances of the IIAB irons to a system with 6 wt. % S and 1.5 wt. % P are shown in **Fig. A5.4**. This model does not properly account for the Pd abundances of the IIAB irons, indicating that this initial S content is too low to account for the HSE systematics of the IIAB irons, or partitioning behavior that is different from experimental observations.

5.7.3 Fractional crystallization modeling of IID irons

Wasson and Huber (2006) interpreted the observations of low FeS abundances in the most chemically evolved IID irons (i.e., Needles and Wallapai) to mean that solid metal-liquid metal mixing was negligible, and determined that the parental melt S content of the

IID irons was 0.7 wt. %, in order for Wallapai to be produced as a solid directly by fractional crystallization. In contrast to this conclusion, Goldstein et al. (2009) determined that the Ir, Au, and Ga abundances of the IID irons were most consistent with a parental melt S content of 6 to 12 wt. %. The HSE abundances of the IID irons are most consistent with crystallization from a melt with ~10 wt. % S, 1 wt. % P, <0.05 wt. % C, and Re, Os, Ir, Ru, Pt, and Pd abundances of 370, 4400, 4100, 6300, 8000 and 4300 ppb, respectively (**Fig. A5.5**). For this model, five of the 12 studied IID irons are accounted for as solids formed directly by fractional crystallization. The other seven irons require various amounts of equilibrium solid metal-liquid metal mixing, ranging from mixing of initial solid and liquid, to mixing of solid and liquid produced after 25 % of crystallization. Comparisons of HSE abundances to the Wasson and Huber (2006) model with a parental melt abundance of 0.7 wt. % S are shown in **Fig. A5.6**. While a parental melt composition with 0.7 wt. % S can account for the Re and. Pd abundances of the IID irons, it fails to account for abundances of the other HSE, making this initial composition unlikely.

5.7.4 Fractional crystallization modeling of IIIAB irons

Although large-scale variations in siderophile element abundances are broadly consistent with fractional crystallization, many of the highly evolved IIIAB iron meteorites or Cape York suite cannot be explained as direct products of it (e.g., Cook et al., 2004). This has led to numerous explanations of their origins, including division of the core into separate magma chambers by early formed dendrites (Haack and Scott, 1993), crystallization from immiscible S-rich and P-rich liquids (Ulff-Møller, 1998),

equilibrium mixing of solids and trapped liquids by diffusion (Wasson, 1999; Chabot, 2019), and non-equilibrium mixing of primitive solids with evolved liquids (Cook et al., 2004). Further, past studies have also proposed parental melt S contents for the IIIAB irons ranging from 1.4 to 12 wt. % (Willis and Goldstein, 1982; Jones and Drake, 1983; Haack and Scott, 1993; Ulff-Møller, 1998; Chabot and Drake, 1999; Wasson, 1999; Wasson and Richardson, 2001; Chabot, 2004, 2019; Goldstein et al., 2009). Here, the HSE abundances of five of the IIIAB irons with limited fractionations of HSE were modeled. The best fit model is characterized by initial parameters of 12 wt. % S, 0.2 wt. % P, <0.05 wt. % C, and Re, Os, Ir, Ru, Pt, and Pd abundances of 260, 2800, 2800, 4400, 5900, and 3100 ppb, respectively. Using this parental melt composition, two of the five examined IIIAB irons can be explained as direct products of fractional crystallization while the others likely required additional processes, such as equilibrium solid metal-liquid metal mixing (**Fig. A5.7**). The HSE abundances of the IIIAB iron meteorites are compared to a model using 1.4 wt. % S in **Fig. A5.8**. As highlighted by the Re *vs*. Pd systematics, the IIIAB iron meteorites are not consistent with crystallizing from a parental melt with a S content this low.

5.7.5 Fractional crystallization modeling of IIIF irons

The IIIF irons examined have HSE abundances that can largely be accounted for by a simple fractional crystallization model, with most representing equilibrium solids (**Fig. A5.9**). The best fit model is characterized by initial parameters of 5 wt. % S, 1 wt. % P, and <0.05 wt. % C, as well as Re, Os, Ir, Ru, Pt, and Pd abundances of 275, 3600, 3100, 4300, 6100, and 4000 ppb, respectively. The IIIF iron Klamath Falls deviates slightly

from the solid metal HSE evolution curves, suggesting it may have been affected by an additional process, such as equilibrium solid metal-liquid metal mixing.

5.7.6 Assessment of uncertainties

Potential sources of uncertainties when modeling parental melt HSE, S, P, and C contents include uncertainties from measured HSE abundances as well as uncertainties on experimentally-determined D values. As uncertainties on HSE abundances are <3 %, the dominant sources of uncertainties for this modeling are from D_o, β_S, β_P, and β_C values, the uncertainties on which range from 4 to 9 %, 4 to 10 %, 12 to 69 %, and 23 to 133 %, respectively (Chabot et al., 2017). To assess the effect of these uncertainties on the calculation of D values, the maximum and minimum values of the 2σ expansions of error on D_o, β_S, β_P, and β_C values are applied to the fractional crystallization model of the IIIF iron meteorites (**Fig. A5.10**). Results of varying these values within the 2σ ranges indicate that some elements (e.g., Re, Ru, and Pd) provide better constraints on parental melt composition than others, due to differences in the uncertainties on HSE D values. The greatest variations are observed when coupling two elements together (e.g., Re/Os and Pt/Os).

The results of varying S content on parental melt modeling is shown in **Fig. A5.11**. Typically, most scatter around a given fractional crystallization model is accounted for by a parental melt S content uncertainty of ±1.5 wt. % (Chabot, 2004). As highlighted in **Fig. A5.11**, adjusting the parental melt S content by ±1.5 wt. % results in corresponding changes to the HSE concentration of the initial solid. In order to keep the concentration of the initial solid consistent between all models within ±1.5 wt. % S, in the case of the IIIF

irons, requires adjusting the parental melt Re, Os, Ir, Ru, Pt, and Pd content by ±18 %, ±21 %, ±19 %, ±14 %, ±16 %, and ±3 %, respectively. These percentages are interpreted to be representative of the uncertainties on HSE parental melt compositions for the IIAB, IID, IIIAB, and IIIF iron meteorites.

Table A5.1. Comparison of HSE abundances to previous studies.

Sample	Re	Re (literature)	Os	Os (literature)	Ir	Ir (literature)	Ru	Ru (literature)	Pt	Pt (literature)	Pd	Pd (literature)
IIAB irons												
Forsyth County	3700	4044[a]	44554		39270	40400[a]	27300		37610	35100[a]	1754	
Cincinnati	1530	172 [a]	13199		19940	20300[a]	24070		33330	30000[a]	1757	
Braunau	772.5	877[a]	5445.9		11020	11300[a]	17680		30080	30400[a]	1820	
North Chile	208.8	212[a], 199.61[b]	1067.5	1033.4[b]	3585	3430[a]	15810		26590	21800[a], 25340[b]	2006	
Sikhote-Alin	1.528	<30[a]	12.110		23.08	24[a]	4862		5377	5500[a]	2449	
IID irons												
NEA 002	1960	2150[c]	28741		21480	22600[c]	16990	20300[c]	22310	22400[c]	2774	
Arltunga	1914	2070[c]	26255		20540	20600[c]	17220	19800[c]	23180	21600[c]	2868	
Losttown	1912	2020[c]	26303		20490	20700[c]	17340		22660	19300[c]	2988	
N'Kandhla	1779	1940[c]	23869		19160	19600[c]	16970		22780	19900[c]	2959	
Bridgewater	1767	2020[c]	23628		19100	19700[c]	17000		22880	22000[c]	2950	
Mount Ouray	1586	1740[c]	20594		17240	17800[c]	16510		22550	23000[c]	3280	
Elbogen	1415	1580[c]	18114		15570	15900[c]	15080		20700	19000[c]	2890	
Carbo	1292	1420[c]	15544		14080	14300[c]	16030		22080	22400[c]	3097	
Puquios	1263	1390[c]	16060		14190	14300[c]	15550		20500	19900[c]	3185	
Rodeo	754.1	1070[c]	9383.0		8726	10200[c]	12180		16690	15500[c]	3930	
Needles	453.8	510[c]	5056.0		5139	5370[c]	10200		14610	13300[c]	4935	
Wallapai	343.7	410[c]	3532.0		3830	3990[c]	9449		12530	11600[c]	5133	
IIIAB irons												
Costilla Peak	1421	1429.8[b]	18319	18675[b]	13750	14000[d]	12740		15870	17400[b], 13400[d]	3349	
Henbury	1287		15053		13630		13180		16670		2127	
Charcas	150.8	149.40[b]	1082.3	1090.9[b]	2240		8411		12110	12530[b]	2619	
Tamarugal	33.88	36.104[b]	235.30	255.19[b]	562.6	570[d]	4854		7624	7859[b], 6300[d]	3336	
Maldyak	25.37		167.01		462.5		4602		7148		4325	
IIIF irons												
Nelson County	794.8		11970		8650		7064		10310		2517	
Clark County	665.1		9271.0		7240		6747		10150		2681	
Oakley	507.2		6500.8		5529		6307		9635		3016	
Cerro del Inca	282.9		2873.2		3251		6348		8719		3298	
St. Genevieve County	159.8		1345.7		1950		5651		8315		3554	
Moonbi	110.2		854.60		1398		5126		7611		3782	
Klamath Falls	0.2787		1.3166		3.229		1033		1455		5702	

[a]Wasson et al. (2007), [b]Cook et al. (2004), [c]Wasson and Huber (2006), [d]Wasson (1999), Schaudy et al. (1972), Scott and Wasson (1976), Pernicka and Wasson (1987), Grossman (2000).

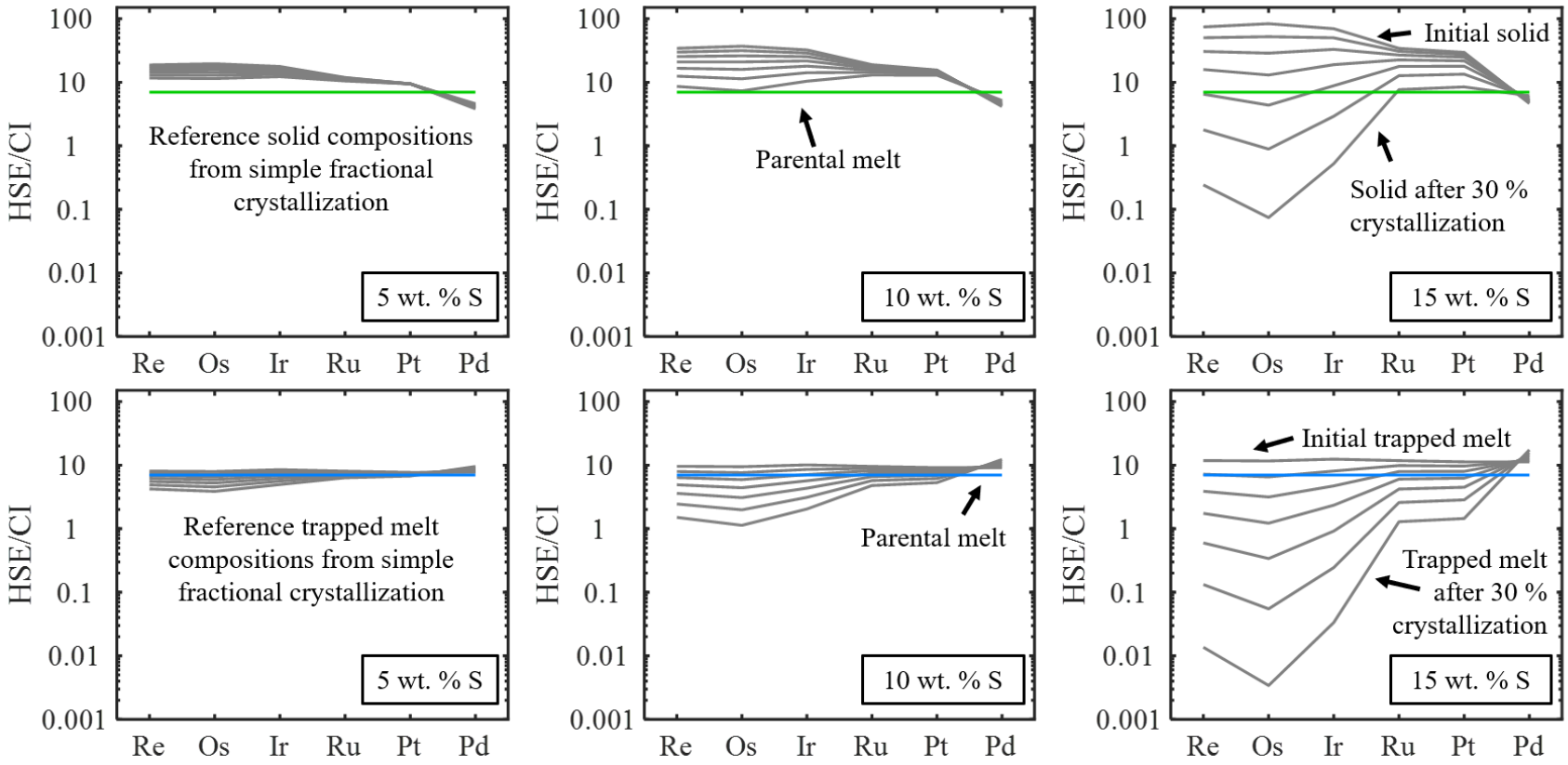

Fig. A5.1. Model HSE abundances, normalized to CI-chondrites (Horan et al., 2003), of solid and trapped melt produced at 5 % intervals between initial and 30 % fractional crystallization for three different S parental melt contents.

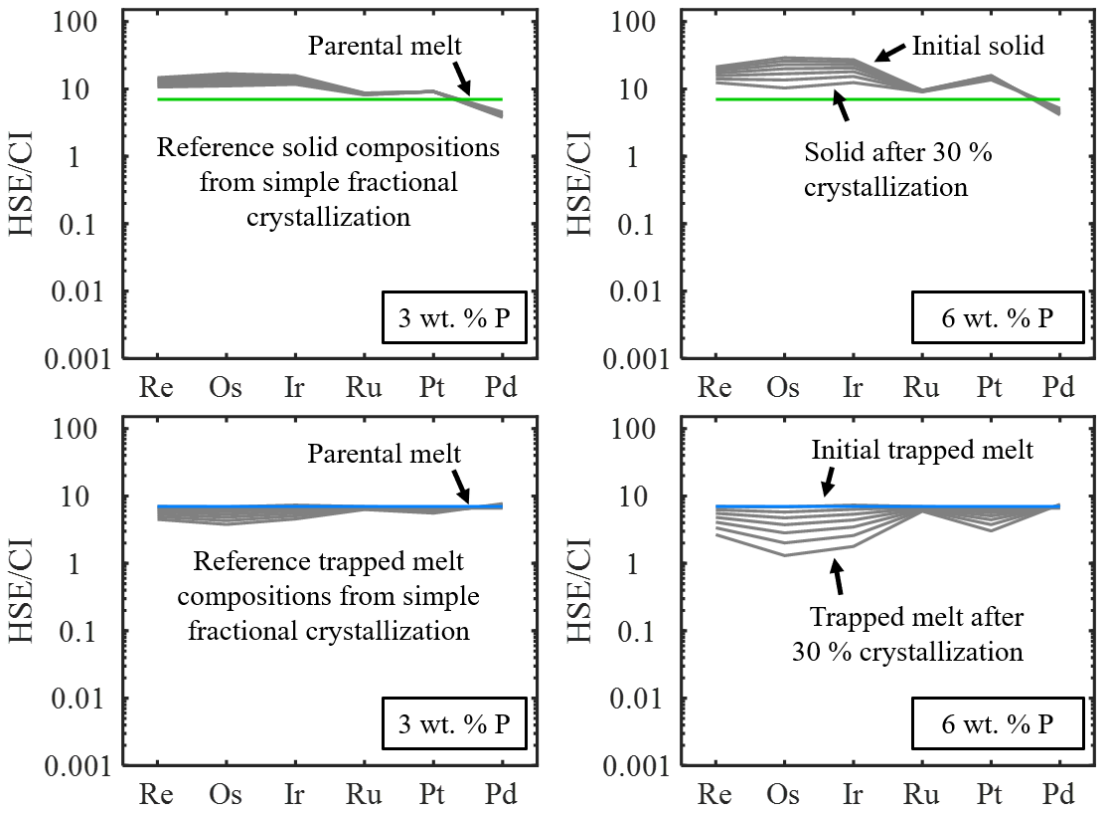

Fig. A5.2. Model HSE abundances, normalized to CI-chondrites (Horan et al., 2003), of solid and trapped melt produced at 5 % intervals between initial and 30 % fractional crystallization for two different P parental melt contents.

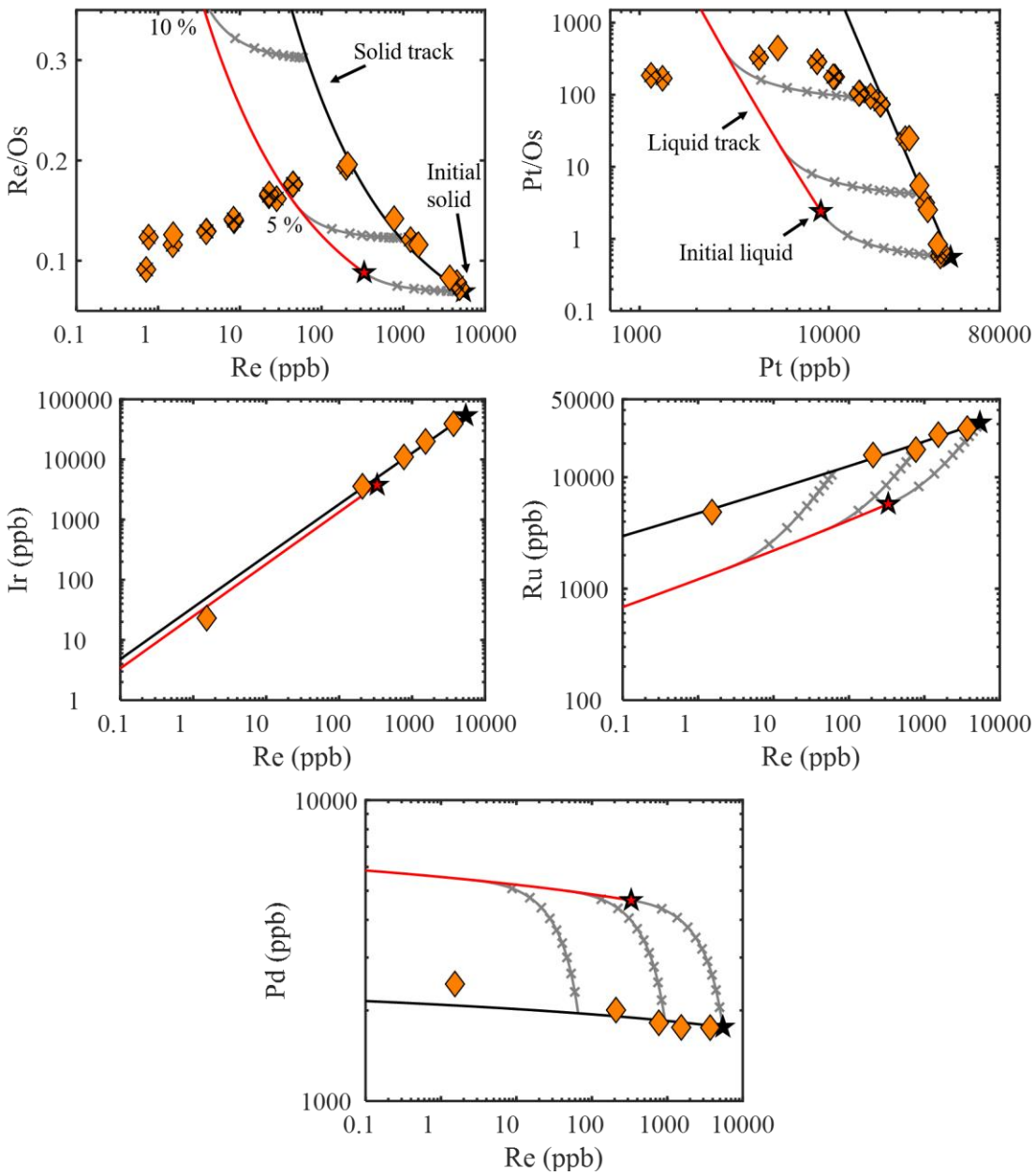

Fig. A5.3. Fractional crystallization model compared to the HSE abundances of IIAB irons (orange diamonds). Additional IIAB Re, Os, and Pt data from Cook et al. (2004) are shown as orange diamonds with black crosses. Solid metal and liquid metal evolution lines are shown in black and red, respectively. Initial solid and liquid compositions are shown as black and red stars, respectively. Grey lines reflect equilibrium mixing of solid and liquid at initial, 5 %, and 10 % crystallization steps. Tick marks on mixing lines reflect 10 % increments.

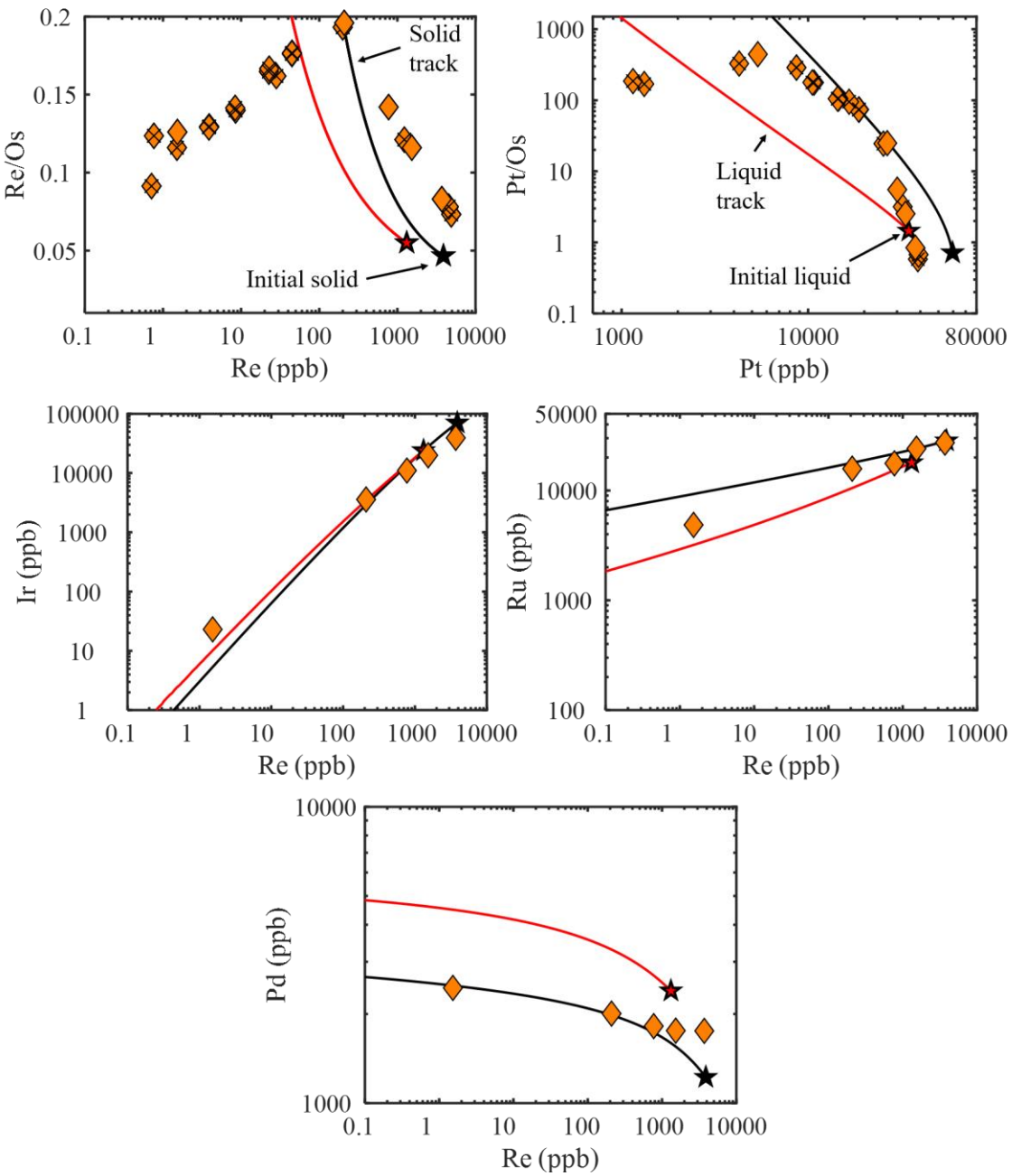

Fig. A5.4. Fractional crystallization model of 6 wt. % S and 1.5 wt. % P compared to the HSE abundances of IIAB irons (orange diamonds). Additional IIAB Re, Os, and Pt data from Cook et al. (2004) are shown as orange diamonds with black crosses. Solid metal and liquid metal evolution lines are shown in black and red, respectively. Initial solid and liquid compositions are shown as black and red stars, respectively.

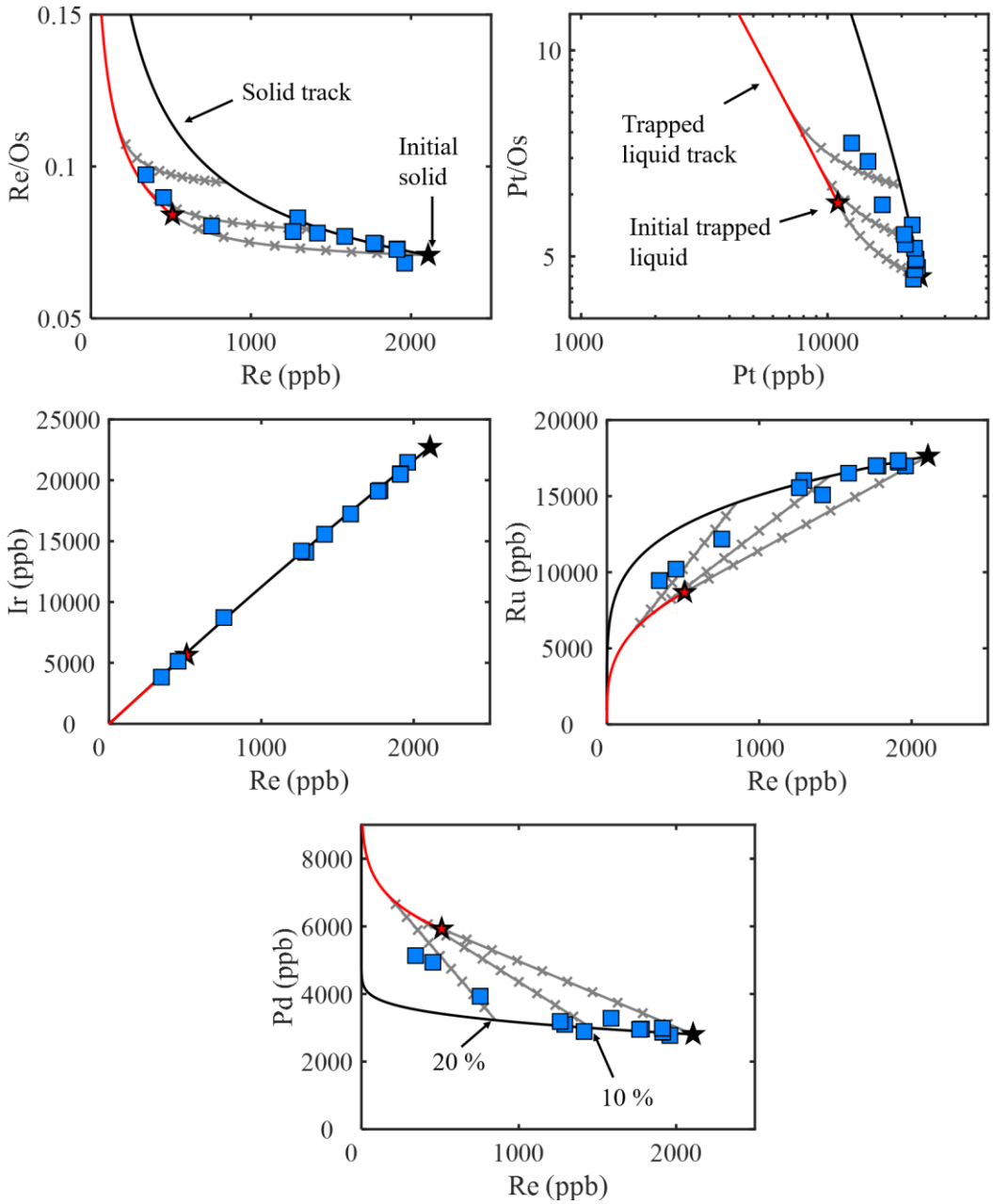

Fig. A5.5. Fractional crystallization model compared to the HSE abundances of IID irons (blue squares). Solid metal and liquid metal evolution lines are shown in black and red, respectively. Initial solid and liquid compositions are shown as black and red stars, respectively. Grey lines reflect equilibrium mixing of solid and liquid at initial, 10 %, and 20 % crystallization steps. Tick marks on mixing lines reflect 10 % increments.

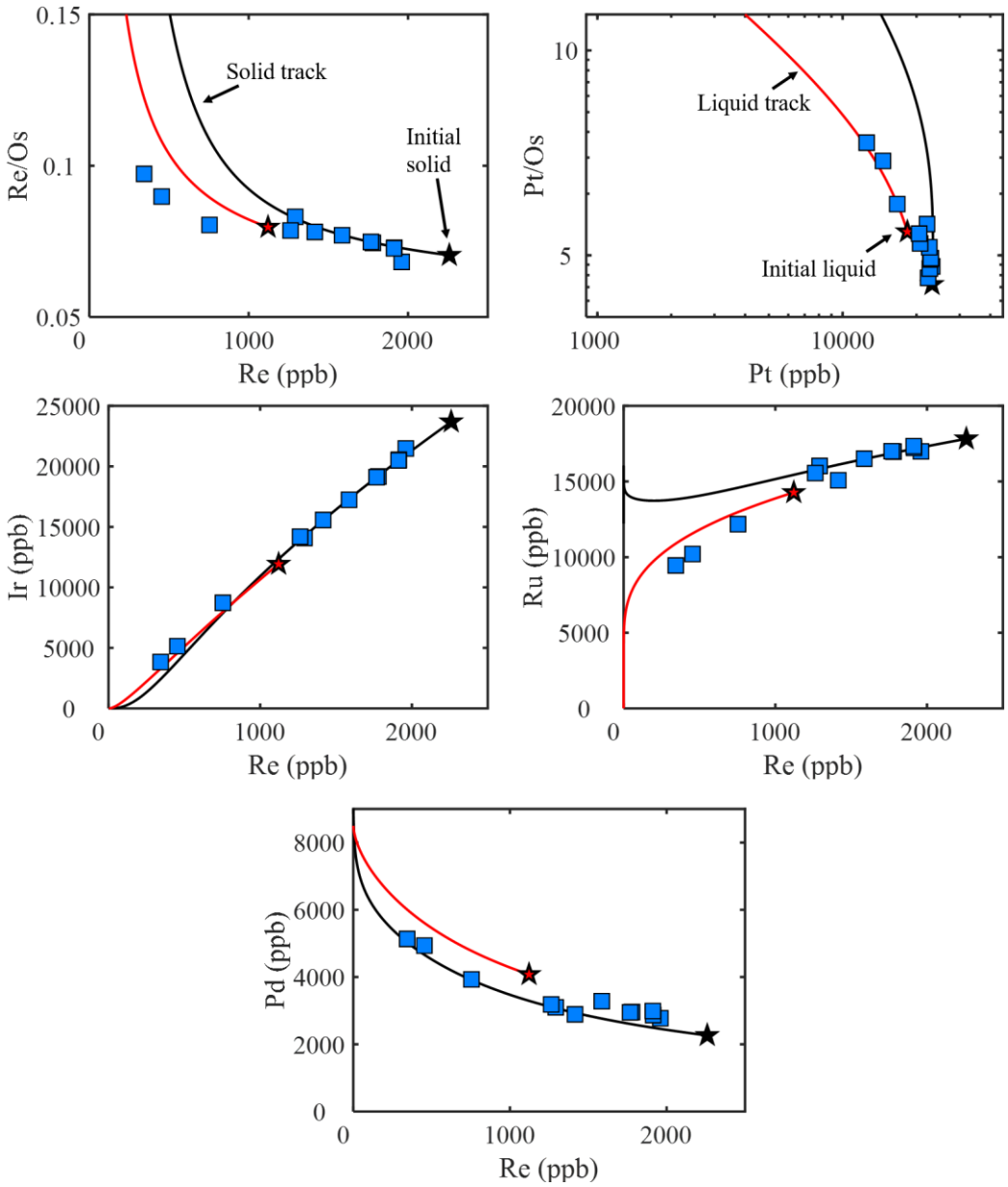

Fig. A5.6. IID fractional crystallization model assuming an initial S content of 0.7 wt. % (and corresponding 2 wt. % P) compared to the HSE abundances of IID irons (blue squares). Solid metal and liquid metal evolution lines are shown in black and red, respectively. Initial solid and liquid compositions are shown as black and red stars, respectively.

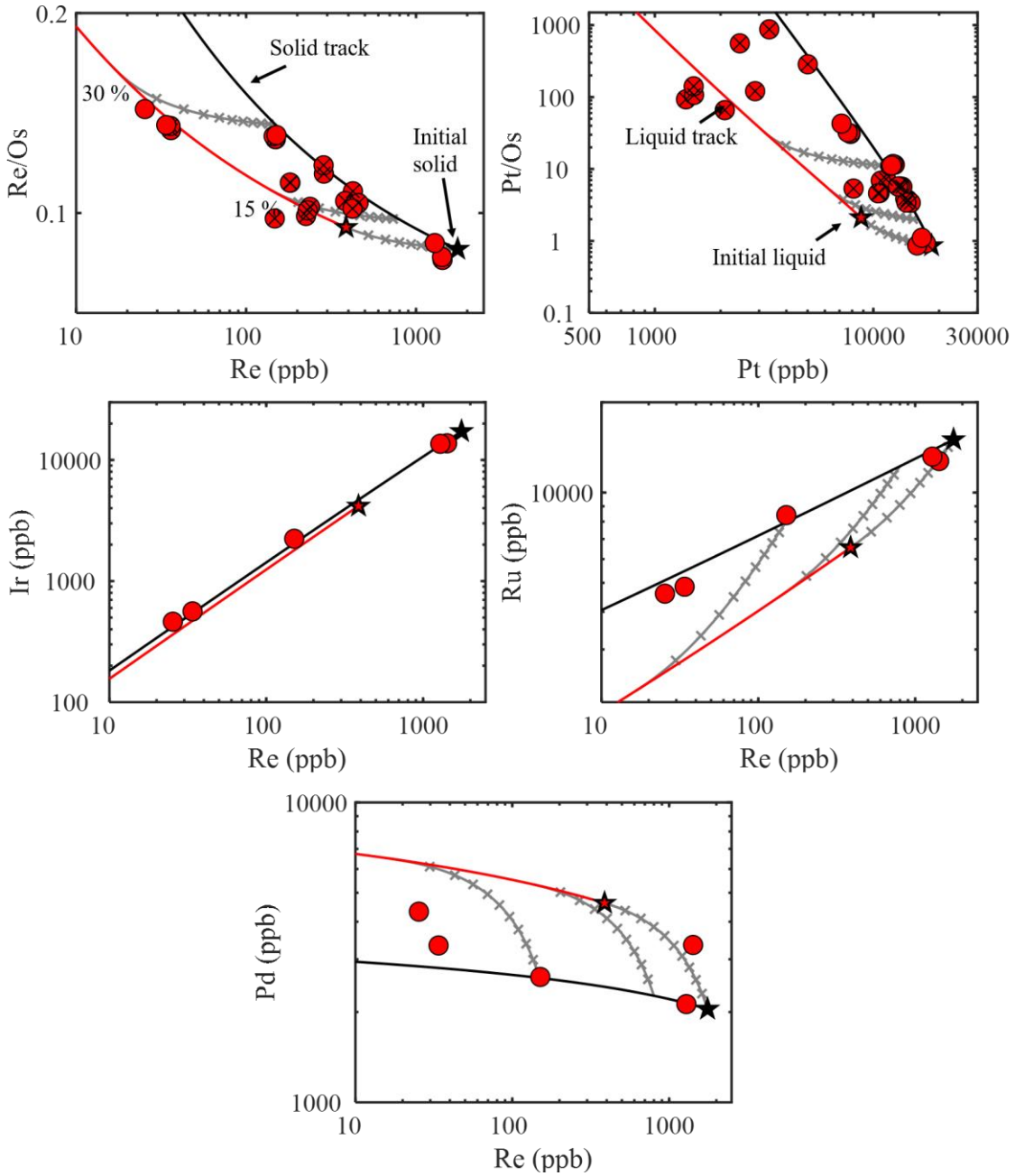

Fig. A5.7. Fractional crystallization model compared to the HSE abundances of IIIAB irons (red circles). Additional IIIAB Re, Os, and Pt data from Cook et al. (2004) are shown as red circles with black crosses. Solid metal and liquid metal evolution lines are shown in black and red, respectively. Initial solid and liquid compositions are shown as black and red stars, respectively. Grey lines reflect equilibrium mixing of solid and liquid at initial, 15 %, and 30 % crystallization. Tick marks on mixing lines reflect 10 % increments.

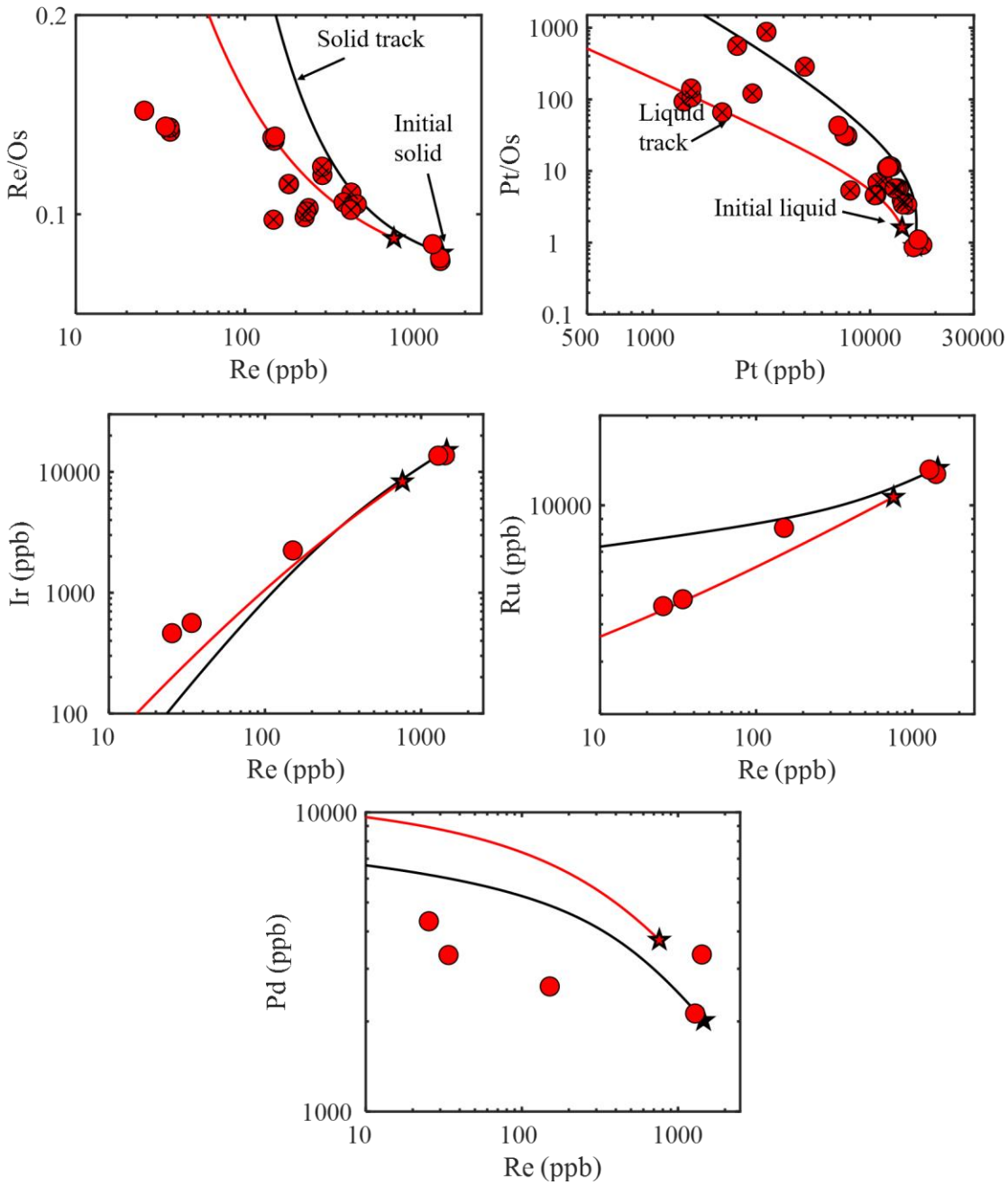

Fig. A5.8. Fractional crystallization model of 1.4 wt. % S compared to the HSE abundances of IIIAB irons (red circles). Additional IIIAB Re, Os, and Pt data from Cook et al. (2004) are shown as red circles with black crosses. Solid metal and liquid metal evolution lines are shown in black and red, respectively. Initial solid and liquid compositions are shown as black and red stars, respectively.

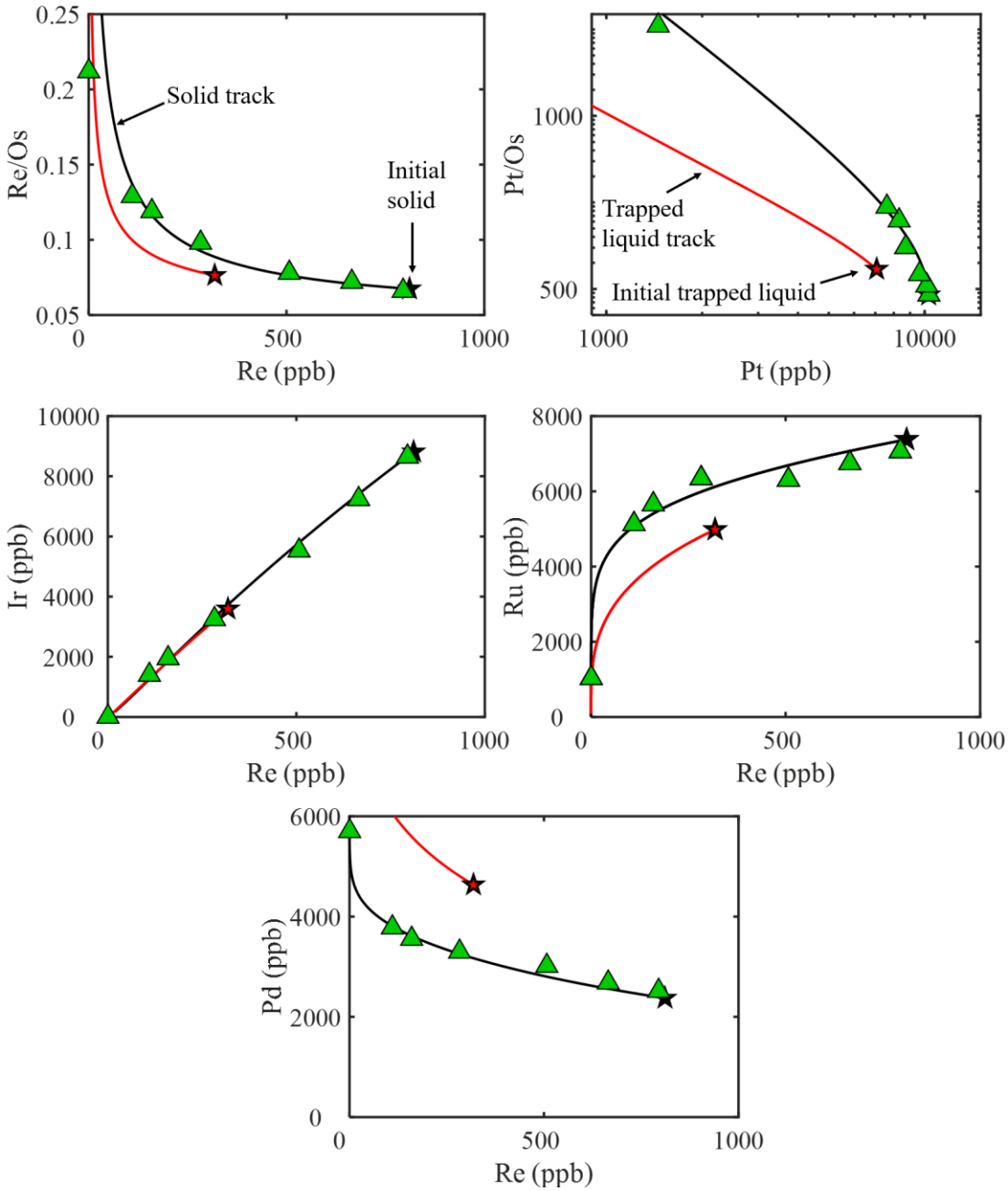

Fig. A5.9. Fractional crystallization model compared to the HSE abundances of IIIF irons (green triangles). Solid metal and liquid metal evolution lines are shown in black and red, respectively. Initial solid and liquid compositions are shown as black and red stars, respectively.

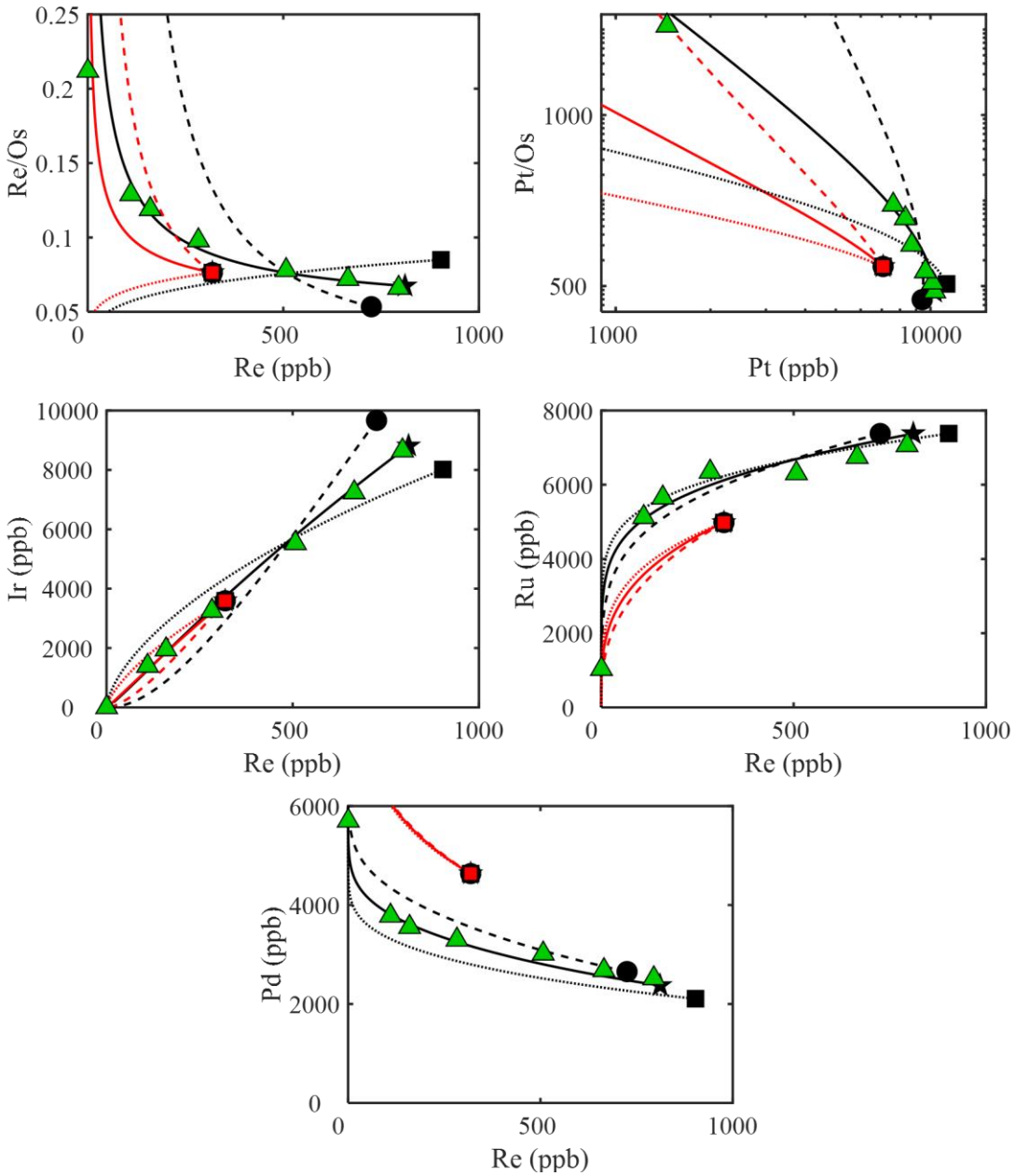

Fig. A5.10. The fractional crystallization model of the IIIF iron meteorites (solid lines) compared to models using the minimum and maximum expansion of 2σ uncertainties on D_o, β_S, β_P, and β_C values (Chabot et al., 2017). Solid metal and liquid metal evolution lines are shown in black and red, respectively. Initial solid and liquid compositions are shown as black and red symbols, respectively.

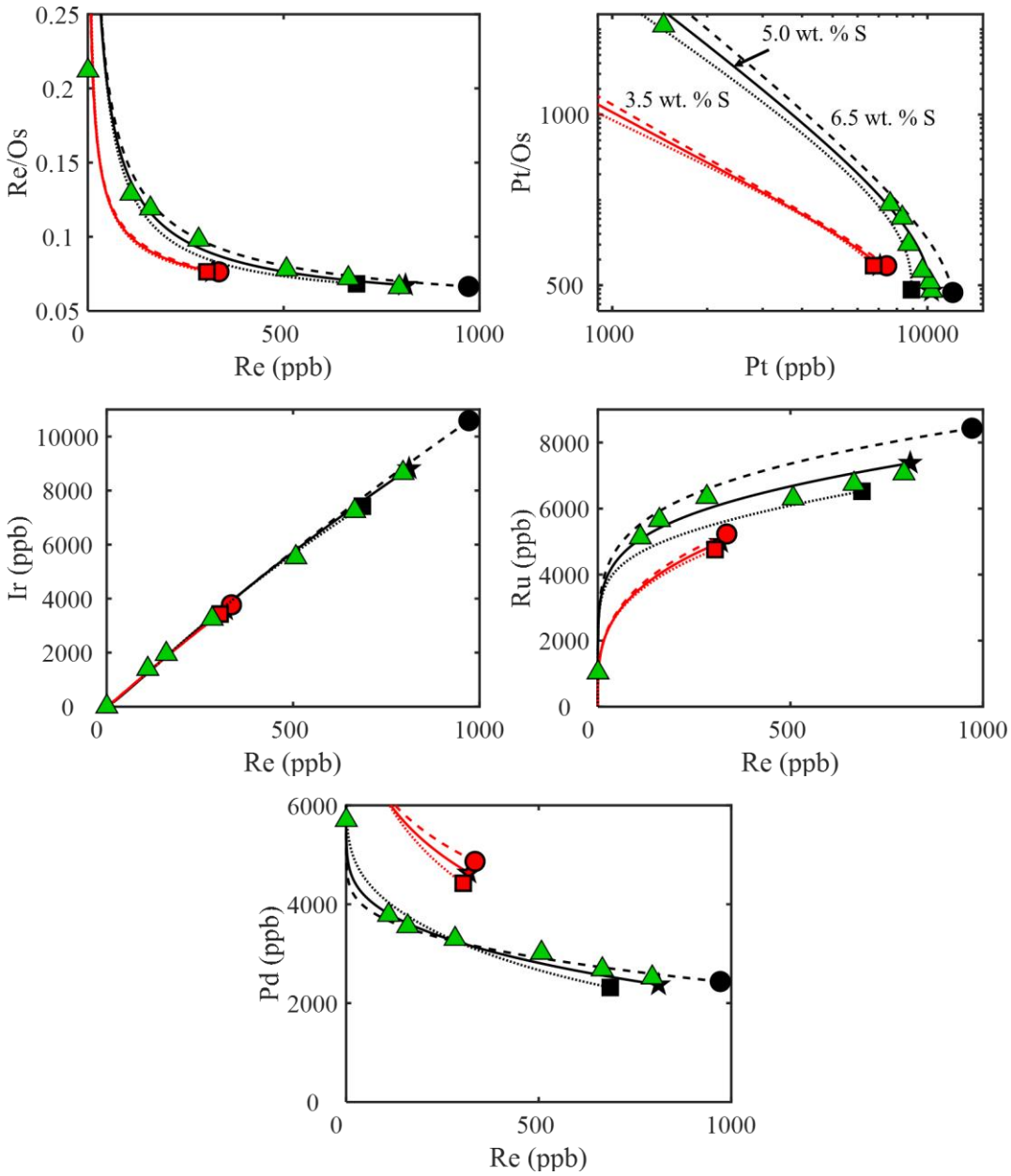

Fig. A5.11. The fractional crystallization model of the IIIF iron meteorites (solid lines) compared to models using parental melt S contents of 3.5 and 6.5 wt. % (5±1.5 wt. % S range). Solid metal and liquid metal evolution lines are shown in black and red, respectively. Initial solid and liquid compositions are shown as black and red symbols, respectively.

Chapter 6: Decoupled variations in the genetics and ages of iron meteorites from the noncarbonaceous (NC) and carbonaceous (CC) reservoirs

6.1 Abstract

Potential relationships between radiogenic W isotopic compositions and genetic Mo isotopic compositions of iron meteorites from the noncarbonaceous (NC) and carbonaceous (CC) reservoirs are explored. New Mo and W isotopic data for six ungrouped iron meteorites are consistent with a relationship between radiogenic W isotopic compositions and genetic Mo isotopic compositions for NC-type iron meteorites, while no relationship is apparent for CC-type iron meteorites. The meaning behind this observation remains unconstrained.

6.2 Introduction

Studies coupling various nucleosynthetic isotopic compositions of bulk meteorites have shown that two isotopically distinct reservoirs, referred to as the noncarbonaceous (NC) and carbonaceous (CC) reservoirs, were present in the early Solar System (e.g., Warren, 2011). While this observation was initially limited to silicate-bearing meteorites, studies over the last five years have expanded the understanding of isotopic variations between and within these reservoirs for siderophile (iron-loving) elements (e.g., Budde et al., 2016a; Poole et al., 2017; Worsham et al., 2017, 2019; Bermingham et al., 2018; Ek et al., 2019; Nanne et al., 2019). This has allowed for further study of the origins and evolution of the NC and CC reservoirs through iron meteorites.

Iron meteorites have proven particularly useful for studying the origins of the NC and CC reservoirs since the process of melting portions of a planetary body to cause metal-silicate segregation and iron meteorite formation homogenizes the various, isotopically diverse precursor materials in a planetesimal. As such, nucleosynthetic, "genetic" isotopic compositions of iron meteorites provide constraints on the bulk genetic isotopic compositions of the planetary bodies from which they were derived. In addition, the timing of metal-silicate segregation leading to iron meteorite formation can be constrained by the ^{182}Hf-^{182}W chronometer (e.g., Kruijer et al., 2014a). In some cases, this timing can then be translated into an accretion age of the planetesimal (e.g., Kruijer et al., 2017).

Most attention by past studies has been paid to grouped iron meteorites, which consist of, at minimum, five iron meteorites that can be chemically related to a common metal liquid (Wasson, 1974). Currently, 13 iron meteorite groups, consisting of the IAB-complex, IC, IIAB, IIC, IID, IIE, IIF, IIG, IIIAB, IIIE, IIIF, IVA, and IVB iron meteorites, are known based on this criteria. Due to the ability to compare chemical compositions of multiple iron meteorites from a common group, grouped iron meteorites can then be classified as "magmatic" or "nonmagmatic" based largely on whether chemical compositions can be accounted for by fractional crystallization processes or not, respectively (e.g., Scott, 1972; Wasson and Kallemeyn, 2002). Magmatic iron meteorites are interpreted to sample fragments of planetary cores while nonmagmatic iron meteorites have been interpreted to be products of partial differentiation and/or impact melting/mixing of a planetesimal (Kracher, 1985; Benedix et al., 2000; Wasson and

Kallemeyn, 2002; Worsham et al., 2016a, 2017; Kruijer and Kleine, 2019; Hilton and Walker, 2020).

Less attention has been paid to "ungrouped" iron meteorites, of which there are currently over 100. Ungrouped iron meteorites likely sample >20 distinct parent bodies. While constraining the origin of ungrouped meteorites as magmatic or nonmagmatic is problematic without the chemical context provided by additional group members, ungrouped irons nevertheless provide important new insights to the genetics and ages of NC- and CC-type planetary bodies. As such, six ungrouped iron meteorites are targeted here to assess the extent of isotopic heterogeneity observed among NC- and CC-type planetary bodies as well as constrain the relative timing of metal-silicate segregation occurring on these bodies.

6.3 Methods

Chunks of ungrouped iron meteorites Chinga, Santiago Papasquero, Sombrerete, Tishomingo, and Willow Grove were obtained from the Smithsonian Institution, Department of Mineral Sciences, National Museum of Natural History, and a chunk of Auburn was obtained from Arizona State University. Pieces were cut from each meteorite chunk using a water-cooled *Leco Vari-cut* saw and a 12.7 cm diamond-wafering blade. The blade was cleaned with SiC blocks prior to cutting each meteorite. The surface of each cut meteorite piece was polished using a range of coarse- to fine-grit SiC sandpaper to remove sawblade marks, and then sonicated multiple times in ethanol.

Pieces of each iron meteorite were dissolved using 40 mL 8M HCl per gram metal at 130 °C for 72 hours in Teflon® beakers. The resulting solutions were then processed

using the methods discussed by Hilton et al. (2019) and Hilton and Walker (2020) (Chapters 2 and 3 of this dissertation, respectively). In brief, aliquots of solution were removed for Os isotopic measurements and processed using a Carius Tube method, a CCl_4 solvent-extraction method, and a microdistillation method (Shirey and Walker, 1995; Cohen and Waters, 1996; Birck et al., 1997). The remaining solution was processed through the W column chemistry procedure of Touboul and Walker (2012). The primary cation exchange column was repeated until Fe was significantly separated from the solution. The sample was then processed through an anion exchange column, in which W, Mo, and Pt were separately eluted. Tungsten and Mo were then each processed through two additional anion exchange columns following methods outlined by Touboul and Walker (2012) and Worsham et al. (2016b), respectively, while Pt was processed through a single anion exchange column following the method of Hunt et al. (2017b). Isotopic compositions for Os, W, and Mo were measured by TIMS, while isotopic compositions for Pt were measured by MC-ICP-MS.

Analytical uncertainty was assessed by measuring standard solutions multiple times during an analytical campaign and assigning either the two-standard deviation (2SD) value for the standards or the 2SE value of the samples, whichever were greater. Reproducibility (2SD) of the Johnson Matthey Os standard over three analytical campaigns ranged from $^{189}Os/^{188}Os$ = 5 to 7 ppm and the reproducibility (2SD) of the *Alfa Aesar Specpure*® W standard over five analytical campaigns ranged from $^{182}W/^{184}W$ = 4 to 9 ppm and $^{183}W/^{184}W$ = 3 to 8 ppm (186/184 normalized). The reproducibility (2SD) of the *Alfa Aesar Specpure*® Mo standard over five analytical campaigns ranged from $^{94}Mo/^{96}Mo$ = 7 to 45 ppm, $^{95}Mo/^{96}Mo$ = 8 to 24 ppm, and $^{97}Mo/^{96}Mo$ = 3 to 9 ppm

and the reproducibility (2SD) of a Pt standard made from a high purity Pt ribbon over a single analytical campaign was $^{196}Pt/^{195}Pt$ = 7 ppm. Results of isotopic measurements are reported in μ units (part per million difference in the isotopic ratio of a sample compared to a standard).

6.4 Results

It is important to monitor cosmic ray exposure (CRE) and, when necessary, correct for its effects when reporting certain isotopic compositions of meteorites. Exposure to galactic cosmic rays results in nuclear reactions within meteorites that cause creation and burnout of, for example, ^{182}W isotopes (e.g., Masarik, 1997; Leya et al., 2003). Measuring Os or Pt isotopes in the same meteorite aliquot being studied for Mo or W isotopic composition has proven useful to monitor and correct for CRE (Kruijer et al., 2017; Worsham et al., 2017). For this, the $^{189}Os/^{188}Os$ and $^{196}Pt/^{195}Pt$ ratios are the most sensitive to CRE effects and increasingly greater CRE effects result in increasingly negative $\mu^{189}Os$ values and increasingly positive $\mu^{196}Pt$ values. The $\mu^{189}Os$ and $\mu^{196}Pt$ values of the ungrouped irons range from -33 ± 6 to +7 ± 6 and +10 ± 7 to +48 ± 7, respectively (**Table 6.1**). Based on the 2SD reproducibility of the $^{189}Os/^{188}Os$ ratio (±5 to 8 ppm) and the $^{196}Pt/^{195}Pt$ ratio (±7 ppm) of the terrestrial laboratory standards analyzed for this study, it is assumed that meteorite pieces with $\mu^{189}Os$ and $\mu^{196}Pt$ values within ±8 ppm and ±7 ppm, respectively, of zero were minimally affected by CRE. As such, Chinga, Santiago Papasquero, and Sombrerete are interpreted to be minimally affected by CRE, whereas corrections are necessary for Tishomingo and Willow Grove. The $\mu^{189}Os$

value of Auburn suggests it was minimally affected by CRE whereas its μ^{196}Pt value suggests a CRE correction is necessary.

Table 6.1. Osmium and Pt isotopic compositions of ungrouped iron meteorites.

Iron Meteorite	μ^{189}Os	μ^{196}Pt
NC-type		
Auburn	+7 ± 6	+13 ± 7
Santiago Papasquero	+0 ± 5	n.d.
CC-type		
Chinga	+1 ± 7	n.d.
Sombrerete	+4 ± 8	n.d.
Tishomingo	-9 ± 6	+10 ± 7
Willow Grove	-33 ± 6	+48 ± 7

The Mo and W isotopic compositions of the ungrouped iron meteorites are provided in **Tables 6.2** and **6.3**, respectively. The μ^{94}Mo values for these meteorite range from +62 ± 35 to +190 ± 17, μ^{95}Mo values from +25 ± 24 to +121 ± 7, and μ^{97}Mo values from +12 ± 3 to +51 ± 7. The measured μ^{182}W values (uncorrected for CRE) of the ungrouped irons range from -363 ± 7 to -282 ± 9, and the μ^{183}W values range from +2 ± 8 to +22 ± 4.

Table 6.2. CRE-uncorrected Mo isotopic compositions of ungrouped iron meteorites.

Sample	n[a]	μ^{92}Mo	μ^{94}Mo	μ^{95}Mo	μ^{97}Mo	μ^{100}Mo
NC-type						
Auburn	2	+157 ± 43	+118 ± 17	+46 ± 8	+24 ± 9	+49 ± 5
Santiago Papasquero	1	+95 ± 98	+62 ± 35	+25 ± 24	+12 ± 3	+34 ± 19
CC-type						
Chinga	3	+309 ± 59	+190 ± 17	+121 ± 7	+51 ± 7	+104 ± 28
Tishomingo	9	+210 ± 26	+141 ± 11	+99 ± 4	+46 ± 5	+75 ± 13
Willow Grove	4	+125 ± 21	+110 ± 10	+61 ± 6	+42 ± 3	+75 ± 5

[a] n is the number of analyses for Mo isotopic composition. The reported isotopic values reflect the average values obtained for each meteorite piece. Uncertainties reflect the largest (of n analyses) 2SD of the standards run during an analytical campaign ($n \leq 4$) or 2SE ($n > 4$) of the sample values.

Table 6.3. Tungsten isotopic compositions of ungrouped iron meteorites.

Sample	μ^{182}W	μ^{183}W	$\mu^{182}W_{CRE\text{-}corrected}$	$\mu^{182}W_{Nuclsyn\text{-}corrected}$	ΔT_{CAI}
NC-type					
Auburn	-351 ± 4	+4 ± 3	-334 ± 10	-334 ± 10	1.3 ± 0.9
Santiago Papasquero	-323 ± 8	+2 ± 8	-323 ± 8	-323 ± 8	2.3 ± 0.8
CC-type					
Chinga	-294 ± 6	+15 ± 7	-294 ± 6	-315 ± 12	3.1 ± 1.2
Sombrerete	-282 ± 9	+12 ± 5	-282 ± 9	-299 ± 11	4.8 ± 1.3
Tishomingo	-288 ± 8	+22 ± 4	-276 ± 12	-307 ± 13	3.9 ± 1.5
Willow Grove	-363 ± 7	+16 ± 4	-300 ± 12	-323 ± 13	2.3 ± 1.3

The μ^{182}W and μ^{183}W values are reported for each meteorite piece and the uncertainties reflect the 2SD of the standards run during an analytical campaign. The CRE-corrected μ^{182}W values represent the measured μ^{182}W values corrected for CRE, when necessary, using either μ^{189}Os or μ^{196}Pt values. The Nuclsyn-corrected μ^{182}W values represent the CRE-corrected μ^{182}W values corrected for nucleosynthetic anomalies, when necessary, using the μ^{183}W values (Kruijer et al., 2014b). The ΔT_{CAI} ages were calculated from the $\mu^{182}W_{Nuclsyn\text{-}corrected}$ values.

6.5 Discussion

6.5.1 Genetics

The heterogeneous accretion of isotopically diverse precursor materials among asteroids from the NC and CC reservoirs results in differences among the genetic isotopic compositions of some iron meteorites. For example, NC-type meteorites have Mo isotopic compositions that reflect a variable *s*-process depletion from terrestrial standards and W isotopic compositions that reflect no variations. By contrast, CC-type meteorites have Mo isotopic compositions that reflect even greater *s*-process depletions and Mo and W isotopic compositions that reflect an additional *r*-process component compared to terrestrial materials (Kruijer et al., 2017). The CRE assessed and, when necessary, corrected (**Table 6.4**) Mo isotopic compositions of Auburn, Chinga, Santiago Papasquero, Tishomingo, and Willow Grove fall within the ranges of Mo isotopic compositions defined by previously studied NC- and CC-type iron meteorites (**Fig. 6.1**). This is the same observation for the genetic $\mu^{183}W$ values of these meteorites (**Fig. 6.2**). Taken together, the Mo and W genetic isotopic compositions of Auburn and Santiago Papasquero indicate that these iron meteorites are derived from planetesimals that accreted in the NC reservoir whereas Chinga, Sombrerete, Tishomingo, and Willow Grove are derived from planetesimals that accreted in the CC reservoir.

Table 6.4. CRE-assessed Mo isotopic compositions of ungrouped irons.

Sample	μ^{92}Mo	μ^{94}Mo	μ^{95}Mo	μ^{97}Mo	μ^{100}Mo
NC-type					
Auburn	+157 ± 43	+118 ± 17	+46 ± 8	+24 ± 9	+49 ± 5
Santiago Papasquero	+95 ± 98	+62 ± 35	+25 ± 24	+12 ± 3	+34 ± 19
CC-type					
Chinga	+309 ± 59	+190 ± 17	+121 ± 7	+51 ± 7	+104 ± 28
Tishomingo	+221 ± 27	+146 ± 11	+104 ± 5	+47 ± 5	+76 ± 13
Willow Grove	+164 ± 23	+131 ± 12	+79 ± 7	+47 ± 5	+76 ± 5

Uncertainties include the uncertainties from the Mo isotopic compositions, Os isotopic compositions, and μ^{189}Os *vs*. μ^{x}Mo regressions reported by Worsham et al. (2017).

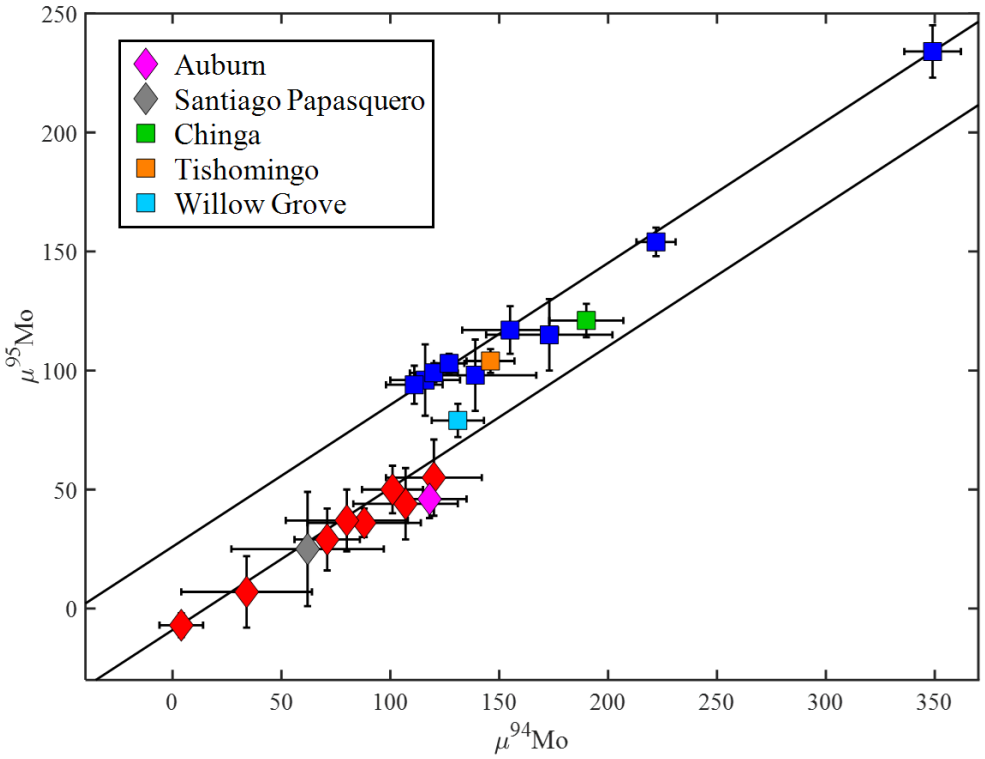

Fig. 6.1. Compilation of μ^{94}Mo *vs.* μ^{95}Mo data for iron meteorites from Kruijer et al. (2017), Poole et al. (2017), Worsham et al. (2017), Bermingham et al. (2018), and Hilton et al. (2019). Blue squares represent meteorites classified as CC type (including IIC, IID, IIF, IIIF, IVB, South Byron Trio (SBT), Wiley, Dronino, and Sombrerete), and red diamonds represent meteorites classified as NC type (including IC, IIAB, IIIAB, IIIE, IVA, IIE, IAB-MG, and Gebel Kamil). Black lines represent the NC and CC lines reported by Budde et al. (2019).

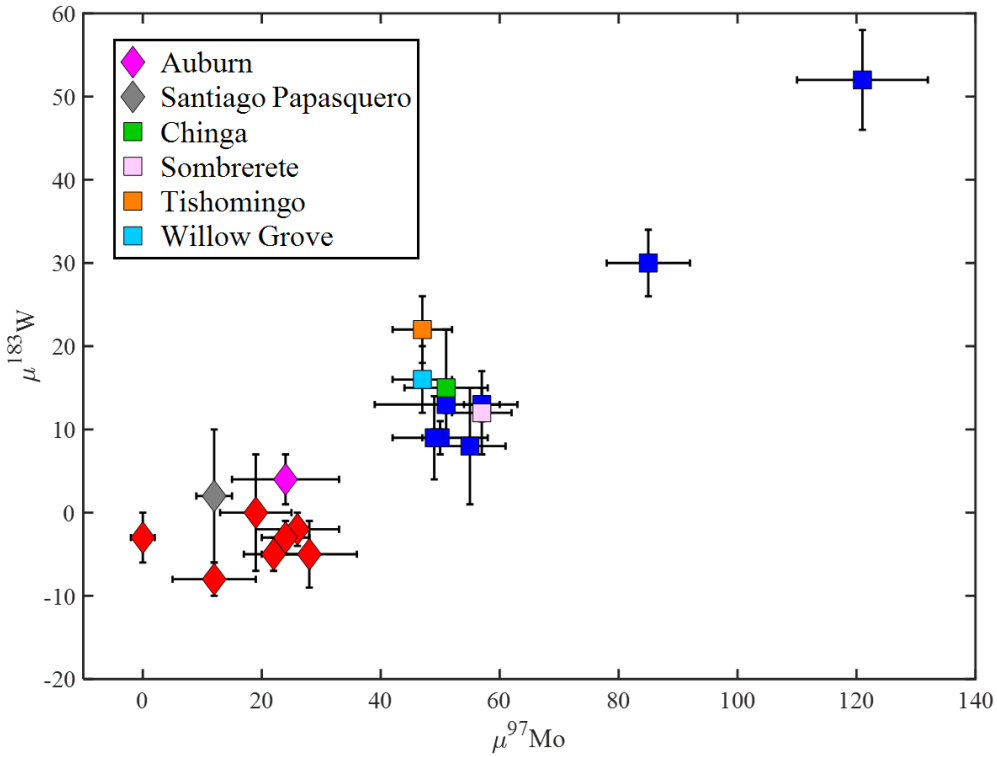

Fig. 6.2. Compilation of μ^{97}Mo *vs.* μ^{183}W data for iron meteorites from Kruijer et al. (2017), Worsham et al. (2017), Hilton et al. (2019), and Hilton and Walker (2020). Blue squares represent meteorites classified as CC type (including IIC, IID, IIF, IIIF, IVB, SBT, and Wiley) and red diamonds represent meteorites classified as NC type (including IC, IIAB, IIIAB, IIIE, IVA, IIE, and IAB-MG).

6.5.2 Ages

Ages of metal-silicate segregation (model ^{182}W age) leading to the formation of iron meteorites are commonly calculated using the ^{182}Hf-^{182}W chronometer, in which ^{182}Hf double beta decays to ^{182}W with a half-life of 8.9 Myr (Vockenhuber et al., 2004). During silicate-metal fractionation, Hf remains in silicate melt while W preferentially partitions into metallic melt. As such, the ^{182}W/^{184}W ratio of an iron meteorite is proportional to the relative amount of time since the start of the Solar System that iron meteorite formation occurred. Model ^{182}W ages are calculated using Eq. 1, in which the μ^{182}W value of Ca-Al-rich inclusions (CAI) is used as a proxy for the ^{182}W/^{184}W ratio of the initial Solar System and the μ^{182}W value of carbonaceous chondrites is used as a proxy for the present-day, bulk ^{182}W/^{184}W ratio of an asteroid.

$$\text{Eq. 1: } \Delta t_{CAI} = -\frac{1}{\lambda} \ln \left[\frac{\mu^{182}W_{Sample} - \mu^{182}W_{Chondrite}}{\mu^{182}W_{CAI} - \mu^{182}W_{Chondrite}} \right]$$

In order to calculate meaningful metal-silicate segregation ages from iron meteorites, measured μ^{182}W values of iron meteorites must first be corrected for CRE and nucleosynthetic anomalies, when necessary (e.g., Kruijer et al., 2017). Auburn, Tishomingo, and Willow Grove were corrected for effects of CRE using measured μ^{196}Pt values and the μ^{196}Pt *vs.* μ^{182}W regression reported by Kruijer et al. (2017) and CRE-assessed μ^{182}W values of Chinga, Sombrerete, Tishomingo, and Willow Grove were corrected for effects of nucleosynthetic anomalies, assessed by μ^{183}W anomalies, using the μ^{183}W *vs.* μ^{182}W regression reported by Kruijer et al. (2014b) (**Table 6.3**). Ages of metal-silicate segregation were then calculated from these corrected μ^{182}W values (**Table 6.3**). If NC- and CC-type iron meteorite parent bodies have a constant parental Hf/W ratio, then the metal-silicate segregation ages of most of the ungrouped iron meteorites

examined in this study are not resolved (**Fig. 6.3**). Only the NC-type Auburn has a resolved older age than the CC-type Sombrerete. If the parental Hf/W ratio of these parent bodies was identical to that of the CC-type carbonaceous chondrites, then these iron meteorites formed between 1.3 ± 0.9 to 4.8 ± 1.3 Myr after CAI formation.

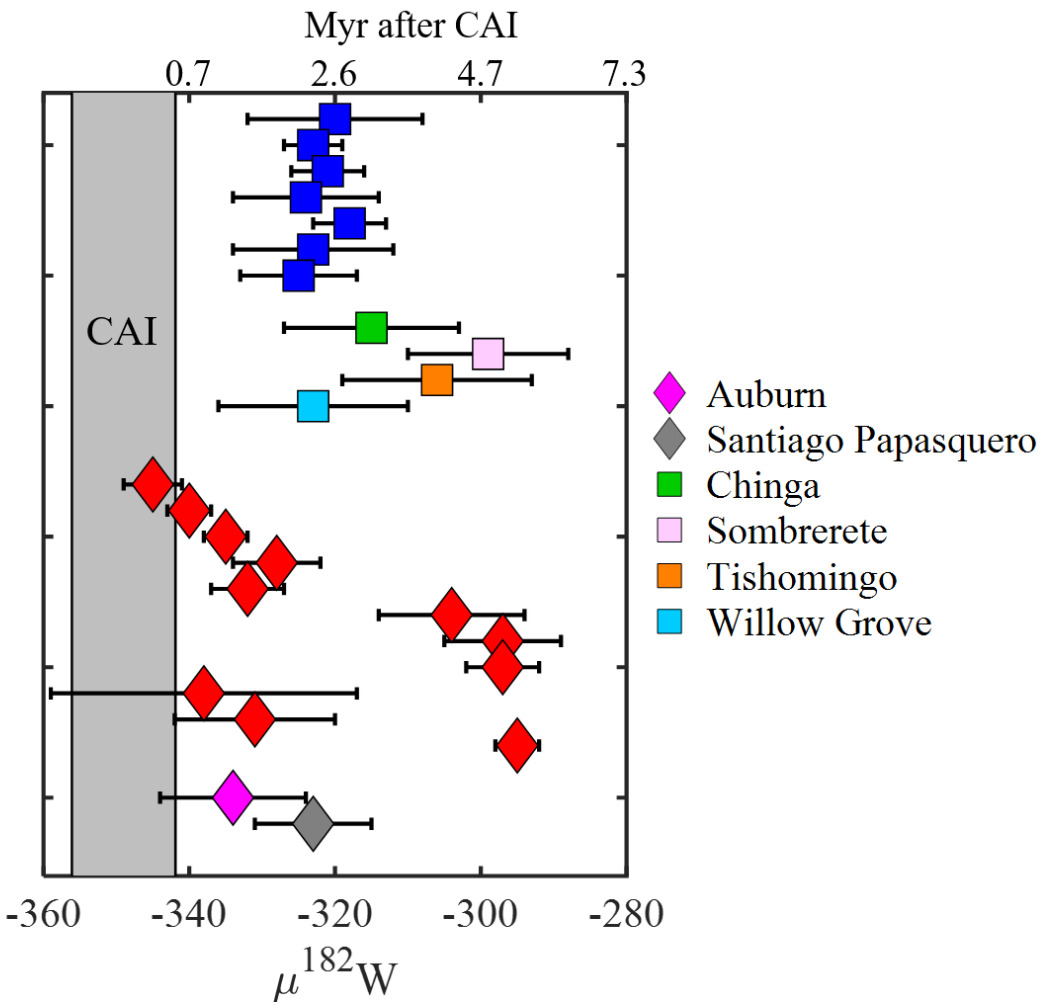

Fig. 6.3. Compilation of $\mu^{182}W$ values and model ^{182}W metal-silicate segregation ages (post CAI formation in Myr assuming carbonaceous chondrite parental Hf/W ratio) for iron meteorites from Kruijer et al. (2017), Worsham et al. (2017), Hilton et al. (2019), and Hilton and Walker (2020). Blue squares represent meteorites classified as CC type (including IIC, IID, IIF, IIIF, IVB, SBT, and Wiley) and red diamonds represent meteorites classified as NC type (including IC, IIAB, IIIAB, IIIE, IVA, IIE, IAB-MG, IAB-sLL, IAB-sLM, IAB-sHH, and IAB-sHL).

6.5.3 Genetics vs. ages

One key aspect to constraining the origins of the NC and CC reservoirs is determining the relative timing of isotopic heterogeneity in the early Solar System. Past studies have sought to provide such constraints through the comparison of genetic isotopic compositions to ages of metal-silicate segregation. For magmatic iron meteorites, ages of

metal-silicate segregation correspond to core formation ages. These ages, in turn, can be compared to thermal models of heat production by the decay of ^{26}Al, the primary heat-producing element in the early Solar System, in a planetary body. Kruijer et al. (2017) concluded from the determination of μ^{182}W isotopic compositions of NC- and CC-type magmatic iron meteorites that NC-type materials were initially present in the Solar System and CC-type materials were added to the outer Solar System approximately 0.5 Myr later.

Less attention has been focused on the relative timing of developing isotopic heterogeneity within a given reservoir. In part, this may be due to the debated interpretation of how nonmagmatic iron meteorites formed (impact heating *vs.* internal heating). Nonmagmatic iron meteorites in certain cases have distinct genetic isotopic compositions from magmatic iron meteorites but without constrained origins, the interpretation of their metal-silicate segregation ages are ambiguous. Nevertheless, this exercise was attempted by Hilton and Walker (2020) for NC-type iron meteorites. The authors of that study argued that a metal-silicate segregation age for nonmagmatic iron meteorites at least provide a lower age limit for tracing the timing of developing isotopic heterogeneity. This is because the precursor materials that form a planetesimal must have been in a given reservoir prior to the melting and metal-silicate segregation of the asteroid. By comparing genetic μ^{97}Mo and radiogenic μ^{182}W values, Hilton and Walker (2020) proposed that there was an addition of s-process rich material to the NC reservoir, and/or destruction and removal of a coupled r-/p-process rich component. Whether this was a rapid or gradual event was not constrained.

The genetic μ^{97}Mo and radiogenic μ^{182}W values of Auburn and Santiago Papasquero fall along the relationship observed by Hilton and Walker (2020) for NC-type iron meteorites (**Fig. 6.4**), permissive of a change in the isotopic composition of NC-type precursor materials with time. The same comparison for CC-type iron meteorites (**Fig. 6.5**) shows no relationship between μ^{97}Mo and μ^{182}W values for iron meteorites from this reservoir. Overall, this decoupled behavior for genetic μ^{97}Mo and radiogenic μ^{182}W values between the NC and CC reservoirs suggests that the causes of isotopic heterogeneity between these reservoirs may have differed.

Whether variations in μ^{182}W values among NC- and CC-type iron meteorites dominantly reflect differences in timing of metal-silicate segregation, however, has recently been challenged (Hellmann et al., 2019). Hellmann et al. (2019) proposed that variations may also reflect differences in parental Hf/W ratios and proposed that these ratios differed between NC- and CC-type parent bodies. If so, then identical μ^{182}W values of iron meteorites derived from parent bodies with variable parental Hf/W ratios could result in metal-silicate segregation ages that vary by 0 to 10 Myr (Hilton and Walker, 2020). As such, whether the μ^{182}W values of the ungrouped iron meteorites examined here reflect differences in metal-silicate segregation ages cannot currently be constrained and whether variations in genetic μ^{97}Mo and radiogenic μ^{182}W values partially or wholly represent variations in the isotopic composition of precursor materials with Hf/W ratio must also be considered.

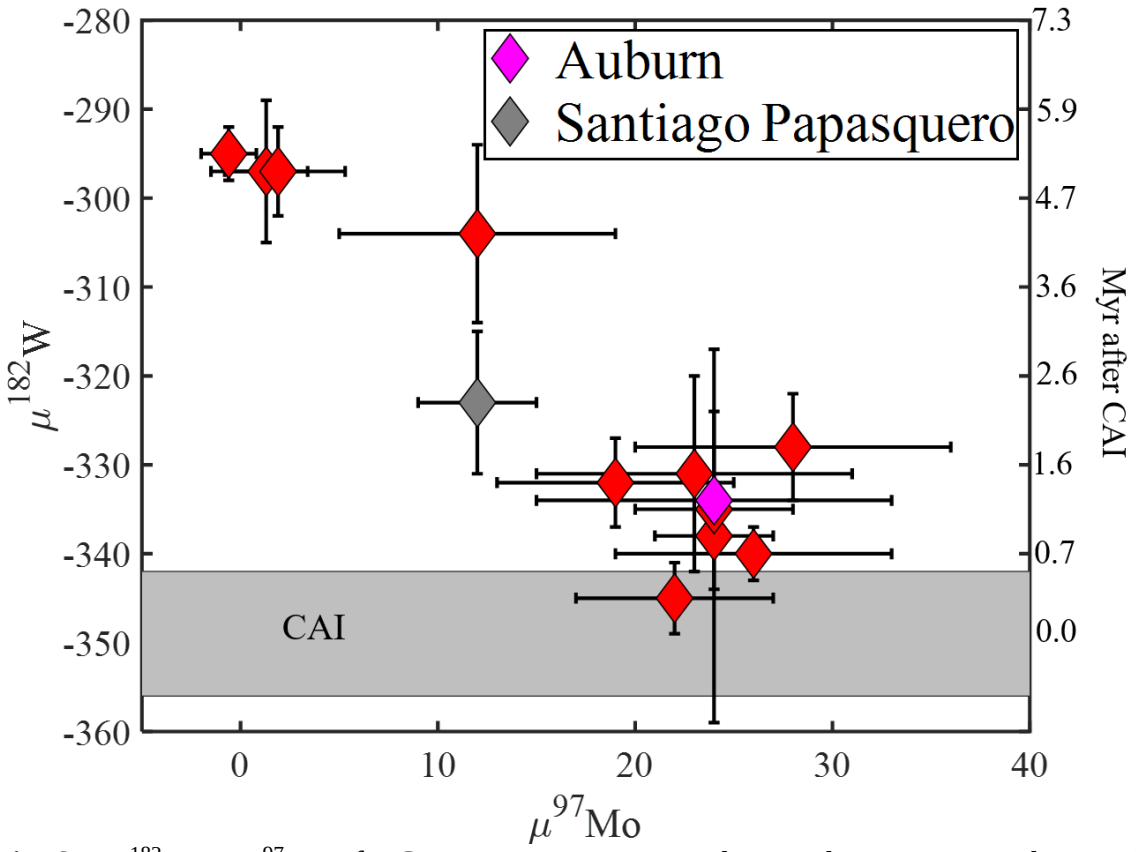

Fig. 6.4. μ^{182}W *vs.* μ^{97}Mo of NC-type iron meteorites. The gray box represents the initial μ^{182}W value of CAI (Kruijer et al., 2014b). Data are from Kruijer et al. (2017), Worsham et al. (2017), Kruijer and Kleine (2019), and Hilton and Walker (2020).

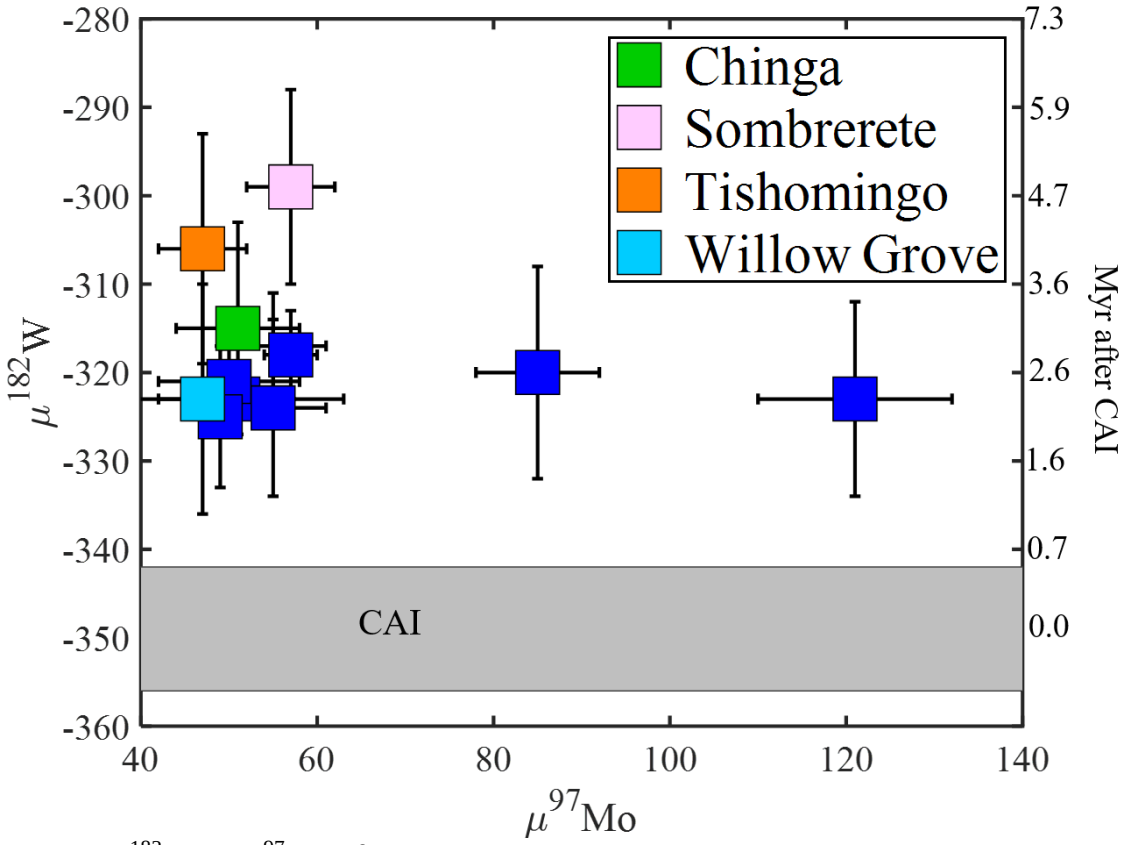

Fig. 6.5. μ^{182}W *vs.* μ^{97}Mo of CC-type iron meteorites. The gray box represents the initial μ^{182}W value of CAI (Kruijer et al., 2014b). Data are from Kruijer et al. (2017) and Hilton et al. (2019).

6.6 Conclusions

Genetic μ^{97}Mo and radiogenic μ^{182}W values of NC-type iron meteorites form a relationship while such a relationship among CC-type iron meteorites is absent. This observation may indicate that the isotopic composition of the NC reservoir varied with time, while the isotopic variability of the CC reservoir was not time-related.

Chapter 7: Conclusions

7.1 Key conclusions

This dissertation examines the origin and evolution of the noncarbonaceous (NC) and carbonaceous (CC) reservoirs by providing constraints on the genetics, ages, and chemical compositions of distinct, bulk planetary bodies sampled by iron meteorites. In Chapter 2, the genetics, ages, and chemical compositions of the South Byron Trio are reported, resulting in the isotopic and chemical characterization of a unique planetary body. In Chapter 3, the genetics and ages of NC-type meteorites are explored, and a potential relationship between these parameters is identified, suggesting that the isotopic composition of the NC reservoir may have changed with time, from a *s*-process depleted composition, relative to terrestrial materials, to a composition with no *s*-process depletion. In Chapters 4 and 5, the chemical compositions of the group IIAB, IID, IIF, IIIAB, and IIIF iron meteorite parent bodies are estimated, and relationships between bulk planetesimal chemical compositions and genetics/ages are examined. Finally, in Chapter 6, relationships between the genetics and ages of CC- and NC-type iron meteorites are explored. Variations in the genetic isotopic composition of iron meteorites with ages of metal-silicate segregation are decoupled between these two reservoirs. Overall, the major conclusions of this dissertation are:

1. Genetics *vs.* ages: Accretion ages of NC- and CC-type iron meteorite parent bodies are permissive of precursor materials to either reservoir being initially present in the Solar nebula. As such, it remains possible that the reservoirs formed simultaneously and the isotopic heterogeneity of these reservoirs reflects an initially heterogeneous parental molecular cloud or that some

isotopic heterogeneity was inherited from the parental molecular cloud while other heterogeneity was subsequently developed through a certain process, such as thermal processing, late injection of material, or physical sorting of materials. Finally, it remains possible that the initial parental molecular cloud was isotopically homogenous and a certain process caused isotopic heterogeneity in the Solar nebula.

Genetic isotopic compositions of iron meteorite parent bodies in the NC reservoir vary with the ages of iron meteorite formation while no such variations are observed for iron meteorite parent bodies from the CC reservoir. This indicates some time dependent association with isotopic evolution in at least one of the reservoirs. As such, the isotopic heterogeneity of the CC reservoir may be inherited from the parental molecular cloud while that of the NC reservoir may have evolved from thermal processing, late injection of material, or physical sorting of materials in the Solar nebula.

2. Genetics *vs.* chemical compositions: Comparison of the siderophile element chemical characteristics of NC- and CC-type iron meteorite parent bodies indicate that the processes setting planetesimal genetic isotopic compositions and planetesimal chemical characteristics in early-formed iron meteorite parent bodies were largely decoupled. If true, this may indicate that the cause of isotopic heterogeneity was due to the thermal processing, late injection, or physical sorting of materials with relatively large isotopic anomalies. As such, the minor addition or removal of an element from a given region of the Solar

nebula could impose an isotopic anomaly on the parent body scale without affecting the bulk chemical characteristics of the body.

3. Ages *vs*. chemical compositions: Bulk core chemical compositions and oxidation states of NC- and CC-type iron meteorite parent bodies may account for some differences in core formation ages among these planetesimals. If true, chemical characteristics of a parent body may account for some of the earlier core formation ages observed for NC-type parent bodies rather than an earlier formation age of the NC reservoir. The core/mantle mass ratios of NC-type iron meteorite parent bodies are estimated to be relatively larger than for CC-type iron meteorite parent bodies, indicating that more iron was segregated into NC-type cores. This, in turn, suggests that NC-type bodies may have been more reduced than CC-type bodies. This observation may indicate that NC-type bodies formed in the inner Solar System while CC-type bodies formed in the outer Solar System. As the outer Solar System is interpreted to be a more oxidizing, ice-rich environment, the accretion of a greater proportion of ice to CC bodies may hinder the melting of metal and silicate in these parent bodies and, therefore, delay core formation.

7.2 Future directions

The isotopic heterogeneity observed on the bulk meteorite scale for some elements indicates the heterogeneous accretion of isotopically distinct precursor materials by asteroids. This process has been proposed to be a product of the heterogeneous distribution of isotopically distinct precursor materials in the parental molecular cloud,

the heterogeneous distribution of isotopically distinct precursor materials in the Solar nebula, or a combination of these two ideas. This dissertation attempts to discern between these possibilities through the coupled genetic, chronologic, and chemical study of iron meteorite parent bodies. Ultimately, no clear relationships are observed among these parameters on the planetary scale that highlight the origin of isotopic heterogeneity for planetary bodies.

Consequently, I propose that additional study of the precursor materials to planetary bodies is needed. Since the isotopic heterogeneity of iron meteorite parent bodies is not clearly related to the chemical characteristics of these bodies, the cause of isotopic heterogeneity may be due to the processing or late injection of materials with highly variable isotopic compositions. As such, minor variations in the accretion of these materials may induce significant isotopic anomalies without altering chemical compositions on the planetary scale. It is, therefore, critical to identify the most isotopically anomalous materials in the parental molecular cloud and Solar nebula. These materials may be presolar grains, CAIs, chondrules, or matrix components.

Coupled isotopic and chemical study of presolar grains, CAIs, chondrules, or matrix components may allow for identifying the most isotopically anomalous materials as well as identify the materials that have been most affected by thermal processing, oxidation processing, physical sorting, or other conditions/processes that may have acted on nebular materials. This task could be completed through leaching protocols of chondrites. The occurrence of thermal processing may be evaluated by measuring the abundances of volatile elements in different leachates with isotopic composition whereas the occurrence

of oxidation processing may be evaluated by measuring the abundances of redox-sensitive elements.

The potential for a late injection of isotopically distinct materials to the Solar nebula may be explored by providing additional age constraints to presolar grains, CAIs, chondrules, and matrix components. Such age constraints, however, may require precise ages with < 1 Myr uncertainties. If isotopic anomalies are found for later forming materials, it may provide clear evidence for the late addition of materials.

Bibliography

Allègre C.J. and Luck J.-M. (1980) Osmium isotopes as petrogenetic and geological tracers. *Earth Planet. Sci. Lett.* **48**, 148–154.

Amelin Y., Krot A.N., Hutcheon I.D., Ulyanov A.A. (2002) Lead isotopic ages of chondrules and calcium-aluminum-rich inclusions. *Science* **297**, 1678-1683

Anders E. (1964) Origin, age, and composition of meteorites. *Space Science Reviews* **3**, 583-714.

Archer G.J., Ash R.D., Bullock E.S., Walker R.J. (2014) Highly siderophile elements and ^{187}Re-^{187}Os isotopic systematics of the Allende meteorite: Evidence for primary nebular processes and late-stage alteration. *Geochim. Cosmochim. Acta* **131**, 402-414.

Archer G.J., Mundl A., Walker R.J., Worsham E.A., Bermingham K.R. (2017) High-precision analysis of ^{182}W/^{184}W and ^{183}W/^{184}W by negative thermal ionization mass spectrometry: per-integration oxide corrections using measured ^{18}O/^{16}O. *Int. J. Mass Spectrom.* **414**, 80-86.

Archer G.J., Walker R.J., Tino J., Blackburn T., Kruijer T.S., Hellmann J.L. (2019) Siderophile element constraints on the thermal history of the H chondrite parent body. *Geochim. Cosmochim. Acta* **245**, 556-576.

Baker R.G.A., Schönbächler M., Rehkämper M., Williams H.M., Halliday A.N. (2010) The thallium isotope composition of carbonaceous chondrites – new evidence for live ^{205}Pb in the early solar system. *Earth Planet. Sci. Lett.* **291**, 39-47.

Benedix G.K., McCoy T.J., Keil K., Love S.G. (2000) A petrologic study of the IAB iron meteorites: Constraints on the formation of the IAB-Winonaite parent body. *Meteorit. Planet. Lett.* **35**, 1127-1141.

Bermingham K.R., Walker R.J., Worsham E.A. (2016) Refinement of high precision Ru isotope analysis using negative thermal ionization mass spectrometry. *Int. J. Mass Spectrom.* **403**, 15-26.

Bermingham K.R., Worsham E.A., Walker R.J. (2018) New insights into Mo and Ru isotope variation in the nebula and terrestrial planet accretionary genetics. *Earth Planet. Sci. Lett.* **487**, 221-229.

Birck J.-L., Roy-Barman M., Capmas F. (1997) Re–Os isotopic measurements at the femtomole level in natural samples. *Geostand. Newsl.* **20**, 9–27.

Boesenberg J.S., Delaney J.S., Hewins R.H. (2012) A petrological and chemical reexamination of main group pallasite formation. *Geochim. Cosmochim. Acta* **89**, 134-158.

Bouvier A., Gattacceca J., Agee C., Grossman J., Metzler K. (2017) The meteoritical bulletin, No. 104. *Meteorit. Planet. Sci*. **1**, 1-247.

Brennecka G.A., Borg L.E., Wadhwa M. (2013) Evidence for supernova injection into the solar nebula and the decoupling of r-process nucleosynthesis. *Proc. Natl. Acad. Sci.* **110** (43), 17241–17246.

Brennecka G.A., Budde G., Kleine T. (2015) Uranium isotopic composition and absolute ages of Allende chondrules. *Meteorit. Planet. Sci.* **50**, 1995-2002.

Buchwald V. F. (1975) *Handbook of Iron Meteorites*. University of California Press, Berkeley, CA.

Budde G., Burkhardt C., Brennecka G.A., Fischer-Godde M., Kruijer T.S., Kleine T. (2016a) Molybdenum isotopic evidence for the origin of chondrules and a distinct heritage of carbonaceous and non-carbonaceous meteorites. *Earth Planet. Sci. Lett.* **454**, 293-303.

Budde G., Kleine T., Kruijer T.S., Burkhardt C., Metzler K. (2016b) Tungsten isotopic constraints on the age and origin of chondrules. *Proc. Natl. Acad. Sci.* **113**, 2886-2891.

Budde G., Kruijer T.S., Kleine T. (2018) Hf-W chronology of CR chondrites: Implications for the timescales of chondrules formation and the distribution of ^{26}Al in the solar nebula. *Geochim. Cosmochim. Acta* **222**, 284-304.

Budde G., Burkhardt C., Kleine T. (2019) Molybdenum isotopic evidence for the late accretion of outer Solar System material to Earth. *Nature Astronomy* **3**, 736-741.

Burbidge, E.M., Burbidge, G.R., Fowler, W.A., Hoyle, F. (1957) Synthesis of the elements in stars. *Rev. Mod. Phys*. **29**, 547-650.

Burkhardt C., Kleine T., Oberli F., Pack A., Bourdon B., Wieler R. (2011) Molybdenum isotope anomalies in meteorites: constraints on solar nebula evolution and origin of the Earth. *Earth Planet. Sci. Lett*. **312**, 390-400.

Burkhardt C., Kleine T., Dauphas N., Wieler R. (2012) Origin of isotopic heterogeneity in the solar nebula by thermal processing and mixing of nebular dust. *Earth Planet. Sci. Lett.* **357-358**, 298-307.

Burkhardt C., Dauphas N., Hans U., Bourdon B., Kleine T. (2019) Elemental and isotopic variability in solar system materials by mixing and processing of primordial disk reservoirs. *Geochim. Cosmochim. Acta* **261**, 145-170.

Campbell A.J., Simon S.B., Humayun M., Gossman L. (2003) Chemical evolution of metal in refractory inclusions in CV3 chondrites. *Geochim. Cosmochim. Acta* **67**, 3119-3134.

Campbell A. J. and Humayun M. (2005) Compositions of group IVB iron meteorites and their parent melt. *Geochim. Cosmochim. Acta* **69**, 4733–4744.

Carlslaw H. S. and Jaeger J. C. (1959) *Conduction of heat in solids*. Oxford: Oxford University Press.

Chabot N.L. and Drake M.J. (2000) Crystallization of magmatic iron meteorites: The effects of phosphorus and liquid immiscibility. *Meteor. Planet. Sci.* **35**, 807-816.

Chabot N. L. and Jones J. H. (2003) Parameterizing iron meteorite partitioning experiments. *Meteorit. Planet. Sci*. **37**, 1425–1436.

Chabot N.L. (2004) Sulfur contents of the parental metallic cores of magmatic iron meteorites. *Geochim. Cosmochim. Acta* **68**, 3607-3618.

Chabot N.L., Wollack E.A., McDonough W.F., Ash R.D., Saslow S.A. (2017) Experimental determination of partitioning in the Fe-Ni system for applications to modeling meteoritic metals. *Meteorit. Planet. Sci* **52**, 1133-1145.

Chabot N.L. (2019) Revised trapped melt model for iron meteorites. *82nd Annual Meeting of The Meteoritical Society*, 6025 (abst).

Chen J.H., Papanastassiou D.A., Wasserburg G.J. (2010) Ruthenium endemic isotope effects in chondrites and differentiated meteorites. *Geochim. Cosmochim. Acta* **74**, 3851–3862.

Clayton, R.N. and Mayeda, T.K. (1996) Oxygen isotope studies of achondrites. *Geochim. Cosmochim. Acta* **60**, 1999-2017.

Cohen A.S. and Waters F.J. (1996) Separation of osmium from geological materials by solvent extraction for analysis by thermal ionization mass spectrometry. *Anal. Chimica Acta* **332**, 269–275.

Connolly, Jr H.C., Zipfel J., Grossman J.N., Folco L., Smith C., Jones R.H., Righter K., Zolensky M., Russell S.S., Benedix G.K., Yamaguchi A., Cohen B.A. (2006). The meteoritical bulletin, No. 90, 2006 September. *Meteorit. Planet. Sci.* **41**, 1383-1418.

Connelly J.N. and Bizzarro M. (2009) Pb-Pb dating of chondrules from CV chondrites by progressive dissolution. *Chem. Geol.* **259**, 143-151.

Connelly, J.N., Bizzarro, M., Krot, A.N., Nordlund, A., Wielandt, D., Ivanova, M.A. (2012) The absolute chronology and thermal processing of solids in the solar protoplanetary disk. *Science* **338**, 651-655.

Cook D.L., Walker R.J., Horan M.F., Wasson J.T., Morgan J.W. (2004) Pt–Re–Os systematics of group IIAB and IIIAB iron meteorites. *Geochim. Cosmochim. Acta* **68**, 1413–1431.

Cook D.L. and Schönbächler M. (2016) High-precision measurement of W isotopes in Fe-Ni alloy and the effects from the nuclear field shift. *J. Anal. At. Spectrom.* **31**, 1400-1405.

Corrigan C.M., McCoy T.J., Nagashima K. (2017) Oxygen isotopes of chromite in IVB iron meteorites: relationships to other meteorite groups and implications for formation. *Lunar Planet. Sci. Conf. XLVIII*, 2556 (abst).

Dauphas N., Marty B., Reisberg L. (2002) Molybdenum evidence for inherited planetary scale isotope heterogeneity of the protosolar nebula. *Astrophys. Journ.* **565**, 640-644.

Dauphas N., Davis A.M., Marty B., Reisberg L. (2004) The cosmic molybdenum-ruthenium isotope correlation. *Earth Planet. Sci. Lett.* **226**, 465-475.

Dauphas N., Remusat L., Chen J.H., Roskosz M., Papanastassiou D., Stodolna J., Guan Y., Ma C., Eiler J.M. (2010) Neutron-rich chromium isotope anomalies in supernova nanoparticles. *Astrophys. J.* **720**, 1577–1591.

Davis, A.M. and Olsen, E.J. (1991) Phosphate in pallasite meteorites as probes of mantle processes in small planetary bodies. *Nature* **353**, 637-640.

Davis A.M. (2006) Volatile Evolution and Loss. *Meteoritics and the Early Solar System II*. 295-307.

Davison T., Ciesla F., Collins G.S. (2012) Post-impact thermal evolution of porous planetesimals. *Geochim. Cosmochim. Acta* **95**, 252-269.

Dodson R. W., Forney G. J., Swift E. H. (1936) The extraction of ferric chloride from hydrochloric acid solutions by isopropyl ether. *J. Am. Chem. Soc.* **58**, 2573-2577.

Dottin J.W., Farquhar J., Labidi J. (2018) Multiple sulfur isotopic composotion of main group pallasites support genetic links to IIIAB iron meteorites. *Geochim. Cosmochim. Acta* **224**, 276-281.

Ek M., Hunt A.C., Lugaro M., Schönbächler M. (2019) The origin of *s*-process isotope heterogeneity in the solar protoplanetary disk. *Nature Astronomy* **4**, 273-281.

Fischer-Gödde M., Becker H., Wombacher F. (2010) Rhodium, gold, and other highly siderophile element abundances in chondritic meteorites. *Geochim. Cosmochim. Acta* **74**, 356-379.

Fischer-Gödde M., Burkhardt C., Kruijer T.S., Kleine T. (2015) Ru isotope heterogeneity in the solar protoplanetary disk. *Geochim. Cosmochim. Acta* **168**, 151–171.

Fischer-Gödde M. and Kleine T. (2017) Ruthenium isotopic evidence for an inner Solar System origin of the late veneer. *Nature* **541**, 525-527.

Gao X. and Thiemens M.H. (1993) Isotopic composition and concentration of sulfur in carbonaceous chondrites. *Geochim. Cosmochim. Acta* **57**, 3159-3169.

Garaud P., and Lin D.N.C. (2007) The effects of internal dissipation and surface irradiation on the structure of disks and the location of the snow line around Sun-like stars. *Astrophys. J.* **654**, 606–624.

Goldberg E., Uchiyama A., Brown H. (1951) The distribution of nickel, cobalt, gallium, palladium, and gold in iron meteorites. *Geochim. Cosmochim. Acta* **2**, 1-25.

Goldstein J.I., Scott E.R.D., Chabot N.L. (2009) Iron meteorites: Crystallization, thermal histories, parent bodies, and origin. *Chemie der Erde* **69**, 293-325.

Grossman L. (1972) Condensation in the primitive solar nebula. *Geochim. Cosmochim. Acta* **36**, 597-619.

Grossman J.N. (2000) The Meteoritical Bulletin, No. 84, 2000 August. *Meteorit. Planet. Sci.* **35**, A1999-A225.

Haack H. and Scott E.R.D. (1992) Asteroid core crystallization by inward dendritic growth. *J. Geophys. Res.* **97**, 14727-14734.

Haack H. and Scot E.R.D. (1993) Chemical fractionations in Group IIIAB iron meteorites: Origin by dendritic crystallization of an asteroidal core. *Geochim. Cosmochim. Acta* **57**, 3457-3472.

Hellmann J.L., Kruijer T.S., Van Orman J.A., Metzler K., Kleine T. (2019) Hf-W chronology of ordinary chondrites. *Geochim. Cosmochim. Acta* **258**, 290-309.

Hevey P.J. and Sanders I.S. (2006) A model for planetesimal meltdown by ^{26}Al and its implications for meteorite parent bodies. *Meteorit. Planet. Sci* **41**, 95-106.

Hilton C.D., Bermingham K.R., Walker R.J., McCoy T.J. (2019) Genetics, crystallization sequence, and age of the South Byron Trio iron meteorites: New insights to carbonaceous chondrite (CC) type parent bodies. *Geochim. Cosmochim. Acta* **251**, 217-228.

Hilton C.D. and Walker R.J. (2020) New implications for the origin of the IAB main group iron meteorites and the isotopic evolution of the noncarbonaceous (NC) reservoir. *Earth Planet. Sci. Lett.* **540**, 116248.

Hilton C.D., Ash R.D., Walker R.J. (In revision) Origin of the Eagle Station Pallasites from the IIF iron meteorite core. *Meteorit. Planet. Sci.*

Horan M.F., Walker R.J., Morgan J.W., Grossman J.N., Rubin A.E. (2003) Highly siderophile elements in chondrites. *Chem. Geol.* **196**, 5-20.

Humayun M., Teplyakova S.N., Lorenz C.A., Ivanova M.A., Korochantsev A.V. (2014) Siderophile element abundances in Karavannoe: implications for the origin of the Eagle Station Pallasites. *Lunar Planet. Sci. Conf*. XLV, 2293 (abst).

Hunt A.C., Benedix G.K., Hammond S.J., Bland P.A., Rehkämper M., Kreissig K., Strekopytov S. (2017a) A geochemical study of the winonaites: Evidence for limited partial melting and constraints on the precursor composition. *Geochim. Cosmochim. Acta* **199**, 13-30.

Hunt A.C., Ek M., Schönbächler M. (2017b) Separation of platinum from palladium and iridium in iron meteorites and accurate high-precision determination of platinum isotopes my multi-collector ICP-MS. *Geostand. Geoanal. Res.* **41**, 633-647.

Hunt A.C., Cook D.L., Lichtenberg T., Reger P.M., Ek M., Golabek G.J., Schönbächler M. (2018) Late metal-silicate separation on the IAB parent asteroid: Constraints from combined W and Pt isotopes and thermal modelling. *Earth Planet. Sci. Lett.* **482**, 490-500.

Jacobsen B., Yin Q.-z., Moynier F., Amelin Y., Krot A.N., Nagashima K., Hutcheon I.D., Palme H. (2008) ^{26}Al-^{26}Mg and ^{207}Pb-^{206}Pb systematics of Allende CAIs: canonical solar system initial ^{26}Al/^{27}Al ratio reinstated. *Earth Planet. Sci. Lett.* **272**, 353-364.

Jones J.H. and Drake M. J. (1983) Experimental Investigations of Trace Element Fractionation in Iron Meteorites, II: The influence of sulfur. *Geochim. Cosmochim. Acta* **47**, 1199-1209.

Jones J. H. and Malvin D. J. (1990) A nonmetal interaction model for the segregation of the trace metals during solidification of Fe–Ni–S, Fe–Ni–P, Fe–Ni–S–P alloys. *Metall. Trans*. B 21B, 697–706.

Jones R.H., Wasson J.T., Larson T., Sharp Z.D. (2003) Milton: a new, unique pallasite. *Lunar Planet. Sci. Conf. XXXIV*, 1683 (abst).

Kaminski E., Limare A., Kenda B., Chaussidon M. (2020) Early accretion of planetesimals unraveled by the thermal evolution of the parent bodies of magmatic iron meteorites. *Earth Planet. Sci. Lett*. **548**, 116469.

Kelly W.R. and Larimer J.W. (1977) Chemical fractionations in meteorites-VIII. Iron meteorites and the cosmochemical history of the metal phase. *Geochim. Cosmochim. Acta* **41**, 93-111.

Kennedy G.M. and Kenyon S.J. (2008) Planet formation around stars of various masses: the snow line and the frequency of giant planets. *Astrophys. J*. **673**, 502–512

Kleine, T., Mezger, K., Münker, C., Palme, H., Bischoff, A. (2004) ^{182}Hf–^{182}W isotope systematics of chondrites, eucrites, and Martian meteorites: chronology of core formation and mantle differentiation in Vesta and Mars. *Geochim. Cosmochim. Acta* **68**, 2935–2946.

Kleine T., Touboul M., Bourdon B., Nimmo F., Mezger K., Palme H., Jacobsen S.B., Yin Q.-Z., Halliday A.N. (2009) Hf-W chronology of the accretion and early evolution of asteroids and terrestrial planets. *Geochim. Cosmochim. Acta* **73**, 5150-5188.

Korochantsev A.V., Lorenz C.A., Ivanova M.A., Teplyakova S.N., Kononkova N.N., Roshina I.A., Borisovsky S.E., Bychkova Y.V., Franchi I.A., Greenwood R.C. (2013) Karavannoe: a new member of the Eagle Station Pallasite grouplet. *Lunar Planet. Sci. Conf*. XLIV, 2020 (abst).

Kracher A., Willis J., Wasson J.T. (1980) Chemical classification of iron meteorites-IX. A new group (IIF), revision of IAB and IIICD, and data on 57 additional irons. *Geochim. Cosmochim. Acta* **44**, 773-787.

Kracher A. (1985) The evolution of partially differentiated planetesimals: evidence from iron meteorite groups IAB and IIICD. *J. Geophys. Res.* **90**, C689-C698.

Krot, A.N., Keil, K., Goodrich, C.A., Scott, E.R.D., Weisberg, M.K., 2004. Classification of meteorites. In: Davis, A.M. (Ed.), Treatise on Geochemistry. : Meteorites, Comets, Planets, 1. Elsevier-Pergamon, Oxford, pp. 83–128.

Kruijer T.S., Fischer-Gödde M., Kleine T., Sprung P., Leya I., Wieler R. (2013) Neutron capture on Pt isotopes in iron meteorites and the Hf-W chronology of core formation in planetesimals. *Earth Planet. Sci. Lett*. **361**, 162-172.

Kruijer T.S., Touboul M., Fischer-Gödde M., Bermingham K.R., Walker R.J., Kleine T. (2014a) Protracted core formation and rapid accretion of protoplanets. *Science* **344**, 1150–1154.

Kruijer T.S., Kleine T., Fischer-Gödde M., Burkhardt C., Wieler R. (2014b) Nucleosynthetic W isotope anomalies and the Hf-W chronometry of Ca-Al-rich inclusions. *Earth Planet. Sci. Lett.* **403**, 317-327.

Kruijer T.S., Burkhardt C., Budde G., Kleine T. (2017) Age of Jupiter inferred from the distinct genetics and formation times of meteorites. *Proc. Natl. Acad. Sci.* **114**, 6712-6716.

Kruijer T.S. and Kleine T. (2018) No ^{182}W excess in the Ontong Java Plateau source. *Chem. Geol.* **485**, 24-31.

Kruijer T.S. and Kleine T. (2019) Age and origin of IIE iron meteorites inferred from Hf-W chronology. *Geochim. Cosmochim. Acta* **262**, 92-103.

Kruijer T.S., Kleine T., Borg L.E. (2019) The great isotopic dichotomy of the early Solar System. *Nat. Astron.*

Lacar M., Podolak M., Sasselov D., Chiag E. (2006) On the location of the snow line in a protoplanetary disk. *Astrophys. J.* **640**, 1115–1118.

LaTourrette T. and Wasserburg G.J. (1998) Mg diffusion in anorthite: Implications for the formation of early solar system planetesimals. *Earth Planet. Sci. Lett*. **158**, 91–108.

Lee D.-C. and Halliday A.N. (2000) Accretion of primitive planetesimals: Hf-W isotopic evidence from enstatite chondrites. *Science* **288**, 1629-1631.

Leya I., Wieler R., Halliday A.N. (2003) The influence of cosmic-ray production on extinct nuclide systems. *Geochim. Cosmochim. Acta* **67**, 529-541.

Leya I., Schönbächler M., Wiechert U., Krahenbuhl U., Halliday A.N. (2008) Titanium isotopes and the radial heterogeneity of the solar system. *Earth Planet. Sci. Lett*. **266**, 233–244.

Leya I. and Masarik J. (2013) Thermal neutron capture effects in radioactive and stable nuclide systems. *Meteorit. Planet. Sci* **48**, 665-685.

Lodders K. and Fegley B. (1998) The Planetary Scientist's Companion. Oxford Univ Press, New York, 371 pp.

Lodders K. (2003) Solar System abundances and condensation temperatures of the elements. *Ap. J.* **591**, 1220-1247.

Lovering J.F., Nichiporuk W., Chodos A., Brown H. (1957) The distribution of gallium, germanium, cobalt, chromium, and copper in iron and stony-iron meteorites in relation to nickel content and structure. *Geochim. Cosmochim. Acta* **11**, 263-278.

Lu Q. and Masuda A. (1994) The isotopic composition and atomic weight of molybdenum. *Int. J. Mass Spectrom. Ion Process*. **130**, 65–72.

Ludwig K. R. (2003) User's Manual for Isoplot 3.00. Berkeley Geochronology Center Special Publication No. 4, Berkeley, CA, 70 pp.

Malvin D.J., Wasson J.T., Clayton R.N., Mayeda T.K., da Silva Curvello W. (1985) Bocaiuva – A silicate-inclusion bearing iron meteorite related to the Eagle-Station pallasites. *Meteoritics* **20**, 259-273.

Markowski A., Quitte´G., Halliday A.N., Kleine T. (2006) Tungsten isotopic compositions of iron meteorites: chronological constraints vs. cosmogenic effects. *Earth Planet. Sci. Lett.* **242**, 1–15.

Masarik J. (1997) Contribution of neutron-capture reactions to observed tungsten isotopic ratios. *Earth Planet. Sci. Lett*. **152**, 181-185.

McCoy T.J., Walker R.J., Goldstein J.I., Yang J., McDonough W.F., Rumble D., Chabot N.L., Ash R.D., Corrigan C.M., Michael J.R., Kotula P.G. (2011) Group IVA irons: new constraints on the crystallization and cooling history of an asteroidal core with a complex history. *Geochim. Cosmochim. Acta* **75**, 6821-6843.

McCoy T.J., Corrigan C.M., Nagashima K., Reynolds V.S., Walker R.J., McDonough W.F., Ash R.D. (2017) Milton and the South Byron Trio: an oxidized parent body with an outside-in crystallization core. *Lunar Planet. Sci. Conf. XLVIII*, 2241 (abst).

McCoy T.J., Corrigan C.M., Nagashima K., Reynolds V.S., Ash R.D., McDonough W.F., Yang J., Goldstein J.I., Hilton C.D. (2019) The Milton pallasite and South Bryon Trio irons: Evidence for oxidation and core crystallization. *Geochim. Cosmochim. Acta* **259**, 358-370.

McSween H.Y. and Richardson S.M. (1977) The composition of carbonaceous chondrite matrix. *Geochim. Cosmochim. Acta* **41**, 1145-1161.

Mittlefehldt D. W. (1980) The composition of mesosiderite olivine clasts and the implications for the origins of pallasites. *Earth Planet. Sci. Lett*. **51**, 29–40.

Mundl A., Touboul M., Jackson M.G., Day J.M.D., Kurz M.D., Lekic V., Helz R.T., Walker R.J. (2017) Tungsten-182 heterogeneity in modern ocean island basalts. *Science* **356**, 66-69.

Mundl A., Walker R.J., Reimink J.R., Rudnick R.L., Gaschnig R.M. (2018) Tungsten-182 in the upper continental crust: Evidence from glacial diamictites. *Chem. Geol.* **494**, 144-152.

Nagai H., Honda M., Imamura M., Kobayashi K. (1993) Comogenic ^{10}Be and ^{26}Al in metal, carbon, and silicate of meteorites. *Geochim. Comochim. Acta* **57**, 3705-3723.

Nanne J.A.M., Nimmo F., Cuzzi J.N., Kleine T. (2019) Origin of the non-carbonaceous-carboanceous meteorite dichotomy. *Earth Planet. Sci. Lett.* **511**, 44-54.

Nicolussi G.K., Pellin M.J., Lewis R.S., Davis A.M., Amari S., Clayton R.N. (1998a) Molybdenum isotopic composition of individual presolar silicon carbide grains from the Murchison meteorite. *Geochim. Cosmochim. Acta* **62**, 1093-1104.

Nicolussi G.K., Pellin M.J., Lewis R.S., Davis A.M., Clayton R.N., Amari S. (1998b) Zirconium and molybdenum in individual circumstellar graphite grains: New isotopic data on the nucleosynthesis of heavy elements. *Astrophys. J.* **504**, 492-499.

Nier A.O. (1950) A redetermination of the relative abundances of the isotopes of carbon, nitrogen, oxygen, argon, and potassium. *Phys. Rev*. **77,** 789–793.

Nishiizumi K., Finkel R. C. and Caffee M. W. (1995) Cosmogenic radionuclides in Dongling and Nantan iron meteorites: case of heavily shielded Chinese twins? *Meteoritics* **30**, 556

Nittler L.R., O'D Alexander C.M., Liu N., Wang J. (2018) Extremely 54Cr- and 50Ti-rich presolar oxide grains in a primitive meteorite: Formation in rare types of supernovae and implications for the astrophysical context of solar system birth. *Astrophys. J.* **856**, 1-7.

Norris T.L., Gancarz A.J., Rokop D.J., Thomas K.W. (1983) Half-life of ^{26}Al. *J. Geophys. Res.* **88**, B331-B333.

Pernicka E. and Wasson J.T. (1987) Ru, Re, Os, Pt and Au in iron meteorites. *Geochim. Cosmochim. Acta* **51**, 1717-1726.

Poole G.M., Rehkamper M., Coles B.J., Goldberg T., Smith C.L. (2017) Nucleosynthetic molybdenum isotope anomalies in iron meteorites-new evidence for thermal processing of solar nebula material. *Earth Planet. Sci. Lett.* **473**, 215-226.

Qin L., Dauphas N., Janney P.E., Wadhwa M. (2008) Tungsten nuclear anomalies in planetesimal cores. *Astrophys. Journ.* **674**, 1234–1241.

Rasmussen K.L., Malvin D.J., Buchwald V.F., Wasson J.T. (1984) Compositional trends and cooling rates of group IVB iron meteorites. *Geochim. Cosmochim. Acta* **48**, 805-813.

Rasmussem K.L., Haack H., Ulff-Møller F. (2001) Metallographic cooling rates of group IIF iron meteorites. *Meteorit. Planet. Sci.* **36**, 883-896.

Rayleigh L. (1942) The stone–iron meteorites called pallasites: a synthetic study of their structure and probable mode of formation. *Proc. R. Soc. Lond*. A 179, 386–393.

Regelous M., Elliott T., Coath C.D. (2008) Nickel isotope heterogeneity in the early Solar System. *Earth Planet. Sci. Lett*. **272**, 330–338.

Rubin A.E. (2018) Carbonaceous and noncarbonaceous iron meteorites: Differences in chemical, physical, and collective properties. *Meteorit. Planet. Sci.* **53**, 2357-2371.

Schaudy R. and Wasson J.T. (1972) The chemical classification of iron meteorites. VI. A reinvestigation of irons with Ge concentrations lower than 1 ppm. *Icarus* **17**, 174-192.

Schiller M., Bizzarro M., Fernandes V.A. (2018) Isotopic evolution of the protoplanetary disk and the building blocks of Earth and the Moon. *Nature* **555**, 507-510.

Schulz T., Münker C., Palme H., Mezger K. (2009) Hf-W chronometry of the IAB iron meteorite parent body. *Earth Planet. Sci. Lett*. **280**, 185-193.

Schulz T., Upadhyay D., Münker C., Mezger K. (2012) Formation and exposure history of non-magmatic iron meteorites and winonaites: Clues from Sm and W isotopes. *Geochim. Cosmochim. Acta* **85**, 200-212.

Scott E.R.D. (1972) Chemical fractionation in iron meteorites and its interpretation. *Geochim. Cosmochim. Acta* **36**, 1205-1236.

Scott E.R.D., Wasson J.T., Buchwald V.F. (1973) The chemical classification of iron meteorites-VII. A reinvestigation of irons with Ge concentrations between 25 and 80 ppm. *Geochim. Cosmochim. Acta* **37**, 1957-1983.

Scott E.R.D. and Wasson J.T. (1976) Chemical classification of iron meteorites-VIII. Groups IC, IIE, IIIF and 97 other irons. *Geochim. Cosmochim. Acta* **40**, 103-115.

Scott E.R.D. (1977a) Geochemical relationships between some pallasites and iron meteorites. *Mineralogical magazine* **41**, 265-272.

Scott E.R.D. (1977b) Composition, mineralogy and origin of group IC iron meteorites. *Earth Planet. Sci. Lett.* **37**, 273-284.

Scott E.R.D. (1977c) Formation of olivine–metal textures in pallasite meteorites. *Geochim. Cosmochim. Ac*ta **41**, 693–710.

Scott E.R.D. (1977d) Pallasites-metal composition, classification and relationships with iron meteorites. *Geochim. Cosmochim. Acta* **41**, 349-360.

Scott E.R.D. and Taylor J.G. (1990) Origins of pallasites at the core–mantle boundaries of asteroids. *Lunar Planet. Sci. Conf*. XXI, 1119-1120 (abst).

Shirey S.B. and Walker R.J. (1995) Carius tube digestion for low-blank rhenium-osmium analysis. *Anal. Chem*. **34**, 2136-2141.

Shirey S.B. and Walker R.J. (1998) The Re-Os isotope system in cosmochemistry and high-temperature geochemistry. *Annu. Rev. Earth Planet. Sci*. **26**, 423-500.

Smoliar M.I. (1996) Re-Os isotopic study of magmatic iron meteorites. Ph.D. dissertation, University of Maryland, 105 pp.

Smoliar M.I., Walker R.J., Morgan J.W. (1996) Re–Os ages of group IIA, IIIA, IVA, and IVB iron meteorites. *Science* **271**, 1099–1102.

Sprung P., Scherer E.E., Upadhyay D., Leya I., Mezger K. (2010) Non-nucleosynthetic heterogeneity in non-radiogenic stable Hf isotopes: implications for early solar system chronology. *Earth Planet. Sci. Lett.* **295**, 1-11.

Sugiura N. and Fujiya W. (2014) Correlated accretion ages and ε^{54}Cr of meteorite parent bodies and the evolution of the solar nebula. *Meteorit. Planet. Lett.* **49**, 772-787.

Taylor G.J. (1992) Core formation in asteroids. *J. Geophys. Res.* **97**, 14717-14726.

Theis K.J., Schönbächler M., Benedix G.K., Rehkämper M., Andreasen R., Davies C. (2013) Palladium-silver chronology of IAB iron meteorites. *Earth Planet. Sci. Lett*. **361**, 402-411.

Tornabene H.A. (2020) Genetics, age and crystallization of group IC and IIC iron meteorites. Masters thesis, University of Maryland, 99 pp.

Tornabene H.A., Hilton C.D., Bermingham K.R., Ash R.D., Walker R.J. (2020) Genetics, age and crystallization history of group IIC iron meteorites. *Geochim. Cosmochim. Acta* **288**, 36-50.

Touboul M., Kleine T., Bourdon B., Van Orman J.A., Maden C., Zipfel J. (2009) Hf-W thermochronometry: II. Accretion and thermal history of the acapulcoite-lodranite parent body. *Earth Planet. Sci. Lett.* **284**, 168-178.

Touboul M. and Walker R.J. (2012) High precision tungsten isotope measurement by thermal ionization mass spectrometry. *Int. J. of Mass Spectrom.* **309**, 109-117.

Trinquier A., Birck J.-L., Allégre C.J. (2007) Widespread ^{54}Cr heterogeneity in the inner solar system. *Astrophys. J.* **655**, 1179-1185.

Trinquier A., Elliot T., Ulfbeck D., Coath C., Krot A.N., Bizzarro M. (2009) Origin of nucleosynthetic isotope heterogeneity in the solar protoplanetary disk. *Science* **324**, 374-376.

Ulff-Møller F. (1998) Effects of liquid immiscibility on trace element fractionation in magmatic iron meteorites: A case study of group IIIAB. *Meteorit. Planet. Sci.* **33**, 207-220.

Urey H.C. (1966) Chemical evidence relative to the origin of the solar system. *Mon. Not. R. Astr. Soc.* **131**, 199-223.

Vockenhuber C., Oberli F., Bichler M., Ahmad I., Quittem G., Meier M., Halliday A.N., Lee D.-C., Kutschera W., Steier P., Gehrke R.J., Helmer R.G. (2004) New half-life measurement of ^{182}Hf: Improved chronometer for the early solar system. *Physical Review Lette*rs **93**, 172501-1-172501-4.

Vogel N. and Renne P.R. (2008) ^{40}Ar-^{39}Ar dating of plagioclase grain size separates from silicate inclusions in IAB iron meteorites and implications for the thermochronological evolution of the IAB parent body. *Geochim. Cosmochim. Acta* **72**, 1231-1255.

Volkening J., Köppe M., Heumann K.G. (1991) Tungsten isotope ratio determinations by negative thermal ionization mass spectrometry. *Int. J. Mass Spectrom.* **107**, 361–368.

Walker R.J., McDonough W.F., Honesto J., Chabot N.L., McCoy T.J., Ash R.D., Bellucci J.J. (2008) Modeling fractional crystallization of group IVB iron meteorites. *Geochim. Cosmochim. Acta* **72**, 2198-2216.

Walker R.J. (2012) Evidence for homogeneous distribution of osmium in the protosolar nebula. *Earth Planet. Sci. Lett.* **351-352**, 36-44.

Walker R.J. (2016) Siderophile elements in tracing planetary formation and evolution. *Geochemical Perspectives* **5**, 1-145.

Wallerstein G. et al. (1997) Synthesis of the elements in stars: forty years of progress. *R. Mod. Phys.* **69**, 995-1084.

Warren P.H. (2011) Stable-isotopic anomalies and the accretionary assemblage of the Earth and Mars: a subordinate role for carbonaceous chondrites. *Earth Planet. Sci. Lett.* **311**, 93–100.

Wasson J.T. (1967) The chemical classification of iron meteorites: I. A study of iron meteorites with low concentrations of gallium and germanium. *Geochim. Cosmchim. Acta* **31**, 161-180.

Wasson J.T. and Kimberlin J. (1967) The chemical classification of iron meteorites-II. Irons and pallasites with germanium concentrations between 8 and 100 ppm. *Geochim. Cosmchim. Acta* **31**, 2065-2093.

Wasson J.T. (1969) The chemical classification of iron meteorites-III. Hexadrites and other irons with germanium concentrations between 80 and 200 ppm. *Geochim. Cosmochim. Acta* **33**, 859-876.

Wasson J.T. (1974) Meteorites–Classification and Properties. Springer, New York, 316 pp.

Wasson J.T., Ouyang X., Wang J., Jerde E. (1989) Chemical classification of iron meteorites: XI. Multi-element studies of 38 new irons and the high abundance of ungrouped irons from Antarctica. *Geochim. Cosmochim. Acta* **53**, 735-744.

Wasson J.T. (1999) Trapped melt in IIIAB irons: solid/liquid elemental partitioning during the fractionation of the IIIAB magma. *Geochim. Cosmochim. Acta* **63**, 2875-2889.

Wasson J.T. and Richardson J.W. (2001) Fractional trends among IVA iron meteorites: contrasts with IIIAB trends. *Geochim. Cosmochim. Acta* **65**, 951-970.

Wasson J.T. and Kallemeyn G.W. (2002) The IAB iron-meteorite complex: a group, five subgroups, numerous grouplets, closely related, mainly formed by crystal segregation in rapidly cooling melts. *Geochim. Cosmochim. Acta* **66**, 2445–2473.

Wasson J.T. and Choi B.-G. (2003) Main-group pallasites: chemical composition, relationship to IIIAB irons, and origin. *Geochim. Cosmochim. Acta* **67**, 3079-3096.

Wasson J.T. and Huber H. (2006) Compositional trends among IID irons; their possible formation from the P-rich lower magma in a two-layer core. *Geochim. Cosmochim. Acta* **70**, 6153-6167.

Wasson J.T., Huber H., Malvin D.J. (2007) Formation of IIAB iron meteorites. *Geochim. Cosmochim. Acta* **71**, 760-781.

Wasson J.T. and Choe W.-H. (2009) The IIG iron meteorites: Probable formation in the IIAB core. *Geochim. Cosmochim. Acta* **73**, 4879-4890.

Willis J. (1981) Antimony in iron meteorites. *Earth Planet. Sci. Lett.* **53**, 1-10.

Willis, J., and J. I. Goldstein (1982) The effects of C, P, and S on trace element partitioning during solidification in Fe-Ni alloys, Proc. Lunar Planet. Sci. Conf. 13th. in *J. Geophys. Res*. **87**, A435-A445.

Wittig N., Humayun M., Brandon A.D., Huang S., Leya I. (2013) Coupled W-Os-Pt isotope systematics in IVB iron meteorites: In situ neutron dosimetry for W isotope chronology. *Earth Planet. Sci. Lett.* **361**, 152-161.

Wood J. A. (1978) Nature and evolution of the meteorite parent bodies: evidence from petrology and metallurgy. In NASA, Washington Asteroids (SEE N78-29007 19-91), pp. 45–55.A

Wood J.A. (2005) The chondrite types and their origins. In: Krot, A.N., Scott, E.R.D., Reipurth, B. (Eds.), Chondrites and the Protoplanetary Disk, Astronomical Society of Pacific Conference Series, **247**, 953–971.

Woolum D. S. and Cassen P. (1999) Astronomical constraints on nebular temperatures: Implications for planetesimal formation. *Meteorit. Planet. Sci* **34**, 897–907.

Worsham E.A., Bermingham K.R., Walker R.J. (2016a) Siderophile element systematics of IAB complex iron meteorites: new insights into the formation of an enigmatic group. *Geochim. Cosmochim. Acta* **188**, 261-283.

Worsham E.A., Walker R.J., Bermingham K.R. (2016b) High-precision molybdenum isotope analysis by negative thermal ionization mass spectrometry. *Int. J. Mass Spectrom.* **407**, 51-61.

Worsham E.A., Bermingham K.R., Walker R.J. (2017) Characterizing cosmochemical materials with genetic affinities to the Earth: Genetic and chronological diversity within the IAB iron meteorite complex. *Earth Planet. Sci. Lett*. **467**, 157-166.

Worsham E.A., Burkhardt C., Budde G., Fischer-Gödde M., Kruijer T.S., Kleine T. (2019) Distinct evolution of the carbonaceous and non-carbonaceous reservoirs: Insights from Ru, Mo, and W isotopes. *Earth Planet. Sci. Lett.* **521**, 103-112.

Yamakawa A., Tamashita K., Makishima A., Nakamura E. (2010) Chromium isotope systematic of achondrites: chronology and isotopic heterogeneity of the inner solar system bodies. *Astrophys. J.* **720**, 150-154.

Yang J., Goldstein J.I., Scott E.R.D. (2010) Main-group pallasites: thermal history, relationship to IIIAB irons, and origin. *Geochim. Cosmochim. Acta* **74**, 4471–4492.